Università degli Studi di Roma
"La Sapienza"

Facoltà di Scienze Matematiche, Fisiche e Naturali

Ph.D. Thesis in Astronomy - XIX Course

OLIMPO
A Components Separator of the Microwave Sky

Author
Luca Conversi

Supervisor
Dott.ssa Silvia Masi

Referee
Prof. Paolo de Bernardis

Academic Year 2006-2007

A young specialist in English Literature
lectured me severely on the fact that
in every century people have thought
they understood the Universe at last,
and in every century they were proved to be wrong.
It follows that the one thing we can say about
our modern "knowledge" is that it is wrong.

My answer to him was:
≪When people thought the Earth was flat, they were wrong.
When people thought the Earth was spherical, they were wrong.
But if you think that thinking the Earth is spherical
is just as wrong as thinking the Earth is flat,
then your view is wronger than both of them put together.≫

Isaac Asimov

Contents

Introduzione

La scoperta nel 1965 da parte dei due premi Nobel Penzias e Wilson della presenza di una radiazione diffusa avente lo spettro di corpo nero a $T_{CMB} = 2.725K$ è la più evidente conferma sperimentale della *teoria del Big Bang*. Poiché questo segnale, diffuso in tutto il cielo, ha il picco di emissione a lunghezze d'onda millimetriche ($\nu = 70 \div 200 GHz$), viene chiamato *radiazione di fondo cosmico a microonde* (*Cosmic Microwave Background*, CMB). Esso fornisce, assieme alle sue anisotropie, importanti indicazioni sulle fasi primordiali e sull'evoluzione dell'Universo. La prima verifica sperimentale della presenza di anisotropie nello spettro della radiazione di fondo cosmico si è avuta nel 1992 grazie a *COBE*, ma solo nel 2000 grazie agli esperimenti *BOOMERanG* e *MAXIMA* sono state risolte con alto rapporto segnale rumore la anisotropie a scale inferiori al grado, mentre nel 2003 è stata portata a termine dal satellite *WMAP* la prima survey ad alta risoluzione angolare a tutto cielo.

Lo spettro della CMB può venire deformato a causa dell'effetto Sunyaev-Zel'dovich, cioè all'interazione tra il gas caldo presente negli ammassi di galassie e la radiazione di fondo cosmico. Inoltre, all'allontanarsi delle lunghezze d'onda di massima emissione della CMB, il contributo della polvere interstellare ed il segnale di fondo dovuto a sorgenti non risolte ad alto redshift sono dominanti. Quelli che a prima vista sembrano dei disturbi da rimuovere, sono in realtà degli "strumenti astrofisici" molto utili.

L'esperimento *OLIMPO* (*Osservatorio nel Lontano Infrarosso Montato su Pallone Orientabile*) si propone di indagare porzioni di cielo selezionate, alle frequenze $\nu = 143$, 217, 353 e $545 GHz$, con risoluzione migliore di $\sim 5'$. Esso è costituito da un telescopio *Cassegrain* di $2.6m$ di diametro e da quattro mosaici di bolometri (uno per banda) all'interno di un criostato ad ^{3}He che permette di raffreddare i rivelatori ad una temperatura di $300mK$. L'esperimento viene agganciato ad un pallone stratosferico, per effettuare voli circumpolari a lunga durata ($10 \div 15$ giorni), il primo dei quali è previsto per luglio 2008.

L'alta risoluzione angolare e l'ampio intervallo di frequenze coperte da *OLIMPO* permettono di realizzare i seguenti obiettivi scientifici:

- Rivelare le anisotropie della radiazione di fondo cosmico ad alti multipoli ($\ell \gtrsim 600$): misure di alta precisione sono state effettuate solamente con interferometri a basse frequenze ($\nu \sim 30 GHz$) e con bolometri a $140 GHz$ dal polo sud. Grazie alla maggiore sensibilità ed alla copertura spettrale molto più estesa, OLIMPO migliorerà sensibilmente questa misura, che permette lo studio della coda di smorzamento dello spettro di potenza angolare della CMB (*Silk damping*).

- Misurare l'effetto Sunyaev-Zel'dovich dovuto agli ammassi di galassie: non è possibile studiare le caratteristiche di ammassi ad alto redshift da misure nei raggi X, poiché il segnale è troppo debole. La peculiarità dell'effetto Sunyaev-Zel'dovich di essere indipendente dal redshift dell'ammasso lo rende uno strumento fondamentale per misure cosmologiche. Con esso si potrà fare una statistica più completa degli ammassi e della loro formazione, da cui ricavare informazioni sui parametri cosmologici.

- Studio della radiazione di fondo nel lontano infrarosso (*Far InfraRed Background*, FIRB), dovuto a galassie non risolte ad alto redshift, con relative implicazioni riguardo la formazione di galassie e l'epoca immediatamente successiva alla ricombinazione.

Durante questi anni di lavoro di ricerca nell'ambito del Dottorato in Astronomia, mi sono occupato principalmente della progettazione, ottimizzazione, sviluppo e realizzazione delle ottiche dell'esperimento; ho inoltre effettuato delle simulazioni atte a verificare la capacità di *OLIMPO* di separare le diverse componenti astrofisiche nonché di distinguere tra diversi modelli fenomenologici.

La tesi è articolata in sei capitoli, che affrontano le seguenti tematiche:

Capitolo 1 Introduzione teorica sui processi fisici rilevanti nelle bande osservate dall'esperimento *OLIMPO*: la radiazione di fondo cosmico a microonde e sue anisotropie, l'effetto Sunyaev-Zel'dovich, le polvere interstellare ed il fondo cosmico infrarosso extragalattico.

Capitolo 2 Descrizione generale dell'esperimento *OLIMPO*: telescopio, modulazione del segnale, criostato e rivelatori.

Capitolo 3 Analisi e simulazioni di diverse configurazioni ottiche: di ognuna vengono mostrati vantaggi e svantaggi, sia da un punto di vista ottico che meccanico e realizzativo. Sono infine state svolte ulteriori analisi sulla configurazione definitiva.

Capitolo 4 Progettazione e realizzazione meccanica delle ottiche e della scatola che dovrà contenerle; successivamente si sono analizzate e pulite le loro superfici; infine, si sono effettuati i test di allineamento.

Capitolo 5 Introduzione all'analisi in ottica Gaussiana e disegno del profilo delle antenne che verranno usate nei mosaici di bolometri.

Capitolo 6 Descrizione dei modelli usati per simulare i processi fisici dominanti nei quattro canali di *OLIMPO*, tenendo conto dei suoi parametri sperimentali; generazione delle mappe e successiva separazione delle componenti; infine, analisi dei segnali estratti e loro sensibilità alla variazione dei modelli usati.

Introduction

The discovery in 1965 made by the two Nobel prizes Penzias and Wilson of the presence of diffuse radiation with a black body spectrum at $T_{CMB} = 2.725K$ is the most relevant experimental verification of the *Big Bang theory*. Since this signal emits in the whole sky and has its emission maximum at millimeter wavelengths ($\nu = 70 \div 200 GHz$), it is called *Cosmic Microwave Background* (CMB). It provides, together with its anisotropy, significant information on the primordial phases and on the evolution of the Universe. The first experimental proof of the presence of anisotropies in the spectrum of the cosmic background radiation was achieved in 1992 by *COBE*. Only in 2000 CMB anisotropy was resolved at angular scales below 1° with a high signal to noise ratio by the *BOOMERanG* and *MAXIMA* experiments. The first high resolution all sky survey was completed in 2003 by the *WMAP* satellite.

The CMB spectrum can be deformed by the Sunyaev-Zel'dovich effect, i.e. the interaction between the hot gas present in the cluster of galaxies and the photons of the cosmic background radiation. Moreover, at shorter wavelengths in respect to the CMB emission maximum, the contribution of the interstellar medium and the background signal due to unresolved sources at high redshift dominates over the CMB anisotropy. Those that at a first sight look like nuisance foreground signals, are instead very useful "astrophysical tools".

The purpose of the *OLIMPO* experiment (*Osservatorio nel Lontano Infrarosso Montato su Pallone Orientabile*) is to observe selected portions of sky at frequencies $\nu = 143$, 217, 353 and $545 GHz$, with an angular resolution better than $\sim 5'$. OLIMPO is composed of a *Cassegrain* telescope of $2.6m$ of diameter with four arrays of bolometers in the focal plane, cooled at $300mK$ by a long duration ^{3}He cryostat. The experiment is mounted on a stratospheric balloon payload, and uses long duration ($10 \div 15$ days) circumpolar flights: the first of them is foreseen for july 2008.

The high angular resolution and the wide range of frequencies covered by *OLIMPO* allow to achieve the following scientific goals:

- Measuring CMB anisotropies at high multipoles ($\ell \gtrsim 600$). High accuracy measurements have been done only with low frequency ($\nu \sim 30 GHz$) interferometers and with bolometers at $140 GHz$ from the south pole. Taking advantage of the wider frequency coverage and of the highest sensitivity, OLIMPO will significantly improve this measurement, which allows to study the damping tail of the angular power spectrum of the CMB (*Silk damping*).

- Measuring the Sunyaev-Zel'dovich effect due to cluster of galaxies. It is not possible

to study the characteristics of high redshift clusters from X-Ray data, since the signal is too faint. The Sunyaev-Zel'dovich effect, instead, is independent of the redshift of the cluster: thus, it is a fundamental tool for cosmological measurements. The survey of a number of clusters by OLIMPO will permit a more complete statistical analysis of the cluster distribution and of their evolution.

- Studying the *Far InfraRed Background* (FIRB), due to unresolved galaxies at high redshift. This measurement will improve our knowledge of the galaxy formation process, and in general of the epoch immediately following recombination.

During these years of Astronomy Ph.D. research, I worked mainly on the design, optimization, development and manufacturing of the experiment's optics; moreover, I made detailed simulations devoted to verify the capability of *OLIMPO* in separating the various components and in selecting between different phenomenological models.

Thesis is subdivided into six chapters, discussing the following topics:

Chapter 1 Theoretical introduction to the physical processes producing relevant signals in the wavelength bands covered by the *OLIMPO* experiment: the cosmic microwave background radiation and its anisotropies, the Sunyaev-Zel'dovich effect, the emission of the interstellar medium and of the extragalactic cosmic infrared background.

Chapter 2 General description of the *OLIMPO* experiment: telescope, signal modulation, cryostat and receivers.

Chapter 3 Analysis and simulations of different optical configurations: advantages and drawbacks of each solution are pointed out, from both optical, mechanical and manufacturing points of view. Finally, a detailed analysis on the final configuration is reported.

Chapter 4 Design and mechanical realization of the optical components and box that will accommodate them. Analysis and optimization of the surfaces; polishing of the surfaces; alignment tests.

Chapter 5 Introduction to Gaussian optics analysis and design of the profile of the feed horn arrays for all the bolometers.

Chapter 6 Description of the models of the physical processes considered to simulate the signals in the four channels of *OLIMPO*, taking into account the instrumental parameters; generation of maps and subsequent components separation; finally, analysis of the extracted signals and of their sensitivity to variations of the models used.

Chapter 1

The microwave sky

Only two things are infinite:
the Universe and human stupidity,
and I am not sure about the former.

Albert Einstein

This chapter describes the origin and the resulting emission spectra for the different components relevant in the sky at millimeter, submillimeter and far infrared bands ($\nu = 30 \div 3000 GHz$, $\lambda = 10 \div 0.1 mm$).

The extragalactic sky has three main sources of emission: the *Cosmic Background Radiation* (CMB) and its primary anisotropy, the emission from clusters of galaxies that give rise to *Sunyaev-Zel'dovich* (SZ) effect and the *Far InfraRed Background* (FIRB) due to unresolved point-sources. The *cosmological window* extends roughly from 1 to $5mm$ ($\nu = 300 \div 60 GHz$): at lower frequencies, interstellar emission of spinning dust grains, *bremsstrahlung* and synchrotron dominate over the anisotropy of the cosmological background; at higher frequencies the emission of interstellar dust distributed in clumpy cirrus clouds dominates the sky brightness even at high galactic latitudes.

In particular, I will focus on the signals that are preeminent in the wavebands of the *OLIMPO* experiment and at the same time constitute its scientific goals: CMB anisotropies, SZ effect, galactic dust emission and FIRB.

1.1 Cosmic microwave background

The cosmic microwave background, first discovered in 1965 by Penzias & Wilson, is the main signal in the millimeter band. This radiation and its properties are the strongest confirmations of the *standard cosmological model* that describes the physical evolution of the Universe in terms of its general characteristics, of elements composition and formation of structures.

1.1.1 The evolution of the Universe

The standard cosmological model assumes that the Universe evolves from a hot, dense and uniform state (called *Big Bang*) to the present cold, low-pressure and inhomogeneous state.

In the hypothesis of isotropic and homogeneous Universe (*cosmological principle*), well verified on large scales ($100 Mpc$ or more; $1 Mpc \simeq 3 \cdot 10^{22} m$), the space-time metric which describes an expanding Universe is the so-called *Robertson-Walker metric*. In spherical coordinates:

$$ds^2 = (c\,dt)^2 - a(t)^2 \left[\frac{dr^2}{1 - Kr^2} + r^2 (d\vartheta^2 + \sin^2 \vartheta \, d\varphi^2) \right] \tag{1.1}$$

where $a(t)$ is the *scale factor* or *expansion parameter*, and K is the *curvature parameter*, specifying the geometry of the Universe.

We introduce the *redshift* $z = (a_0 - a)/a$, where $a_0 \equiv a(t = t_0)$: it is used to express the distance of the object that emitted the photons and the time at which photons are emitted.

Einstein equations of General Relativity give the relation between space-time metric and matter energy-momentum tensor T_{ij}. Idealizing the primordial Universe as a perfect fluid, which has an energy-momentum tensor $T_{ij} = diag\,(\varrho, -p, -p, -p)$ where ϱ is the energy density and p the fluid's pressure, and given the metric described in eq. (1.1), we obtain the *Friedmann equations* whose solution is the evolution of the scale factor:

$$\left(\frac{\dot{a}}{a} \right)^2 = \frac{8\pi}{3} G\varrho - \frac{Kc^2}{a^2} \tag{1.2a}$$

$$\frac{\ddot{a}}{a} = -\frac{4\pi}{3} G \left(\varrho + 3\,\frac{p}{c^2} \right) \tag{1.2b}$$

here c is the speed of light, G is the Newton's universal gravitational constant and $\dot{a}/a = H$ is called *Hubble constant*. In first approximation, we can say that this parameter describes the Universe's horizon dimension: if we assume that the Universe expands at a constant speed equal to the speed of light, its horizon radius will be $r_{Hubble} = cH^{-1}$ (this derives from the *Hubble law* on galaxy recession $v = Hd$). Usually, the Hubble constant is expressed as $H = 100h\, km/s/Mpc$, where $h \simeq 0.7$ includes the experimental uncertainty on the estimate of H_0 [53, 88, 118].

ϱ includes the energy densities of the different components that constitute the Universe: baryons ϱ_B, photons ϱ_γ, neutrinos ϱ_ν, cold dark matter ϱ_{CDM} and dark energy ϱ_Λ. The last component was originally introduced by Einstein in eqs. (1.2) as a *cosmological constant* Λ to allow for a steady state solution $a(t) = const$, even if Λ is not necessary in General Relativity equations. Nowadays, this constant (called *dark energy*) has been re-introduced to explain the results coming from supernovae and CMB experiments. Λ and ϱ_Λ are related by:

$$\varrho_\Lambda = \frac{\Lambda}{8\pi G} \tag{1.3}$$

Every component follows energy conservation equation of a perfect fluid that is expanding adiabatically [58]:

$$\dot{\varrho} + 3H(p + \varrho) = 0 \tag{1.4}$$

Considering that the equation of state of fluids is $p = w\varrho$, normalizing the energy density to its present value ϱ_0, the solution of eq. (1.4) is:

$$\varrho = \varrho_0 \left(\frac{a_0}{a}\right)^{-3(1+w)} \tag{1.5}$$

with w different for the various components: non-relativistic matter, relativistic matter and dark energy.

- Non-relativistic matter is made of baryons, cold dark matter and non-interacting particles with velocities much lower than c. This component is well described by a fluid with no pressure, i.e. $w = 0$, that leads to $\varrho \propto a^{-3}$.
- Relativistic matter is made of photons and neutrinos and has a pressure $p = \varrho/3$ which gives $\varrho \propto a^{-4}$.
- In the standard cosmological model (called ΛCDM) the energy density of dark energy is constant, which implies that $w = -1$. Anyway, there are models in which w is a function of redshift.

Let us consider a galaxy that is at a distance r from us: it has a kinetic energy $K = m(H_0 R)^2/2$, while gravitational potential energy is $U = -4\pi G m \varrho R^2$. The critical energy density, defined as the density zeroing the total energy, is:

$$\varrho_c = \frac{3H^2}{8\pi G} \tag{1.6}$$

It is worth noting that if $\varrho_0 < \varrho_c$ the expansion will continue, otherwise it will collapse. We define the density parameter:

$$\Omega_i = \frac{\varrho_i}{\varrho_c} \tag{1.7}$$

where the index i represents the Universe's components ($i = B$, γ, ν, CDM, Λ). We can also introduce a density parameter regarding the curvature component:

$$\Omega_K = \frac{K}{a^2 H^2} \tag{1.8}$$

Ω_K can be rewritten as $\Omega_K = 1 - (\Omega_B + \Omega_{CDM} + \Omega_\gamma + \Omega_\nu + \Omega_\Lambda) = 1 - \Omega_0$, where Ω_0 is the total energy density of the Universe. Given eqs. (1.6) and (1.7), it is now evident the meaning of the curvature parameter:

- $\Omega_0 < 1 \left(\sum_i \varrho_i < \varrho_c\right) \Rightarrow K < 0 \Rightarrow$ open space, negative curvature.
- $\Omega_0 = 1 \left(\sum_i \varrho_i = \varrho_c\right) \Rightarrow K = 0 \Rightarrow$ Euclidean space, flat curvature.
- $\Omega_0 > 1 \left(\sum_i \varrho_i > \varrho_c\right) \Rightarrow K > 0 \Rightarrow$ closed space, positive curvature.

Considering eqs. (1.5), (1.6) and (1.7), eq. (1.2a) becomes:

$$H^2 = H_0^2 \left[(\Omega_B + \Omega_{CDM}) \left(\frac{a_0}{a}\right)^3 + (\Omega_\nu + \Omega_\gamma) \left(\frac{a_0}{a}\right)^4 + (1 - \Omega_0) \left(\frac{a_0}{a}\right)^2 + \Omega_\Lambda\right] \tag{1.9}$$

It is also possible to introduce a density parameter for relativistic matter, $\Omega_R = \Omega_\gamma + \Omega_\nu$, and one for non relativistic matter, $\Omega_M = \Omega_B + \Omega_{CDM}$.

This set of quantities (called *cosmologica parameters*, see Tab. 1.1) are needed to described the evolution of the Universe. Many recent experiments (among others *BOOMERanG* [24, 71], *MAXIMA* [67, 110], *Archeops* [4] and *WMAP* [3, 105]) measured cosmological parameters; they agree that $\Omega_0 = 1$, as predicted by *inflationary theory* (see § 1.1.3).

The other important side of modern cosmology, strictly linked to the evolution of the scale factor, is the study of the evolution of the large scale structure. This evolution is studied by linear perturbation theories. Initial conditions are also included in the cosmological parameters and are expressed as the exponent in the power law of the perturbations' power spectrum as they enter in the causal horizon, n_s:

$$P_k = Ak^{n_s} \tag{1.10}$$

where A is the overall amplitude of perturbations. Usually, this amplitude is given in terms of galaxies fluctuation's amplitude σ_8.

Parameters	**WMAP only**	**WMAP + 2dFGRS**	**WMAP + SN Gold**
$100\,\Omega_B h^2$	$2.233^{+0.072}_{-0.091}$	$2.223^{+0.066}_{-0.083}$	$2.227^{+0.065}_{-0.082}$
$\Omega_M h^2$	$0.1268^{+0.0072}_{-0.0095}$	$0.1262^{+0.0045}_{-0.0062}$	$0.1349^{+0.0056}_{-0.0071}$
h	$0.734^{+0.028}_{-0.038}$	$0.732^{+0.018}_{-0.025}$	$0.827^{+0.045}_{-0.053}$
Ω_M	$0.238^{+0.030}_{-0.041}$	$0.236^{+0.016}_{-0.024}$	$0.276^{+0.023}_{-0.031}$
A	$0.801^{+0.043}_{-0.054}$	$0.799^{+0.042}_{-0.051}$	$0.827^{+0.045}_{-0.053}$
τ	$0.088^{+0.028}_{-0.034}$	$0.083^{+0.027}_{-0.031}$	$0.079^{+0.028}_{-0.034}$
n_s	$0.951^{+0.015}_{-0.019}$	$0.948^{+0.014}_{-0.018}$	$0.946^{+0.015}_{-0.019}$
σ_8	$0.744^{+0.050}_{-0.060}$	$0.737^{+0.033}_{-0.045}$	$0.784^{+0.035}_{-0.049}$

Table 1.1: *Cosmological parameters of ΛCDM model as obtained by WMAP* [105]. *From left to right: values obtained by WMAP data alone, joint likelihoods derived including data from 2dFGRS survey* [21] *or from the supernovae gold sample* [99].

1.1.2 Primordial radiation

As already said, the Universe starts at a very high temperature and cools down due to expansion. In the first seconds after the *Big Bang*, temperature and density are so high that particles and anti-particles annihilate each other producing pairs of high-energy photons. These γ's are soon converted back into particles and anti-particles. In these conditions there is a tight contact among all Universe's components, that are in *thermal equilibrium* (i.e. their temperatures are the same).

It is during these primordial phase that the asymmetry between matter and anti-matter arises, resulting in the substantial amounts of residual matter that comprise the Universe today. The hypothetical physical processes that produced this asymmetry is called *baryogenesis*, the most important being electroweak and *Grand Unification Theory* (GUT) baryogenesis.

There are three necessary conditions (called *Sakharov conditions*) that a baryon generating interaction must satisfy to produce matter and anti-matter at different rates:

1. Baryon number B violation.
2. C symmetry and CP symmetry violation.
3. Interactions out of thermal equilibrium.

While CP violation is found in the neutral kaon system, there is no experimental evidence of particle interactions where the conservation of baryon number is broken: all observed particle reactions have equal baryon number before and after. Mathematically, the commutator of the baryon number quantum operator with the Standard Model hamiltonian is zero: $[B, H] = BH - HB = 0$. This suggests physics beyond the Standard Model (like Supersymmetry or Grand Unification Theories).

The last condition states that the rate of a reaction which generates baryon-asymmetry must be less than the rate of expansion of the Universe. In this situation the particles and their corresponding anti-particles do not achieve thermal equilibrium due to rapid expansion decreasing the occurrence of pair annihilation.

The "size" of the asymmetry is quantified by the parameter $\eta = (n_B - n_{\bar{B}})/n_\gamma$. In fact, it relates the overall number density difference between baryons and anti-baryons (n_B and $n_{\bar{B}}$ respectively) and the number density of cosmic background radiation photons n_γ.

During this first phase, the Universe is mainly made of relativistic matter. Hence this is called the *Radiation Dominated Era* (RDE). As shown in eq. (1.9), during this epoch the Universe expands as $H^{-1} \propto a^2$. Since $\Omega_R \propto a^{-4}$ while $\Omega_M \propto a^{-3}$, there will be an epoch, called *equivalence*, in which $\Omega_R = \Omega_M$: this happens at $z \simeq 11000$. After that, the Universe enters the *Matter Dominated Era* (MDE), during which it expands as $H^{-1} \propto a^{3/2}$ while the temperature decreases as $T \propto a^{-3}$. The frequency of interactions decreases and more complex elements are produced: first protons and neutrons, then nucleus of deuterium, helium and lithium (*Big Bang Nucleosynthesis* (BBN), about three minutes after *Big Bang*). The rate of elements production strongly depend on the value of the baryon to photon ratio η: measurements of the concentration of elements produced during BBN gives $\eta \simeq 3 \cdot 10^{-10}$.

Interactions between photons and matter continue until hydrogen recombines: this phase, called *recombination epoch*, starts at a temperature $T \simeq 4500K$, much lower than

the ionization temperature of hydrogen ($T \simeq 156000K$), because of the very small baryon to photon ratio. Before recombination, the mean free path of photons is very short, due to Compton scattering, and we can consider the primordial Universe as a hot plasma, is opaque to radiation (and similar to the gaseous nucleus of a star). Only when Universe reaches a temperature $T \simeq 3000K$ (*decoupling epoch* (about 380000 years after the *Big Bang*, or $z \simeq 1100$), almost all hydrogen recombines, and the mean free path of photons becomes very large, larger than the causal horizon. Photons undergo their last scatter and travel freely hereafter. The *Last Scattering Surface* (LSS) may be defined as the surface where photons, that we see today as microwaves dominating the cosmic radiation, are last scattered during the recombination phase.

After the decoupling, photons and matter evolve independently: this means that the photon distribution *today* is an image of the primordial Universe. In fact, we see an almost perfect blackbody spectrum at a temperature $T_{CMB} = 2.725 \pm 0.004$, (discovered in 1965 by Penzias & Wilson [89] and more recently (1990) measured by COBE satellite [39, 75, 76, 104]). This reflects the highly isotropic and homogeneous primordial state of the Universe (see Fig. 1.1). Since a $3K$ blackbody has its maximum brightness in the microwaves band and photons propagated from LSS in every direction, this background is called the *Cosmic Microwave Background Radiation* (CMBR).

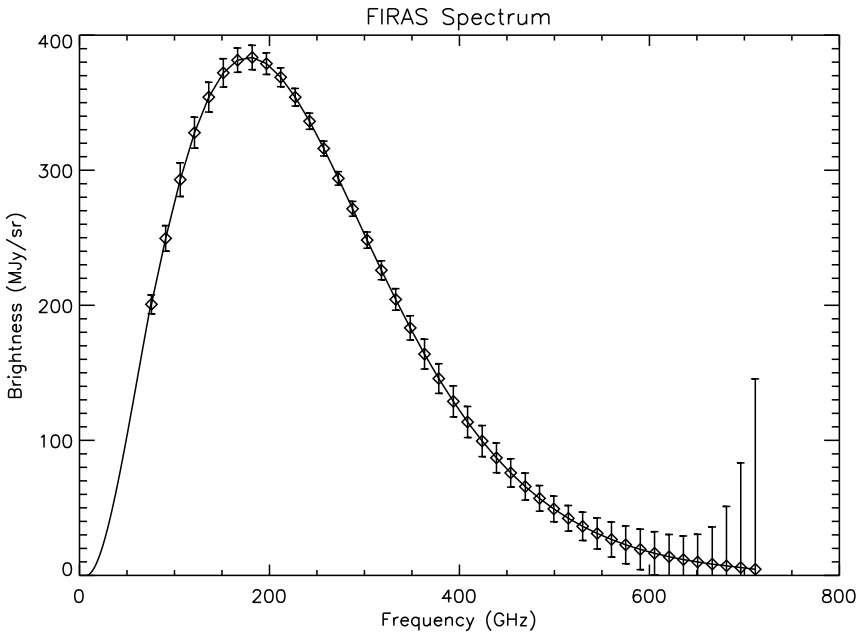

Figure 1.1: *Blackbody spectrum at $T_{CMB} = 2.725K$ as measured by FIRAS, the spectrometer mounted on the COBE satellite. The error bars are increased by a factor* 500 *in order to be visible.*

COBE firstly verified the homogeneity of CMB spectrum: this confirms the *cosmological principle*, which predicts the *isotropy and homogeneity of the Universe at large scales.* Nevertheless a perfect homogeneous spectrum cannot explain the highly inhomogeneity at small scales of actual Universe: on CMB spectrum, at scales of 1° or less, there must

be anisotropies, i.e. temperature's fluctuations that differ from blackbody spectrum, even if only for a part over 10^4. Structures, like galaxies and clusters of galaxies, form starting from these small CMB inhomogeneities, as predicted by the *theory of gravitational collapse*. The basic idea is that cold dark matter, that is the main matter component in the Universe, is not homogeneous, so it perturbs the metric creating gravitational potential wells into which normal matter falls when the interaction with radiation becomes negligible.

1.1.3 The origin of CMB anisotropy

The origin of CMB anisotropy is explained by the *theory of inflation* [48]: in an epoch prior to GUT (*Grand Unification Theory*, $\sim 10^{-35} s$ after the *Big Bang*, at an energy scale of $\sim 10^{15} GeV$) there is a phase of ultrafast expansion of Universe due to a scalar field, described by an equation similar to that of Klein-Gordon. Inflation is also needed to solve *flatness and horizon paradoxes*.

Flatness paradox It regards the density of the Universe: different experiments verified it is equal to critical density ($\Omega_0 = 1$), even if this is a very unstable solution of the Friedmann equations. In fact the density contrast (or density fluctuations) $\delta = \delta\varrho/\varrho$ grows as the scale factor $a(t)$ (so $\delta \propto t^{1/2}$ in RDE and $\delta \propto t^{2/3}$ in MDE) and it increases of many orders of magnitude. The homogeneity of Universe implies $\delta\varrho/\varrho \ll 1$ today. In order to get this value, the density parameter at *Planck epoch* must be $\Omega_0 = 1 \pm 10^{-44}$. Thus, there is a fine tuning problem. Inflation provides a solution: during inflation the density contrast falls down as ($\delta \propto e^{-t}$): when the inflationary epoch ends, $\Omega_0 = 1$ independently of initial conditions.

Horizon paradox At $z \simeq 1100$ the causal horizon is $\sim 100 h^{-1} Mpc$ (which corresponds to an angular scale of $\sim 1^\circ$). This means that two regions that are more distant than $\sim 1^\circ$ at recombination are and have been previously causally disconnected. Radiation starting from one region does not have enough time to reach the bother one. It is thus impossible to explain how the whole sky has the same temperature $T = 2.725K$. Inflationary theory predicts that these regions where causally connected prior to inflation. With the superluminal expansion of space during inflation they get out of causal contact (*horizon crossing*) and after the end of inflationary epoch they start to reenter (see Fig. 1.2). In fact, scale dimensions always grow as the scale factor $a(t)$ while horizon's expansion (i.e. H^{-1}) depends on the epoch.

We now want to derive the spectrum of the perturbations. The most general perturbed metric can be written as $g_{\mu\nu} = g^{(0)}_{\mu\nu} + a^2 g^{(1)}_{\mu\nu}$, where $g^{(0)}_{\mu\nu} = \eta_{\mu\nu}$ is the unperturbed metric, while:

$$g^{(1)}_{\mu\nu} = \begin{pmatrix} -2\psi & w_i \\ w_i & -2\phi\,\delta_{ij} + h_{ij} \end{pmatrix} \tag{1.11}$$

ψ and ϕ are space scalars, w_i is a 3-vector and h_{ij} is a traceless 3-tensor. Since General Relativity equations are invariant with respect to a general coordinate change, we can always choose a specific gauge in which $w_i = 0$ (*Newtonian gauge*). The metric element of the perturbed metric will be:

$$ds^2 = a^2[-(1 + 2\psi)\, d\tau^2 + (1 - 2\phi)\, dx^i\, dx_j] \tag{1.12}$$

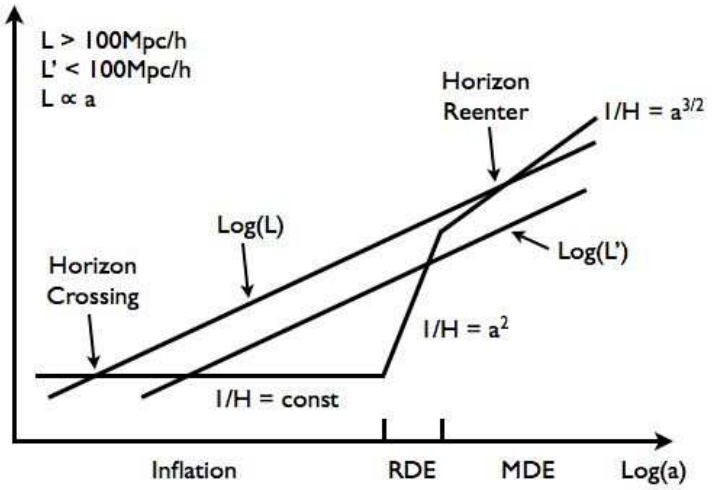

Figure 1.2: *Horizon H^{-1} and perturbations scales as a function of the scale factor at various epochs.*

where $d\tau = c\,dt/a(t)$ is the conformal time. We also introduce the perturbed quantities $\delta = \delta\varrho/\varrho$, $\varphi = \delta\phi$ and $\theta = ik^i v_i$, where v_i is the matter peculiar velocity with respect to the general expansion and k is the mode in Fourier space: in fact, it is convenient to Fourier expand the perturbed quantities δ, ϕ, ψ and δ. Now, we must perturb the Einstein equations of General Relativity:

$$R_{\mu\nu} - \frac{1}{2}\,g_{\mu\nu}\,R = \frac{8\pi\,G}{c^4}\,T_{\mu\nu} \tag{1.13}$$

Let us evaluate the Newtonian limit, i.e. small scales ($k \gg H$). Fluctuations of a pressureless fluid grow indefinitely because there is no counteracting force; however, the Universal fluid has a finite pressure that will resist gravity and will stop the collapse. Consider a fluid which is pressureless when unperturbed but has a finite velocity dispersion, much smaller than the speed of light, otherwise the Newtonian approximation is not valid anymore: $c_s = \delta p/\delta\varrho \ll 1$. After some computations we get:

$$\dot{\delta} = -\theta \tag{1.14a}$$

$$k^2\phi = -\frac{3}{2}H^2\delta \tag{1.14b}$$

$$\dot{\theta} = -H\theta + c_s k^2\delta + k^2\phi \tag{1.14c}$$

Deriving eq. (1.14a) and substituting into it eqs. (1.14b) and (1.14c) we obtain:

$$\ddot{\delta} + H\dot{\delta} + \left(k^2 c_s^2 - \frac{3}{2}\,H^2\right)\delta = 0 \tag{1.15}$$

It is worth noting that in the Minkowski limit, i.e. a steady Universe with $H = 0$, eq. (1.15) reduces to fluid's wave equation with a *sound velocity* c_s. Eq. (1.15) shows

perturbation does not grow when:

$$k^2 c_s^2 - \frac{3}{2} H^2 > 0 \tag{1.16}$$

i.e. comoving perturbation scale $\lambda = 2\pi a/k$ is smaller than the *Jeans length* $\lambda_J = c_s\sqrt{\pi/\varrho}$. In this case, the perturbation undergoes damped oscillations: given the initial condition $\dot{\delta}(0) = 0$ and $\delta(0) = -2\phi/3$, the solution is $\delta = \phi/3 \cdot \cos(c_s k t)$, where $\phi \propto a^{-1}$ because of the expansion of the Universe. The various components have different trends:

Photons They have $c_s \simeq c/\sqrt{3}$ so that $\lambda_J \simeq H^{-1}a^{-1}$. Growth is prevented on all scales smaller than horizon.

Baryons Their sound velocity is comparable to γ's velocity before decoupling, so that their perturbations are damped out. The sound speed drops rapidly after decoupling: baryons are free to fall inside dark matter gravitational potential wells and their perturbation spectrum catches the CDM one.

CDM Its velocity dispersion is always negligible, hence putting $c_s = 0$ in eq. (1.15) we get that perturbations grow freely and that there are two modes: $\delta_+ \propto a$ and $\delta_- \propto a^{-3/2}$. The decaying mode can be neglected for primordial perturbations.

In the large scale limit ($k \ll H$), we have two trends: during the radiation dominated era $\delta \propto a^2$, while in the matter dominated era $\delta \propto a$. So perturbations *always grow* when scales are larger than horizon.

Summarizing, since fluctuations are small, the quantitative way to approach the problem is to expand the small perturbations in Fourier modes and to compute the anisotropy from each mode individually. After it enters the causal horizon, each Fourier mode follows the equation of a forced and damped harmonic oscillator. Photons and baryons are tightly coupled due to Compton scattering and primordial plasma is compressed by gravitation and expanded by photon pressure. The resulting pressure oscillations are frozen at recombination, each with its phase of oscillation. All modes are then combined and projected on the last scattering surface to form the temperature distribution we can detect.

In 2000, the *BOOMERanG* [24, 55] and *MAXIMA* [67, 110] balloon experiments produced the first maps of CMB anisotropies on selected patches of sky (about 5% of the whole sky); in 2003, the *WMAP* satellite [3, 51] made the first all sky measurement of these fluctuations (see Fig. 1.3).

1.1.4 Anisotropy power spectrum

As seen in § 1.1.3, the density contrast of the perturbations grows until their dimension becomes larger than the *Jeans length*; after that the perturbations start to oscillate. CMB temperature fluctuations rely on the phase of these oscillations: smaller scales are damped and perform several oscillations, larger scales have time to do only one; even larger scales, that are outside the causal horizon do not oscillate at all (see Fig. 1.4).

Thus, the number of oscillations depend on the perturbation scale, i.e. the wavenumber k. The power spectrum is thus computed in terms of k and then, since the CMB signal

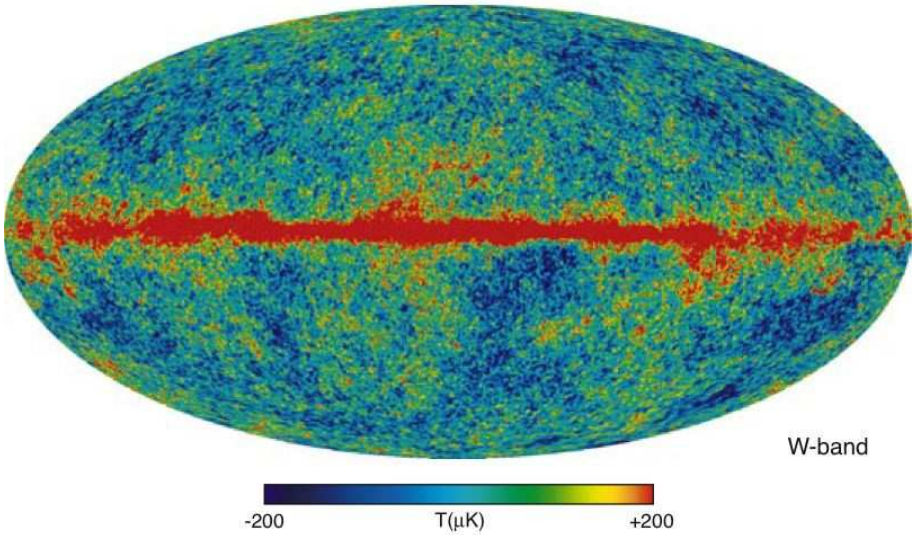

Figure 1.3: *Image of the cosmic microwave background radiation from the WMAP satellite (three years data). The data are plotted in galactic coordinates, mollview projection. The image comes from the WMAP W-band at* $94GHz$.

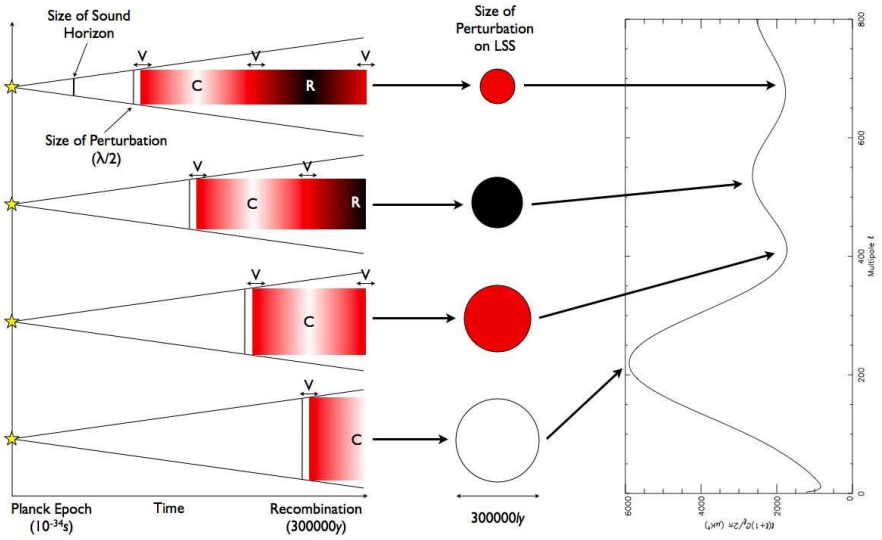

Figure 1.4: *Perturbation density fluctuations at different scales: in the primeval plasma, photons and baryons density perturbations start to oscillate only when the sound horizon becomes larger than their linear size. Small wavelength perturbations do more oscillations than larger one.*

is projected onto a spherical surface, it is projected and expanded in spherical harmonics, normalized in respect to mean temperature $T_{CMB} = 2.725K$:

$$\frac{\Delta T}{T_{CMB}}(\vartheta,\varphi) = \sum_{\ell=1}^{\infty}\sum_{m=-\ell}^{\ell} a_{\ell m}\, Y_{\ell m}(\vartheta,\varphi) \tag{1.17}$$

In the hypothesis of a gaussian distribution of fluctuations [59], statistical information is given by the standard deviation of the distribution, which in spherical harmonic expansion has the form:

$$\begin{aligned}
\left\langle \left(\frac{\Delta T}{T_{CMB}}\right)^2 \right\rangle &= \frac{1}{4\pi}\int \left|\frac{\Delta T}{T_{CMB}}(\vartheta,\varphi)\right|^2 d\vartheta\, d\varphi \\
&= \frac{1}{4\pi}\sum_{\ell\ell'}\sum_{mm'} \langle a_{\ell m}\, a^*_{\ell' m'}\rangle \int Y_{\ell m}(\vartheta,\varphi)\, Y^*_{\ell' m'}(\vartheta,\varphi)\, d\vartheta\, d\varphi \\
&= \frac{1}{4\pi}\sum_{\ell\ell'}\sum_{mm'} \langle a_{\ell m}\, a^*_{\ell' m'}\rangle\, \delta_{\ell\ell'}\, \delta_{mm'} = \frac{1}{4\pi}\sum_{\ell=1}^{\infty}\sum_{m=-\ell}^{\ell} \langle |a_{\ell m}|^2\rangle \\
&= \frac{1}{4\pi}\sum_{\ell=1}^{\infty}\sum_{m=-\ell}^{\ell} C_\ell = \frac{1}{4\pi}\sum_{\ell=1}^{\infty}(2\ell+1)\, C_\ell
\end{aligned} \tag{1.18}$$

Here brackets indicate ensemble averaging; moreover, due to isotropy, deviations are m-independent. The quantity $C_\ell = \langle a_{\ell m}\, a^*_{\ell' m'}\rangle\, \delta_{\ell\ell'}\, \delta_{mm'}$ is defined as the anisotropy angular power spectrum. The best estimator we have for the ℓ component is:

$$\widehat{C}_\ell = \frac{1}{2\ell+1}\sum_{m=-\ell}^{\ell} a_{\ell m}\, a^*_{\ell' m'} \tag{1.19}$$

Due to the fact that we have only one realization of the Universe, errors on the measured spectrum are theoretically limited (*cosmic variance*). Every C_ℓ has its uncertainty that cannot be reduced because it does not depend on the measurement procedure, but it is intrinsic in the statistical nature of the theory. The standard deviation of the anisotropy angular power spectrum is given by:

$$\sigma^2_{C_\ell} = \frac{2}{2\ell+1}\, C_\ell^2 \tag{1.20}$$

It is worth noting that $\ell = 180/\vartheta$, where ϑ represents the angle (in degrees) under which we see a given structure on the LSS. So, the relation between the multiple moment and the perturbation scale is $\ell \propto \lambda$, because $\vartheta \sim \lambda/\Delta t$, where Δt is the interval time between reionization and today.

As we have seen in these paragraphs, the shape of this spectrum depends on both the cosmological parameters and the initial conditions. These latter define the density contrast of baryons, cold dark matter, photons and neutrinos when fluctuations reenter the horizon, and are usually of two kinds: *adiabatic* and *isocurvature*.

Adiabatic Characterized by the conservation of entropy per baryon fraction, thus the conservation of particles' number per unit volume of every species with respect to the number of baryons: $n_i/n_B = const$. This implies that the total relative density fluctuation is not zero, and that there is an exact proportion between the initial density contrast for all the components. Inflationary models with simple scalar fields predicts this kind of initial perturbations.

Isocurvature In this case, the relative densities in initial conditions are not proportional, but the total energy density fluctuation is zero. Therefore gravitational potential is zero as well (isocurvature).

As seen in § 1.1.3, the origin of the acoustic peaks is due to the fact that Universe is filled with standing density waves. All modes with a given wavenumber k oscillate in phase, and there is perfect coherence. This phase dependency produces the peaks in the angular power spectrum. Phase coherence of all perturbations of a given wavenumber is a consequence of the fact that these perturbations cross the causal horizon at the same time, thus starting synchronous oscillations.

The best measurement of the anisotropy angular power spectrum to date has been obtained by the *WMAP* satellite [59] and it is reported in Fig. 1.5. Cosmological parameters and initial conditions can thus be inferred from power spectrum measurements. For example, the fact that the first peak is at $\ell \simeq 180$ implies that $\Omega_0 h^{-1} = 1$: as already seen in § 1.1.3, the horizon dimension at recombination is $\sim 100 h^{-1} Mpc$, which corresponds to an angular scale of $\vartheta \simeq 1°$, i.e. $\ell = 180/\vartheta \simeq 180$ in Euclidean space. Positions and heights of the peaks constrain other cosmological parameters, such as Ω_B, Ω_Λ or H_0. Stronger constrains and other important parameters, like the reionzation redshift or the spectral index of the initial power spectrum of the perturbations, can be estimated by means of CMB polarization measurements [22, 52, 56, 62, 61, 121]. The first CMB polarization detection was obtained by the *DASI* experiment in 2002 [63, 69] and later by *WMAP* [57, 84] and *BOOMERanG* [79, 91].

1.2 Sunyaev-Zel'dovich effect

The Sunyaev-Zel'dovich effect is the inverse Compton scattering between CMB photons and the hot gas of electrons present in the *Intra-Cluster Medium* (ICM) [113, 114, 122]. This effect causes a change in the apparent brightness of the CMB in clusters of galaxies, and its measurement provide information about cluster's properties complementary to those coming from X-Ray images. Since the SZ effect is redshift-indipendent, it can provide a unique probe of the structure of the Universe on the largest scales.

1.2.1 CMB comptonization

The presence of hot gas in intracluster medium is proved by the fact that clusters of galaxies are luminous sources of X-Rays. The X-Ray spectrum has a strong continuum component, due to photons produced in *bremsstrahlung* processes [102] of electrons on nuclei. In these conditions, the electronic component of the gas is able to diffuse CMB

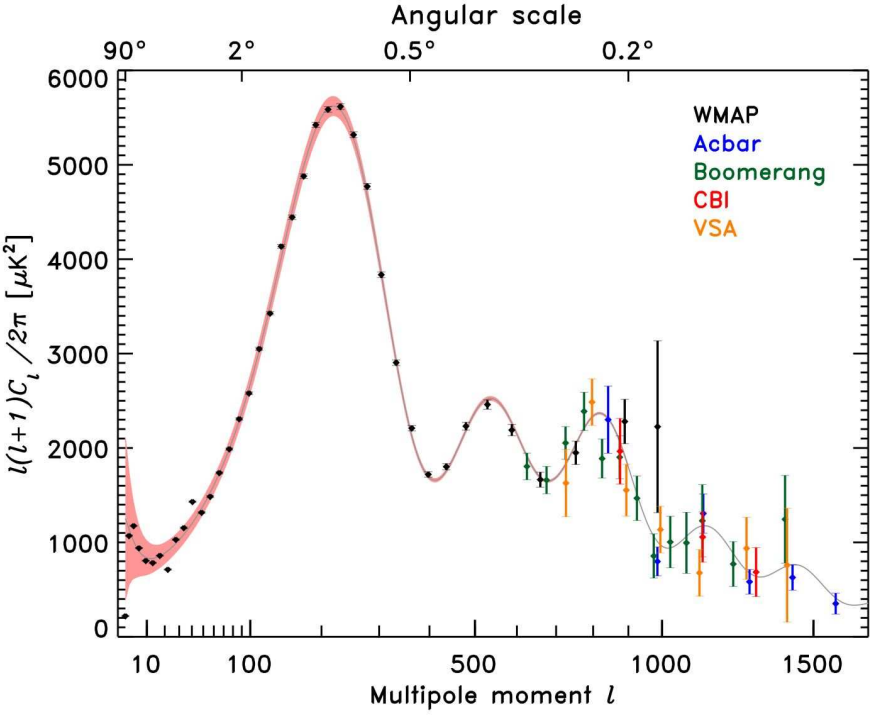

Figure 1.5: *The WMAP three year power spectrum (in black) compared to other recent measurements of the CMB angular power spectrum, including BOOMERanG* [55]*, Acbar* [64]*, CBI* [95] *and VSA* [28]*. The data confirm the turnover in the third acoustic peak and prove the presence of Silk damping.*

photons efficiently: for a single event, given the angle ϕ_{12} between the scattered and the incident γ (see Fig. 1.6), the kinematics of this process is described by *Compton scattering*:

$$\varepsilon' = \frac{\varepsilon}{1 + (1 - \cos\phi_{12}) \cdot \dfrac{\varepsilon}{m_e\, c^2}} \tag{1.21}$$

where $\varepsilon = h\nu$ is the incident photon energy, $\varepsilon' = h\nu'$ is photon energy after interaction and m_e is electron's mass. Eq. (1.21) is obtained in the electron rest frame before interaction and implies conservation of quadri-impulse between the initial and the final states (relativistic extension of a classical elastic scattering).

For low-energy photons (like the CMB ones) and moderatly relativistic or non-relativistic electrons, $\varepsilon \ll m_e c^2$, so that electron is unperturbed. The process is almost elastic ($\varepsilon' = \varepsilon$) while the photon changes only its direction: in this limit, the process is simply a *Thomson scattering* with cross section $\sigma_T = 7.94 \cdot 10^{-30} m^2/sr$.

With reference to Fig. 1.6, the scattering probability of an incident photon with an angle between ϑ and $\vartheta + d\vartheta$ is [5]:

$$p_{In}(\vartheta)\, d\vartheta = p(\mu)\, d\mu = \frac{1}{2\gamma^4(1 - \beta\mu)^3}\, d\mu \tag{1.22}$$

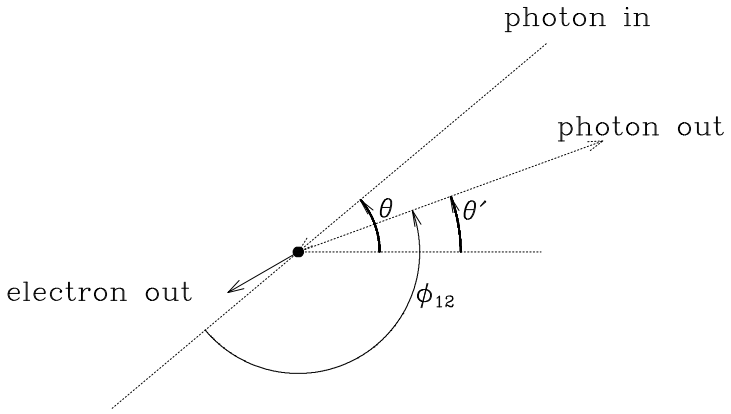

Figure 1.6: *Compton scattering geometry, in the electron's rest frame before interaction. An incoming photon, at angle ϑ relative to the x_e axis, is deflected by angle ϕ_{12}, and emerges after the scattering at angle ϑ' with almost unchanged energy, as given by* eq. (1.22)*. In the observer's frame, where the electron is moving with velocity v_e along the x_e axis, the photon changes its energy by an amount depending on v_e and on the angles ϑ and ϑ', as described in* eq. (1.24)*.*

where $\beta = v_e/c$, v_e is electron's velocity and $\mu = \cos\vartheta$. The probability to have a scattering at an angle between ϑ' and $\vartheta' + d\vartheta'$ is [18, 119]:

$$p_{Out}(\mu';\mu)\,d\mu' = \frac{3}{8}\left[1 + \mu^2\mu'^2 + \frac{1}{2}(1-\mu^2)(1-\mu'^2)\right]d\mu' \tag{1.23}$$

where $\mu' = \cos\vartheta'$. In the laboratory reference frame, the photons does not change only its direction, but also its frequency and energy:

$$\nu'' = \nu \cdot \frac{(1+\beta\mu')}{(1-\beta\mu)} \tag{1.24}$$

In a *classical* Compton scattering process, when the photon hits the electron, the latter absorbs part of the photon energy, and both particles change direction. In this case, since the energy of the electron is much higher than photon's one, the electron gives a small part of its energy to the other particle, so that the photon frequency increases after the scattering, and only the photon changes its trajectory. This is the so-called *inverse Compton scattering.*

It is usual to express the scattering final state in terms of logarithmic frequency shift [96, 111, 112]:

$$s = \ln\left(\frac{\nu''}{\nu}\right) \tag{1.25}$$

so that the probability to produce a shift between s and $s + ds$ due to an interaction between a photon and an electron of velocity v_e is given by:

$$P(s;\beta)\,ds = \int p_{In}(\mu)\,p_{Out}(\mu';\mu)\left(\frac{d\mu'}{ds}\right)d\mu\,ds \tag{1.26}$$

Using eqs. (1.22), (1.23) and (1.24), eq. (1.26) becomes:

$$P(s;\beta) = \frac{3}{16\gamma^4\beta}\int_{\mu_1}^{\mu_2} \frac{(1+\beta\mu')\left[1+\mu^2\mu'^2+(1-\mu^2)(1-\mu'^2)/2\right]}{(1-\beta\mu)^3}\,d\mu \tag{1.27}$$

where μ' can be expressed in term of μ and s: using eqs. (1.24) and (1.25), we get: $\mu' = [e^s\,(1-\beta\mu)-1]/\beta$. The integral in eq. (1.27) must be calculated only on real angles, hence:

$$\mu_1 = \begin{cases} -1 & s \le 0 \\ \dfrac{1-e^{-s}\,(1+\beta)}{\beta} & s \ge 0 \end{cases} \tag{1.28a}$$

$$\mu_2 = \begin{cases} \dfrac{1-e^{-s}\,(1+\beta)}{\beta} & s \le 0 \\ -1 & s \ge 0 \end{cases} \tag{1.28b}$$

Eq. (1.27) can be integrated for several values of β (see Fig. 1.7): non-zero initial momenta imply a non-zero probability that a photon is diffused and changes energy (in the limit $\beta \to 0$, eq. (1.27) becomes a Dirac's δ centered in the original frequency). As β increases, the asymmetry of $P(s;\beta)$ grows because of the relativistic effect on the angle conversion between reference frames; also the width increases: the higher the electron's velocity, the larger the frequency's shift.

1.2.2 Thermal SZ effect

The probability distribution of s for a single scatter is obtained integrating $P(s;\beta)$ over β, weighted on the electrons' velocity distribution $p_e(\beta)$:

$$P_1(s) = \int p_e(\beta)\,P(s;\beta)\,d\beta \tag{1.29}$$

It is assumed that electrons' velocity follows a relativistic Maxwellian distribution:

$$p_e(\beta)\,d\beta = \frac{\gamma^5\,\beta^2\,\exp\left(\dfrac{-\gamma}{\Theta}\right)}{\Theta\,K_2\left(\dfrac{1}{\Theta}\right)}\,d\beta \tag{1.30}$$

where Θ is an adimensional variable which contains temperature information:

$$\Theta = \left(\frac{k_B T_e}{m_e c^2}\right) \tag{1.31}$$

and K_2 is a modified Bessel function of second kind and second order. Since the distortion's probability depends on the temperature of electrons gas T_e, this interaction is called *thermal Sunyaev-Zel'dovich effect*.

A photon that interacts with a population of electrons can be diffused many times. Given an electronic cloud of density number n_e, the *optical depth* τ_e is defined as:

$$\tau_e = \sigma_T \int n_e\,dl \tag{1.32}$$

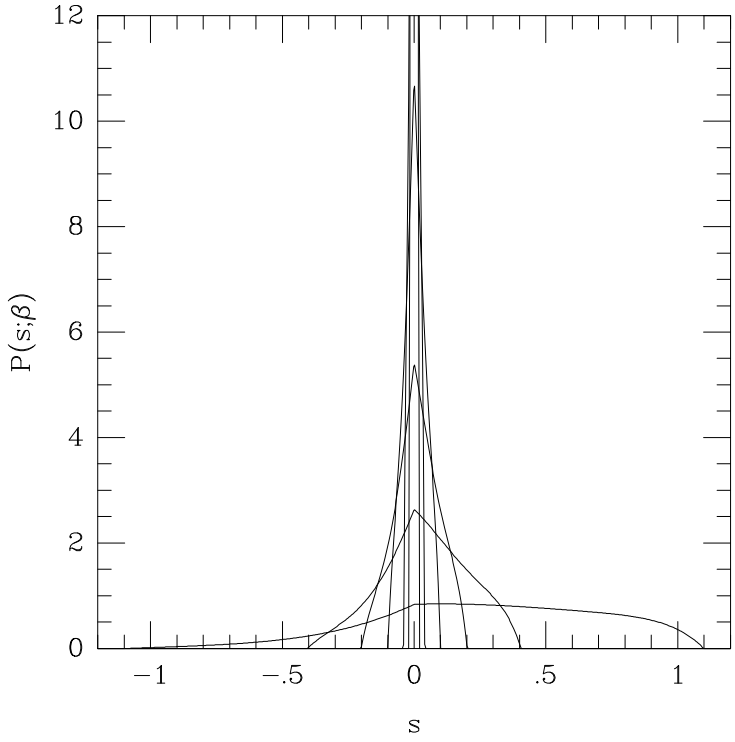

Figure 1.7: *The scattering probability function $P(s;\beta)$, for $\beta = 0.01$, 0.02, 0.05, 0.10, 0.20, and 0.50. The function becomes increasingly asymmetric and broader as β increases.*

where the integration is made along the line of sight. The probability that a photon passes through the electronic cloud without scatter is $p_0 = e^{-\tau_e}$; the probability to have one interaction is $p_1 = \tau_e e^{-\tau_e}$; the probability to be diffused N times will be described by a Poisson function:

$$p_N = \frac{\tau_e^N e^{-\tau_e}}{N!} \tag{1.33}$$

Hence, the full frequency redistribution function from scattering is:

$$P(s) = e^{-\tau_e}\left(\delta(s) + \tau_e P_1(s) + \frac{1}{2!}\tau_e^2 P_2(s) + \dots\right) \tag{1.34}$$

where the function $P_n(s)$ can be expressed as a convolution product of $P_1(s)$ with itself for n times:

$$P_2(s) = \int P_1(t_1)\, P_1(s - t_1)\, dt_1 \tag{1.35a}$$

$$P_3(s) = \int P_1(t_1)\, P_1(t_2)\, P_1(s - t_1 - t_2)\, dt_1\, dt_2 \tag{1.35b}$$

$$\vdots$$

Usually, the optical depth of the electronic cloud is so thin ($\tau_e \ll 1$) that first order approximation is valid: $P(s) = (1 - \tau_e)\,\delta_s + \tau_e P_1(s)$.

Starting from eq. (1.24), which describes the frequency shift of the radiation due to a single scattering, it is possible to reconstruct the spectrum of the CMB after diffusion. The spectrum of incident CMB photons is described by a blackbody at a temperature $T_{CMB} = 2.725$:

$$I_0(\nu) = \frac{2h\nu^3}{c^2} \cdot \frac{1}{e^{h\nu/k_B T_{CMB}} - 1} \tag{1.36}$$

If the photon is diffused only once, its spectrum after the scattering becomes:

$$\frac{I(\nu)}{\nu} = \int_0^\infty P_1(\nu, \nu_0) \frac{I_0(\nu_0)}{\nu_0} d\nu_0 \tag{1.37}$$

where $P_1(\nu, \nu_0)$ is the probability that a diffusion with a frequency shift between ν_0 and ν happens. Since $P_1(\nu, \nu_0) = P_1(s)/\nu$, from eqs. (1.25) and (1.29) it follows that eq. (1.37) can be written in term of the variable s as:

$$I_\nu = \int_{-\infty}^{+\infty} P_1(s)\, I_0(\nu_0)\, ds \tag{1.38}$$

Eq. (1.38) can be generalized for multiple scatterings, using the approximated form of $P(s)$ instead of $P_1(s)$. Taking eqs. (1.36) and (1.38), the frequency shift of the radiation is finally:

$$\begin{aligned} \Delta I_T(\nu) &\equiv I(\nu) - I_0(\nu) = \\ &= \frac{2h}{c^2} \tau_e \int_{-\infty}^{+\infty} \left(\frac{\nu_0^3}{e^{h\nu_0/k_B T_{CMB}} - 1} - \frac{\nu^3}{e^{h\nu/k_B T_{CMB}} - 1} \right) P_1(s)\, ds \end{aligned} \tag{1.39}$$

In Fig. 1.8 it is reported the numerical integration of eq. (1.39): it is worth noting that ΔI_T changes sign as frequency increases. Moreover, it is redshift-independent, while depends only on the intrinsic properties of the scattering medium: these are described by the factors τ_e and $P_1(s)$.

1.2.3 Kompaneets approximation

Under the hypothesis that the electrons gas is isotropic and non-relativistic, the scattering process simplifies substantially and it is possible to approximate eq. (1.39) using the Kompaneets equation [60, 88]: this describes the change in the $n(\nu)$ due to the diffusion process. Given the electrons density n_e and temperature T_e, the radiation temperature T_{CMB} and for a given adimensional frequency $x = h\nu/k_B T_{CMB}$, in the limit $T_e \gg T$ (which is always valid for CMB photons and hot electrons), the Kompaneets equation has the form:

$$\frac{\partial n}{\partial t} = \frac{k_B T_{CMB}}{m_e c} \frac{\sigma_T n_e}{x^2} \frac{\partial}{\partial x} \left[x^4 \left(\frac{T_e}{T_{CMB}} \frac{\partial n}{\partial x} \right) \right] \tag{1.40}$$

Assuming that the radiation field is slightly diffused by the gas, the density occupation number $n(\nu)$ can be substituted by the mean occupation number of a Planck spectrum $n_P(x) = (e^x - 1)^{-1}$. Integrating along the line of sight across the cluster, we obtain the spectral distortion:

$$\Delta I_T(x) = \frac{2(k_B T_{CMB})^4}{h^3 c^2} \cdot y \cdot g(x) \tag{1.41}$$

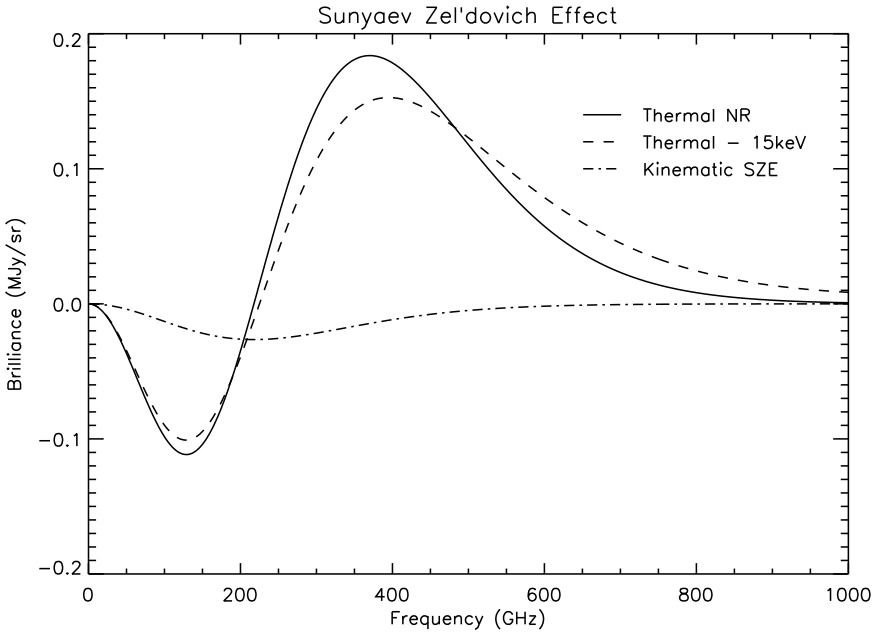

Figure 1.8: *The spectral deformation of the CMB caused by inverse Compton scattering by a thermal population of electrons. The figure shows the result of the numerical integration of* eq. (1.39)*. The solid line represents the spectral deformation due to thermal SZ effect in the Kompaneets approximation (see* § 1.2.3*) for a cluster having a comptonization parameter* $y = 10^{-4}$*. The dashed line shows the SZE including relativistic corrections up to the fifth order (see* § 1.2.4*) for a cluster with an electrons' temperature* $T_e = 15keV$ *and* $y = 10^{-4}$*. The dot-dashed line is the contribution due to kinematic SZE (see* § 1.2.5*) for a cluster with a peculiar velocity* $V_r = 500km/s$*.*

The $g(x)$ function includes the spectral dependence of the thermal SZ effect; its trend is shown in Fig. 1.9 (solid line), while its analytic expression is:

$$g(x) = \frac{x^4 e^x}{(e^x - 1)^2} \left[x \cdot \frac{e^x + 1}{e^x - 1} - 4 \right] \tag{1.42}$$

The y term is called the *comptonization parameter*; it depends on cluster characteristics and observation direction, and is given by:

$$y = \int \frac{k_B T_e}{m_e c^2} n_e \, \sigma_T \, dl \tag{1.43}$$

where integration is done along the line of sight, across the whole cluster's extension.

It is usual to quantify the thermal SZ effect in terms of a CMB temperature variation, as already done for CMB anisotropy :

$$\frac{\Delta T}{T_{CMB}} = \left[x \cdot \frac{e^x + 1}{e^x - 1} - 4 \right] \cdot y = \coth\left(\frac{x}{2}\right) \cdot xy - 4y \tag{1.44}$$

It is worth noting that in the Kompaneets approximation, the spectral distortion does not depend on cluster parameters: it only depends on a scale factor, the comptonization parameter y, as shown in eq. (1.41). So, the positions of the minimum, of the maximum and of the zero (*crossover* point) of the SZ spectrum are fixed:

$$\begin{aligned} x_{Min} = 2.26 \quad &\Rightarrow \quad \nu_{Min} = 128.73\,GHz \\ x_{Zero} = 3.83 \quad &\Rightarrow \quad \nu_{Zero} = 218.16\,GHz \\ x_{Max} = 6.51 \quad &\Rightarrow \quad \nu_{Max} = 370.82\,GHz \end{aligned} \tag{1.45}$$

As a final step we need a model for the cluster electronic density and temperature profiles, in order to be able to estimate the comptonization parameter y. The model must be compatible with surface brightness X-Ray data, which is given by:

$$b_X(E) = \frac{1}{4\pi(1+z)^3} \int n_e^2(r)\, X(E, T_e)\, dl \tag{1.46}$$

here $n_e(r)$ and T_e are density and temperature of the gas, $X(E, T_e)$ is gas spectral emissivity at observed energy E; the factor of 4π arises from the assumption that this emissivity is isotropic, while the $(1+z)^3$ factor takes into account cosmological transformations of spectral surface brightness and energy. It is not possible to obtain $n_e(r)$ and $T_e(r)$ from eq. (1.46), because there is no unique inversion: thus it is not possible to predict accurately the distribution of y on the sky, and hence the shape of the Sunyaev-Zel'dovich effect. It is necessary to introduce a parameterized model for the properties of the scattering gas in the cluster, and to fit the values of these parameters to X-Ray data. The most popular model is the so-called *isothermal β model*, where it is assumed that electron temperature is constant inside the cluster and that electrons number density follows a spherical distribution [15, 16]:

$$n_e(r) = n_{e,0} \left(1 + \frac{r^2}{r_c^2}\right)^{-\frac{3}{2}\beta} \tag{1.47}$$

where r_c represents the typical length of the model, also known as *core radius*. From eq. (1.47) follows expressions regarding optical depth, comptonization parameter and X-Ray surface brightness:

$$\tau_e(\vartheta) = \tau_{e,0} \left(1 + \frac{\vartheta^2}{\vartheta_c^2}\right)^{\frac{1}{2}-\frac{3}{2}\beta} \tag{1.48a}$$

$$y(\vartheta) = y_0 \left(1 + \frac{\vartheta^2}{\vartheta_c^2}\right)^{\frac{1}{2}-\frac{3}{2}\beta} \tag{1.48b}$$

$$b_X(\vartheta) = b_{X,0} \left(1 + \frac{\vartheta^2}{\vartheta_c^2}\right)^{\frac{1}{2}-3\beta} \tag{1.48c}$$

which have central values:

$$\tau_{e,0} = n_{e,0}\,\sigma_T\,r_c\,\sqrt{\pi}\cdot\frac{\Gamma\left(\frac{3\beta}{2}-\frac{1}{2}\right)}{\Gamma\left(\frac{3\beta}{2}\right)} \tag{1.49a}$$

$$y_0 = \tau_{e,0}\cdot\frac{k_B\,T_e}{m_e\,c^2} \tag{1.49b}$$

$$b_{X0} = \frac{1}{4\pi(1+z)^3}\cdot n_{e,0}^2\,X(E,T_e)\,r_c\,\sqrt{\pi}\cdot\frac{\Gamma\left(\frac{3\beta}{2}-\frac{1}{2}\right)}{\Gamma(3\beta)} \tag{1.49c}$$

In eqs. (1.47) and (1.49), ϑ is the angle between the center of the cluster and the direction of interest while $\vartheta_c = r_c/D_A$ is the cluster's angular core radius as deduced from the X-Ray data. D_A is the angular distance of the cluster, that is a function of the cosmological parameters [58, 83, 88]:

$$D_A = \frac{1}{1+z}\,\frac{c}{H_0}\int_0^z \frac{dz}{\sqrt{\Omega_R(1+z)^4+\Omega_M(1+z)^3+\Omega_\Lambda+(1-\Omega_0)(1+z)^2}} \tag{1.50}$$

1.2.4 Relativistic corrections

Many efforts have been spent to calculate the relativistic corrections for the thermal Sunyaev-Zel'dovich effect [54, 97]. Introducing such corrections, the position of the maximum, minimum and crossover points of the spectrum vary with T_e. Also the intensity amplitude becomes a complicated function of T_e. To first order in Θ, which is sufficient for temperatures $k_BT_e < 20keV$ ($\Theta < 0.04$), the positions shift as:

$$\begin{aligned} x_{Min} &= 2.26 \\ x_{Zero} &= 3.83\cdot(1+1.13\,\Theta) \\ x_{Max} &= 6.51\cdot(1+2.15\,\Theta) \end{aligned} \tag{1.51}$$

Relativistic corrections are obtained by working to higher order in Θ from eq. (1.39) or from Boltzmann equation. The resulting expressions for Δn or ΔI_T are usually written as a series in increasing powers of Θ [17, 54]. The latest results give an approximation up to the fifth term: they provide a useful analytical expression for the thermal SZ effect for hot clusters for a wide range of frequencies. However, there are still approximations: these rely on the assumptions that the cluster is optically thin and that the electron distribution function is that of a single-temperature gas as given by eq. (1.30). Both assumptions are still under discussion and we need more precise results, better than 1%.

It is worth noting that relativistic corrections can be used to estimate cluster characteristics without using X-Ray data: as shown in Fig. 1.9, relativistic corrections break the degeneracies between the comptonization parameter y and the cluster gas temperature T_e due to the positions shift described in eq. (1.52). Once the cluster comptonization parameter y is obtained, it is possible to deduce the electrons number density n_e.

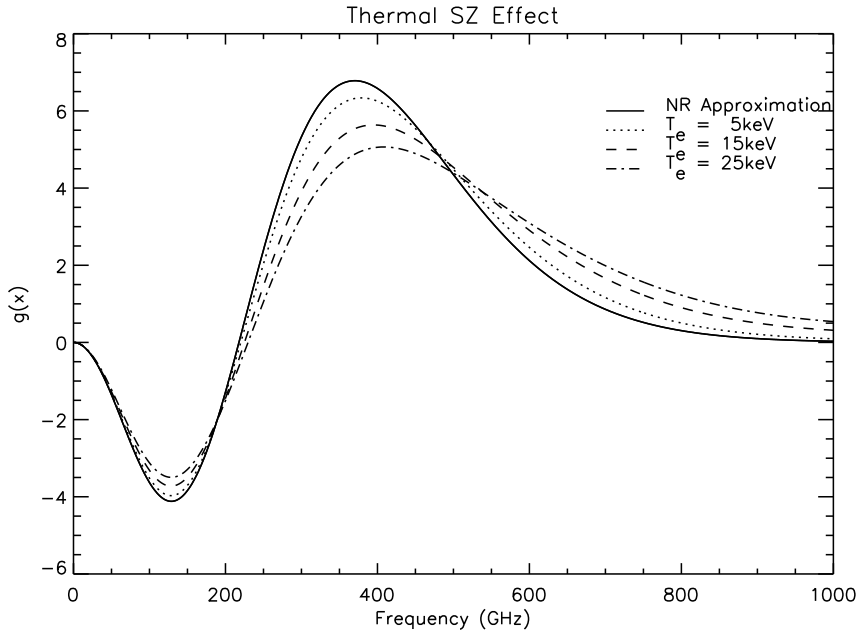

Figure 1.9: *The $g(x)$ function includes all the spectral dependence. In the non-relativistic limit (Kompaneets approximation, see § 1.2.3), $g(x)$ is independent of electrons temperature T_e (solid line), while it is only a function of the adimensional frequency $x = h\nu/k_B T_{CMB}$. Dotted, dashed and dot-dashed lines represent the spectral distortions due to electrons temperature of $T_e = 5keV$, $15keV$ and $25keV$ respectively. Relativistic corrections up to fifth order have been used for the computation (see § 1.2.4).*

The thermal Sunyaev-Zel'dovich effect provides another potential probe for intracluster gas: since this effect is proportional to the integral of n_e along the line of sight, it should be a more sensitive probe than the X-Ray emission for studying the diffuse gas especially in the peripheral regions of the clusters.

1.2.5 Kinematic SZ effect

When a cluster has a non-zero peculiar velocity in the CMB reference frame, a second effect adds to the purely thermal SZ effect previously described: the *kinematic Sunyaev-Zel'dovich effect*. In the reference frame of the scattering gas, CMB radiation appears anisotropic, and the effect of the inverse Compton scattering is to re-isotropize the radiation slightly.

In the observer rest frame, the radiation field is no longer isotropic, but shows a structure towards the scattering atmosphere with amplitude proportional to $\tau_e V_z/c$, where V_z is the peculiar velocity's component of the scattering atmosphere along the line of sight [98, 114], positive or negative for approaching or receding cluster respectively.

Assuming that thermal and kinematic effect are independent (a well verified hypothe-

sis), it is possible to calculate the kinematic correction to the spectrum:

$$\Delta I_K(x) = -\frac{2\,(k_B\,T_0)^4}{h^3\,c^2} \cdot \frac{V_r}{c} \cdot \tau_e \cdot h(x) \tag{1.52}$$

where τ_e is the optical depth defined in eq. (1.32) while $h(x)$ is:

$$h(x) = \frac{x^4\,e^x}{(e^x-1)^2} \tag{1.53}$$

Eq. (1.52) has the same form of eq. (1.41) while this time all the spectral dependence is included in the $h(x)$ term. However, the kinematic distortion is completely different: as shown in Figs. 1.8 and Fig. 1.10, its maximum is roughly where the thermal SZ effect has the crossover point. In principle, a photometric measure at $x \simeq 3.83$ ($\nu \simeq 220 GHz$) is able to detect a non-zero cluster's peculiar velocity along the line of sight: given this parameter, it is possible to subtract the kinematic SZ signal at the other frequencies and separate the thermal component. Therefore, this effect can be used to measure large scales motion of objects that are at high redshifts. However, the spectrum of the kinematic SZ is identical to the spectrum of primary CMB anisotropy: so it is almost impossible to separate the two contributions on the same line of sight.

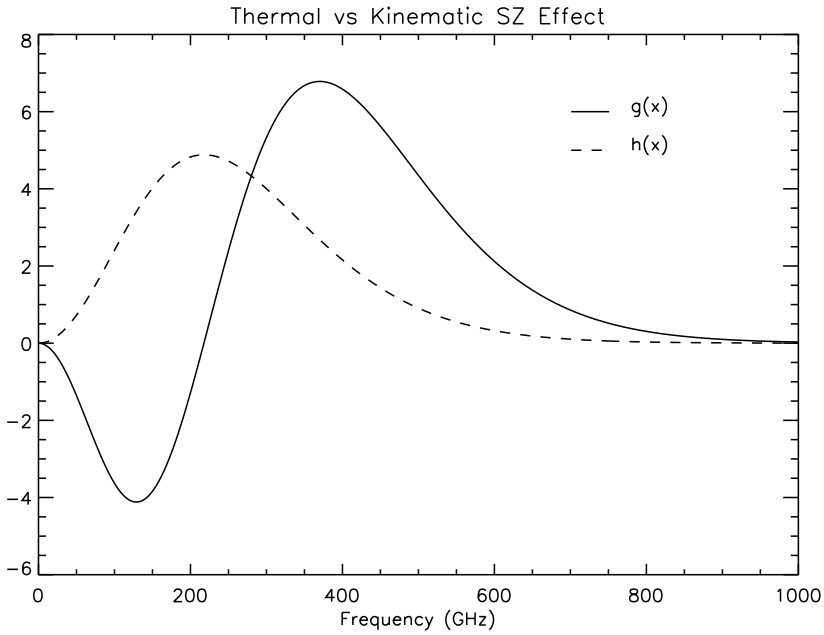

Figure 1.10: *Spectral deformation due to kinematic SZ effect, compared to thermal component. This figure shows only the functions $g(x)$ (solid line, related to thermal SZ effect) and $h(x)$ (dashed line, kinematic SZ effect): these include the spectral dependence and, in the non-relativistic limit, give the spectral deformations modulo multiplicative factors. The full spectral distortion is shown in* Fig. 1.8.

1.3 Foregrounds

The term *foreground* defines all the galactic and extragalactic sources of diffuse emission of astrophysical (but not cosmological) origin. Their characteristics do not depend on the cosmological parameters; on the contrary, they interact and deform the CMB signal. Foreground sources have characteristic spectra, different from the spectrum of the CMB: multi-frequency experiments are needed to disentangle such local contributions from the cosmic microwave background anisotropy, which is subdominant at almost every frequency. Foregrounds must be removed to obtain good estimation of CMB power spectrum and cosmological parameters. Nevertheless, they hold informations on various astrophysical process; also, they must be studied in order to be properly removed.

The most important contaminants are *thermal bremsstrahlung* (or *free-free*) and synchrotron due to charged particles in the interstellar medium, thermal emission due to dust, and emission by extragalactic sources. The latter form the so-called *Far Infrared Background* (FIRB), since they are not resolved.

The dust and FIRB signals increase with frequency, and are expected to dominate the *OLIMPO* channels at the higher frequencies (see Chap. 6): their origin will be discussed in detail in § 1.4 and § 1.5, while the models used in the simulations of signals due to dust and FIRB are described in § 6.1 and § 6.2. Instead, *bremsstrahlung* and synchrotron decrease with frequency and dominate below $100\,GHz$, so that they do not affect *OLIMPO* measurements and will only briefly summarized.

Bremsstrahlung *Free-free* emission is due to the Coulombian scattering between hot electrons ($T \geqslant 10^4 K$) and ionized particles of interstellar gas. It happens typically in the HII regions, i.e. zones of hydrogen ionized by stellar activity. This emission is dominant in the range $25 \div 65\,GHz$ and has an power angular spectrum that decreases as $\ell^{-\beta}$, with $\beta \sim 2.5 - 3$.

Synchrotron It is produced by relativistic electrons accelerated in the galactic magnetic field. It dominates at low frequencies ($\nu \leqslant 50\,GHz$); its power spectrum depends on the energy spectrum of charged particles. Its angular power spectrum is similar to the *bremsstrahlung* emission one [2] but is not as steep.

Both these emissions can be polarized, only slightly for the free free (in anisotropic regions) and quite strongly for synchrotron emission (up to 75%): its study can give important information regarding the galactic magnetic field. The full spectrum of the foreground components is shown in Fig. 1.11.

1.4 Galactic dust emission

InterStellar Medium (ISM) is supplied of matter by supernovae explosions, which scatter the major part of the heavy elements formed during final phases of stars. Some of this matter forms new stars; residual elements aggregate in small solid grains forming the *InterStellar Dust* (ISD).

The components of the interstellar medium can be divided into *material* and *energetic* elements. The former are dust and gas: dust consists of amorphous silicates, *Polycyclic*

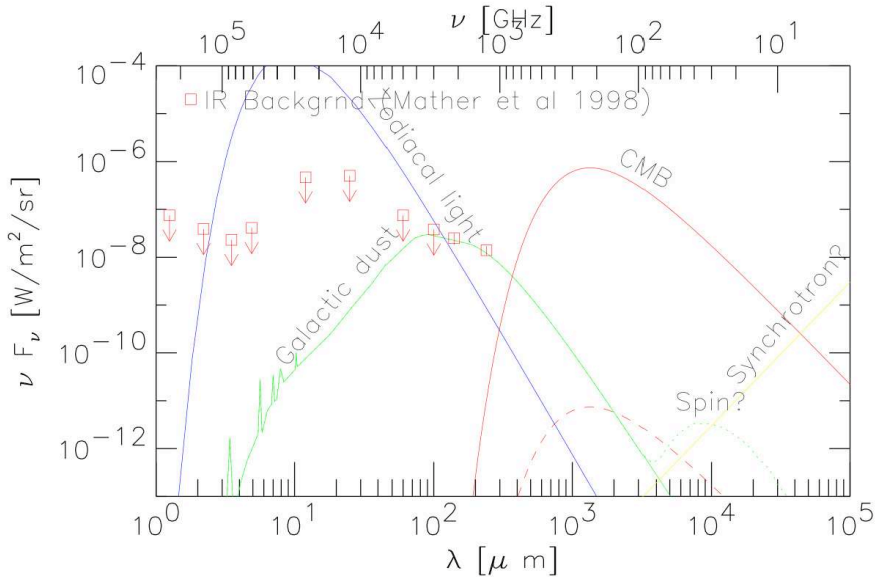

Figure 1.11: *Comparison between the Cosmic Microwave Background spectrum* (*red line*) *and spectra of foregrounds of different origin, in the microwave, millimeter and infrared bands. Synchrotron* (*yellow line*) *dominates at lower frequencies* (*longer wavelengths*), *while at higher frequencies* (*shorter wavelengths*) *the spectrum is dominated by diffuse galactic dust emission* (*green line*). *The emission of interplanetary dust is also shown* (*zodiacal light, blu line*).

Aromatic Hydrocarbons (PAH), graphite and carbon; gas is mainly constitute by hydrogen and helium. Dust and gas are distributed randomly in diffuse or molecular clouds, which differ because of the presence or absence of H_2 or CO molecules. These clouds have a peculiar velocity of $\sim 10 km/s$. Denser regions have good conditions for star formation, since they are inhomogeneous, with substructures or "condensations" forming protostars.

The energetic constituents of the interstellar medium are cosmic rays and radiation coming from young stars, in particular UV photons. Their average number density is $n_{UV} \simeq 6 \cdot 10^{-9} m^{-3}$: they are absorbed by dust which re-emits at lower frequencies (in the infrared band). Cosmic rays also interact with dust, but their effect is negligible when compared to the UV.

There are two types of interactions between dust and photons: extinction and emission. The former happens when dust absorb or scatters photons, thus decreasing the flux coming from stars in the background. Extinction it is very efficient for UV and blue radiation. The latter is the thermal re-emission of the absorbed energy, in the far infrared.

Let us consider one or more particles hit by electromagnetic radiation with energy U_0: the energy received by a detector will be $U < U_0$, because part of it has been extinguished by dust. Energy conservation requires that the absorbed energy is re-emitted in all directions. Extinction is measured using the *couple method*: it consists in a spectroscopic comparison between two stars with the same spectral class. If one star has a negligible dust foreground, while the other one is obscured, the comparison between the two spectra

gives a measure of the extinction as a function of frequency. Stellar radiation passing through a dust cloud is weakened as:

$$I(\nu) = I_0(\nu) \cdot e^{-\tau(\nu)} \tag{1.54}$$

where τ is the cloud optical depth, i.e. the sum of grains surfaces exposed to radiation per unit area A, along the line of sight:

$$\tau(\nu) = \sum_i \frac{C_{Ext,i}(\nu)}{A} \tag{1.55}$$

and C_{Ext} is the extinction cross section, defined as the ratio between the extinction power and the intensity of incident radiation: $C_{Ext} = W_{Ext}/I_{Inc}$. The morphology of interstellar dust is complex: it is made of obscure clouds and long filaments that cross the sky. The discovery of ISD is due to obscuration or extinction of radiation emitted by stars lying behind the clouds. The attenuation depends on the dimensions of the grains, on their type and size distribution: studying the spectrum of dust allows us to deduce its characteristics, such as the chemical composition and the density.

1.4.1 Infrared emission

Interstellar grains are heated primarily by absorbing stellar photons. A small fraction of absorbed energy goes into photoluminescence or emits a photoelectron, while the major part excites vibrational modes, i.e. it heats the grains.

Fig. 1.12 shows, as a function of time, the stimulated temperature of four grains exposed to interstellar radiation. For grains with typical radius of $r \gtrsim 100$Å, photon absorption is frequent and the thermal capacity is sufficiently high, so that temperature variation consequent to absorption is relatively small. In this case it is reasonable to consider the grain temperature as constant in time, at a value $T \sim 20K$. These grains emit photons only in the far infrared region, i.e. $\lambda \geqslant 100\mu m$ ($\nu \leqslant 3000GHz$). Grains with $r \lesssim 50$Å have low thermal capacity: a single absorption increases their temperature far above the mean value, and temperature decreases significantly between two subsequent events. In this case, the emission occurs in the mid infrared, i.e. up to $\lambda \geqslant 20\mu m$.

Emission observed at $12\mu m$ implies temperatures as high as $\sim 200K$, and consequently very small grains: photons having an energy of $6eV$ (about 3 order magnitudes larger than the energy of CMB photons) can heat a grain of $N \sim 280$ atoms up to $200K$. Emission observed at smaller wavelength can be produced only by even smaller particles.

Fig. 1.13 shows the average emission spectrum of interstellar dust based on the observations in the mid infrared region at high galactic latitudes and in the galactic plane. Approximately 21% of total power is emitted in the $3 \div 12\mu m$ band; another 14% between 12 and $50\mu m$, needing many extremely small grains, since they contribute up to 35% of the total absorbing stars' radiation. The remaining 65% is radiated in the far infrared region: observations confirm that this component is emitted by grains large enough to keep their temperature constant.

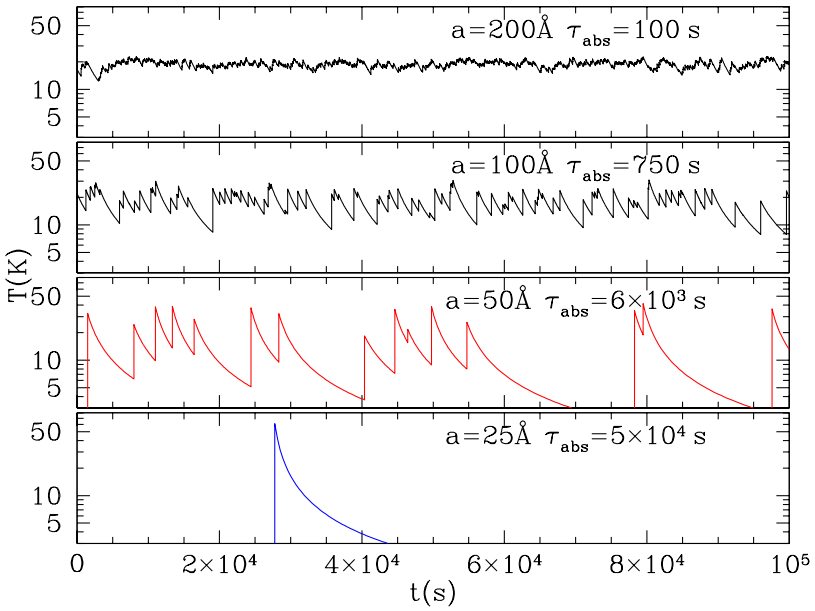

Figure 1.12: *Temperature variations, of 4 carbonaceous grains exposed to the average starlight background.* τ_{Abs} *is the mean time between photons absorptions.*

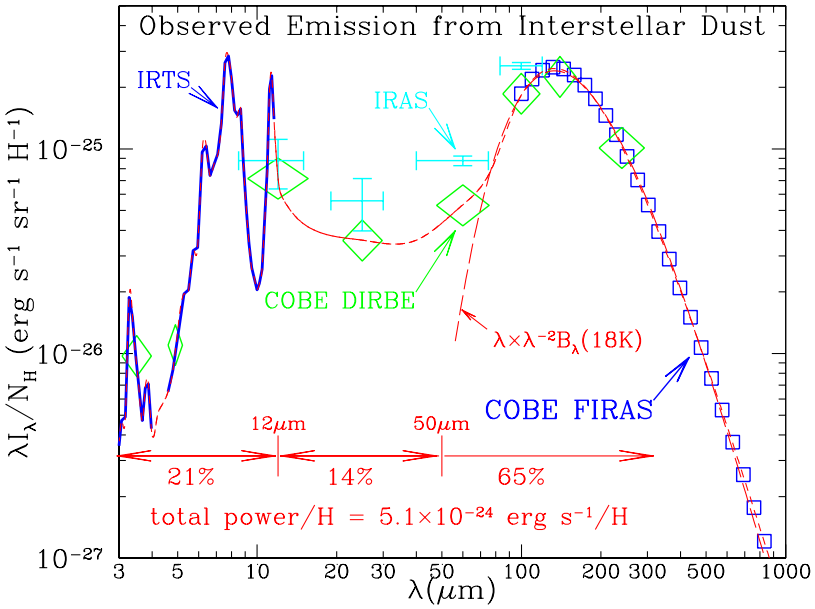

Figure 1.13: *Observed emission spectrum of diffuse interstellar dust in the Milky Way. Crosses: IRAS* [12]*; squares: FIRAS* [38]*; diamonds: DIRBE* [1]*; heavy curve for* $3-4.5\mu m$ *and* $5-11.5\mu m$*: IRTS* [82, 116]*. The total power* $\sim 5.1\cdot10^{-24} erg/s/H$ *is estimated from the interpolated broken line.*

1.4.2 Microwave emission

Interstellar dust microwave emission was discovered by CMB experiments, which revealed at these frequencies ($30 \div 300 GHz$) a strong brightness, correlated to thermal emission of interstellar matter at $3000 GHz$. The spectrum of this emission does not fit a synchrotron one [25], produced by relativistic electrons, and its intensity is higher than the *bremsstrahlung* emission due to ionized gas (see § 1.3). The excess of signal, particularly between 14 and $90 GHz$, can be generated only by dust.

There are three mechanisms which lead to dust emission in microwave region: *vibrational*, *magnetic* and *rotational* emissions.

Vibrational emission It is due to thermal fluctuations in the distribution of charge, i.e. vibrational emission of electric dipole. The major part of power irradiated by interstellar dust comes from this emission, which has its maximum at $\sim 3000 GHz$, but it is not observed below $60 GHz$.

Magnetic emission This is the magnetic dipole emission, and is related to thermal fluctuation in the magnetization of the material near the position of minimum energy. The intensity of the fluctuations of magnetic emission depends mainly on the magnetic properties of the grains. In fact, magnetization is due to electron spin alignment; the maximum frequency needed to rearrange spins is the precession frequency of an electron subject to the magnetic field in the material : this frequency can be as large as $20 GHz$. If the oscillation frequency of the magnetic field is similar to the precession frequency of electron spin ($\sim 10 GHz$), magnetic emission becomes considerable, especially if grain is strongly magnetic. In the latter case, magnetic dipole emission dominates thermal emission in the microwaves [31].

Rotational emission This last mechanism is electric dipole rotational emission, due to rotation of grains around their axis (*spinning*). Rotational emission is proportional to the forth power of angular velocity, so that only extremely small grains can rotate fast enough (angular velocity $\gtrsim 10 GHz$) to produce detectable microwave emission. If these grains have electric dipole momentum, there will be rotational emission in the microwaves: this component is relevant for frequencies higher than $1 GHz$ [30].

The observation of microwave radiation emitted by a dense dust cloud is a good way to distinguish between emission due to grains *spinning* and magnetic one. Studies on the extinction spectrum [77] tell that in dense regions small grains are fewer than expected, so rotational emission in such clouds must be weak.

1.5 Far infrared background

The formation of structures in the primordial Universe is of great significance. Matter aggregates into stars and galaxies; the evolution of these systems is related to gravitational and nuclear processes, which lead to emission of radiative energy. Cosmic expansion and absorption of radiation due to dust transform this radiative energy into a *Cosmic Infrared Background* (CIB) emission: so, the CIB is the product of structure formation processes.

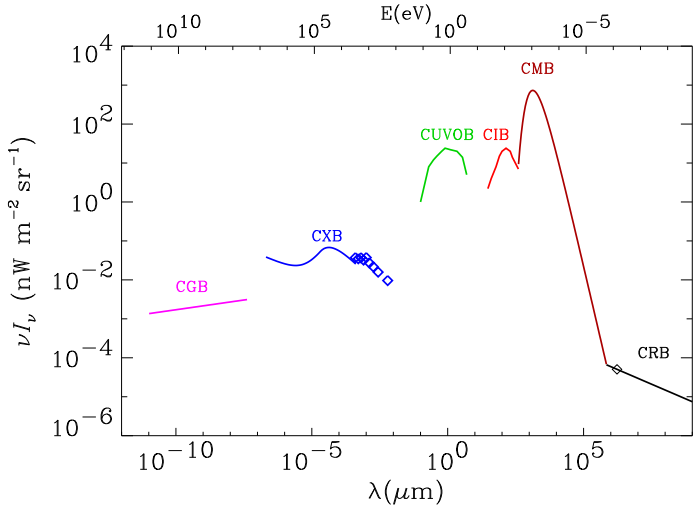

Figure 1.14: *Cosmic background radiation spectrum: the radio background* (*CRB*) *is represented by the spectral law* $\nu I_\nu \propto \nu^{0.3}$, *normalized at* 170*cm* [13]. *CMB is shown as a blackbody spectrum at* $T_{CMB} = 2.725K$. *UV-optical* (*CUVOB*) *e infrared* (*CIB*) *backgrounds estimates are obtained by* [50]. *X-Ray background* (*CXB*) *data are taken from* [120], *while the analytic curve is described in* [37]. γ*-Ray background* (*CGB*) *is represented by a power law* [108].

As shown in Fig. 1.14, the microwave sky is dominated by CMB radiation, followed by the *Extragalactic Background Luminosity* (EBL).

The discovery of this background is due to the *IRTS* satellite in the late 80's, and was later confirmed by the *FIRAS* and *DIRBE* experiments, both mounted on the *COBE* satellite [94, 40]. An infrared background radiation was predicted many years before it was measured [85] as the sign of first phases of galaxy and star formation. There are some indirect evidences for the CIB, due to the attenuation of γ-Rays at TeV energies. Fig. 1.15 shows the actual limits on CIB estimation: it is well known in the UV and optical wavebands, while in the microwave bands there is still a lot of uncertainty.

There are two different methodologies to detect radiation coming from these galaxies: the first one is to resolve them; instead of doing a survey, it is possible to study the integrated emission. This is made using submillimeter satellite telescopes: *FIRAS* measured the spectrum at submillimeter wavelengths [94, 35, 50, 45], while *IRAS* and *ISO* resolved fluctuations in the FIRB at high frequencies [66, 78]. Surveys can be done with large, ground based, submillimeter telescopes [86], but they are hampered by atmospheric instability. Forthcoming experiments, like the 10m *South Pole Telescope* and the *ALMA* interferometer will definitely improve submillimeter measurements. Higher frequencies surveys must be made from space, like the *MIPS* for Spitzer satellite: it can resolve primordial galaxies at 1.9THz, 4.3THz and 12.5THz (160, 70 and 24μm respectively). Submillimeter surveys are dominated by diffuse emission due to interstellar dust, particularly at small scales, as shown in Fig. 1.16.

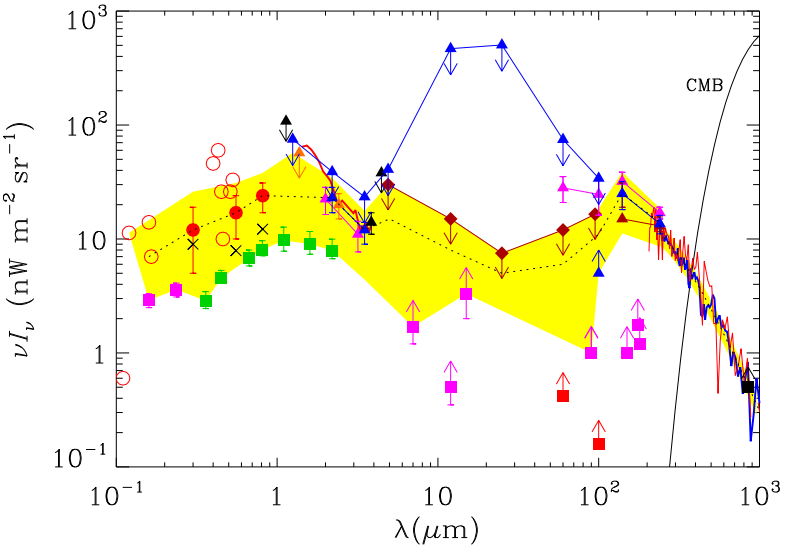

Figure 1.15: *Measures of extragalactic background made with various methods. In the range* $2.2 \div 3.5\mu m$*, they come from direct observations of sky brightness; at longer wavelengths, there are only lower limits obtained by integrated flux of resolved extragalactic sources. Curves shown in the range* $200 - 1000\mu m$ *are given by the analysis made in* [40]*. Yellow region points out upper and lower limits of the CIB energy spectrum, based on all the available measures.*

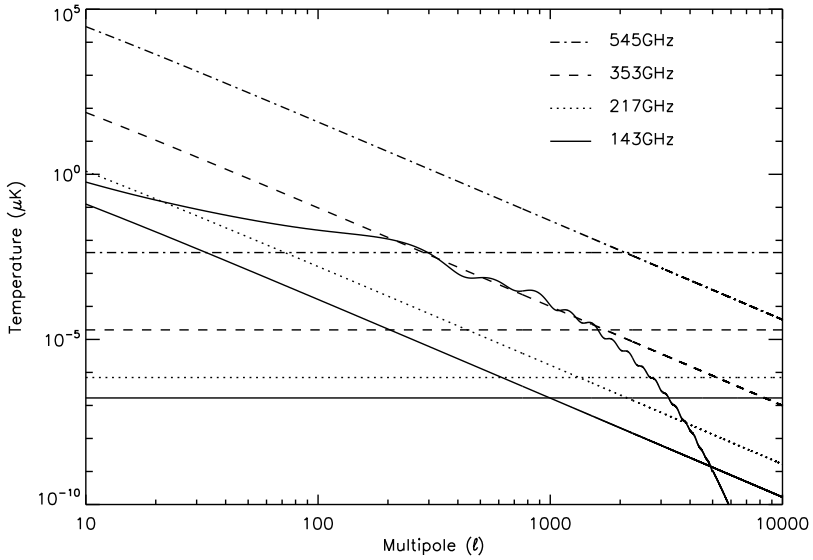

Figure 1.16: *Diffuse emission angular power spectrum at high galactic latitudes. Horizontal lines* $P(\ell) \sim P_0$ *are the FIRB spectrum, while diagonal lines* $P(\ell) \sim \ell^{-3}$ *represent the dust spectrum, both superimposed at CMB anisotropies angular power spectrum.*

1.5.1 Extragalactic background luminosity

As shown in Fig. 1.15, there are two relative maximum in the EBL spectrum, one in the infrared, the other in the optical band. This slope suggests that background is caused by thermal radiation emitted by dust in the far infrared and star radiation *redshifted*, i.e. radiation shifted from UV to optical and near infrared due to source redshift. The existence of a peak at long wavelengths demonstrates that dust is the main source of EBL. Remembering that brightness is defined as the radiative power per unit solid angle and unit area, i.e. $I \equiv dW/d\Omega/dA$, typical values (expressed in $nW\,m^{-2}sr^{-1}$) of the components that constitute EBL at different wavelengths are (values in parenthesis indicate minima and maxima estimations):

$$\begin{array}{ll} I_{Star} = 54\,(19 \div 100) & \lambda = 0.16 \div 3.5\,\mu m \\ I_{Dust} = 34\,(11 \div 58) & \lambda = 3.5 \div 140\,\mu m \\ I_{Dust} = 15 \pm 2 & \lambda = 140 \div 1000\,\mu m \\ I_{CIB} = 76\,(36 \div 120) & \lambda = 1 \div 1000\,\mu m \\ I_{EBL} = 100\,(45 \div 170) & \lambda = 0.16 \div 1000\,\mu m \end{array}$$

The EBL spectral intensity observed at frequency ν_0, $I_{\nu_0}(\nu_0)$, is given by the integral over all the sources [34, 88]:

$$I_\nu(\nu) = \left(\frac{c}{4\pi}\right) \int_0^\infty \mathcal{L}_\nu(\nu, z) \left|\frac{dt}{dz}\right| dz \tag{1.56}$$

where $\mathcal{L}_\nu(\nu, z)$ is the luminosity spectral density of all the radiative particles and luminous objects in a comoving volume at redshift z; $\nu = \nu_0(1+z)$ is the frequency in the source rest frame, while:

$$H_0 \left|\frac{dt}{dz}\right| = \frac{1}{1+z} \cdot \frac{1}{\sqrt{(1+z)^2(1+\Omega_M z) - z(2+z)\Omega_\Lambda}} \tag{1.57}$$

Eq. (1.56) is obtained under the assumption that the Universe is optically thin at every frequency of interest. In a Universe without dust, the spectral density $\mathcal{L}_\nu(\nu, z)$ is simply obtained by the emitted spectrum of the source; the presence of dust does not change the total intensity, but it redistributes energy over the whole spectrum. The emitted spectrum depends on the absorbed wavelength, on the spatial distribution of dust and sources, on dust abundance and scattering properties: these depend on dust composition and dimensions (see § 1.4). The total spectrum depends also on evolution factors, such as history of the dust formation and the processes that destroy, modify and redistribute dust.

Cosmic expansion reduces the contribution to the EBL due to sources with $z > 2$ [49], even though high redshift, luminous infrared sources can dominate CIB in the submillimeter range, due to the negative *K-correction* effect.

1.5.2 The K-correction

Due to the expansion of the Universe, there is a clear relationship between source recession velocity and radial distance; furthermore, sources observed at different redshifts but at

the same frequency cannot be compared. The transformation from observed photometric measurements to rest frame ones is called *K-correction*.

Let us consider a source observed at redshift z. For this source photons observed at frequency ν_0 were emitted at frequency $\nu_e = (1+z)\nu_0$. The relationship between the apparent flux of the source, observed in a band R, and the intrinsic luminosity, emitted in a band Q, is given by the *K-correction*: observed and emitted bands can be different in shape and in frequency position. Given a source with apparent magnitude m_R, absolute magnitude M_Q, the *K-correction* K_{QR} is defined as:

$$m_R = M_Q + DM + K_{QR} \tag{1.58}$$

where DM is the distance modulus $DM = 5\,\log(D_L/10\,pc)$, with D_L defined as the luminosity distance of the source, which is related to the angular distance described in eq. (1.50) as $D_L = D_A \cdot (1+z)^{-2}$. The apparent magnitude of the source m_R is related to the flux spectral density $f_\nu(\nu)$, i.e. the energy per unit time, area and frequency, by:

$$m_R = -2.5\log\left[\frac{\displaystyle\int \frac{d\nu_0}{\nu_0}\, f_\nu(\nu_0)\, R(\nu_0)}{\displaystyle\int \frac{d\nu_0}{\nu_0}\, g_\nu^R(\nu_0)\, R(\nu_0)}\right] \tag{1.59}$$

where $g_\nu^R(\nu)$ is the flux spectral density of the standard source, Vega; $R(\nu)$ describes the signal measured by the detector for an incident photon of frequency ν.

The absolute magnitude M_Q, defined as the apparent magnitude of the source when this is at a distance of $10pc$, is related to the specific luminosity of the source $\mathcal{L}_\nu(\nu)$:

$$M_Q = -2.5\log\left[\frac{\displaystyle\int \frac{d\nu_e}{\nu_e}\, \frac{L_\nu(\nu_e)}{4\pi(10pc)^2}\, Q(\nu_e)}{\displaystyle\int \frac{d\nu_e}{\nu_e}\, g_\nu^Q(\nu_e)\, Q(\nu_e)}\right] \tag{1.60}$$

where $Q(\nu)$ is equivalent to $R(\nu)$ for the Q band. As already said, in general the *K-correction* does not require that $Q = R$ or $g_\nu^Q = g_\nu^R$. It is worth noting that the integral in eq. (1.59) is computed over the observed frequencies ν_0, while the one in eq. (1.60) is over the emitted frequencies ν_e.

If the source is at redshift z, its luminosity is related to flux by:

$$\mathcal{L}_\nu(\nu_e) = \frac{4\pi D_L^2}{1+z}\, f_\nu(\nu_0) \tag{1.61}$$

Substituting eqs. (1.59), (1.60) and (1.61) into eq. (1.58), we get the analytic expression of the *K-correction* in the case of a source observed in the R band with absolute magnitude M_Q in the Q band:

$$K_{QR} = -2.5\log\left[(1+z)\,\frac{\displaystyle\int \frac{d\nu_0}{\nu_0}\, f_\nu(\nu_0)\, R(\nu_0) \int \frac{d\nu_e}{\nu_e}\, g_\nu^Q(\nu_e)\, Q(\nu_e)}{\displaystyle\int \frac{d\nu_0}{\nu_0}\, g_\nu^R(\nu_0)\, R(\nu_0) \int \frac{d\nu_e}{\nu_e}\, f_\nu\left(\frac{\nu_e}{1+z}\right) Q(\nu_e)}\right] \tag{1.62}$$

Hence, in order to estimate accurately the *K-correction*, it is necessary to know the flux density $f_\nu(\nu)$, the flux density of the standard source in the R and Q bands, $g_\nu^R(\nu)$ and $g_\nu^Q(\nu)$, and the bands $R(\nu)$ and $Q(\nu)$: in real life, all these functions are not properly known.

The classic *K-correction* implies $R(\nu) = Q(\nu)$ and $g_\nu^R(\nu) = g_\nu^Q(\nu)$. These simplify the integrals over the flux densities of standard sources, while an accurate knowledge of source's density flux $f_\nu(\nu)$ is still needed. Many recent surveys are trying to obtain $R(\nu) \sim Q([1+z]\nu)$ and to reduce the dependence on $f_\nu(\nu)$: for high redshifts, this requires a good knowledge of the absolute density flux of the standard sources, but this absolute calibration is still uncertain.

1.5.3 Models of EBL spectrum

There are many models that try to explain the evolution of the spectral energy density $\mathcal{L}_\nu(\nu, z)$ as a function of redshift. Most of them are used to determine the galaxy counts in deep photometric surveys, aiming to study galactic evolution. These models can be divided into four groups, which differ in their degree of complexity, physical realism, and ability to account for observations or to make predictions:

- *Backward Evolution* models (BE).
- *Forward Evolution* models (FE).
- *Semianalytical* models (SA).
- *Cosmic Chemical Evolution* models (CCE).

Backward evolution models

These models extrapolate spectral properties of local galaxies to higher redshifts, using a parametric function for their evolution. In their simplest form, commonly referred to as no-evolution models, they assume that neither the *Spectral Energy Density* (SED) nor the comoving number density of galaxies evolve with time. This implies that the luminosity spectral density is redshift independent: $\mathcal{L}_\nu(\nu, 0) = \mathcal{L}_\nu(\nu, z)$. The EBL is then obtained by integrating the local luminosity density up to a maximum redshift, z_{Max}, the epoch when the earliest galaxies formed. Fundamental differences exist between determinations of $\mathcal{L}_\nu$ at UV, optical, and near infrared wavelengths, where the emission is primarily made of starlight, and at mid to far infrared wavelengths, where the emission is dominated by thermal emission from dust.

In the optical and infrared wavelengths, luminosity function is described by the Press-Schechter function [92], with parameters that depend on the morphology and the spectral classification of the galaxy. Galactic SEDs are constructed by fitting population synthesis models to the observed UV-optical spectra or photometric data for each galaxy type. The extension of this model to wavelengths $\lambda \geqslant 10\mu m$ is not trivial, because the SED is dominated by dust thermal emission.

Number counts predicted by no-evolution models are often used as benchmarks to be compared with observations. In general, the predicted counts are much lower than

the observed ones, requiring to abandon the simple assumptions made in these models. Evolution can be introduced into BE models as pure luminosity evolution, manifested as a global scaling of galaxy spectra as a function of redshift, or as pure density evolution, manifested as a change in the comoving number density of galaxies with redshift. The evolution is usually characterized by an empirical factor $(1+z)^{\gamma}$, where γ can vary with redshift.

The *Cosmic Star Formation Rate* (CSFR) is characterized by the Rowan-Robinson model. It includes four spectral components to describe the CIB's sources: cirrus, *Active Galactic Nuclei* (AGNs) and two types of starburst similar to M82 and Arp220. The parameters are determined by fitting the color-luminosity relation obtained by *IRAS*: galaxy counts at $60\mu m$, $175\mu m$ and $850\mu m$, CIB spectrum at $140\mu m$ and $750\mu m$. BE models implicitly assume a growth of CSFR for $z \gtrsim 1 \div 1.5$, with a rate roughly constant during primordial epochs. Fig. 1.17 shows a comparison between observations and the extragalactic background luminosity predicted by a backward evolution models.

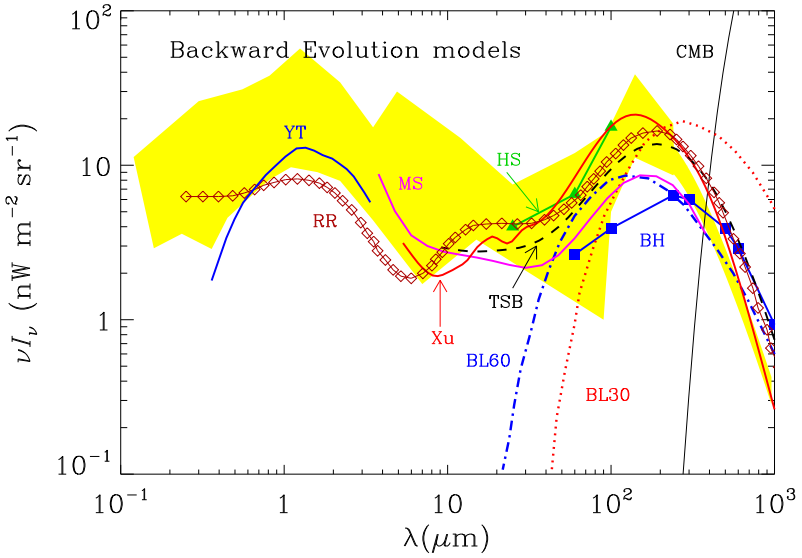

Figure 1.17: *Extragalactic background luminosity as predicted by backward evolution models. Shaded region: experimental limits on EBL as described in* Fig. 1.15. *See* [50] *and references therein.*

Forward evolution models

Some of the imperfections of BE models are corrected in forward evolution models. The key point of these models is a spectral evolution code that evolves stellar population and calculates the stellar, gas, and metallicity content and SED of a galaxy as a function of time, starting at the onset of star formation. These models were introduced in 1974 by Tinsley and are now used to date SEDs of globular clusters and many galaxies types.

Models input parameters include a prescription for CSFR, stellar initial mass function and chemical evolution. Models rely on a wide range of computational and observational

data sets, such as stellar evolutionary tracks, libraries of observed and calculated stellar atmospheres and the observed luminosity functions of galaxies. Models are then set in a cosmological framework by specifying the values of H_0, Ω_M and Ω_Λ. Assuming an initial formation epoch, these parameters are used to map the temporal evolution of galaxies into redshift space, allowing direct comparison of the models predictions with observations. Model parameters are adjusted to match the galaxy number counts, spectral energy distribution, colors, and metallicity as a function of redshift. In this sense, FE models are essentially elaborate BE models that allow for a consistent "backward" evolution of galaxy parameters with time.

Drawbacks of FE models reside in the assumption of a monolithic star formation rate, i.e. galaxies form and at the same time evolve quiescently. Fig. 1.18 shows a comparison between observations and the extragalactic background luminosity predicted by backward evolution models.

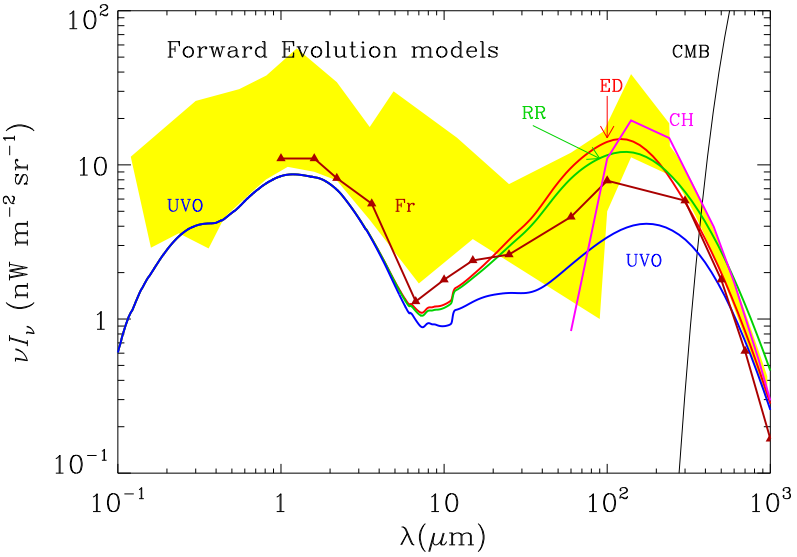

Figure 1.18: *Extragalactic background luminosity as predicted by forward evolution models. Shaded region: experimental limits on EBL as described in* Fig. 1.15. *See* [50] *and references therein.*

Semianalytical models

Some shortcomings of the FE models can be partially worked out using SA models for structure formation to predict the observable characteristics of galaxies and the intensity and spectrum of the EBL. Semianalytical models represent a useful formalism to describe evolution of galaxies and galaxy clusters in a hierarchical scenario for galaxy formation [20].

These models take into account many physical processes to correctly reproduce the observable properties of galaxies. These include the cooling of gas that falls into the halos, a prescription on star formation, a feedback mechanism that modulates the star formation

efficiency, a stellar initial mass function and a star formation efficiency during merger events. Moreover, they require stellar spectra evolution and chemical evolution models that are used in forward evolution models.

The use of SA models does not solve any of the fundamental problems associated with computing the extinction and SED of galaxies. These quantities depend on dust parameters, on the geometry of emitters and absorbers, and on the evolution of these properties, none of which are provided by the models. The main advantage of SA models is that, in spite of the many adjustable parameters, they provide a physical approach to the formation and evolution of galaxies.

SA models divide star formation rate into two different components: a *quiescent* one, which represents stellar formation into the galactic disc, and a *stochastic* one, which is the contribution of star formation *burst* during galactic interactions and merging processes. Since these events are more probable at high redshifts, semianalytical models should better describe the source counts obtained by recent and upcoming experiments. Sources discovered by *SCUBA* are presumably high redshift counterparts of local ultraluminous infrared galaxies, most of which are mergers.

Even though SA models have great success, there are still discrepancies between predictions and observations due to intrinsic difficulties of these models. Other critical elements are the approximation on physical processes and the uncertainties on the input data.

Cosmic chemical evolution models

Because the EBL is an integrated measure of cosmic activity, summed over time and over the wide variety of processes and systems that have populated the Universe, it can only give information regarding global characteristics of the cosmic history. An approach that deals with average properties of the Universe rather than the many complex details involved, is naturally related to this background radiation.

CCE models use this approach, relating the history of a few global properties of the Universe in a self-consistent way. The main advantage consists in the intrinsic simplicity and global nature of this methodology. These models provide a picture of mean density evolution of stars, interstellar gas, metals and radiation averaged on the whole galaxy population in a comoving volume big enough.

Inputs to CCE models are tracers of stellar activity (emitted radiation) and of interstellar medium in galaxies (absorbed radiation). Equations of cosmic chemical evolution are solved to guarantee consistency between the global rates of interstellar gas depletion, star formation and chemical enrichment. Models do not require a detailed knowledge of the complex processes involved in galaxy formation, merging and evolution. Since they use a global approach, CCE models do not predict galaxy number counts.

Fig. 1.19 shows comparison between current measurements and EBL spectrum predicted by semianalytical and cosmic chemical evolution models. The latter (red curve, labeled PFH) clearly yields a double peaked spectral energy distribution: this is consistent with far infrared and UV-optical emissivity data used as model's input, although it cannot explain the recently reported UV-optical and near infrared measurements, while the low levels predicted in the mid infrared are still consistent with observations.

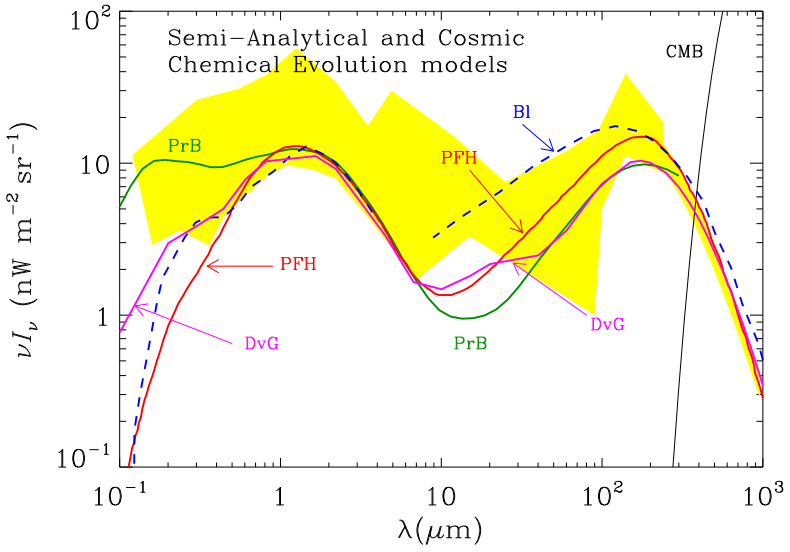

Figure 1.19: *Extragalactic background luminosity as predicted by as predicted by semianalytical (PrB, DvG and BL) and cosmic chemical evolution (PFH) models. Shaded region: experimental limits on EBL as described in* Fig. 1.15. *See* [50] *and references therein.*

1.5.4 Submillimeter galaxies

There are two fundamental components of radiation due to galaxies at submillimeter wavelengths: continuum thermal emission coming from dust grains (ISM solid state) and emission lines generated by atomic and molecular transitions of interstellar gas.

Surveys of distant galaxies at millimeter wavelengths have so far been made using cameras that detect only continuum dust emission, while the search for line emission is becoming increasingly significant. The spectral resolution provided by line observations reveals much more about the physical and chemical conditions in the interstellar medium, to study kinematics, metallicity and excitation conditions. Molecular lines can also be used to obtain a very accurate spectroscopic redshift for the ISM in high redshift galaxies.

The best studied regions of the Universe in the submillimeter waveband are *Giant Molecular Clouds* (GMC) in the Milky Way, where ongoing star formation is taking place. GMC are perhaps very low luminosity representative of distant dusty galaxies, although these galaxies have far infrared luminosities that are up to four orders of magnitude greater than that of the whole Milky Way.

Another class of galaxies well studied similar in luminosity, and perhaps in physical properties, to high redshift submillimeter galaxies are the *UltraLuminous InfraRed Galaxies* (ULIRGs), first discovered by the *IRAS* all-sky survey in the mid 80s. *IRAS* only discovered low redshift galaxies ($z \leqslant 0.3$); the first high redshift ULIRG ($z = 2.3$) was found in 1991 [100]. Fig. 1.20 shows the infrared spectral energy density of some low redshift ULIRGs and a synthesis of results for sampled SEDs of high redshift dusty galaxies.

About 99% of the energy released by galaxies in the submillimeter and far infrared bands is produced by thermal emission from dust grains; the remainder comes from atomic

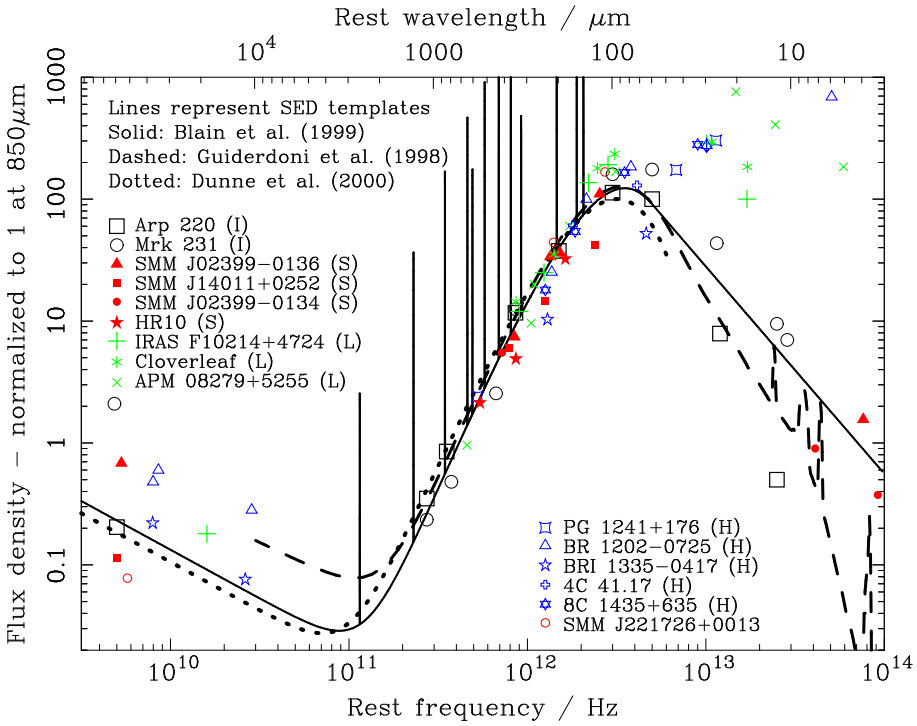

Figure 1.20: *Various observed restframe spectral energy distributions (SED) of galaxies from the radio to the near infrared bands. White symbols (I): two examples of the most luminous low redshift galaxies detected by IRAS; red symbols: four very luminous high redshift galaxies directly detected in deep submillimeter surveys; green symbols (L): three high redshift galaxies magnified by gravitational lensing effect of foreground galaxies; blue symbols (H): five high redshift AGNs detected in optical or radio surveys. The lines representing three SEDs template are shown. Dotted line includes properties of CO and atomic fine structure emission lines at wavelengths from* 100 *to* $3000\mu m$ [6]*; dashed one includes polycyclic aromatic hydrocarbon (PAH) molecular emission features at wavelengths* $\sim 10\mu m$ *in the mid infrared band* [47]*; solid one is normalized to the typical SED of a sample of low redshift IRAS galaxies* [32].

and molecular rotational lines emission. However, the source of the energy that heats dust is often unclear. Any intense source of optical or UV radiation, such as young high mass stars or accretion disk surrounding black hole, would heat dust grains. Since dust emits a featureless modified blackbody spectrum, submillimeter continuum observations can reveal little information about the physical conditions within the sources. Regions of intense dust emission are very optically thick, hence little information can be obtained by observing optical or UV radiation.

Two parameters are necessary to describe emission due to dust grains: dust temperature T_D and emissivity function ε_ν. Every galaxy has a temperature distribution that represents the different nature and environment of the grains. In most cases, spatially and spectrally resolved images of galaxies are not available, so it is reasonable to assume an emissivity function averaged on a volume and function of frequency, $\varepsilon_\nu \propto \nu^\beta$, where the

spectral index usually assumes a value in the range $\beta = 1 \div 2$. Scattering theory predicts $\beta \to 2$ for low frequencies ($\nu \lesssim 100 GHz$), while it is needed $\beta \simeq 1$ at high frequencies ($\nu \gtrsim 1000 GHz$) in order to match the general slope of the interstellar extinction curve describing the absorption properties of the ISM at optical and UV wavelengths.

The simplest form of emission spectrum f_ν is obtained assuming that $f_\nu \propto \varepsilon_\nu B_\nu$, where B_ν is the Planck function. This formula implies that the emitting source is optically thin; a more rigorous analysis must include an optical depth term:

$$f_\nu \propto (1 - e^{-\tau_\nu})\, B_\nu \tag{1.63}$$

where the optical depth term τ_ν is proportional to the emissivity ε_ν and depends on the frequency. At lower frequencies, eq. (1.63) tends to the simpler $\varepsilon_\nu B_\nu$ function. It is reasonable to assume that in the mid infrared, the SED can be interpolated by a blackbody function modified by a power law $f_\nu \propto \nu^\alpha$. There is a significant correlation between β and T_D when few datapoints are fitted. This makes difficult to associate dust mass and dust temperature obtained by galaxy's SED with real physical conditions of the galaxy itself.

Galactic SEDs can be divided into two categories [33]: the first one includes galaxies having a spectrum with a typical temperature of $40K$, i.e. typically the most luminous galaxies; the other one involves galaxies with a colder single temperature SED, much more similar to normal spiral galaxies.

An alternative approach to determine SEDs consists in using the observed flux density distribution of galaxies in the far infrared and submillimeter bands, which are sensitive to objects at low, mid and high redshifts.

1.5.5 The observability of high redshift dusty galaxies

The flux density at observed frequency ν of a galaxy with bolometric luminosity L (i.e. luminosity integrated on all frequencies), at redshift z and intrinsic spectral energy density f_ν is given by:

$$S_\nu = \frac{(1+z)\, f_{\nu(1+z)}}{4\pi\, D_L^2 \int f_{\nu'}\, d\nu'} \cdot L \tag{1.64}$$

where D_L is the luminosity distance at redshift z.

Submillimeter observations of distant galaxies give the possibility of sampling galaxy SEDs at wavelengths where the spectral energy density increases with frequency (Fig. 1.20). This ensures that distant galaxies are observed at a rest frame wavelength closer to the peak of their SEDs: thus, there is a strong, negative *K-correction*, which implies that high redshift galaxies are relatively easy to detect at submillimeter wavelengths if compared with their low redshift counterparts.

This effect is shown in Fig. 1.21: the *K-correction* effect applies for wavelengths longer than $250\mu m$. At these wavelengths the flux density from galaxies at $z > 1$ stops to decline as the inverse square of distance, instead remains approximately constant with increasing redshift. The effect is stronger at longer wavelengths: in the millimeter band more distant galaxies are expected to produce greater flux densities than their closer counterparts.

A submillimeter telescope that is sensible enough to detect a given class of galaxies at redshift $z \simeq 0.5$, will be able to observe similar galaxies at $z \sim 10$. *K-correction* can be determined at redshifts for which sufficient heavy elements are present in the target galaxy ISM to form enough dust to reprocess optical radiation. Besides, *K-correction* is not able to hide the luminosity decrease due to cosmic expansion: it must be considered the normal $(1+z)^{-4}$ reduction in surface brightness, even if it becomes relevant when $z > 5$.

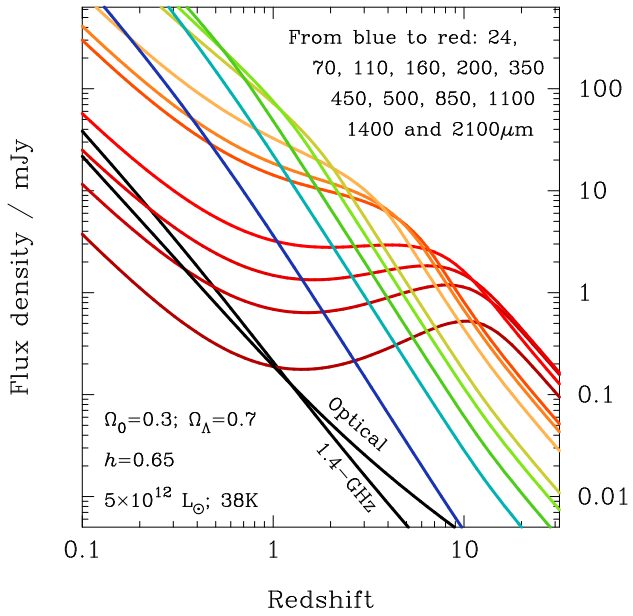

Figure 1.21: *Expected flux density of a dusty galaxy as a function of redshift. The K-correction in the millimeter and submillimeter bands, i.e. $\lambda > 250\mu m$, yields a flux density that is almost independent of redshift* [10].

1.5.6 Star formation rate

The epoch of galaxy formation is highly interesting for cosmology: using number counts of galaxies or extragalactic sources it is possible to study the early phases that follow the decoupling epoch. In the past years, galaxy counts were used to measure the Universe geometry, even though they are more useful for the study of evolution history and galaxies formation: counts models predict the evolution of galaxy population at redshifts greater that one. Together with new observational data, number counts can discriminate between different evolving theories. Galaxy counts can be divided into the two models already cited:

- Backward models.
- Forward models.

The first model considers the luminosity function at present ($z = 0$) and evolves the luminosity and density back in time, assuming a reasonable parameterization [8, 9, 87].

The drawback of this analysis rely in the fact that most of data comes from the *IRAS* survey, so they refer to low redshift sources ($\sim 0.02 \div 0.2$).

The alternative approach computes evolution starting from initial conditions of physical processes, chemical evolution and photometric of stellar population which heat dust [41]. The disadvantage of this model is due to the presence of many undefined parameters.

Millimeter and submillimeter extragalactic surveys will be able to study star formation at all redshifts. Deep field observations were mainly made in the optical band, while recent CIB measurements in the submillimeter and far infrared bands show the "dark side" of galactic formation: in the "local" Universe, about 30% of the bolometric luminosity of galaxies is emitted in the infrared band and a large amount of dust heating is due to young stellar population activity, so that a substantial fraction of submillimeter and far infrared emission is produced by stellar formation processes. Thus, part of stellar and galactic formation signal is hidden by dust, which adsorbs stellar radiation in the UV and optical bands and re-emits it thermally at longer wavelengths.

It is clear that the global *Star Formation Rate* (SFR) inside galaxies is higher than what can be obtained by optical data alone. Fig. 1.22 summarizes existing data on SFR history.

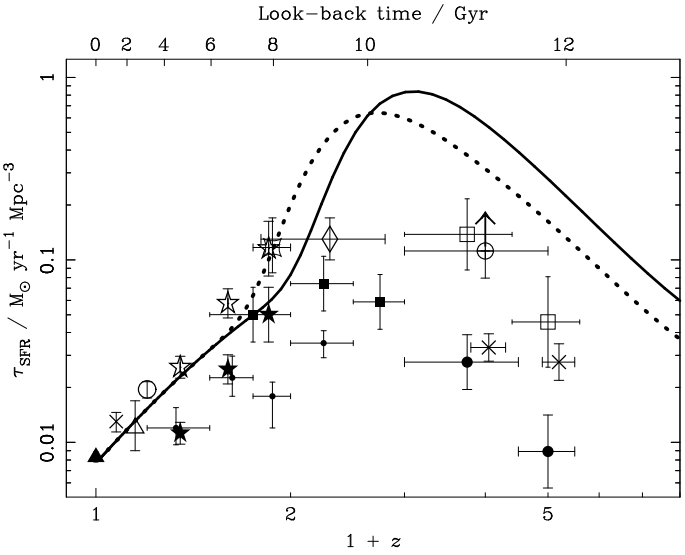

Figure 1.22: *Star formation rate τ_{SFR} as a function of redshift, as inferred from UV, optical and near infrared observations, in order of increasing redshift. See* [7] *and references therein. The high redshift points are derived from analysis of the Hubble Deep Field. Solid and dotted lines represent respectively a gaussian and a modified gaussian SFR model, based on submillimeter wavelength data.*

Nowadays, there are 100 submillimeter galaxies known, even if their redshift and physical properties are highly uncertain. Knowledge of their properties come from observation made with *SCUBA* and *MAMBO* experiments, at wavelengths of 450, 850 and 1200μm. Counts of distant galaxies in the far infrared at 95 and 175μm were obtained by *ISOPHOT*. At even longer wavelengths ($\lambda = 2.8mm$), limits on galaxy counts were carried out by the *BIMA* interferometer. Most relevant data are summarized in Fig. 1.23.

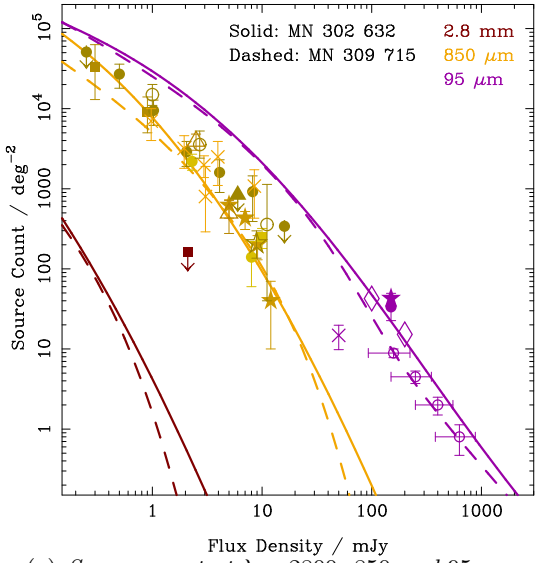

(a) *Source count at* $\lambda = 2800$, 850 *and* 95*mm*

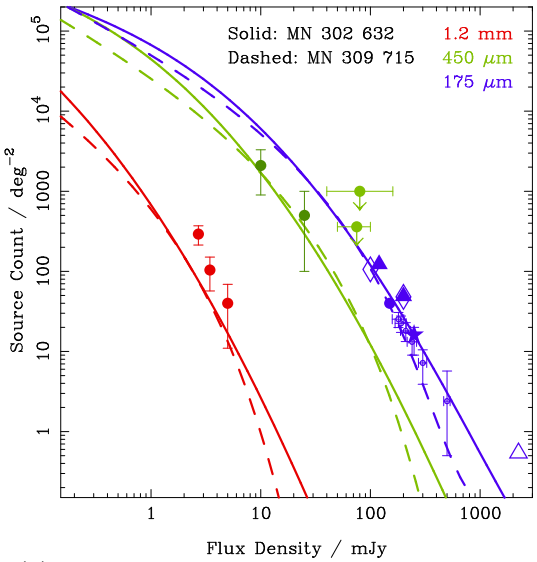

(b) *Source count at* $\lambda = 1200$, 450 *and* 175*mm*

Figure 1.23: *Summary of count data from several millimeter, submillimeter and far infrared surveys. The plotted curves are derived in models that provide good fits to this data compilation, while errors are shown as* 1σ*: see* [7] *and references therein. Data points in the range* $2 \div 10 mJy$ *are consistent with an integrated source count* $N(>S) \propto S^{\alpha}$*, with a power law index* $\alpha \simeq -1.6$*. It is worth noting that counts at fainter flux densities must have* $\alpha < -1$ *to avoid divergence of background radiation intensity, while counts at brighter flux densities fall steeply.*

1.5.7 Confusion noise

One of the main problems of millimeter wavebands observations is related to the difficulty in source resolving (*confusion noise*), i.e. the contribution to noise in an image due to superimposed signals coming from faint sources, on the scale of the telescope beam. This is a problem related to the instrument resolution. In fact, a significant fraction of the noise in the deepest $850 \mu m$ *SCUBA* image can be attributed to confusion noise: actual limits of *SCUBA* observations are $\sim 2 mJy$. This limit makes difficult to determine accurate position of fainter galaxies, rendering follow-up observations more challenging. Unfortunately, most of the high redshift galaxies known are typically fainter than actual confusion limit.

Counts of dusty galaxies shown in Fig. 1.23 can be used to estimate the effect of source confusion in observations made at a wide range of frequencies and angular scales. The distribution of flux density values from pixel to pixel in an image due to confusion noise depends on the detected galaxy counts. Confusion noise becomes relevant when source density is higher than $\sim 0.03\, beam^{-1}$.

The simulated confusion noise distribution can be represented quite accurately by a logarithmic distribution, which fits the higher flux density values better than the gaussian distribution (see Fig. 1.24). The central peak's width of flux density distribution is approximately the same as the flux density at which the sources count exceeds 1 $beam^{-1}$.

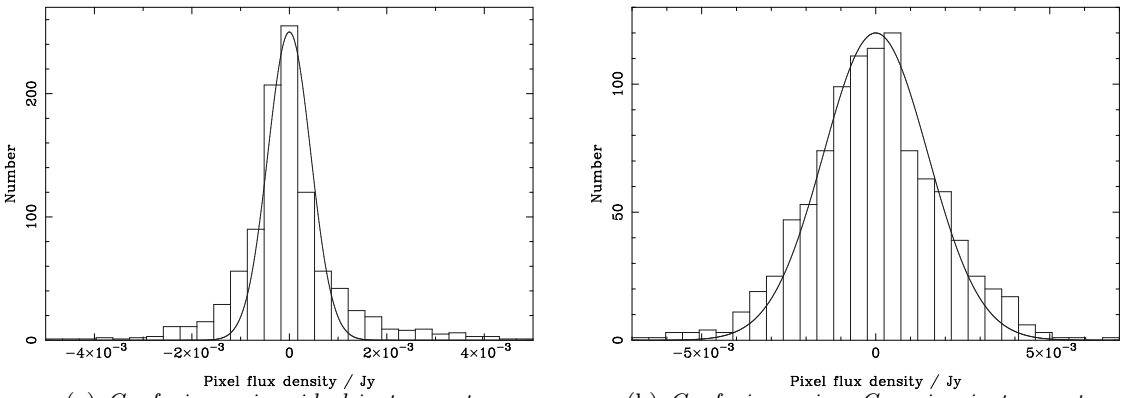

(a) *Confusion noise: ideal instrument* (b) *Confusion noise: Gaussian instrument*

Figure 1.24: *Histograms showing the simulated effects of confusion noise in deep SCUBA integrations at* $850\mu m$*. The left panel shows the expected distribution of pixel flux densities when the telescope samples the sky in a standard* $(-0.5, 1, -0.5)$ *chopping scheme, with overplotted gaussian distribution and no additional noise terms present. The flux distribution is not Gaussian: this is particularly evident in the tails. In the right panel is plotted the same confusion noise distribution convolved with a Gaussian beam and for a sky noise RMS of* $1.7mJy$*, which is the typical noise level of the SCUBA survey.*

This provides a useful indication of the angular scales and frequencies for which confusion noise is significant, and of the limit imposed for a specific instrument to the depth of the survey (see Fig. 1.25).

The real problem of confusion for identifying sources and conducting multiband studies of submillimeter galaxies is illustrated by the results of the first generation of surveys. It is impossible to be certain that the correct source identification is made, simply using optical or submillimeter observations. In many cases, faint radio galaxies can be associate to submillimeter galaxies: observations in millimeter band of these radio galaxies made with high resolution interferometers, together with long observational time, provide more accurate measurements, thus reducing the effects of submillimeter confusion.

As already said, confusion noise is a signal degradation due to low angular resolution (Fig. 1.26), i.e. the instrument ability in resolving two close sources. Predicting or measuring confusion noise depends on the measurement purposes: realizing a far infrared or submillimeter survey and obtaining a complete sampling has different requirements with respect to measuring the SED or the photometric redshift of a source. In the first case, it is necessary to control the statistical properties of the whole sample; in the second one, the absence of completeness is irrelevant and low photometric accuracy is acceptable too.

Confusion noise predictions require the knowledge of the galaxies number counts distribution: it is required to choose a model. Since the slope in the $\log(N) - \log(S_\nu)$ diagram varies with the flux density S_ν, fluctuations of faint sources below S_ν must vary too. Confusion noise can be estimated by the level of fluctuations, using photometric criteria. In the infrared and submillimeter wavebands, below $300\mu m$, confusion noise is better predicted using source density; at longer wavelengths, it is more suitable the photometric criterion.

A sample of faint extragalactic sources is quite incomplete: this can give problems for

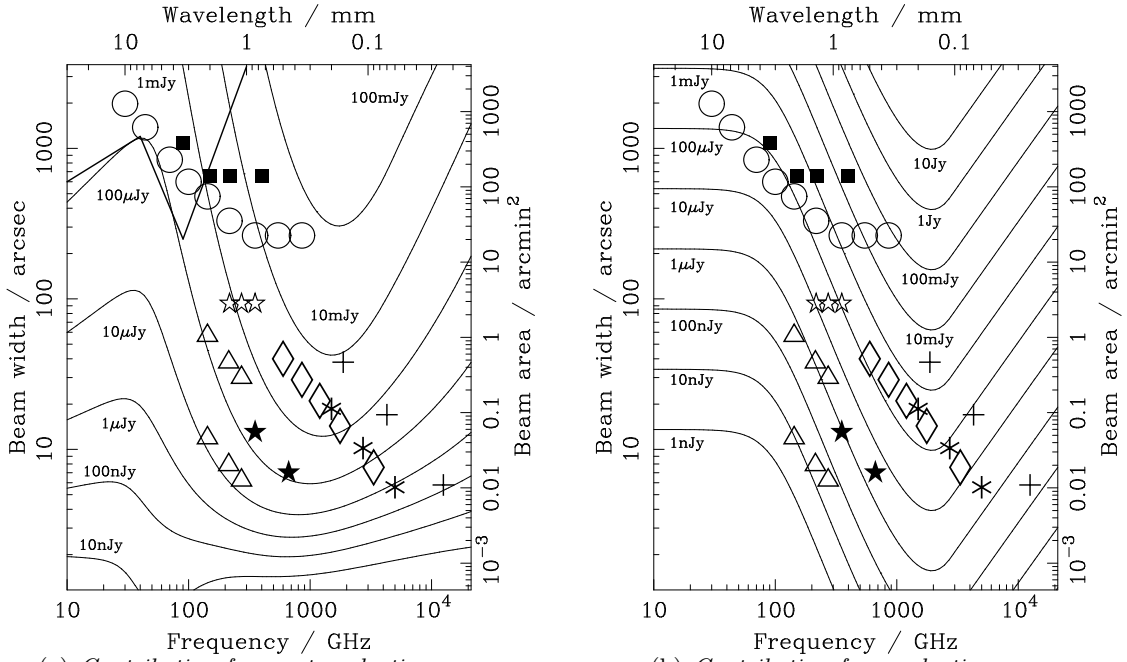

(a) *Contribution from extragalactic sources* (b) *Contribution from galactic sources*

Figure 1.25: *An approximate measure of the* 1σ *confusion noise expected as a function of both observing frequency and angular scale from the millimeter to mid infrared bands. Radio-loud AGNs may give a significant contribution to the top left of the jagged solid line. It is assumed the presence of a galactic cirrus surface brightness of* $B_0 = 1MJy/sr$ *at* $100\mu m$*. The ISM confusion noise is expected to scale as* $B_0^{1.5}$*. Bands and beamsizes reported are described in* [7]*. Circles: Planck; squares: BOOMERanG; empty stars: SuZIE; triangles: BOLOCAM; filled stars: SCUBA; diamonds: Herschel; asterisks: SOFIA; crosses: SIRTF. The resolution limits of the interferometric ALMA experiment lies far below the bottom of the panels. Confusion from extragalactic sources is expected to dominate that from the Milky Way ISM.*

statistical studies, but it can be ignored in the case of photometry of known objects. Relative number counts derive both from data and models, which are based on the assumption that sources follow a Poisson distribution. Most advanced models use an analytic formula which takes into account source clustering: they reach a 90% confidence level [115].

Confusion noise in the infrared waveband is due to galactic cirrus, even if their complex structure is not meaningful at small scales. Infrared cosmological surveys are realized at high galactic latitudes sky regions, lacking of cirrus and where the neutral hydrogen column density is as low as possible. Despite of this, only 2% of the sky has a hydrogen density $N_{HI} \leqslant 1.0 \cdot 10^{20}\, cm^{-2}$. Tab. 1.2 shows the "clean" fraction of sky for a given column density value.

Far infrared and submillimeter observations are interesting to characterize galaxies responsible of cosmic infrared background at redshifts $z \geqslant 1.3$, but these analysis are complicated by confusion noise. One solution consists in extrapolating far infrared and submillimeter properties from radio or mid infrared spectral properties based on small sam-

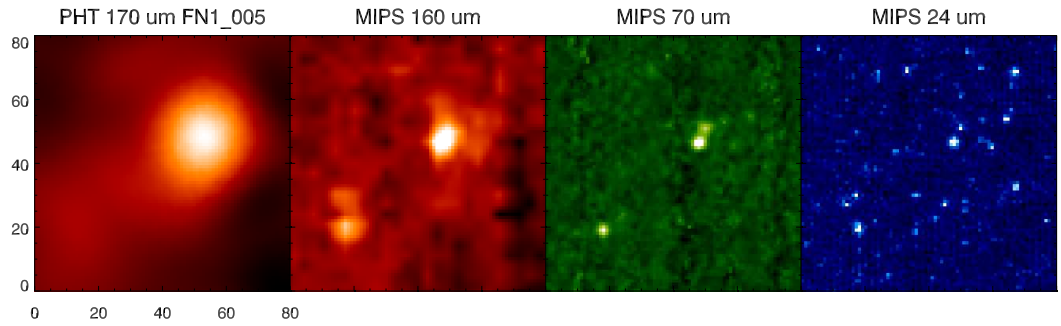

Figure 1.26: *Effects due to confusion noise in far infrared on an observation of a* 400×400 *arcsec*^{2} *area. From left to right:* $373mJy$ *source observed with ISOPHOT at a* $170\mu m$ *and* $180s$ *of integration time; observations at* $160\mu m$, $70\mu m$ *and* $24\mu m$ *made with Spitzer MIPS with* $16s$, $80s$ *and* $160s$ *of integration time respectively. The source at* $170\mu m$ *is only resolved at* $160\mu m$. *The two sources in the lower left corner of the* $160\mu m$ *image produce fluctuations in the ISO* $170\mu m$ *map, introducing the confusion noise when resolution is limited.*

N_{HI} (cm^{-2})	**Sky Fraction**
$\leqslant 1.0 \cdot 10^{20}$	2%
$\leqslant 1.25 \cdot 10^{20}$	5%
$\leqslant 1.6 \cdot 10^{20}$	10%
$\leqslant 2.0 \cdot 10^{20}$	17%
$\leqslant 2.2 \cdot 10^{20}$	20%
$\leqslant 3.0 \cdot 10^{20}$	30%
$\leqslant 3.8 \cdot 10^{20}$	40%
$\leqslant 5.0 \cdot 10^{20}$	52%

Table 1.2: *Fraction of sky for a given column density value, as derived from* [14], *assuming a full sky sampling.*

ples. Another method is the selection of physically homogeneous samples, using shorter wavelengths or high angular resolution data, where far infrared and submillimeter photometry is extracted by. This technique is used to obtain color properties of *SCUBA* galaxies at $70\mu m$ [42].

In conclusion, localized galaxies at different redshifts contribute to form the cosmic infrared background, which has a peak in the far infrared. Most of these contributions are due to ULIRGs between $0.5 \leqslant z \leqslant 1.5$, while submillimeter waveband is dominated by ULIRGs at $z \geqslant 2$. Infrared properties of these luminous galaxies are not known in detail due to confusion noise present in this spectral region.

Chapter 2

The OLIMPO experiment

The whole problem with the world is
that fools and fanatics are always
so certain of themselves,
but wiser people so full of doubts.

Bertrand Russell

OLIMPO (*Osservatorio nel Lontano Infrarosso Montato su Pallone Orientabile*) is a balloon-borne experiment devoted to cosmological and astrophysical survey in the millimeter and submillimeter bands [73, 74, 80]. It implements many advanced technical solutions: a large telescope, a long duration cryostat, a cold re-imaging optical system, arrays of bolometric receivers sensitive in four bands.

OLIMPO is the successor of balloon-borne experiments like *ARCHEOPS*, *BOOMERanG* and *MAXIMA*. Thanks to its characteristics, *OLIMPO* will be able to improve our knowledge of the signals in the so-called *cosmological window*, i.e. a wavelength band that extends roughly from 1 to $5mm$ ($\nu = 300 \div 60 GHz$). At lower frequencies interstellar emission of spinning dust grains, *bremsstrahlung* and synchrotron from charged particles in the ISM dominate the cosmological background; at higher frequencies the clumpy cirrus dust foreground dominates the sky brightness, even at high Galactic latitudes, together with the far infrared emission due to unresolved extragalactic sources.

A stratospheric balloon experiment has an excellent cost−performance ratio: the costs and time necessary to develop are much less than those required by satellite experiments, while the reduction of atmospheric emission in the microwave band boosts the quality of measurements.

The *OLIMPO* payload described in this chapter is constituted by a $2.6m$ Cassegrain telescope mounted on an attitude controlled stratospheric balloon payload. The experiment is designed to perform a long duration circumpolar flight, up to 15 days long. The four bands of *OLIMPO*, centered at $\nu = 143$, 217, 353 and $545 GHz$ ($\lambda = 2100$, 1400, 850 and $550\mu m$ respectively), are chosen to better disentangle the various cosmological signals described in Chap. 1.

2.1 Telescope

The telescope of *OLIMPO* is based on the classical scheme of an on-axis *Cassegrain* system (see Fig. 2.1). It consists of two mirrors: the primary is a concave paraboloid, the secondary in a convex hyperboloid. The two optical axes coincide [103] as well as the focus of the primary and one of the two foci of the secondary mirror. Thus, the equivalent focal distance of the telescope is:

$$f_{Cassegrain} = m \cdot f_{1^{st}} \tag{2.1}$$

where $f_{1^{st}}$ is the focal length of the primary and m is the transverse magnification of the secondary mirror. This is defined as the ratio between the distance of the hyperboloid vertex from the focal plane of the telescope and the focal length $f_{2^{nd}}$ of the secondary mirror. Compared to other configurations, Cassegrain optical systems are very compact, i.e. they have a great ratio between the equivalent focal length and their linear dimensions. This is a fundamental advantage for a balloon-borne experiment.

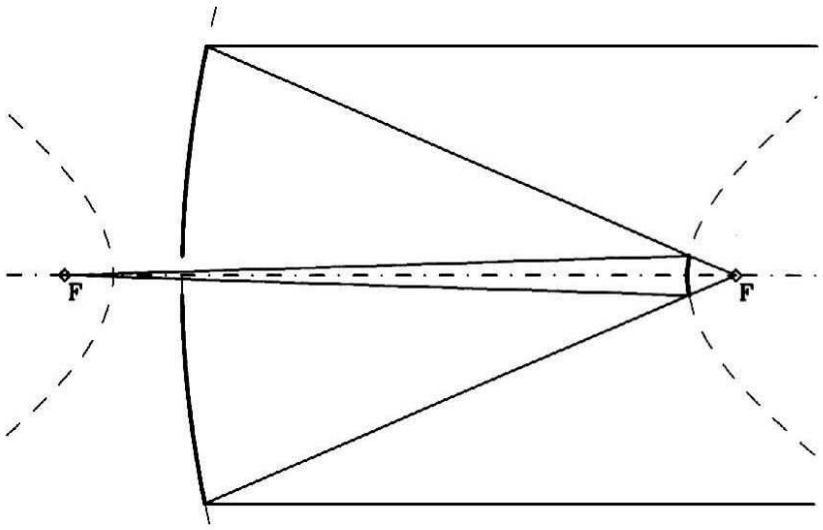

Figure 2.1: *Cassegrain telescope scheme: it is made of a primary parabolic mirror and a secondary hyperbolic one. The dashed curves represents the conics, while the solid curves are the used portion for the mirrors.*

Signal modulation is strongly required for millimeter and submillimeter experiments (see § 2.2). It can be achieved using three possible solutions: rotating the entire payload, wobbling the primary or secondary mirrors. In the latter case, secondary mirror is slightly smaller to avoid looking the edge of the primary. It has two drawbacks: it introduces an offset due to thermal gradients on the primary surface; moreover, the image of the primary mirror refocused on the *Lyot Stop* (see § 3.2.1) moves, thus the *Lyot Stop* dimensions must be reduced to get the intersection of the various images.

The primary mirror can be wobbled around its focus, its barycenter or alternatively the *Lyot Stop* can be wobbled. The optical performances of these three techniques are

analyzed in detail in § 3.1. Wobbling *Lyot Stop* gives good optical performances, but it introduces many drawbacks that cannot be solved (see § 3.1.1).

In order to avoid optical aberrations, the ideal solution is to wobble the primary around its focus (see § 3.1.2). In practice, this cannot be done because the motion would produce a transfer of the angular momentum to the payload, thus introducing microphonic noise in the system and oscillations in the pointing. In fact, it must be noted that the mirror is made of an aluminum alloy and weights $\sim 105Kg$: together with its frame, the total weight is $\sim 180Kg$. Thus, wobbling the primary around its focus is very difficult because of the huge value of the moment of inertia, which requires a very high torque. Furthermore, the telescope will be coupled up the balloon using a chain of $\sim 100m$: an unbalanced torque would induce oscillations modulating the residual atmospherical emission. This emission cannot be removed with the modulation of the primary, compromising the measurements.

The solution adopted is the best one from a mechanical point of view: the primary mirror and its frame must rotate around their center of mas. It minimizes the angular momentum transferred to the payload, thus avoiding microphonics on the receivers and perturbations on the telescope pointing. However, as it will be pointed out in § 3.1.3, optical performance degrades a bit.

In the final configuration, the primary mirror has a diameter of $2.6m$ (see Fig. 2.2): it does a sky scan in *cross elevation* (i.e. the direction orthogonal to the elevation angle) producing a linear modulation on fields having a small difference in elevation. The oscillations have an amplitude up to $\pm 3^\circ$ with a scan velocity of $1^\circ/s$. However, the optical system is optimized for scans of $\pm 0.15'$: they produce a beamthrough equal to $\pm 30'$.

The secondary mirror has a diameter of $0.52m$ and it is suspended by a steel *spider* in its position in front of the primary (see Fig. 2.3). Its parameters are chosen so that the telescope focal plane is inside the cryostat, thus reducing the dimensions of the windows as well as the heat load due to incoming radiation. Moreover, its focal length must be long enough to have the required space between the primary vertex and the cryostat.

Tab. 2.1 summarizes the parameters of the the telescope, while Fig. 2.4 shows a model of the telescope as given by the *ray tracing* program. The *Full Width Half Maximum* (FWHM) of the beam is computed at 90 and $150GHz$: note that the far field at these frequencies is $\sim 20km$. The measurements of the beam obtained at $150GHz$ are shown in Fig. 2.5, compared to the expected *Point Spread Function* (PSF) at the same wavelength, as defined by eq. (3.8).

The optimization of the system was made using the *ray tracing* algorithms of the *ZEMAX* optical design and analysis software. It is worth noting that aberrations are almost absent in the on-axis configuration, as shown in Fig. 2.6: the primary being a parabolic mirror, spherical aberration is negligible, while the chromatic aberration is completely absent because there is no refractive element. When the telescope is off-axis, coma and astigmatism aberrations arise: we optimized the optical design to keep the image of a point source inside the dimensions of the *Airy disc*, i.e. dimensions of the image must be smaller than the circumference that encloses the diffraction figure till the first minimum. The radius of the Airy disc, for an incident radiation of wavelength λ is $R_{Airy} \simeq 1.22 \cdot f/\# \cdot \lambda$. In the case of a single circular aperture, the Airy disc encloses $\sim 84\%$ of the total incident energy.

When the dimensions of the image produced by a point-like source (*spot*) are smaller

Figure 2.2: *Image of OLIMPO telescope mounted on its main frame.*

than the Airy disc radius, the optical system is *diffraction limited*. As it will be described in § 3.1, when the primary is tilted, the optical system is diffraction limited only for the two longer wavelengths ($\lambda = 2100$ and $1400\mu m$, $\nu = 143$ and $217 GHz$ respectively).

The main frame of the experiment (see Figs. 2.2 and 2.7) is made of aluminum alloys and has been optimized to withstand vertical shocks up to $10g$ and horizontal shocks up to $5g$, which could happen at the end of the mission at parachute opening. The telescope and the detector systems are mounted on an inner frame free to move in elevation, while the azimuthal movement is made by rotating the entire payload around a top pivot. The elevation of the inner frame can be set from 0° to 60°: reaching low elevations is very important for ground based calibrations of the telescope and in-flight calibration based on planets.

Figure 2.3: *Image of the back of the OLIMPO secondary mirror and of the spider that keeps it positioned in front of the primary mirror.*

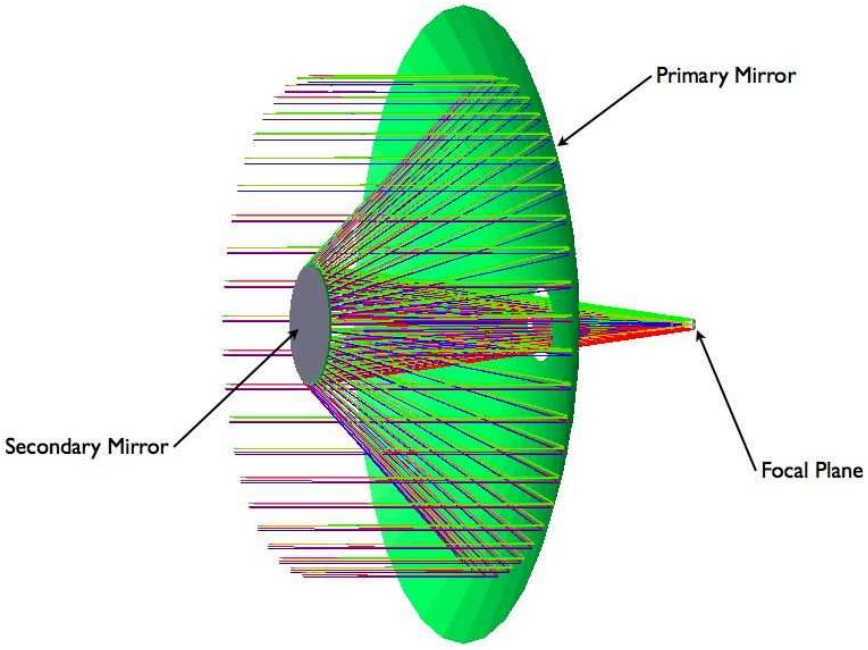

Figure 2.4: 3*D scheme of the OLIMPO telescope obtained with the ZEMAX optical design and analysis software. Only the primary and secondary mirrors, together with the focal plane of the telescope, are shown.*

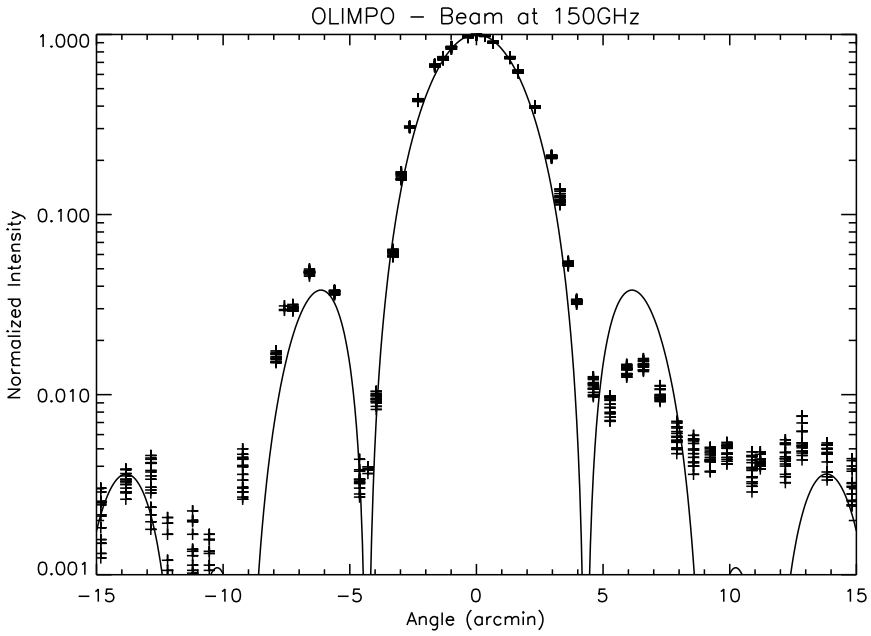

Figure 2.5: *Measurement of the beam of the OLIMPO telescope at* 150*GHz normalized at its maximum value. The plotted curve is the the predicted Point Spread Function at that wavelength.*

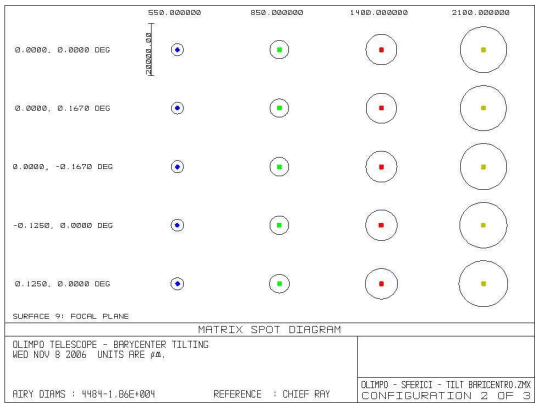

(a) *On-axis spot diagram*

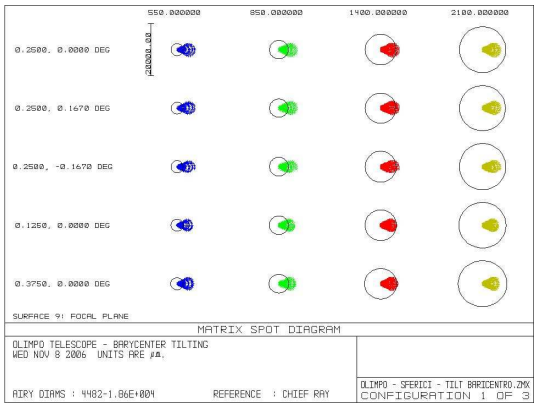

(b) *Off-axis spot diagram*

Figure 2.6: *Spot diagrams on the focal plane of the telescope in the final configuration* (*see* § 3.1.3). *For each wavelength, the dimensions of the spots of the five fields are compared to the radius of the Airy disc.*

Primary mirror	
Outer diameter	$2600mm$
Inner diameter	$150mm$
Input pupil (portion of diameter used)	$2000mm$
Conical constant	-1.009
Focal length	$1247.25mm$
Curvature radius	$-2494.5mm$
$f/\#$	0.48
Secondary mirror	
Diameter	$520mm$
Portion of diameter used	$500mm$
Conical constant	-2.114
Curvature radius	$-708.55mm$
Telescope	
Focal length	$6901.6mm$
$f/\#$	3.45
Corrected focal plane diameter	$70mm$
Primary vertex – secondary vertex distance	$957mm$
Primary vertex – focal plane distance	$659mm$
Primary vertex – primary modulation axis distance	$150mm$

Table 2.1: *Optical parameters of the Cassegrain telescope of OLIMPO. The primary is sub-illuminated to reduce sidelobes contribution, as explained in detail in* § 3.2.1

2.2 Modulation and scan strategy

Scanning strategy is crucial for millimeter and submillimeter experiments in order to optimize the extraction of the signal from noise. In particular, spatial modulation techniques are widely used for their great advantages:

- They allow to remove local background signals, like thermal emission from mirrors or atmospheric emission and noise. The molecules of the atmosphere, at a temperature of $\sim 250K$, produce a strong emission in the far infrared spectrum due to rotovibrational transitions. The resulting effect is that, apart two "windows" in the optical and radio bands, celestial radiation is highly absorbed (see Fig. 2.8). Moreover, the presence of water vapor emits absorbed radiation at millimeter and submillimeter wavelengths, thus affecting cosmological measurements.

- Electronics can be coupled in AC, thus avoiding troubles due to low DC stability of receivers and amplifiers; moreover, this permits the use of synchronous demodulation which increases significantly the signal-to-noise ratio (S/N), thus it is possible to extract a small signal from the overwhelming noise.

Let us suppose $G(t)$ is the quantity to be measured and $N(t)$ is its intrinsic noise. Usually, the radiative signal is converted into an electric signal using a transducer, the bolometric receiver in our case (see § 2.4): this has a responsivity $\mathcal{R}$ and noise $N_R(t)$. The

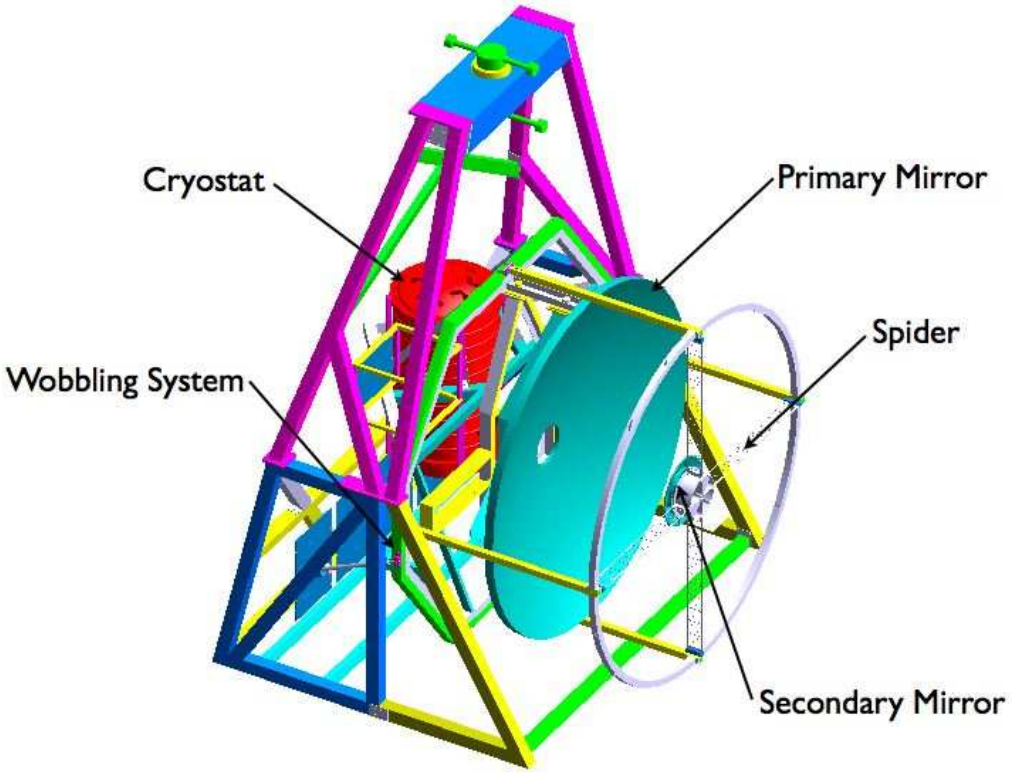

Figure 2.7: *3D view of the OLIMPO main frame: the telescope, the spider system that sustain the secondary mirror and the cryostat are shown.*

electric signal is then processed by an amplifier having gain $\mathcal{A}$ and input noise $N_I(t)$. The signal measured at the output of the amplifier is:

$$V_A(t) = \mathcal{A}\{\mathcal{R}[G(t) + N_R(t)] + R(t) + N_I(t)\} \tag{2.2}$$

The amplifier does not improve the S/N ratio, but it increases the signal so that it can be easily measured. It can be shown that the total noise is the superimposition of a $1/f$ term and a *white noise* one: the former has an intensity that is inversely proportional to the frequency f; the latter has an almost flat spectrum. The signal $G(t)$ is modulated at frequencies high enough so that the contribution of $1/f$ is negligible. Moreover, the signal is measured with a *synchronous demodulator* (*lock-in*): it is a pass-band filter centered on the modulation frequency f_M which is able to "follow" the modulation frequency in the case f_M varies. Thus, only the noise present in the pass-band of the lock-in affects measurements. If τ is the time constant of the filter, the width of the pass-band is $1/2\tau$. Assuming that the spectrum of the input noise is W_N and the integration time is τ, the

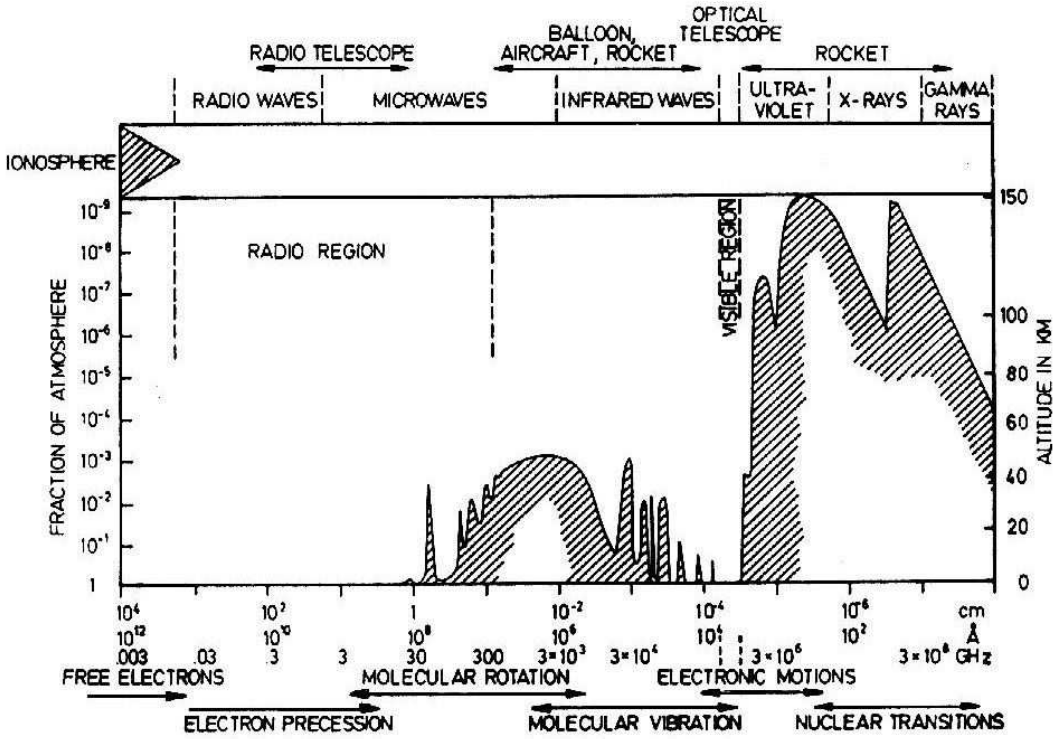

Figure 2.8: *Full spectrum of the atmosphere transmission: figure shows the altitude at which the sky radiation is reduced to* 50%. *The physical mechanisms that produce this absorption are also reported. It is clear that, in order to cover the frequencies above* $\nu \sim 200\,GHz$, *balloon or satellite experiments are mandatory.*

signal-to-noise ratio at the output of the lock-in is:

$$\frac{S}{N} = \frac{V_{Out}}{\sqrt{\langle \Delta V_{Out}^2 \rangle}} = V_S \sqrt{\frac{2\tau}{W_N}} \tag{2.3}$$

where V_S is the amplitude of the input signal at the lock-in, thus directly proportional to $G(t)$. It is worth noting that integrating over a long time constant τ, the S/N ratio increases.

In order to modulate the anisotropic sky signal signal, the basic idea is to produce sky-scans, thus separating the sky signal from the constant nuisance components, like atmospheric and instrument emissions. The simplest sky-scan technique consists in alternatively pointing towards the source of interest and towards a region without sources (*two fields modulation*). This modulation alternates the nuisance contributions and these contributions plus the signal. An offset can still remain since it is not possible to distinguish nuisance gradients along the scans from the real signal. This problem can be significantly reduced using a *three fields modulation*, i.e. pointing alternatively towards the source, then moving to one side, then again towards the source, finally to the other side. With this technique, the only offset that remains is due to non-linear variations of the atmospheric

emission in the three fields. The methods used to modulate the signal are analyzed in § 2.1, while their optical performance are reported in § 3.1.

The strategy that will be used for *OLIMPO* is to move the entire payload in azimuth, the inner frame in elevation and, in addition, to wobble the primary mirror in cross elevation. Consequently, the illuminated region of the primary mirror remains always the same, avoiding scan synchronous offset. There is still a danger in this scanning technique: primary mirror oscillates in cross elevation, so the actual elevation changes a bit during the scan. Signal from atmospheric emission changes with elevation angle, so there could be a scan-synchronous noise left in the measurements.

The first flight foresees to select 40 known cluster of galaxies from a catalogue and to observe them through spatial modulation. Using the IRAS data on the galactic dust contribution and many available catalogues, we look for a sky region at high latitudes, observable from North Pole during summer, poor of dust emission and rich of clusters. The selection falls on an $10^\circ \times 10^\circ$ area centered in 65° galactic latitude and 155° galactic longitude. The selected clusters are reported in Tab. 2.2.

Scan velocity must be compatible with instrumental constraints: it should be high enough to ensure as many samples as possible and to reduce the contribution of the $1/f$ noise, but angular resolution and time response of receivers put an upper limit of about $1^\circ/s$.

2.3 Cryostat

Photons at millimeter and submillimeter wavelengths have not enough energy to be detected using classic quantum receivers, such as CCD cameras. The use of thermal receivers is required: their characteristic is the integration of many incident photons thermalizing their energy and converting it into an electrical signal. In the bands of the *OLIMPO* experiment, the best available receivers are *bolometers*, whose operation principles will be explained in § 2.4.

The introduction of a cooling system is necessary for two main reasons:

1. The Cooler is the temperature, the better is the sensitivity of the bolometers to variations in the incident radiation. As will be analyzed in § 2.4, the best working temperature of the receivers designed for *OLIMPO* is below $300mK$.

2. The external background due to the atmosphere has a spectrum roughly similar to a room temperature grey body, i.e. $T \sim 300K$ during ground calibration and $T \sim 30K$ on flight. Thus, the energy of these photons is much greater than that contained in the signal of interest saturating the receivers. Hence, they must be shielded as much as possible.

The system that permits to cool down the receivers to $300mK$ is called *cryostat*. To reach such a low temperature, the use of cryogenic liquids such as nitrogen, ^{4}He and ^{3}He is required. In order to reduce the heat load, the cryostat has to be designed in an appropriate way, using various layers. The relation between the heat load $\dot{Q}$ (measured in W), the duration of the cryogenic liquid t and its volume V is:

$$\dot{Q} = \frac{L\,V}{t} \tag{2.4}$$

Name	**Latitude**	**Longitude**	**Altitude**	**Azimuth**
Abell 1067	125.5039	125.5039	42.1719	94.2512
Abell 1074	118.0895	118.0895	48.1786	91.0387
Abell 1076	115.8231	115.8231	58.9391	83.9804
Abell 1077	114.3608	114.3608	47.9734	90.7570
Abell 1101	100.7626	100.7626	45.6784	90.4271
Abell 1110	95.2258	95.2258	43.6918	90.7449
Abell 1132	93.1985	93.1985	56.9974	81.8382
Abell 1133	87.8872	87.8872	50.4938	85.9004
Abell 1135	80.9196	80.9196	42.0777	89.6352
Abell 1143	83.3484	83.3484	50.7556	84.7495
Abell 1154	79.9054	79.9054	50.1120	84.3012
Abell 1156	77.4312	77.4312	47.8054	85.4168
Abell 1167	76.5722	76.5722	49.0428	83.9756
Abell 1169	71.2511	71.2511	44.3350	86.1115
Abell 1173	67.9015	67.9015	42.0031	86.7530
Abell 1174	69.6541	69.6541	43.6268	86.0646
Abell 1190	65.5462	65.5462	41.1604	86.4015
Abell 1193	67.2934	67.2934	42.6733	85.6896
Abell 1196	81.6714	81.6714	53.5273	80.2346
Abell 1202	73.6143	73.6143	47.4558	83.2767
Abell 1203	64.0963	64.0963	40.5185	86.0644
Abell 1222	79.3282	79.3282	46.7986	81.8155
Abell 1227	83.2155	83.2155	47.5646	81.1809
Abell 1229	81.4073	81.4073	45.7431	81.8707
Abell 1237	79.5642	79.5642	42.5101	82.8531
Abell 1240	80.4144	80.4144	42.7655	82.7323
Abell 1250	83.6449	83.6449	41.2810	82.9407
Abell 1261	110.3679	110.3679	47.5486	79.6340
Abell 1265	108.3534	108.3534	40.8301	82.2835
Abell 1282	138.5397	138.5397	39.3996	82.1429
Abell 1291	134.1236	134.1236	54.6028	74.5811
Abell 1298	147.5835	147.5835	43.9334	79.9431
Abell 1312	149.1171	149.1171	48.8613	77.2805
Abell 1318	150.1585	150.1585	53.3850	74.2287
Abell 1319	174.9659	174.9659	39.1940	80.7799
Abell 1324	149.3064	149.3064	55.3539	72.7785
Abell 1326	176.7359	176.7359	39.2309	80.5623
Abell 1349	159.8664	159.8664	53.4754	72.7345
Abell 1351	156.1065	156.1065	56.4259	70.6647
Abell 1355	179.4996	179.4996	40.6229	78.6119
Abell 1361	173.4791	173.4791	44.8473	76.6903
Abell 1368	167.2980	167.2980	49.4614	74.2445
Abell 1370	169.8600	169.8600	47.6252	75.0932
Abell 1374	169.4670	169.4670	47.9668	74.7282
Abell 1377	162.0959	162.0959	53.5952	71.4243
Abell 1383	163.5042	163.5042	52.4835	71.7886
Abell 1387	166.9434	166.9434	49.6130	73.1857
Abell 1394	175.9781	175.9781	40.6685	76.4748
Abell 1409	166.5892	166.5892	46.9277	73.1555
Abell 1415	156.5228	156.5228	55.1668	68.1976
Abell 1430	159.8352	159.8352	47.3539	71.6162

Table 2.2: *List of selected clusters that will be observed during flight. We report the galactic coordinates and azimuth and altitude computed on the* 1^{th} *of July* 2007 *from the latitude of Svalbard islands.*

where L is the latent heat. The heat load has three different origins:

Conductive heat load It is mainly due to the presence of a "solid" connection between two layers at different temperatures $T_1 < T_2$. If the material that constitutes the connection has length L, section S and thermal conductivity $k(T)$, the heat load is:

$$\dot{Q} = \frac{S}{L} \int_{T_1}^{T_2} k(T)\, dT \tag{2.5}$$

Convective heat load It happens when there is a fluid (typically gaseous) in the cryostat. The thermal input depends on its pressure and on a constant K which depends on the kind of molecules forming the gas:

$$\dot{Q} = K\, a_0\, p\, (T_2 - T_1) \tag{2.6}$$

Radiative heat load This is due to the emission of the outer and hotter layer. If we suppose to have two surfaces S_1 and S_2 at temperatures T_1 and T_2, with S_2 surrounding S_1 and $T_1 < T_2$, the heat load is:

$$\dot{Q} = F_{12}\, A_1\, \sigma\, (T_2^4 - T_1^4) \tag{2.7}$$

where A_1 is the area, approximately equal, of the two surfaces and F_{12} is a form factor that, for material having low emissivity, is about half their emissivity.

As shown in eqs. (2.5), (2.6) and (2.7), heat loads depend on the difference of the temperatures between layers. Using a system of four cylindrical and concentric shells (see Figs. 2.9 and 2.10), the thermal input is dramatically decreased. Starting from outside, the first shell is the cryostat shield at room temperature ($\sim 300K$ for ground based measurements, $\sim 30K$ on flight); the second layer is a toroidal tank that contains liquid nitrogen at $77K$; the fourth shell is an aluminum shield in thermal contact with the ^{4}He tank; the third layer is a copper shield cooled at $\sim 30K$ using the ^{4}He evaporated by the tank.

The convective heat load is usually negligible, because the gas is pumped out the cryostat: the residual pressure is $\sim 10^{-7} mbar$. Radiative thermal input between two surfaces of the shells is reduced using many layers of *superinsulation* placed on the colder surface. Superinsulation is a thin sheet of *mylar*, a material having an aluminum face, which decreases emissivity and transparency, while the other face is insulator and opaque, in order to avoid the thermal link between subsequent layers. Conductive heat load is due to the filling tubes of the N_2 and ^{4}He tanks and to the thermal link between the various layers: the former can be reduced increasing the lengths of the tubes and decreasing their cross section; the latter is minimized using low conductive materials, such as fiberglass, kevlar strings or vespel.

The liquid ^{4}He has a temperature at room pressure ($\sim 1010 mbar$) of $4.2K$; decreasing the pressure of the gas inside the tank, the temperature can be lowered till $1.6K$, which is not enough to reach the receivers working temperature of $300mK$. This can be achieved using a further cryogenic stage attached to the ^{4}He tank, called *fridge* (see Fig. 2.9). This is a "closed" system containing liquid ^{3}He and made of two parts: an evaporator and a

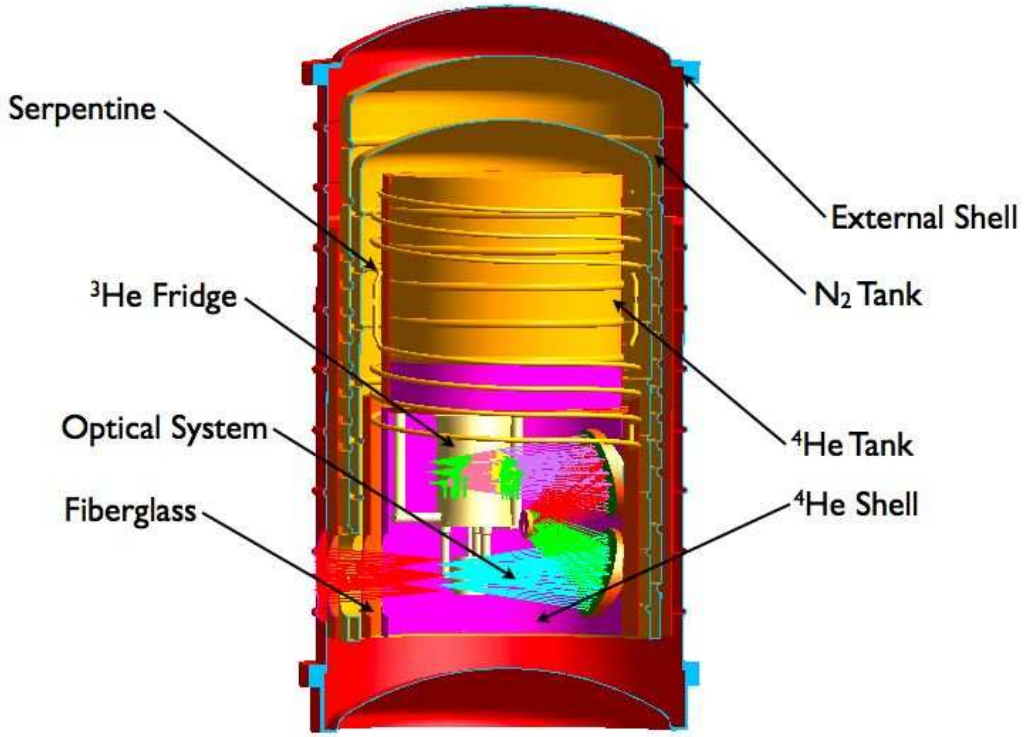

Figure 2.9: *3D model of the OLIMPO cryostat: all the stages are shown, from the external* $300K$ *shield to the* ^{3}He *fridge at* $300mK$*, together with the cryogenic re-imaging optical system.*

cryogenic adsorbing pump (*cryopump*). Both can be thermally connected or disconnected to the ^{4}He tank. The cryopump can be heated up to $\sim 25K$ using a resistor. The cryopump is filled with active carbon, whose characteristic is the extremely high porosity of its grains (surface−volume ratio $\sim 700m^2/cm^3$). At high temperature ($> 20K$), the probability that atoms of ^{3}He are captured is very low, thus the gas is diffused in the whole fridge. As the cryostat is cooled down and the cryopump is thermally linked to the ^{4}He stage, the probability of capture becomes very high, thus all the gaseous ^{3}He is adsorbed: the pressure can decrease till $\sim 10^{-3} mbar$.

The procedure to reach the $300mK$ is time-consuming and can be subdivided into seven steps:

1. The gas present in the cryostat volume between the tanks is pumped out, until a pressure of $\sim 10^{-7} mbar$ is reached.

2. Both N_2 and ^{4}He tanks are filled with liquid nitrogen in order to thermalize the whole system at $77K$.

3. When the system is thermalized, which implies a constant consumption of the nitro-

(a) *External shell*

(b) N_2 *shell*

(c) Vapor *shell*

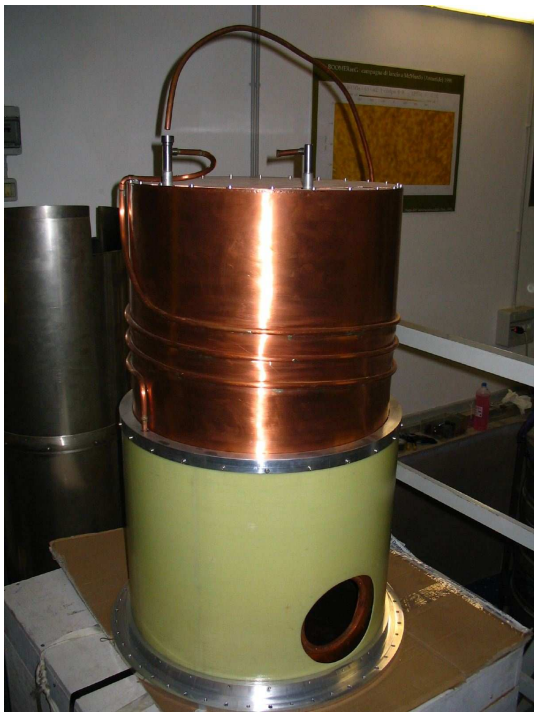

(d) *Serpentine*

Figure 2.10: *Images of the various shells of the OLIMPO cryostat, starting from outside to inside. The external shell is at room temperature; the* N_2 *shell is thermally linked with the liquid nitrogen, hence cooled till* $2K$ *during flight; vapor shell is made of copper and cooled at* $\sim 40K$ *by the vapors of* ^{4}He *using the serpentine welded on the shield.*

gen, N_2 liquid is removed from the ^{4}He tank and is replaced by is ^{4}He liquid; thus the inner shell reaches $4.2K$.

4. Subsequent step consists in cooling the inner shell at $2K$ or less. At room pressure, this must be done pumping on the ^{4}He tank. When the experiment is on flight, the external pressure is $\sim 3mbar$, thus ^{4}He reaches the $2K$ "unassisted".

5. When the cryostat cools down to $2K$, the cryopump, thermally linked with the ^{4}He tank, starts to adsorb the gas of ^{3}He present in the system.

6. After disconnecting the cryopump from the stage at $2K$, it is heated up to $25K$ so that it desorbs the gas; it starts to condensate in the evaporator, still thermally linked to the ^{4}He tank.

7. While the gas is ejected by the cryopump, pressure increases until an equilibrium between liquid and gaseous ^{3}He is reached; then, disconnecting the thermal link between the evaporator and the $2K$ stage and connecting the cryopump to the ^{4}He tank, the cryopump starts to adsorb the residual gas; pressure and temperature of the ^{3}He decrease to $\sim 300mK$.

The particularity of the *OLIMPO* cryostat consists in the structure that sustains the shells: since the cryostat will be mounted behind the telescope and, as described in § 2.1, this can be tilted in elevation up to 60°, we need a strong support. This cannot be achieved using kevlar strings, as was done in the *BOOMERanG* experiment, while vespel would be too expensive. The adopted solution consists in three concentric fiberglass tubes that connect the three inner shells to the outer shield.

All the shells and tanks are made of aluminum, thus decreasing the weight. An exception is the shield cooled by the vapors of the ^{4}He and a small flange that ensures the thermal link between the fridge and the ^{4}He tank (see Fig. 2.9). These are made of *Oxygen-Free High Conductivity* (OFHC) copper, in order to increase as much as possible the thermal conductivity.

The radiative load through the optical path is minimized by appropriate filters. On each shell a low-pass frequency filter is mounted, thermalized at the temperature of the shell. All the re-imaging optics, dichroics, neutral density filter and calibration lamp are thermally linked to the ^{4}He stage, together with the fridge. The receivers, their horns and high-pass frequency filters are cooled down to $300mK$, connected to the evaporator of the fridge using copper strings with very high thermal conductivity.

2.4 Receivers

In the bands of the *OLIMPO* experiment, the energy of photons is too low to be observed using quantum receivers: they work only for wavelengths shorter than $\sim 200\mu m$. In the millimeter and submillimeter bands quantic processes are not efficient enough, thus the use of thermal receivers is required. These are able to absorb many low energy photons, giving rise to a temperature variation of the receivers. This temperature variation produces a variation in a thermometric quantity which, in the case of *bolometers*, is the electrical resistance. In order to neglect the thermal energy fluctuations of the detector below the

energy of the incident photons, cooling down the bolometers at a temperature of $300mK$ or lower is required.

The bolometer is made of a strongly temperature dependent electric resistance. The detector is thermally linked to the ^{3}He bath at temperature T_0 using a link with mean thermal conductivity G. The receiver is fed by a *bias circuit*, whose purpose is to set the working voltage V and current I. Furthermore, the bolometer dissipates a power P due to the Joule effect (see Fig. 2.11) and is heated up by the background radiation. Denoting with Q the radiative power due to the absorbed background radiation, the final temperature of the bolometer is:

$$Q + P = G\,(T - T_0) \tag{2.8}$$

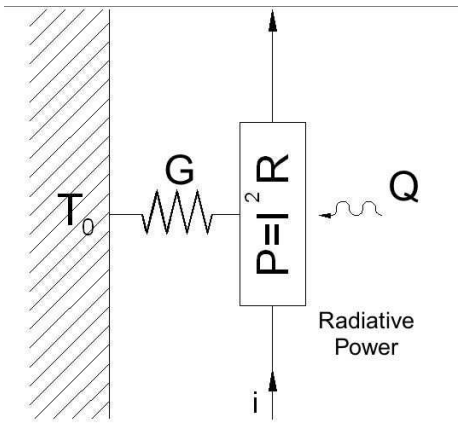

Figure 2.11: *Bolometer scheme: it is thermally linked to a bath at temperature T_0 with a thermal conductivity G, heated up at a temperature $T > T_0$ due to the incident power radiation Q that changes its resistance R and dissipated power $P = I^2R$.*

The main parameter that characterizes a bolometer is its responsivity $\mathcal{R}$, i.e. the ratio between the electric signal at the receiver output, computed in V, and the radiative incident power, measured in W. There are three types of responsivity: static $\mathcal{R}_{Stat}$, dynamic $\mathcal{R}_{Dyn}$ and optical $\mathcal{R}_{Opt}$. The second one is the ratio between output signal and power absorbed by bolometer, while the latter is the ratio between the measured signal and the incident power: thus, denoting with η the absorbing efficiency, $\mathcal{R}_{Opt} = \eta\,\mathcal{R}_{Dyn}$. Both these responsivities are function of the frequency of the input signal, while the static responsivity is defined as the dynamic one at constant dissipated power: $\mathcal{R}_{Stat} = \mathcal{R}_{Dyn}(\omega = 0)$.

Let us suppose that a radiative signal, having power ΔQ, is superimposed to the constant background one. Denoting with R_L the resistance of the bias circuit, we get the

relations:

$$\Delta Q = C\,\frac{d\Delta T}{dt} + G_{Eff}\Delta T \tag{2.9a}$$

$$G_{Eff} = G + \frac{dG}{dT}\,(T - T_0) - P\alpha\,\frac{2R_L - R}{2R_L + R} \tag{2.9b}$$

$$\alpha = \frac{1}{R}\,\frac{dR}{dT} \tag{2.9c}$$

where α is the *resistance parameter*, which defines the variation of the resistance R of the bolometer as a function of its temperature. Usually, α is negative, so that an increasing heat load produces a decrease of the resistance. In this case, the bolometer operates with an effective thermal conductivity G_{Eff} higher than the static one. Given the time constant of the bolometer $\tau_{Eff} = C/G_{Eff}$, the dynamic responsivity is obtained by eqs. (2.9):

$$\mathcal{R}_{Dyn}(\omega) = \frac{\Delta V}{\Delta Q} = \frac{\alpha I}{G_{Eff}\sqrt{1+\omega^2\tau_{Eff}^2}}\,\frac{2R_L R}{R + 2R_L} = \frac{\mathcal{R}_{Stat}}{\sqrt{1+\omega^2\tau_{Eff}^2}} \tag{2.10}$$

Note that it is necessary to find a compromise between high responsivity and short time response of the bolometer. Moreover eqs. (2.9) and (2.10) provide the relation between the thermal and effective time constants:

$$\tau_{Th} = \frac{C}{G} = \tau_{Eff}\,\frac{1}{1 + P\alpha\,\dfrac{2R_L - R}{(2R_L + R)\;G_{Eff}}} \tag{2.11}$$

Thus, a bolometer with resistance parameter $\alpha < 0$ has an effective time constant shorter than the thermal one. As already described in § 2.3, one should decrease as much as possible the bolometers working temperature: however, the background of the atmosphere sets a lower limit on the sensitivity of the receivers. A temperature of $300mK$ is acceptable for balloon experiments that fly at an altitude of $\sim 40km$.

The values of the resistance parameter and of the time constant are not known *a priori*. Hence, eq. (2.10) is not useful to analytically compute the static and dynamic resistance. Instead, this can be estimated using the resistance $R = V/I$ and the impedance $Z = dV/dI$ of the bolometer. These two quantities are identical in the case of isothermal resistors, while for bolometers the relation between I and V is not linear and depends on the dissipated power $P = VI$. It can be demonstrated that the relation between impedance and dynamic responsivity is:

$$\mathcal{R}_{Dyn}(\omega) = \frac{R_L}{IR}\,\frac{Z(\omega) - R}{Z(\omega) + 2R_L} \tag{2.12}$$

This equation shows that a good bolometer should have the characteristic curve $V - I$ highly bended and a current as low as possible. The dynamic responsivity is computed feeding the bolometer with an alternative bias current at the frequency of interest.

The best choice of the voltage bias is obtained considering both dynamic and optical responsivity. The latter is measured observing alternatively two sources having known

brilliance B, using a chopper to set the modulation frequency. Given the throughput $A\Omega$ of the system, the responsivity is obtained by the relation:

$$\mathcal{R}_{Opt}(\omega) = \frac{\Delta V(\omega)}{A\,\Omega\,B} \tag{2.13}$$

OLIMPO will use the next generation of bolometric receivers: *Transition Edge Superconductors* (TES) [44, 68]. These consist of a "normal" metal absorber coupled to a superconducting thermistor; energy of the incident radiation is rapidly thermalized in the normal metal, leading to a prompt temperature rise in the superconducting film. This film is voltage biased in the middle of its transition between superconducting and normal states, so that the temperature increase produces a large change in film resistance. The are three main differences between TES and composite bolometers:

1. TES are voltage biased so that they are kept at the transition temperature, hence they are a null detector.

2. As the temperature increases, the impedance increases as well, thus the resistance parameter α is positive (see Fig. 2.12).

3. The intrinsic impedance is of the order of few ohms, hence much lower than that of composite bolometers.

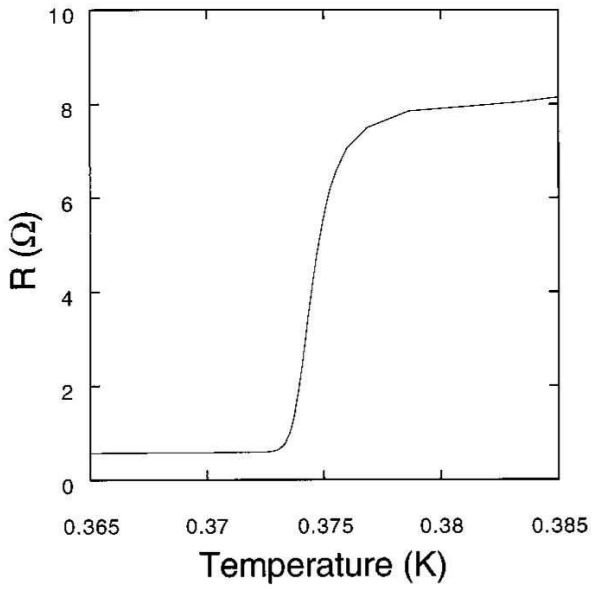

Figure 2.12: *Measured temperature dependance of the thermometer resistance. The largest value of resistive parameter α is ~ 1000.*

These characteristics require the use of *Superconducting QUantum Interference Devices* (SQUID) in place of of *Junction Field Effect Transistors* (JFET). SQUID are able to measure the extremely small magnetic field produced by the bolometer and convert it

into a detectable current. The drawbacks reside in their cost and their high sensitivity to external magnetic fields, which requires very complex shields.

The main advantage of this new technology resides in the manufacturing process (see Fig. 2.13). Classic bolometric receivers consist of two distinct parts, an absorber and a thermistor; the two components are fabricated separately and are coupled during the final process. Thus every bolometer is "handmade" and manufacturing many receivers for large arrays is very time-consuming. TES are fully lithographed, so making large arrays of detectors is relatively easy.

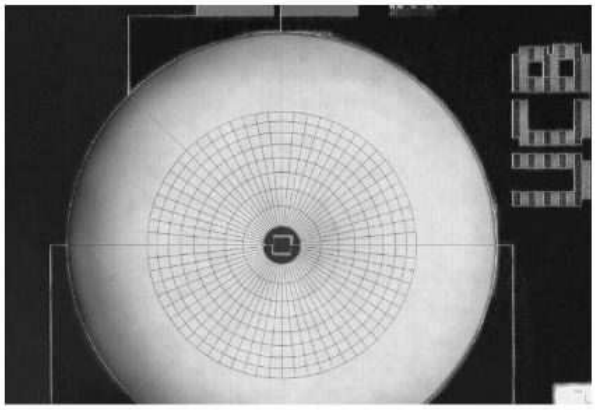

Figure 2.13: *Photograph of a fully lithographed bolometer on a* Si_3N_4 *membrane. The circular mesh is metallized to absorb radiation and is supported by eight radial legs. The voltage biased trilayer thermistor is located on a continuous region of membrane in the center and is electrically connected with superconducting leads.*

It is worth noting that due to the large number of detectors, using separate bias circuits for each bolometer is not possible, because that would increase too much the heat load due to cryoharness and the cost of the readout electronics: thus, detectors multiplexing is required, which can be done in two ways. *Frequency domain* multiplexing send a different AC bias to each row of bolometers. Using the same techniques described in § 2.2, the signal can be extracted at the same time for all the receivers: this would be the best choice, but achieving a stable and low noise bias signal is very difficult. *Time domain* multiplexing feeds one receiver per time, exploiting the time constant of the bolometers, which is usually $\sim 0.1s$: thus, feeding ten bolometers with one bias would require one second. Time domain multiplexing is simpler but implies an upper limit on the scan velocity.

Chapter 3

Optics design and optimization

Reason, Observation and Experience:
the Holy Trinity of Science.

Robert G. Ingersoll

As already described (see § 2.1), *OLIMPO* has a Cassegrain telescope, with a $2.6m$ parabolic primary mirror and a $0.52m$ hyperbolic secondary mirror. Inside the cryostat, cooled down to $\sim 2K$, there is a system of three mirrors (tertiary, *Lyot Stop* and quinary) that re-focuses the image of the focal plane of the telescope onto the focal plane of the experiment (*image surface*), as shown in Fig. 3.1.

Receivers used in millimeter and submillimeter experiments are highly sensitive thermal detectors. In order to increase their sensitivity as much as possible, solid angle and frequency selection of the radiation of interest is required. The introduction of *re-imaging optics* has three main advantages:

1. Solid angle selection consist in rejecting primary edge effects, sidelobes and stray light: this is achieved using a *Lyot Stop*, i.e. a mirror onto which the image of primary mirror is focused in order to define the portion of primary mirror to be used. Only light coming from the selected area reaches the bolometers (see § 3.2.1), while light coming from the edges is focused on a cold absorber surrounding the *Lyot Stop*.

2. *OLIMPO* has four frequency bands: incoming radiation is split by three dichroics into four different focal planes (see Fig. 3.1), while it is filtered entering the cryostat and again just before each focal plane. The presence of these dichroics between the fifth mirror and the image surface implies an increase of the total focal distance, hence the final $f/\#$ must be larger than the telescope's one: due to space requirements, this can be only realized using three mirrors in the refocusing system. The first one (third mirror) is used to re-focalize radiation onto the *Lyot Stop* (fourth mirror) and the third one (fifth mirror) recollects rays from the *Lyot Stop* to the bolometers.

3. There is also a thermal advantage, derived from cooling the re-imaging optics. The small amount of spurious radiation that reaches the receivers is thermalized at $2K$.

Furthermore, the presence of a hole inside the *Lyot Stop* permits to disregard rays coming from the hole of the primary mirror, which is a signal significantly higher than that coming from the sky (see § 3.2.1).

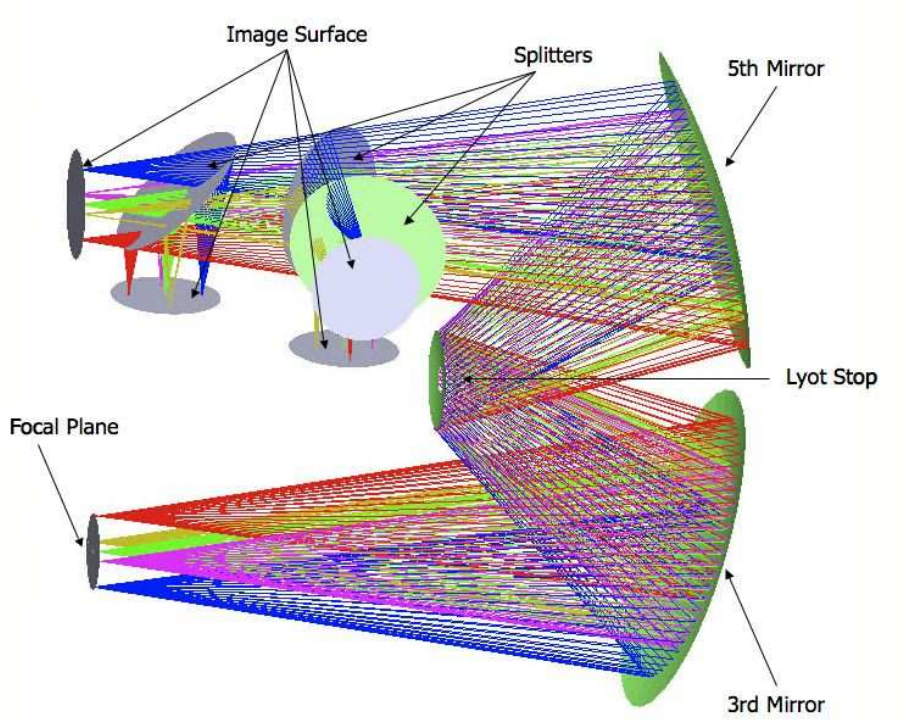

Figure 3.1: *Full design of the cold optical system: the focal plane of the telescope, the tertiary and quinary mirrors, the Lyot Stop, the three dichroics which produce the beam splitting, and the four focal planes of the experiment* (*image surface*) *are shown. The full layout of the system is shown in* Figs. 2.4 *and* 3.3.

In this chapter I will describe the optical solutions studied for the *OLIMPO* experiment, including performance analysis, advantages and drawbacks of each solution. The importance of signal modulation is described in § 2.2: the three solutions taken in consideration differ in the way the signal is modulated.

3.1 Preliminary configurations

The standard procedure to design and optimize an optical system consists in creating a preliminary configuration, determining the parameters that can be varied and looking for parameters values which optimize the system (see Fig. 3.2). This is achieved by minimizing

the *merit function* Ψ:

$$\Psi = \sqrt{\frac{\sum_i w_i \left(c_i - a_i\right)^2}{\sum_i w_i}} \tag{3.1}$$

where the sum is over all the *operands* defining the quality of the optical system. c_i is the actual value of every operand, while a_i is the expected value and w_i is the relative weight.

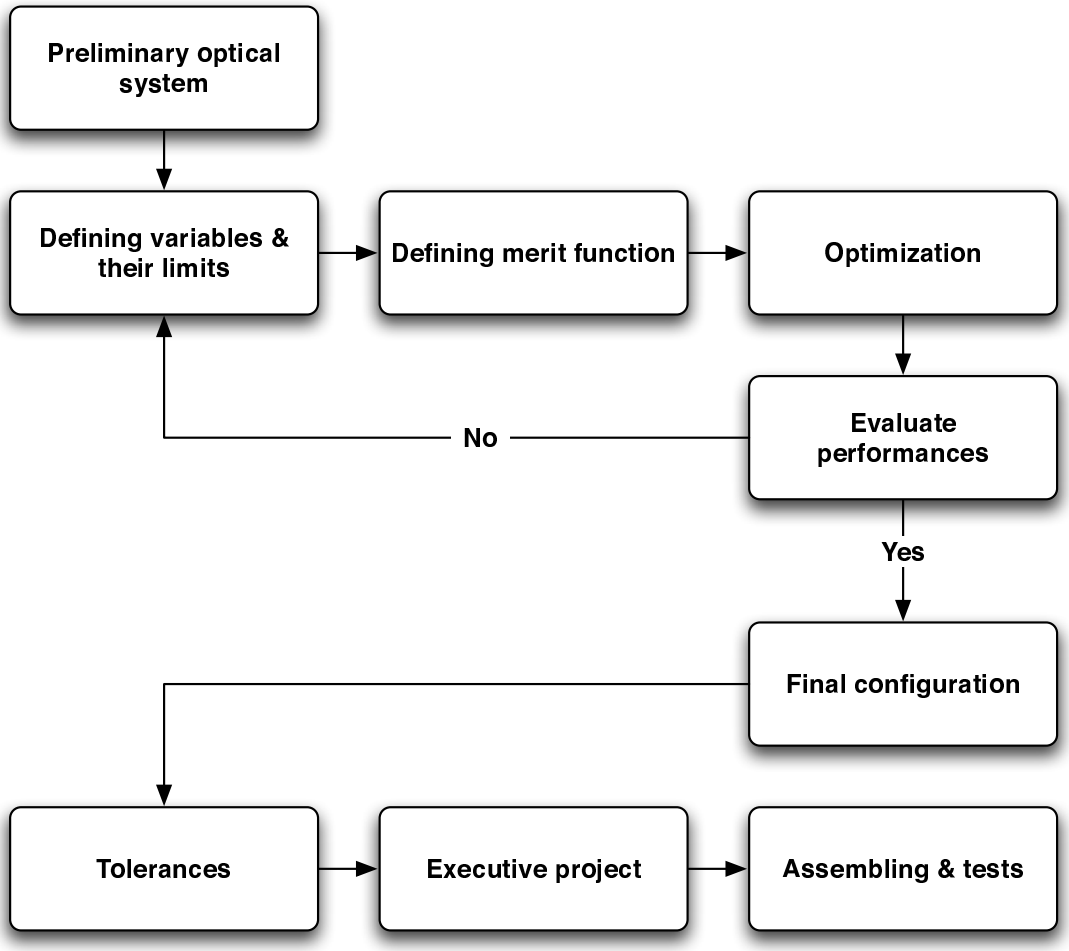

Figure 3.2: *General scheme of the optimization procedure.*

The choice of the merit function is arbitrary, and depends on the quantity to optimize. The *spot* is defined as the image on a given surface produced by a point-like source due to the aberrations introduced by the optical system. Using this quantity as operand and setting its expected value to zero, aberrations are minimized when Ψ is minimized. We have considered five fields, hence the merit function is not computed only on the central one, but also on the edge of the experiment field of view (see Tab. 3.1).

	Sky Coordinates				Focal Plane	
	x (°)	y (°)	x ($'$)	y ($'$)	x (mm)	y (mm)
Field #1	0	0	0	0	0	0
Field #2	0	+0.167	0	+10	0	−20
Field #3	0	−0.167	0	−10	0	+20
Field #4	+0.125	0	+7.5	0	−15	0
Field #5	−0.125	0	−7.5	0	+15	0

Table 3.1: *Coordinates of the five fields of view using in optical analysis. We report the corresponding coordinates of the spots on the focal plane of the experiment. The fields are not the same in x and y because the dichroics partially limit the beam: since they are tilted at 45° in respect to incident radiation, their projection on the beam is an ellipse.*

Optics design and optimization were made using the *ZEMAX* optical design and analysis software. Given the telescope characteristics (see Tab. 2.1), every studied design is realized in four main steps (see Fig. 3.3):

1. The properties of the tertiary mirror are determined by imposing that it reconstructs the primary mirror image onto the *Lyot Stop*. During this procedure, the curvature radius and the conic constant of the third mirror and its distance to the *Lyot Stop* are assumed as free parameters.

2. Since we want all the receivers look at the same portion of the *Lyot Stop*, the quinary mirror must focus parallel rays (i.e. emitted by an object at infinite distance) passing through the image surface onto the *Lyot Stop*. In this case, curvature radius and conic constant of the fifth mirror are free to vary, while the distance *Lyot Stop*−quinary is the same as tertiary−*Lyot Stop*. In fact, due to dimension constraints on the cryostat, it cannot be neither larger nor smaller: the latter would decrease the $f/\#$ of the experiment, decreasing the total field of view, which would be vignetted by the dichroics.

3. The whole system is designed and must be optimized. The only free parameters will be the curvature radius and the conic constant of the *Lyot Stop*, the distances between the focal plain of the telescope (i.e. the cryostat window) and the tertiary mirror and between quinary and focal plane of the experiment (i.e. the image surface).

4. The system is reversed, which means the receivers are now the source and the sky is the image surface. Thus, radiation starts from the focal plane of the experiment and propagates along the mirrors chain (from quinary to primary) until it reaches the sky. This process is made to ensure that receivers see the desired portion of sky, i.e. the optical system defines a good beam on the sky.

We now concentrate on three possible configurations: they differ in the way the signal is modulated (see § 2.2). This can be achieved wobbling either the *Lyot Stop* or the primary mirror around its focus or around its center of mass. The quality of a system can be judged using two indicators:

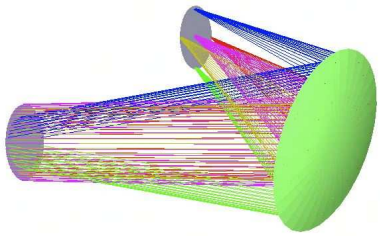

(a) *Design of the tertiary mirror*

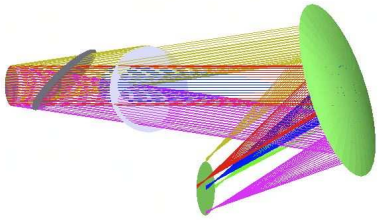

(b) *Design of the quinary mirror*

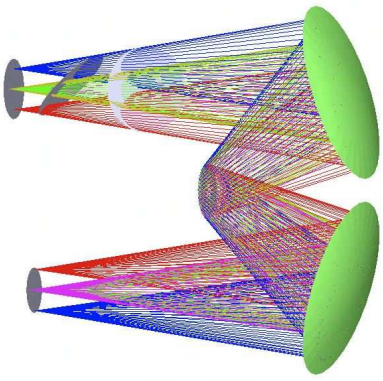

(c) *Cold optics, including dichroics*

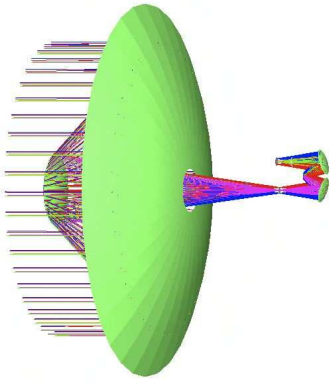

(d) *Optical system, including telescope*

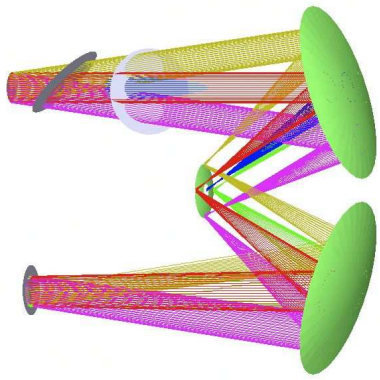

(e) *Cold optics, inverse design*

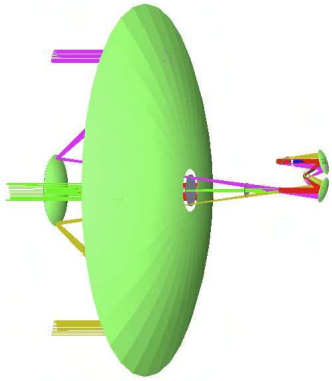

(f) *Optical system, inverse design*

Figure 3.3: *Preliminary design procedure: it starts from the design of tertiary and quinary mirrors, then the whole system is put together and finally it is reversed to ensure receivers see the desired portion of sky.*

Spot Diagram It is the geometrical distribution of rays on the image surface:. The grid of rays can be cartesian, polar or casual. A uniform grid of rays, passing through the pupil entrance, reaches the image surface with a shape depending on the dominant aberrations. A first image analysis compares the spots *r.m.s.* dimensions (defined as the portion of the image including 68% of the total power of the source) with the *Airy disc* at each wavelength. The Airy disc is defined as the circumference enclosing the diffraction pattern up to the first minimum. In the case of a single circular aperture, it includes $\sim$ 84% of the total energy of the incident radiation. The radius of the Airy disc depends on the experiment $f/\#$ and on the radiation wavelength:

$$R_{Airy} \simeq 1.22 \cdot f/\# \cdot \lambda \tag{3.2}$$

When the spots produced by a point source on the image surface are smaller than the Airy disc at that wavelength, the optical system is *diffraction limited*. As the frequency increases, the dimension of the Airy disc decreases: the aberrations become predominant and the system could be no more diffraction limited.

Encircled Energy This is a quantitative approach, because it defines the energy received on the image surface: it is the fraction of total energy E included into a circle of radius r_0 centered around the *chief ray*:

$$EE = \frac{1}{E} \int_0^{2\pi} \int_0^{r_0} I(r, \varphi)\, dr\, d\varphi \tag{3.3}$$

The maximum fraction of the encircled energy cannot exceed the limit imposed by diffraction. The efficiency of the optical system must be related to this maximum value.

3.1.1 Lyot Stop modulation

The *Lyot Stop* is defined as the mirror where the image of the primary is focused on (see § 3.2.1); its oscillation is equivalent to wobble the primary mirror. Since the *Lyot Stop* is much smaller than primary mirror, the introduced aberrations are smaller as well. Image quality is very high without using modulation techniques that require complex mechanical systems, as described in § 3.1.2.

Fig. 3.4 shows the *spot diagram*, i.e. spots dimensions on the image surface for the four frequencies and the five fields. It is clear that, with this configuration, the optical system is always diffraction limited, at every frequency and even in the off-axis configuration. Consequently, the collected energy is close to the maximum allowed value in all cases (see Figs. 3.5, 3.6, 3.7 and 3.8).

Tabs. 3.2, 3.3, 3.4 and 3.5 report the encircled energy for different integration radii, for each wavelength and both *Lyot Stop* positions. EE is computed at three different radii (distances from the chief ray): half of the Airy disc (**A**); the radius of a circle enclosing 70% of the total incident power (**B**); the radius of the Airy disc (**C**).

The diffraction limit value of EE is also shown together with the corresponding field of view. The diffraction limit is lower than the circular aperture case ($\sim$ 84%): obstructions (such as the holes of primary mirror and *Lyot Stop*) are present along the optical path [26].

	Integration Radius (mm)	**On-axis Encircled Energy (%)**	**Off-axis Encircled Energy (%)**	**Diffraction Limit (%)**
A	1.14	$53 \div 56$	$40 \div 46$	55
B	1.66	$68 \div 70$	$55 \div 61$	70
C	2.28	$71 \div 72$	$62 \div 66$	72

Table 3.2: *Encircled energy at a wavelength $\lambda = 550\mu m$ ($\nu = 545 GHz$) in the case of Lyot Stop wobbling around its barycenter. It is computed for different values of integration radius. Intervals mean that spots are different in the five fields, thus the collected energy can be different even in the case of same distance from the chief ray.*

	Integration Radius (mm)	**On-axis Encircled Energy (%)**	**Off-axis Encircled Energy (%)**	**Diffraction Limit (%)**
A	1.77	$53 \div 55$	$47 \div 49$	55
B	2.57	$68 \div 70$	$59 \div 65$	70
C	3.54	$71 \div 72$	$65 \div 69$	72

Table 3.3: *Encircled energy at a wavelength $\lambda = 850\mu m$ ($\nu = 353 GHz$) in the case of Lyot Stop wobbling around its barycenter. It is computed for different values of integration radius. Intervals mean that spots are different in the five fields, thus the collected energy can be different even in the case of same distance from the chief ray.*

	Integration Radius (mm)	**On-axis Encircled Energy (%)**	**Off-axis Encircled Energy (%)**	**Diffraction Limit (%)**
A	2.90	$52 \div 55$	$44 \div 51$	53
B	4.22	$68 \div 70$	$61 \div 66$	70
C	5.80	$71 \div 72$	$65 \div 70$	72

Table 3.4: *Encircled energy at a wavelength $\lambda = 1400\mu m$ ($\nu = 217 GHz$) in the case of Lyot Stop wobbling around its barycenter. It is computed for different values of integration radius. Intervals mean that spots are different in the five fields, thus the collected energy can be different even in the case of same distance from the chief ray.*

	Integration Radius (mm)	**On-axis Encircled Energy (%)**	**Off-axis Encircled Energy (%)**	**Diffraction Limit (%)**
A	4.35	$52 \div 55$	$45 \div 52$	54
B	6.34	$68 \div 70$	$61 \div 68$	70
C	8.70	$70 \div 72$	$66 \div 70$	72

Table 3.5: *Encircled energy at a wavelength $\lambda = 2100\mu m$ ($\nu = 143 GHz$) in the case of Lyot Stop wobbling around its barycenter. It is computed for different values of integration radius. Intervals mean that spots are different in the five fields, thus the collected energy can be different even in the case of same distance from the chief ray.*

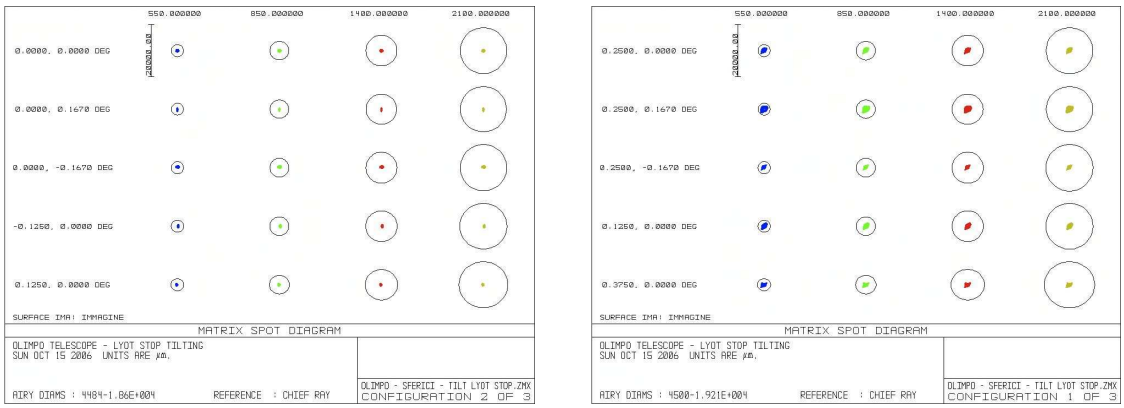

(a) *On-axis spot diagram* (b) *Off-axis spot diagram*

Figure 3.4: *Spot diagrams in the case of Lyot Stop wobbling around its barycenter. For each wavelength, the dimensions of the spots of the five fields are compared to the radius of the Airy disc.*

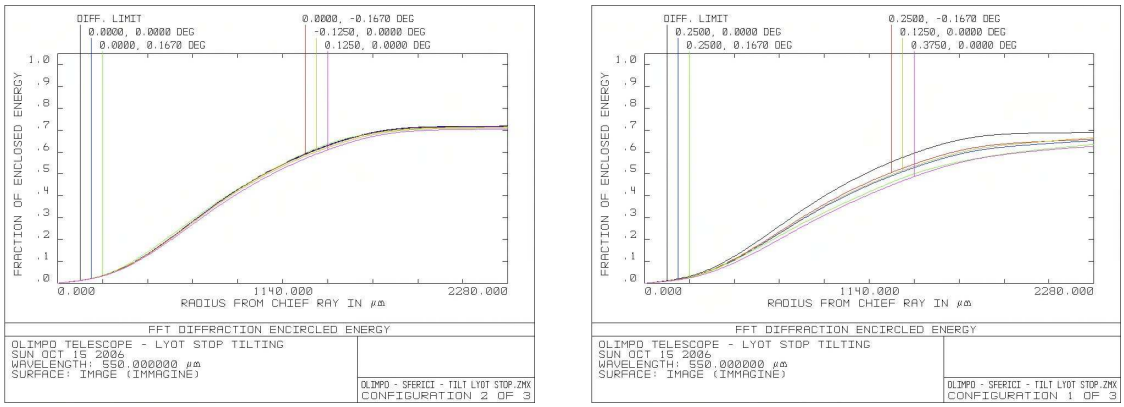

(a) *On-axis encircled energy* (b) *Off-axis encircled energy*

Figure 3.5: *Encircled energy at a wavelength* $\lambda = 550\mu m$ $(\nu = 545\,GHz)$ *in the case of Lyot Stop wobbling around its barycenter. Various curves describe the trend for each field of view; the black one represents the diffraction limit. The integration is computed up to the radius of the Airy disc at* $\lambda = 550\mu m$.

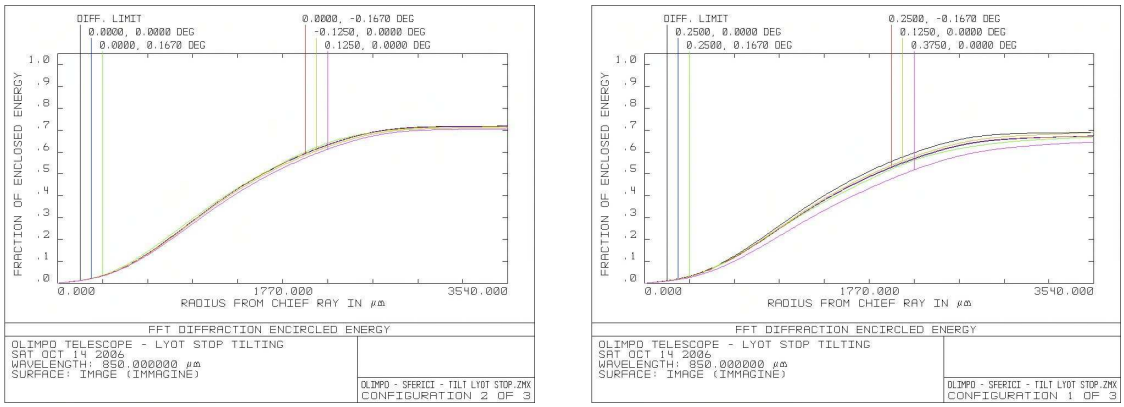

(a) *On-axis encircled energy* (b) *Off-axis encircled energy*

Figure 3.6: *Encircled energy at a wavelength* $\lambda = 850\mu m$ $(\nu = 353GHz)$ *in the case of Lyot Stop wobbling around its barycenter. Various curves describe the trend for each field of view; the black one represents the diffraction limit. The integration is computed up to the radius of the Airy disc at* $\lambda = 850\mu m$*.*

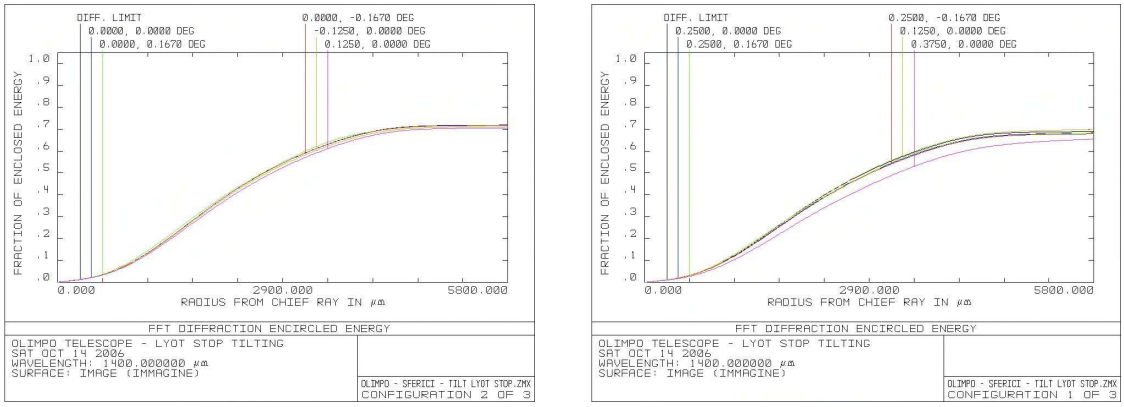

(a) *On-axis encircled energy* (b) *Off-axis encircled energy*

Figure 3.7: *Encircled energy at a wavelength* $\lambda = 1400\mu m$ $(\nu = 217GHz)$ *in the case of Lyot Stop wobbling around its barycenter. Various curves describe the trend for each field of view; the black one represents the diffraction limit. The integration is computed up to the radius of the Airy disc at* $\lambda = 1400\mu m$*.*

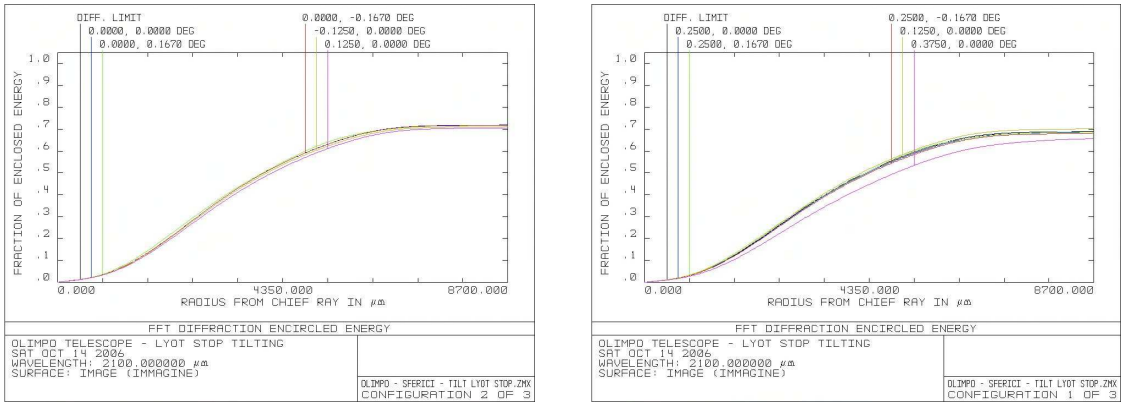

(a) *On-axis encircled energy* (b) *Off-axis encircled energy*

Figure 3.8: *Encircled energy at a wavelength* $\lambda = 2100\mu m$ $(\nu = 143GHz)$ *in the case of Lyot Stop wobbling around its barycenter. Various curves describe the trend for each field of view; the black one represents the diffraction limit. The integration is computed up to the radius of the Airy disc at* $\lambda = 2100\mu m$.

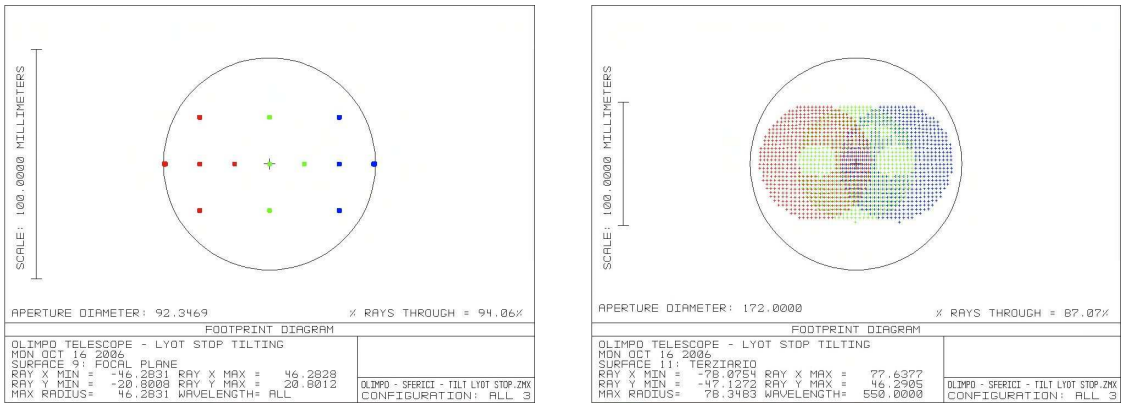

(a) *Footprint on telescope focal plane* (b) *Footprint on tertiary mirror*

Figure 3.9: *Footprint diagrams in the case of Lyot Stop wobbling around its barycenter. It is clear the off-set introduced when the system is off-axis. The footprint on the tertiary mirror is shown to see the effect better: on the focal plane all the five fields are shown, while on the tertiary only the central is reported.*

However, this configuration has two drawbacks. The first is related to cryogenic constrains. The *Lyot Stop* is mounted inside the cryostat, thermally linked to the ^{4}He stage and thus cooled down to $2K$. Mirror wobbling is carried out using appropriate actuators that would increase the heat load on the ^{4}He bath, reducing the hold time. The second drawback is that the oscillation of *Lyot Stop* produces a movement of the telescope image on its focal plane (Fig. 3.9). This introduces a large *offset* in the off-axis measurements; moreover, the cryostat window should be enlarged, increasing the radiative input load and cryostat endurance.

3.1.2 Primary mirror: focus modulation

The best solution from an optical point of view is obtained wobbling the primary mirror around its focus, being at a distance $R = 1247mm$ from the primary vertex, in the direction of the secondary mirror (see Figs. 2.2 and 2.4). This solution requires oscillations of $\pm 15'$ in order to get a sky scan of $\pm 30'$. Furthermore, it minimizes aberrations, because the focus of the primary mirror is the neutral point of the off-axis optical system [26, 103].

Spot diagram for this configuration is shown in Fig. 3.10, while encircled energy curves are reported in Figs. 3.11, 3.12, 3.13 and 3.14. Tabs. 3.6, 3.7, 3.8 and 3.9 report values of EE for different distances from the chief ray, as described in § 3.1.1. It is clear that optical performances are even better than with *Lyot Stop* modulation.

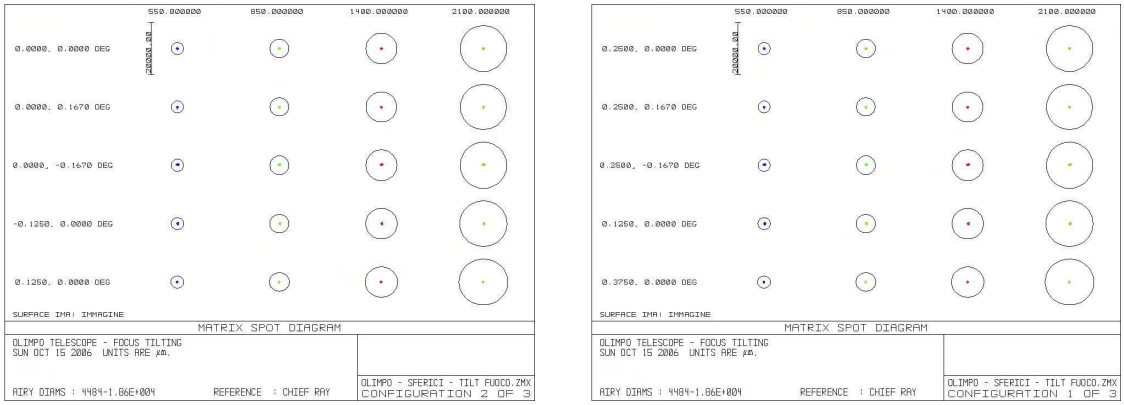

(a) *On-axis spot diagram* (b) *Off-axis spot diagram*

Figure 3.10: *Spot diagrams in the case of primary mirror wobbling around its focus. For each wavelength, the dimensions of the spots of the five fields are compared to the radius of the Airy disc.*

This configuration cannot be used due to power consumption, vibrations and size issues. The focus is very distant from the center of mass of the primary mirror so the moment of inertia of the wobbling system is very high. It is mandatory that the oscillation is around a principal axis of inertia: this means that large and heavy counterbalancing masses should be added, implying a bigger gondola. Moreover, this modulation would introduce vibrations leading to microphonic noise on receivers, decreasing the quality of measurements.

	Integration Radius (mm)	**On-axis Encircled Energy (%)**	**Off-axis Encircled Energy (%)**	**Diffraction Limit (%)**
A	1.14	$52 \div 54$	$52 \div 54$	55
B	1.63	$68 \div 70$	$68 \div 70$	70
C	2.28	$71 \div 72$	$70 \div 72$	72

Table 3.6: *Encircled energy at a wavelength $\lambda = 550\mu m$ ($\nu = 545 GHz$) in the case of primary mirror wobbling around its focus. It is computed for different values of integration radius. Intervals mean that spots are different in the five fields, thus the collected energy can be different even in the case of same distance from the chief ray.*

	Integration Radius (mm)	**On-axis Encircled Energy (%)**	**Off-axis Encircled Energy (%)**	**Diffraction Limit (%)**
A	1.77	$53 \div 55$	$52 \div 55$	55
B	2.57	$69 \div 70$	$68 \div 70$	70
C	3.54	$71 \div 72$	$70 \div 72$	72

Table 3.7: *Encircled energy at a wavelength $\lambda = 850\mu m$ ($\nu = 353 GHz$) in the case of primary mirror wobbling around its focus. It is computed for different values of integration radius. Intervals mean that spots are different in the five fields, thus the collected energy can be different even in the case of same distance from the chief ray.*

	Integration Radius (mm)	**On-axis Encircled Energy (%)**	**Off-axis Encircled Energy (%)**	**Diffraction Limit (%)**
A	2.90	$53 \div 55$	$52 \div 55$	54
B	4.22	$69 \div 70$	$68 \div 70$	70
C	5.80	$71 \div 72$	$71 \div 72$	72

Table 3.8: *Encircled energy at a wavelength $\lambda = 1400\mu m$ ($\nu = 217 GHz$) in the case of primary mirror wobbling around its focus. It is computed for different values of integration radius. Intervals mean that spots are different in the five fields, thus the collected energy can be different even in the case of same distance from the chief ray.*

	Integration Radius (mm)	**On-axis Encircled Energy (%)**	**Off-axis Encircled Energy (%)**	**Diffraction Limit (%)**
A	4.35	$52 \div 54$	$52 \div 54$	54
B	6.34	$69 \div 70$	$68 \div 70$	70
C	8.70	$71 \div 72$	$71 \div 72$	72

Table 3.9: *Encircled energy at a wavelength $\lambda = 2100\mu m$ ($\nu = 143 GHz$) in the case of primary mirror wobbling around its focus. It is computed for different values of integration radius. Intervals mean that spots are different in the five fields, thus the collected energy can be different even in the case of same distance from the chief ray.*

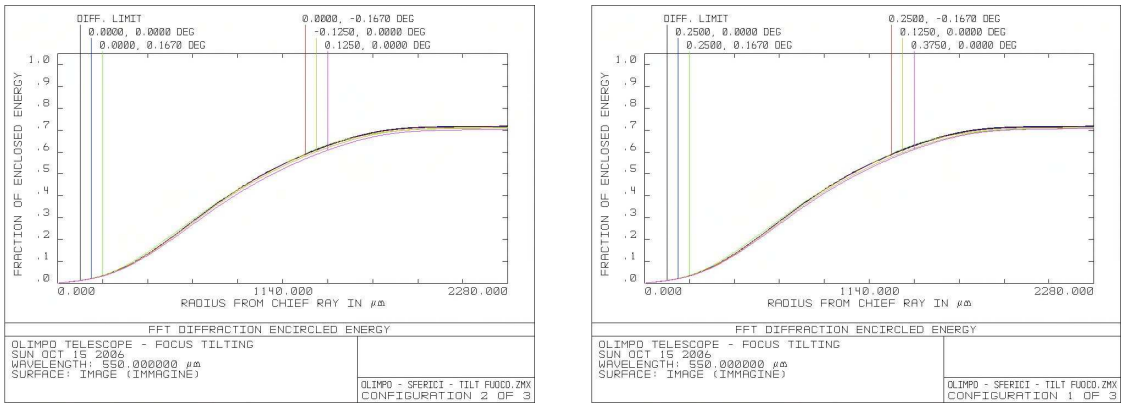

(a) *On-axis encircled energy* (b) *Off-axis encircled energy*

Figure 3.11: *Encircled energy at a wavelength* $\lambda = 550\mu m$ $(\nu = 545GHz)$ *in the case of primary mirror wobbling around its focus. Various curves describe the trend for each field of view; the black one represents the diffraction limit. The integration is computed up to the radius of the Airy disc at* $\lambda = 550\mu m$.

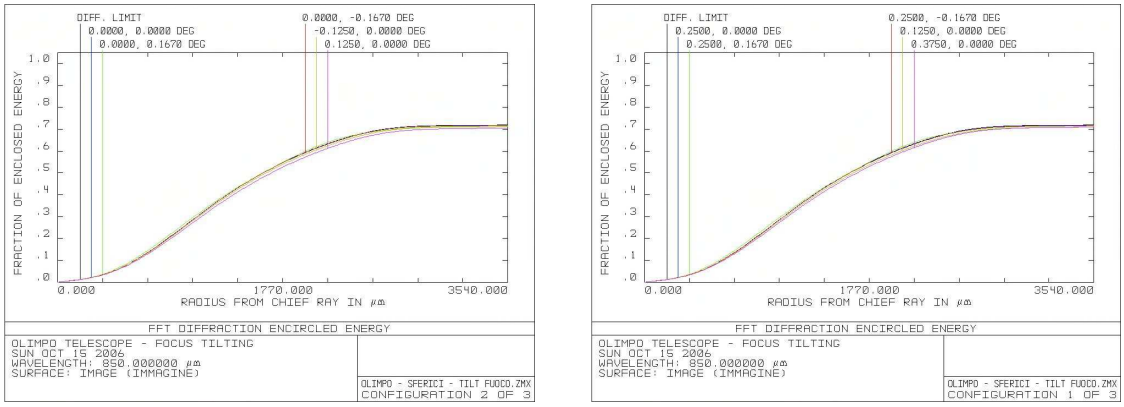

(a) *On-axis encircled energy* (b) *Off-axis encircled energy*

Figure 3.12: *Encircled energy at a wavelength* $\lambda = 850\mu m$ $(\nu = 353GHz)$ *in the case of primary mirror wobbling around its focus. Various curves describe the trend for each field of view; the black one represents the diffraction limit. The integration is computed up to the radius of the Airy disc at* $\lambda = 850\mu m$.

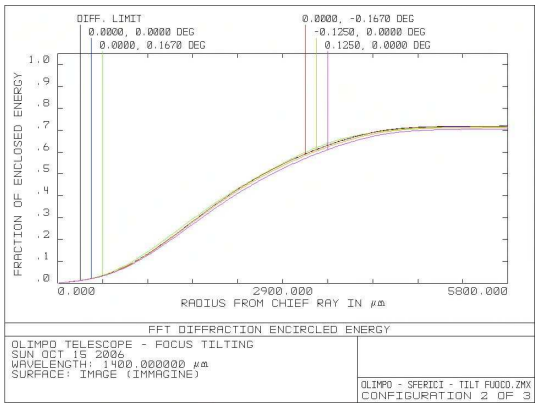

(a) *On-axis encircled energy*

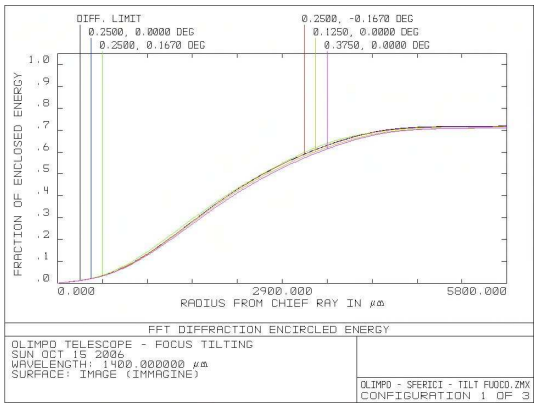

(b) *Off-axis encircled energy*

Figure 3.13: *Encircled energy at a wavelength* $\lambda = 1400\mu m$ $(\nu = 217GHz)$ *in the case of primary mirror wobbling around its focus. Various curves describe the trend for each field of view; the black one represents the diffraction limit. The integration is computed up to the radius of the Airy disc at* $\lambda = 1400\mu m$.

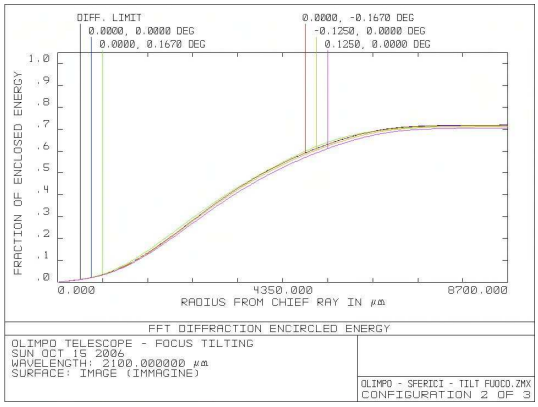

(a) *On-axis encircled energy*

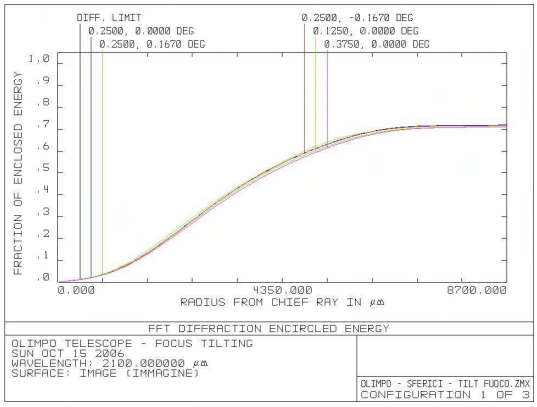

(b) *Off-axis encircled energy*

Figure 3.14: *Encircled energy at a wavelength* $\lambda = 2100\mu m$ $(\nu = 143GHz)$ *in the case of primary mirror wobbling around its focus. Various curves describe the trend for each field of view; the black one represents the diffraction limit. The integration is computed up to the radius of the Airy disc at* $\lambda = 2100\mu m$.

3.1.3 Primary mirror: barycenter modulation

The simplest configuration from a mechanical point of view is obtained wobbling the primary mirror around its center of mass. We have computed its position numerically. Computations do not take into account the rib structure of the primary mirror, nor inhomogeneities eventually present in the structure. Nevertheless, it is important that oscillations take place around the point considered during the optical system optimization, even if it does not coincide exactly with the barycenter. From the optical point of view, every offset from the neutral point of the system decreases the image quality. The computed oscillation point is much closer to the vertex of the primary mirror than the focus; with the approximations made, the center of mass results to be at a distance $R = 146mm$ from vertex, still in the direction of the secondary mirror.

This wobbling solution produces fewer vibrations than focus modulation; furthermore, since the moment of inertia around this axis is much smaller, the required power is acceptable. These are the reasons that lead to the choice of this configuration, even if it is the worst one, but still acceptable, from an optical point of view.

Unfortunately, as already pointed out, the offset from the neutral point of the system decreases the image quality when the system is off-axis. Aberrations increase and the optical system is diffraction limited only for the two longer wavelengths ($\lambda = 1400$ and $2100\mu m$, $\nu = 217$ and $143 GHz$ respectively).

The spot diagram for this configuration is represented in Fig. 3.15, while Figs. 3.16, 3.17, 3.18 and 3.19 show the encircled energy at various wavelengths. As already done before, Tabs. 3.10, 3.11, 3.12 and 3.13 report values of EE for different radii.

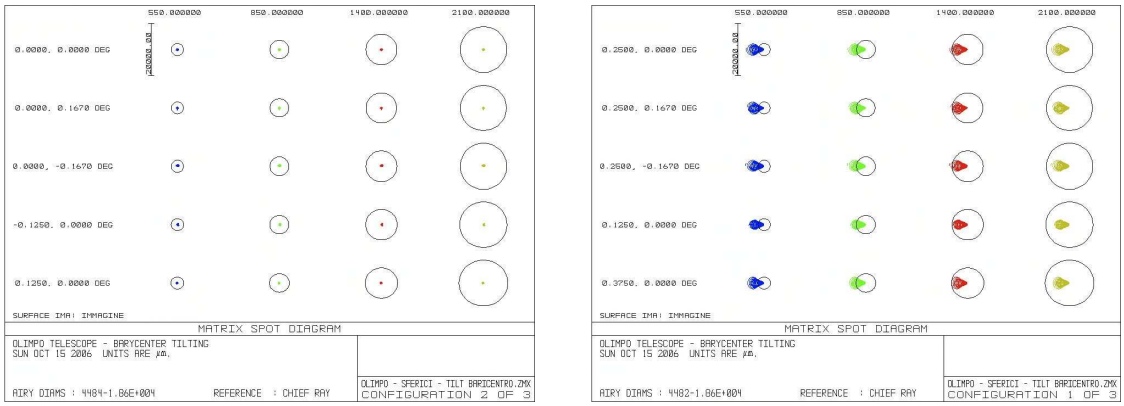

(a) *On-axis spot diagram* (b) *Off-axis spot diagram*

Figure 3.15: *Spot diagrams in the case of primary mirror wobbling around its barycenter. For each wavelength, the dimensions of the spots of the five fields are compared to the radius of the Airy disc.*

	Integration Radius (mm)	**On-axis Encircled Energy (%)**	**Off-axis Encircled Energy (%)**	**Diffraction Limit (%)**
A	1.14	$52 \div 54$	$16 \div 19$	54
B	1.66	$68 \div 70$	$31 \div 36$	70
C	2.28	$70 \div 72$	$51 \div 54$	72

Table 3.10: *Encircled energy at a wavelength $\lambda = 550\mu m$ ($\nu = 545GHz$) in the case of primary mirror wobbling around its barycenter. It is computed for different values of the integration radius. Intervals mean that spots are different in the five fields, thus the collected energy can be different even in the case of same distance from the chief ray.*

	Integration Radius (mm)	**On-axis Encircled Energy (%)**	**Off-axis Encircled Energy (%)**	**Diffraction Limit (%)**
A	1.77	$52 \div 55$	$32 \div 34$	55
B	2.57	$68 \div 70$	$52 \div 54$	70
C	3.54	$70 \div 72$	$65 \div 66$	72

Table 3.11: *Encircled energy at a wavelength $\lambda = 850\mu m$ ($\nu = 353GHz$) in the case of primary mirror wobbling around its barycenter. It is computed for different values of the integration radius. Intervals mean that spots are different in the five fields, thus the collected energy can be different even in the case of same distance from the chief ray.*

	Integration Radius (mm)	**On-axis Encircled Energy (%)**	**Off-axis Encircled Energy (%)**	**Diffraction Limit (%)**
A	2.90	$52 \div 55$	$44 \div 45$	54
B	4.22	$68 \div 70$	$62 \div 63$	70
C	5.80	$71 \div 72$	$69 \div 70$	72

Table 3.12: *Encircled energy at a wavelength $\lambda = 1400\mu m$ ($\nu = 217GHz$) in the case of primary mirror wobbling around its barycenter. It is computed for different values of the integration radius. Intervals mean that spots are different in the five fields, thus the collected energy can be different even in the case of same distance from the chief ray.*

	Integration Radius (mm)	**On-axis Encircled Energy (%)**	**Off-axis Encircled Energy (%)**	**Diffraction Limit (%)**
A	4.35	$52 \div 54$	$48 \div 50$	54
B	6.34	$68 \div 70$	$66 \div 67$	70
C	8.70	$70 \div 72$	$70 \div 71$	72

Table 3.13: *Encircled energy at a wavelength $\lambda = 2100\mu m$ ($\nu = 143GHz$) in the case of primary mirror wobbling around its barycenter. It is computed for different values of the integration radius. Intervals mean that spots are different in the five fields, thus the collected energy can be different even in the case of same distance from the chief ray.*

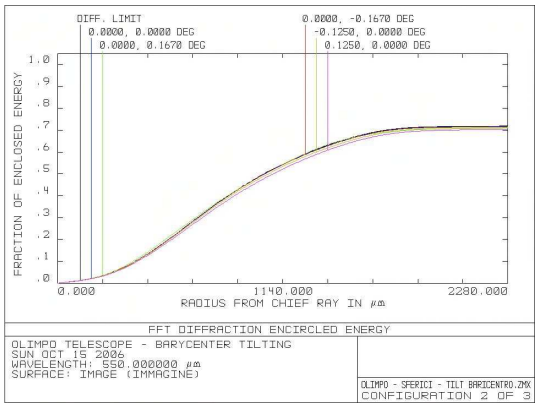

(a) *On-axis encircled energy*

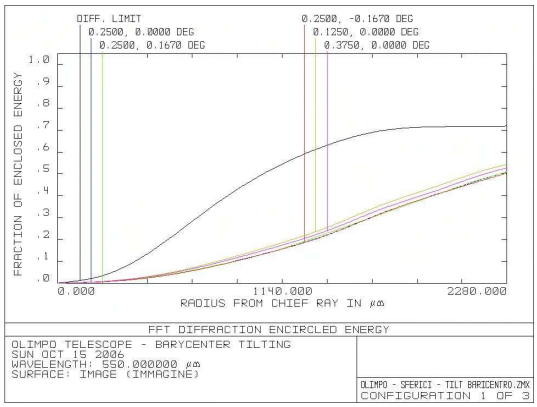

(b) *Off-axis encircled energy*

Figure 3.16: *Encircled energy at a wavelength* $\lambda = 550\mu m$ $(\nu = 545GHz)$ *in the case of primary mirror wobbling around its barycenter. Various curves describe the trend for each field of view; the black one represents the diffraction limit. The integration is computed up to the radius of the Airy disc at* $\lambda = 550\mu m$.

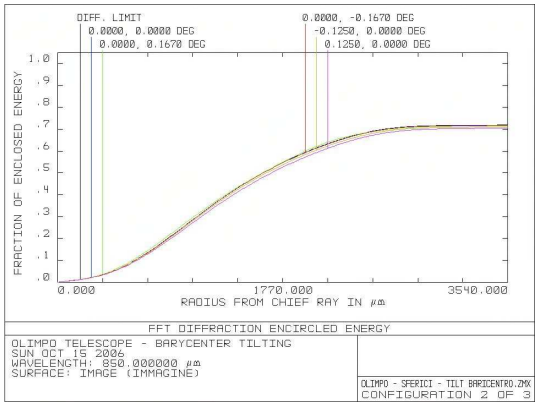

(a) *On-axis encircled energy*

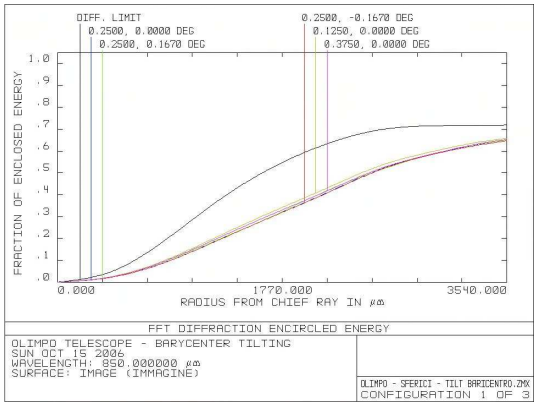

(b) *Off-axis encircled energy*

Figure 3.17: *Encircled energy at a wavelength* $\lambda = 850\mu m$ $(\nu = 353GHz)$ *in the case of primary mirror wobbling around its barycenter. Various curves describe the trend for each field of view; the black one represents the diffraction limit. The integration is computed up to the radius of the Airy disc at* $\lambda = 850\mu m$.

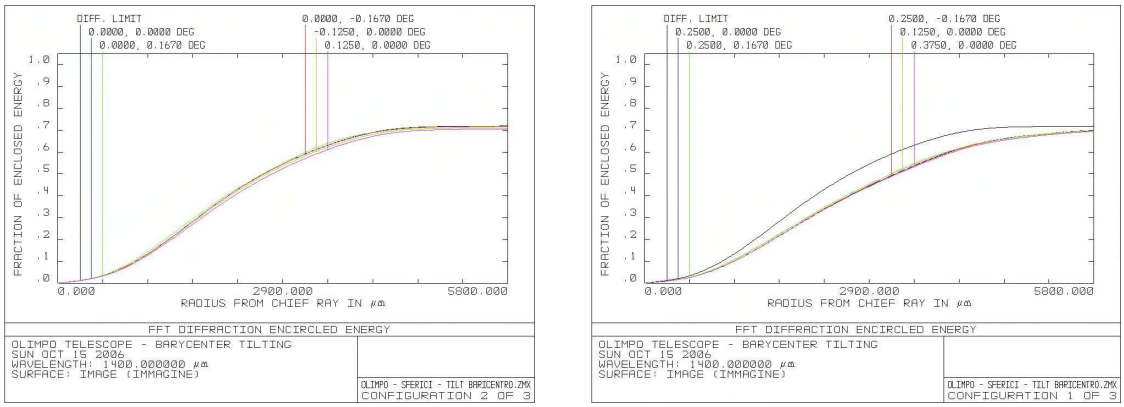

(a) *On-axis encircled energy* (b) *Off-axis encircled energy*

Figure 3.18: *Encircled energy at a wavelength* $\lambda = 1400\mu m$ $(\nu = 217GHz)$ *in the case of primary mirror wobbling around its barycenter. Various curves describe the trend for each field of view; the black one represents the diffraction limit. The integration is computed up to the radius of the Airy disc at* $\lambda = 1400\mu m$.

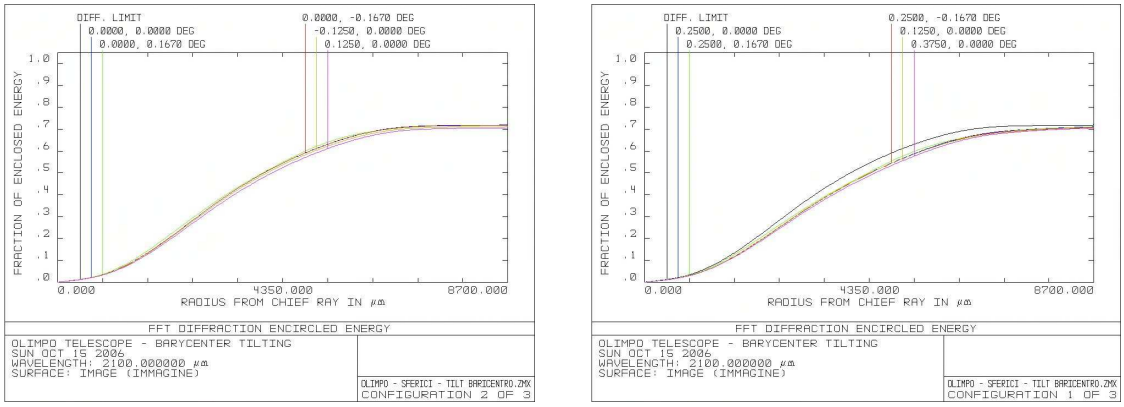

(a) *On-axis encircled energy* (b) *Off-axis encircled energy*

Figure 3.19: *Encircled energy at a wavelength* $\lambda = 2100\mu m$ $(\nu = 143GHz)$ *in the case of primary mirror wobbling around its barycenter. Various curves describe the trend for each field of view; the black one represents the diffraction limit. The integration is computed up to the radius of the Airy disc at* $\lambda = 2100\mu m$.

3.2 Final configuration

A general expression for a rotationally symmetric aspheric surface is:

$$z = \frac{c\,r^2}{1+\sqrt{1-(1+k)\,c^2\,r^2}} + \sum_{i=1}^{N} A_i\,r^i \tag{3.4}$$

where z and r are sagittal and radial coordinates respectively, c is the curvature (defined as the inverse of curvature radius R_c), k is the conic constant and A_i are the aspheric coefficients that describe the surface deviation from conic surface, using a polynomial expansion. The other parameters defining the portion of mirror used are their dimensions and *decenterings*. The latter is defined as the distance between the center of the conic and the incoming chief ray of the central field, i.e. the ray coming from the center of Field 1 of Tab. 3.1 (see Fig. 3.20).

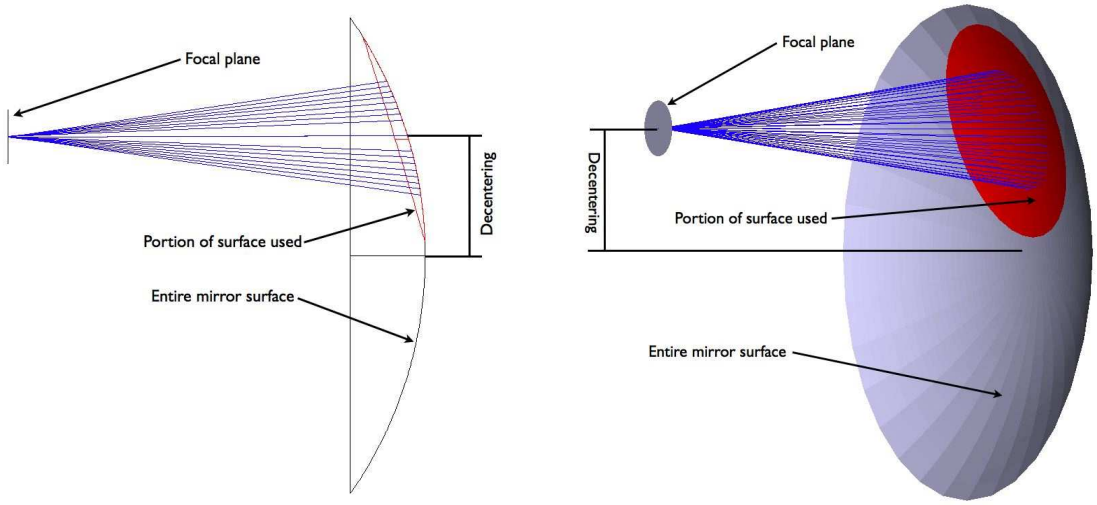

(a) *Decentering definition: 2D design* (b) *Decentering definition: 3D design*

Figure 3.20: *Definition of the ZEMAX decentering parameter, defined as the distance between the center of the conic and the incoming chief ray of the central field. In red, the portion of mirror used (tertiary or quinary, since they are identical) is shown.*

Many possible designs have been studied in these years. The final one, shown in Fig. 3.1, is constituted by three spherical mirrors. The third and fifth mirrors are identical, while the *Lyot Stop* has a curvature radius being half the others, obviously changed in sign: in fact, tertiary and quinary mirrors must concentrate radiation, which means they must be convex and have a positive curvature radii, while the *Lyot Stop* diverges the beam, so a concave mirror with a negative radius of curvature is required.

The centers of *Lyot Stop* and quinary mirrors are aligned: defining the z-axis as the one orthogonal to the image surface, these two centers differ only by the z coordinate. If the tertiary mirror is aligned too, i.e. it lies on the same sphere that defines the fifth mirror, the telescope focal and final image planes would lie on the same plane: without any offset, the system is perfectly symmetric, the telescope focal plane and the image surface

are interchangeable. The introduction of an offset of 1.5mm in height between the centers of tertiary and *Lyot Stop* mirrors shifts behind the image surface, increasing the $f/\#$ of the experiment and the available room to place dichroics, filters, horns and receivers.

Since the mirrors of *OLIMPO* are spherical, they have $A_i = 0$ and $k = 0$. The only free coefficient describing the surface mirror is the curvature. In the case of the third and fifth mirrors, the dimensions are determined observing the beam illumination on each mirror. In order to avoid diffractive effects due to the edge of the mirror, their minimum dimensions are increased by 10%. As pointed out by the *Footprint Diagrams* of the two mirrors (see Fig. 3.21), the quinary might be smaller than the tertiary, but we decided to make them identical to simplify the construction process. Moreover, with this choice the mirrors are interchangeable: since the machined mirror could have curvature and conic constant different from the nominal ones, it could be necessary to distinguish the third and fifth mirrors during the alignment process (see § 4.5).

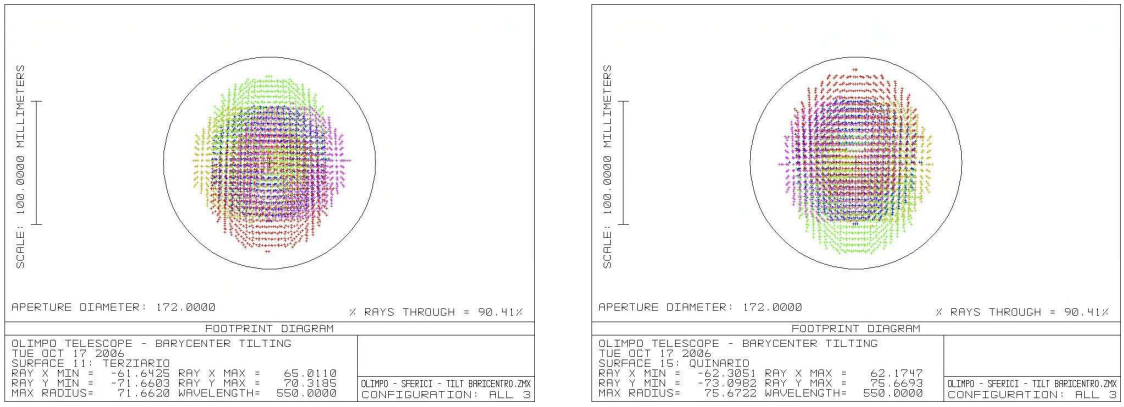

(a) *Footprint on tertiary mirror* (b) *Footprint on quinary mirror*

Figure 3.21: *Footprint on the tertiary and quinary mirrors. The different colors represent the five fields defined in* Tab. 3.1 *while the wobbling of the primary mirror has roughly no effect. The footprint on the tertiary is a little bit smaller than that on the quinary, but the mirrors are identical to simplify the construction process. It is worth noting that the position of the fields is reversed between the tertiary and quinary.*

3.2.1 Lyot Stop design

The introduction of a *cold stop* is of fundamental importance in millimeter experiments, even if it degrades optical system performances. The use of highly sensitive thermal receivers requires the reduction of all the spurious signals, mainly stray light radiation and sidelobes.

Stray light This is the radiation that arrives onto receivers without passing through the whole mirrors chain. It can be reduced using appropriate optical solution, such as some "turns" in the radiation path, so bolometers do not directly see the window of the cryostat.

Sidelobes Every time an incident infinite plane wave with wavevector $\vec{k}_{In}$ encounters an aperture (in our case, optical elements such as mirrors), the outgoing wave is no more plane due to diffraction and has wavevectors $\vec{k}$ in different directions. For small angles ϑ, the vector $\vec{q} = \vec{k} - \vec{k}_{In}$ is in the plane of the aperture and $\vec{q} = \vartheta\vec{k}$ is valid. The diffracted component is the sum of contributions from all the surface elements dS of the aperture, each with its own phase:

$$\begin{aligned} u_q = \iint_S u_0\, e^{-i\vec{q}\cdot\vec{r}}\, dS &= u_0 \int_0^R \int_0^{2\pi} e^{-iqr\cos\varphi}\, r\, d\varphi\, dr = \\ &= 2\pi u_0 \int_0^R J_0(qr)\, r\, dr = u_0\, \frac{2J_1(Rq)}{Rq} \end{aligned} \tag{3.5}$$

where J_0 and J_1 are first type Bessel function of order zero and one. The intensity is the square of the field:

$$\frac{dI}{d\Omega} = I_0 \left[\frac{2J_1(R\vartheta k)}{R\vartheta k}\right]^2 \tag{3.6}$$

The first zero is for $\vartheta_{0,1} = 1.22\,\lambda/2R$ and the value of the *Full Width Half Maximum* (FWHM) is similar. The envelope of the off-axis response scales approximately as ϑ^{-3}, starting from the FWHM. The slope of eq. (3.6) is shown in Fig. 3.22 in the case of $R = 2m$ and $\lambda = 1mm$ and $10mm$ (black and red curves respectively). In the case of mirrors, the main contribution to sidelobes comes from edge effects.

The radiation reaching the receivers is given by the sum of the signal of interest and spurious signals:

$$\begin{aligned} W &= A\left[\int_M B_{Sky}(\vartheta,\varphi)\, RA(\vartheta,\varphi)\, d\Omega + \int_S B_{Noise}(\vartheta,\varphi)\, RA(\vartheta,\varphi)\, d\Omega\right] \\ &\simeq A\left[B_{Sky}(\vartheta,\varphi)\, \langle RA_M(\vartheta,\varphi)\rangle\, \Omega_M + B_{Noise}(\vartheta,\varphi)\, \langle RA_S(\vartheta,\varphi)\rangle\, \Omega_S\right] \end{aligned} \tag{3.7}$$

where A is the area of the telescope, RA is the angular response, the subscript M indicates calculations are made over the mainlobe of the experiment while subscript S indicates the sidelobes. In balloon-borne experiments the main contribution to spurious signal is due to ground radiation ($B_{Noise} \rightleftharpoons 300K$), while the signal of interest has a much lower temperature ($B_{Sky} \rightleftharpoons 1mK$).

Since sidelobes and stray light cannot be cancelled, the solution is to decrease as much as possible the term B_{Noise} of eq. (3.7). This is achieved inserting an optical stop cooled down to cryogenic temperature. In particular, we used a *Lyot Stop* thermally linked with the ^{4}He bath, i.e. cooled to $2K$. The *Lyot Stop* is defined as a mirror onto which the image of the primary is focused: it subsists the same relation that there is between the image of the sky and the focal plane. Its dimensions define the portion of primary mirror used: the *Lyot Stop* will cut the sidelobes due to the primary mirror, but it will introduce its sidelobes. The advantage consists in the fact that it is cold, so $B_{Noise} \rightleftharpoons 2K$, and it is enclosed in a cold absorbing cavity with very low and constant emission. The contribution of this radiation in the sidelobes will be very small (see § 5.3.4) and perfectly constant during the scans of the sky, so that it will be easy to remove from the interesting signal(sky

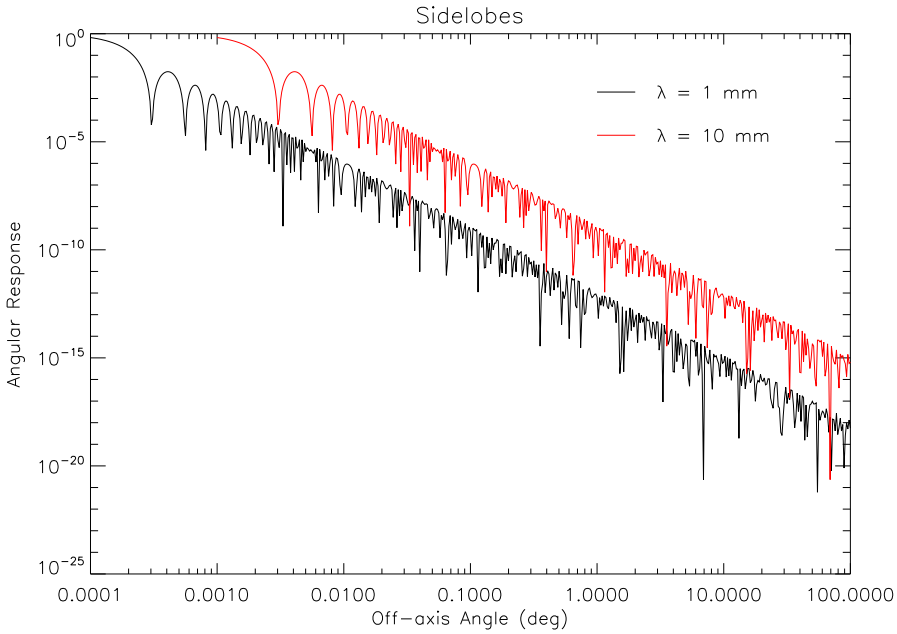

Figure 3.22: *Typical shape of angular response for a millimeter experiment: the sidelobes are visible at large angles. The white curve represents the predicted angular response in the case of a mirror with* $R = 2m$ *and wavelength of incident radiation* $\lambda = 1mm$*. The red one is for* $\lambda = 10mm$*.*

brightness fluctuations). Moreover, stray light radiation cannot reach directly the receivers and it will be thermalized to the optics box temperature (see § 4.4).

The primary mirror is a parabolic one with a diameter of $2.6m$ (see Tab. 2.1). Since the profile of the mirror can be slightly different from the center to the edge and in order to reduce sidelobes of the primary, a portion of $2m$ is used. It must be noted that the five fields move on the *Lyot Stop* (see Fig. 3.23): the dimensions of the fourth mirror are determined choosing the portion of the mirror that includes the intersection of the five fields (see Tab. 3.1), so the *Lyot Stop* is uniformly illuminated on the whole surface during scans. This is achieved with a *Lyot Stop* having an outer diameter of $54mm$.

The *Lyot Stop* has another main feature: it rejects radiation due to the so-called *Narcissus effect*. Since the Cassegrain telescope is an on-axis system, rays from the whole mirror, i.e. including its hole, reach the secondary and are focused onto the focal plane. But rays coming from the hole of the primary originates in the focal plane, so an observer situated in the telescope image surface would see his own image. In other words, the receivers see the primary surface, including its hole, that is a source at a temperature much different than the signal of interest.

The solution is to put a hole into the *Lyot Stop*, whose dimensions depend on those of the primary (see Tab. 2.1), hence bolometers will see only $2K$ radiation: however, a small fraction of the sky radiation is also rejected. Considering the hole of the primary as the source and calculating the encircle energy as a function of the increasing radius of the *Lyot Stop* hole, the ratio of disregarded rays is obtained. The constrains are to reject

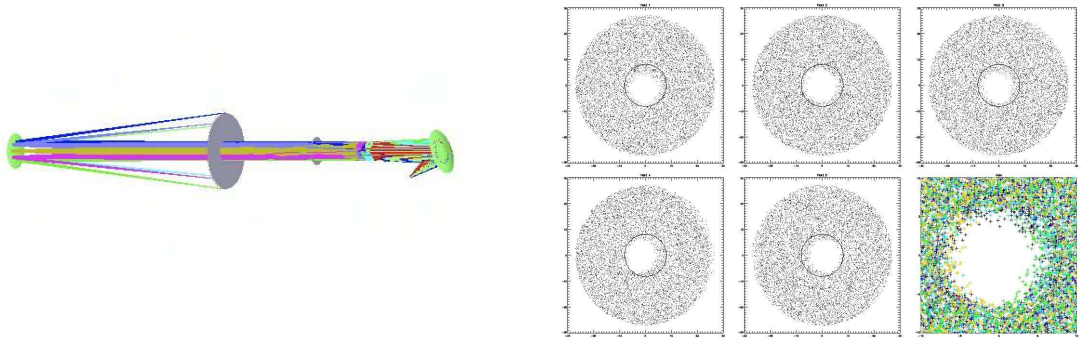

(a) *Lyot Stop design: setup* (b) *Intersection of 5 field*

Figure 3.23: *Design of the Lyot Stop. It must focus the image of the primary mirror, select its diameter and reject rays coming from its hole. On the left, the design of the hole follows the same line of reasoning: in this case, the rays come from the hole of the primary mirror, instead of coming from its surface. The picture on the right shows how the images coming from different fields shift on the Lyot Stop, thus the fourth mirror is the intersection of the various fields.*

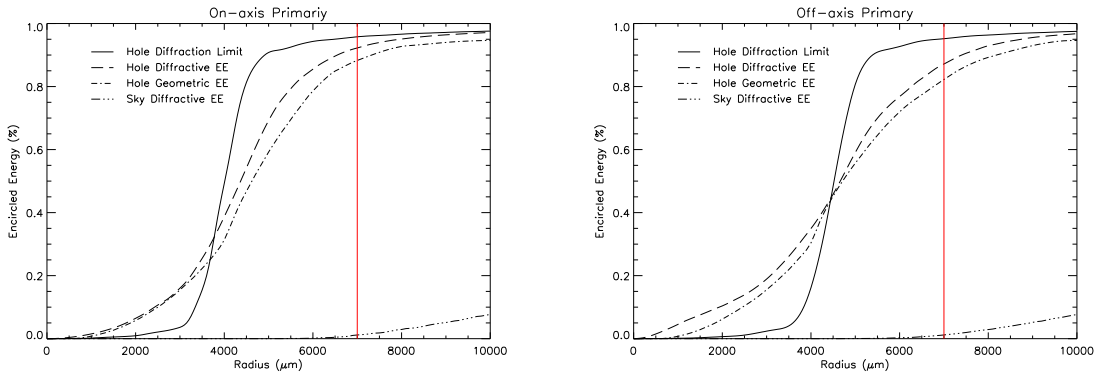

(a) *On-axis encircled energy* (b) *Off-axis encircled energy*

Figure 3.24: *Design of the hole of Lyot Stop. It must reject as many "hole rays" as possible, without neglecting "sky rays". The two figures show the total geometric and diffractive encircled energy, i.e. the sum of the energy from all the field of view taken into account, in the on-axis and off-axis configurations (see* Tab. 3.1*). They are compared to the diffraction limit and encircled energy due to sky radiation, which is small because we are considering only the portion of primary mirror near its hole (see* Fig. 3.23*).*

at least 85% of "hole rays" and to reduce as much as possible the "sky rays" neglected. Arguments used to choose the *Lyot Stop* diameter apply here as well: the hole must include the intersection of the three configurations. Choosing a hole diameter of $14mm$, between 87% and 92% of spurious radiation is rejected (off-axis and on-axis configuration, respectively), while less than 2% of signal radiation is lost (see Fig. 3.24).

3.2.2 Performance analysis

There are two further analysis done to study the performance of the final optical system: they consist in evaluating the *Point Spread Function* (PSF) and of the *Modulation Transfer Function* (MTF).

Point Spread Function It represents the intensity distribution on the image surface of the diffraction image formed by the optical system. In the case of a circular aperture, it consists of concentric rings, gradually darker (*Airy profile*). Rays coming from a point-like source are *spread* when they pass through an optical system, due to both diffraction and aberrations. The image will be no more point-like, but its distribution will be described by the PSF. In the case of a circular aperture with diameter D and an obstruction with diameter εD, i.e. a ring-like aperture (which is the case of the Cassegrain telescope configuration), the PSF is given by:

$$PSF(r,\varphi) = \frac{I(r,\varphi)}{I_0} = \frac{1}{(1-\varepsilon)^2} \cdot \left[\frac{2J_1(v)}{v} - \varepsilon^2 \frac{2J_1(\varepsilon v)}{\varepsilon v} \right]^2 \tag{3.8}$$

where r and φ are the polar coordinates on the image surface, J_1 is the Bessel function of the first type of order one and v is an adimensional variable being generally equal to:

$$v = \frac{2\pi}{\lambda} \frac{a}{R} r = k \frac{a}{R} R \tag{3.9}$$

where $2a$ is the diameter of the exit pupil, k is the wavenumber and R is the radius of the wavefront coming out of the pupil. In the hypothesis of a distant source ($2a/R \Rightarrow D/f$) and of an aperture without obstruction ($\varepsilon = 0$), previous equations simplify and the minimum of the PSF is given by the radius of the Airy disc R_{Airy}. The instrument *resolving power* is related to the value of the Airy disc radius: two point-like sources are considered angularly resolved when the luminosity maximum of the first one coincides with the first minimum of the other one (*Rayleigh criterion*, shown in Fig. 3.25). With this simplification, the *minimum angular resolution* α_1 is given by:

$$\alpha_1 = 1.22 \frac{\lambda}{D} \tag{3.10}$$

A quantitative way to verify the optical system performance using the PSF is computing the *Strehl ratio* (SR), defined as the ratio between the intensity peak of the real PSF and the one of an ideal PSF (the one obtained in the absence of aberrations). It is assumed that a system is diffraction limited when $SR \geqslant 0.8$.

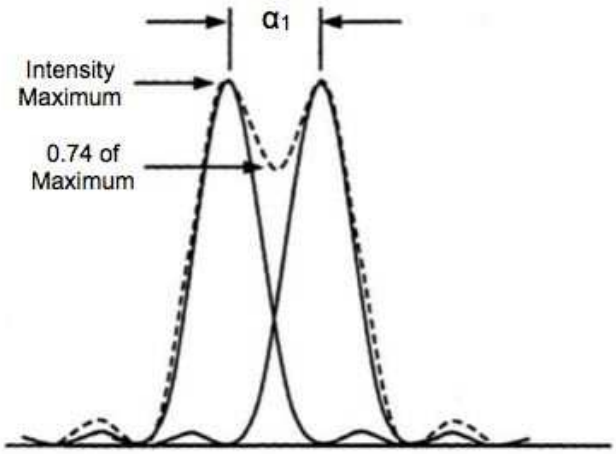

Figure 3.25: *Rayleigh criteria: the minimum separation between two point-like sources in order to distinguish them.*

Modulation Transfer Function The *Optical Transfer Function* (OTF) is defined as the normalized PSF Fourier transform:

$$OTF(u,v) = \frac{\displaystyle\int_{-\infty}^{+\infty}\int_{-\infty}^{+\infty} PSF(x,y)\, e^{2\pi i\,(ux+vy)}\, dx\, dy}{\displaystyle\int_{-\infty}^{+\infty}\int_{-\infty}^{+\infty} PSF(x,y)\, dx\, dy} \tag{3.11}$$

where the spatial coordinates x and y are associated to u and v wavenumbers. If the distribution of luminous intensity of the object is described by $D_O(x,y)$ and $D_I(x,y)$ is the same for the image, they are related by the relation:

$$D_I(x,y) = D_O(x,y) \otimes PSF(x,y) \tag{3.12}$$

where the symbol $\otimes$ represents the convolution product. Applying the Fourier transform to both terms of eq. (3.12), the convolution becomes a simple product, simplifying a lot the analysis:

$$d_I(x,y) = d_O(x,y) \cdot OTF(x,y) \tag{3.13}$$

The physical interpretation of this quantity is that an object can always be decomposed into an infinite number of bright and dark Fourier components of increasing spatial frequency. The optical transfer function describes the response of the optical system in spatial frequencies. Let us consider an object with sinusoidal distribution of luminous intensity, amplitude $A = I_{MAX}/I_{MIN}$, period l and spatial frequency $1/l$: the image of the object will remain sinusoidal, while its contrast will degrade due to the optical system. The OTF modulus, defines as the modulation transfer function, represents the contrast degradation:

$$MTF(u) = \sqrt{\mathrm{Re}^2[OTF(u)] + \mathrm{Im}^2[OTF(u)]} \tag{3.14}$$

In the simplest case of a circular aperture, $MTF(\beta) = 2\,(\beta - \cos\beta \sin\beta)/\pi$ with $\beta = \arccos(\lambda \cdot u \cdot f/\#)$. So, the MTF decreases with u and there is a contrast until the spatial frequency is higher than:

$$u_{Cut-Off} = \frac{1}{\lambda \cdot f/\#} \tag{3.15}$$

PSF (see Figs. 3.26, 3.28, 3.30 and 3.32) and MTF (see Figs. 3.27, 3.29, 3.31 and 3.33) are computed for each wavelength and both primary positions, on-axis and off-axis. The performances are evaluated using the Strehl ratio in the case of PSF, while MTF is compared to the diffraction limit. Once again, the optical system is always diffraction limited at $\lambda = 1400$ and $2100\mu m$, while shorter wavelengths require the on-axis configuration to reach the same performance.

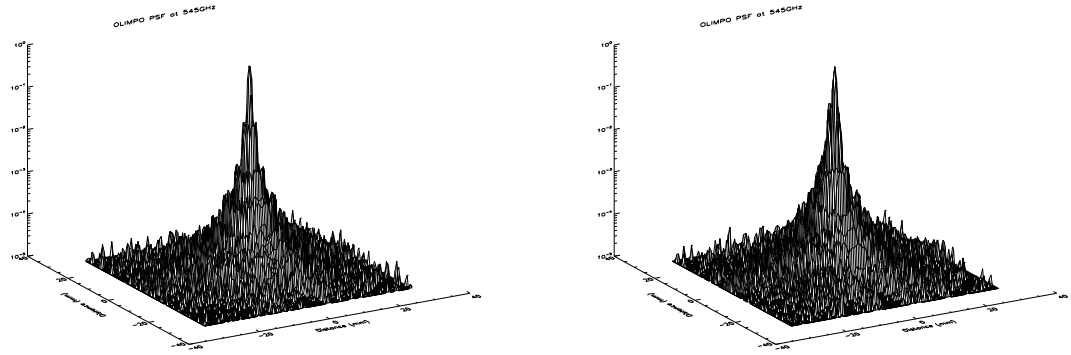

(a) *On-axis point spread function* (b) *Off-axis point spread function*

Figure 3.26: *Point spread function for* $\lambda = 550\mu m$ $(\nu = 545 GHz)$ *in logarithmic scale. It is shown only the central field* (*i.e. the Field* 1 *of* Tab. 3.1) *in both primary positions: on-axis and off-axis. The Strehl ratio is* 0.913 *and* 0.519 *respectively.*

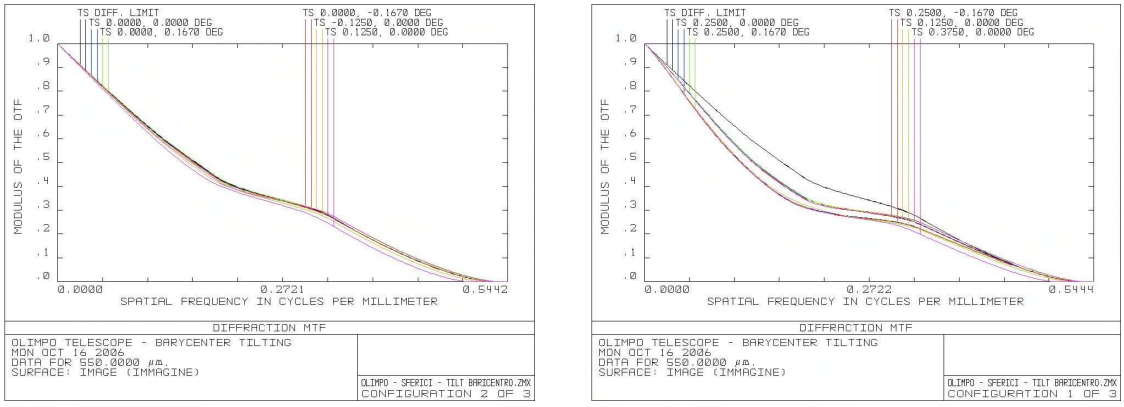

(a) *On-axis modulation transfer function* (b) *Off-axis modulation transfer function*

Figure 3.27: *Modulation transfer function for* $\lambda = 550\mu m$ $(\nu = 545 GHz)$ *of all the five fields of* Tab. 3.1 *compared to the diffraction limit case. The MTF is computed for both primary positions: on-axis and off-axis.*

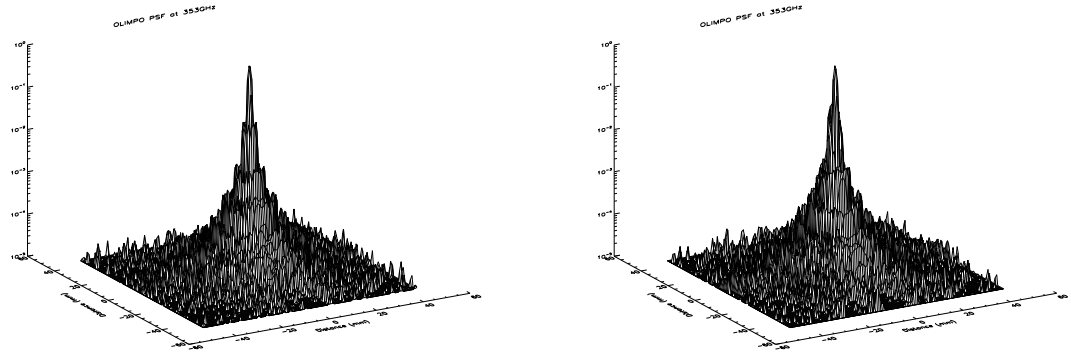

(a) *On-axis point spread function* (b) *Off-axis point spread function*

Figure 3.28: *Point spread function for* $\lambda = 850\mu m$ $(\nu = 353GHz)$ *in logarithmic scale. It is shown only the central field* (*i.e. the Field* 1 *of* Tab. 3.1) *in both primary positions: on-axis and off-axis. The Strehl ratio is* 0.971 *and* 0.722 *respectively.*

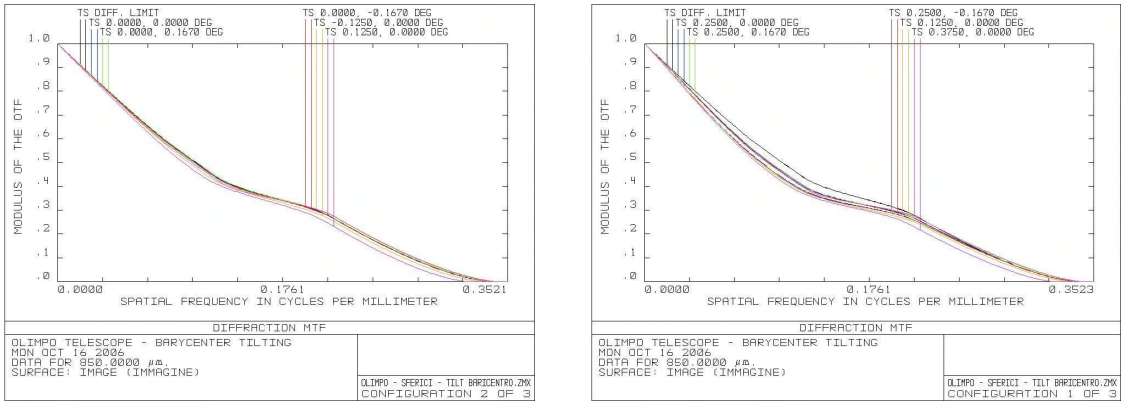

(a) *On-axis modulation transfer function* (b) *Off-axis modulation transfer function*

Figure 3.29: *Modulation transfer function for* $\lambda = 850\mu m$ $(\nu = 353GHz)$ *of all the five fields of* Tab. 3.1 *compared to the diffraction limit case. The MTF is computed for both primary positions: on-axis and off-axis.*

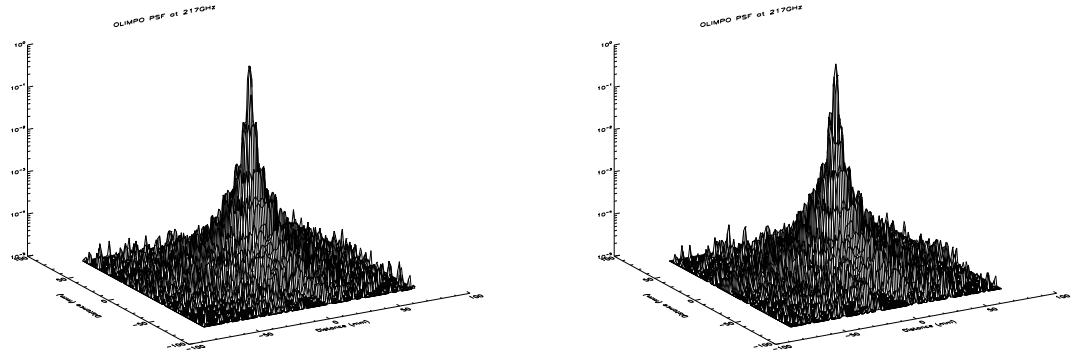

(a) *On-axis point spread function* (b) *Off-axis point spread function*

Figure 3.30: *Point spread function for* $\lambda = 1400\mu m$ $(\nu = 217GHz)$ *in logarithmic scale. It is shown only the central field* (*i.e. the Field* 1 *of* Tab. 3.1) *in both primary positions: on-axis and off-axis. The Strehl ratio is* 0.990 *and* 0.891 *respectively.*

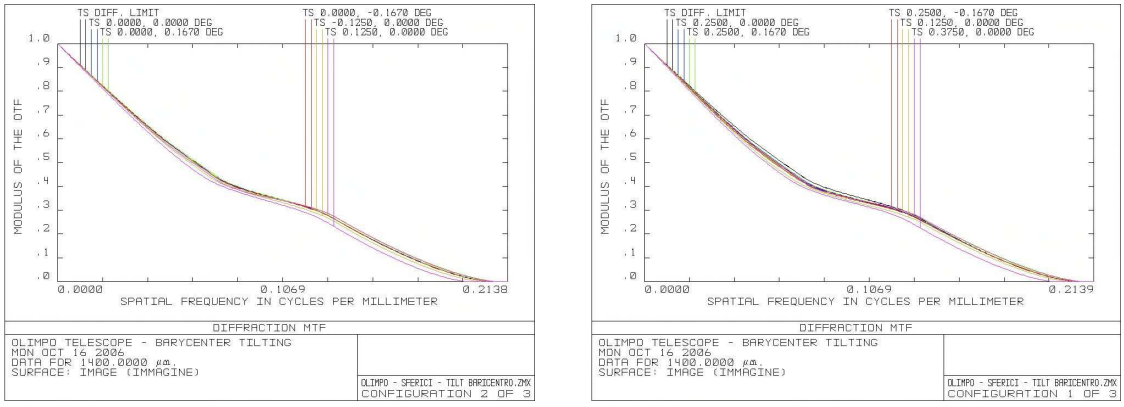

(a) *On-axis modulation transfer function* (b) *Off-axis modulation transfer function*

Figure 3.31: *Modulation transfer function for* $\lambda = 1400\mu m$ $(\nu = 217GHz)$ *of all the five fields of* Tab. 3.1 *compared to the diffraction limit case. The MTF is computed for both primary positions: on-axis and off-axis.*

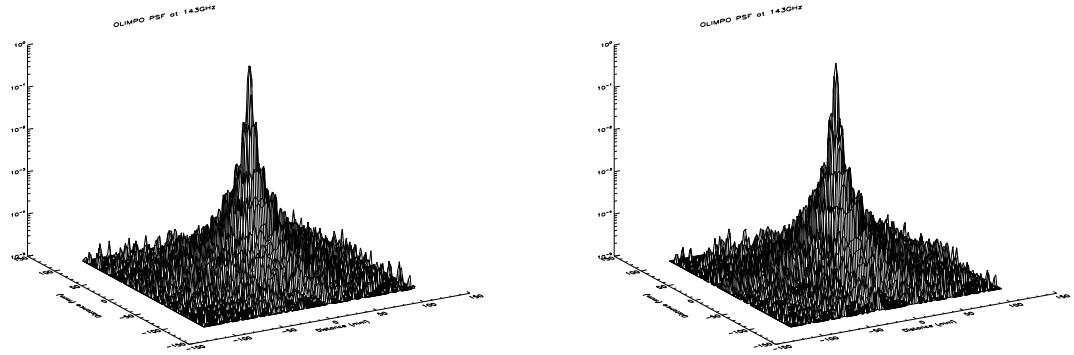

(a) *On-axis point spread function* (b) *Off-axis point spread function*

Figure 3.32: *Point spread function for* $\lambda = 2100\mu m$ $(\nu = 143GHz)$ *in logarithmic scale. It is shown only the central field* (*i.e. the Field* 1 *of* Tab. 3.1) *in both primary positions: on-axis and off-axis. The Strehl ratio is* 0.998 *and* 0.973 *respectively.*

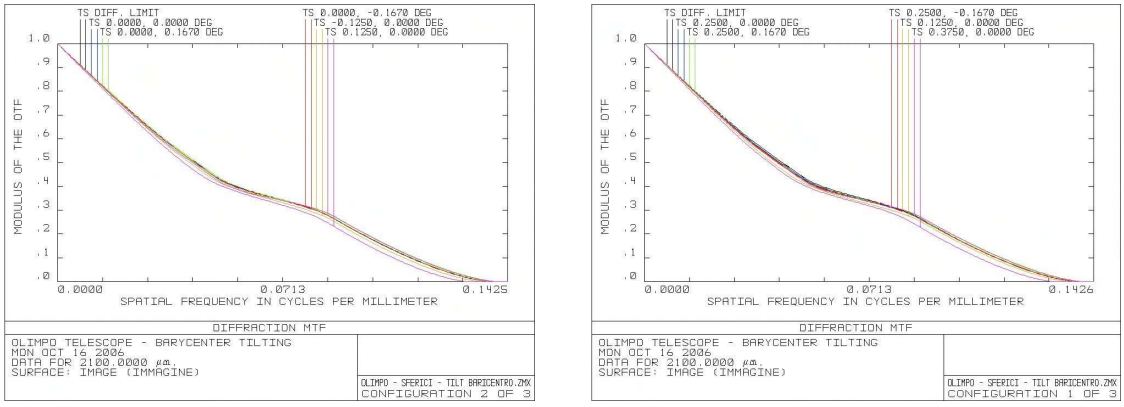

(a) *On-axis modulation transfer function* (b) *Off-axis modulation transfer function*

Figure 3.33: *Modulation transfer function for* $\lambda = 2100\mu m$ $(\nu = 143GHz)$ *of all the five fields of* Tab. 3.1 *compared to the diffraction limit case. The MTF is computed for both primary positions: on-axis and off-axis.*

Chapter 4

Optics tests

I am not young enough
to know everything.

Oscar Wilde

All the re-imaging optics are mounted inside an *optics box* thermally linked to the ^{4}He tank: both mirrors and optics box are made with the same aluminum alloy in order to ensure homologous deformations for all the elements as the temperature decrease. As already pointed out, cooling down the re-imaging optics minimizes the thermal radiation they emit, thus reducing the spurious signal on the receivers. Furthermore, painting the walls of the optics box with an absorbing material, stray light and other spurious radiation are absorbed, thermalized to $2K$ and then reemitted outside the bandwidths of the detectors.

The design of the whole system must take into account the dimensions of the cryostat and the available space at the ^{4}He stage. Moreover, the total weight and the thermal dissipation should be as low as possible. The choice of an aluminum alloy represents a good compromise between lightness, thermal capacity, cost of the material and easiness of manufacturing.

After the design process, mirrors were fabricated in the machine shop of the Department of Physics, University of Rome "La Sapienza". Apart of the prototypes, three samples of the *Lyot Stop* were made, while the identical tertiary and quinary mirrors came in five copies. The tests consist in verifying that the machined surface is comparable to the designed one and eventually computing the parameters of the mirror; measuring the roughness of the surface; choosing, mounting and aligning the best set of three mirrors; finally, evaluating the optical performance of the system.

4.1 Executive project of the mirrors

After designing the reflecting surface of the mirrors using *ZEMAX*, their executive project must take into account two important constraints:

1. The mirrors have to be as light as possible: in fact, the total weight of the system

(tanks, shields and elements inside them) determines the thickness of the fiberglass tubes that support the inner shells of the cryostat (see § 2.3); an increase of the thickness implies a growth of the conductive heat load, as described by eq. (2.5).

2. The re-imaging optics will be mounted inside a shield thermally linked to the ^{4}He bath; it has a radius equal to $240mm$, thus the back of the third and fifth mirrors must fit in such a shield.

These two requirements are achieved using an appropriate shape for the back structure of the third and fifth mirrors. A main cut of 25.6° decreases the mirrors weight and two side cuts of 10.0° and 29.0° allow to fit in the shield. On the back of the mirrors is designed a rib structure, maintaining an effective thickness of $5mm$ (see Fig. 4.1): this allows to further increase the lightness of the mirror without affecting its rigidity. A plane base is present in order to attach the mirrors to the optics box: on each mirror, two reference holes define the alignment of the mirror using pins, while it is kept in position by three M5 screws. The base is filled to increase the thermal conductivity between the mirror and the ^{4}He stage.

The *Lyot Stop* does not need such a structure, since it is considerably smaller and lighter than the tertiary and quinary mirrors; moreover, it is placed at the center of the cryostat, thus it is not necessary to shape its back. Only the design of the hole is of interest: a calibration lamp is required for on-flight calibrations and we decided to place it in the hole of the *Lyot Stop*. The lamp must illuminate the receivers with a beam having focal distance equal to that of the experiment: this is achieved using a Winston cone fabricated by IRLabs sloping of 57° so that it illuminates directly the quinary (see Fig. 4.2). Thus, the hole of the *Lyot Stop* must be designed to accommodate the calibration lamp and its cone (see Fig. 4.3).

The mirrors cannot be fabricated in a single shot, since both front and back must be machined. Hence, it is necessary a precise reference frame in order to reposition the material during the different phases of production. Moreover, the spherical surfaces of these elements require a high tridimensional accuracy, since they are going to be used as mirrors. Hence, the finishing given by the machine is crucial, because it reduces the handmade polishing process thus preserving the correct shape of the machined surface. In order to achieve a good finishing, there are a few requirements that the alloy and machine used have to accomplish:

Prerequisites on the alloy Structural stability in presence of rough machining; dimensional and formable stability in respect to temperature variation; sufficiently compact to allow very high cutting velocities in order to favor mirrors polishing (this minimizes the subsequent handmade operations that could alter the shape of the reflecting surface); properly manufacturable material, which means choosing an alloy easy to be polished.

Prerequisites on the machine Structural rigidity of the devices involved, such as movement axes or machine equipment, which is achieved using a machine in optimal conditions and equipment sufficiently stiff; high strength of the tools, realized using a diamond tool; low width for each pass, hence an accurate programming of the machine; high cutting velocity, obtainable with high rotation velocity.

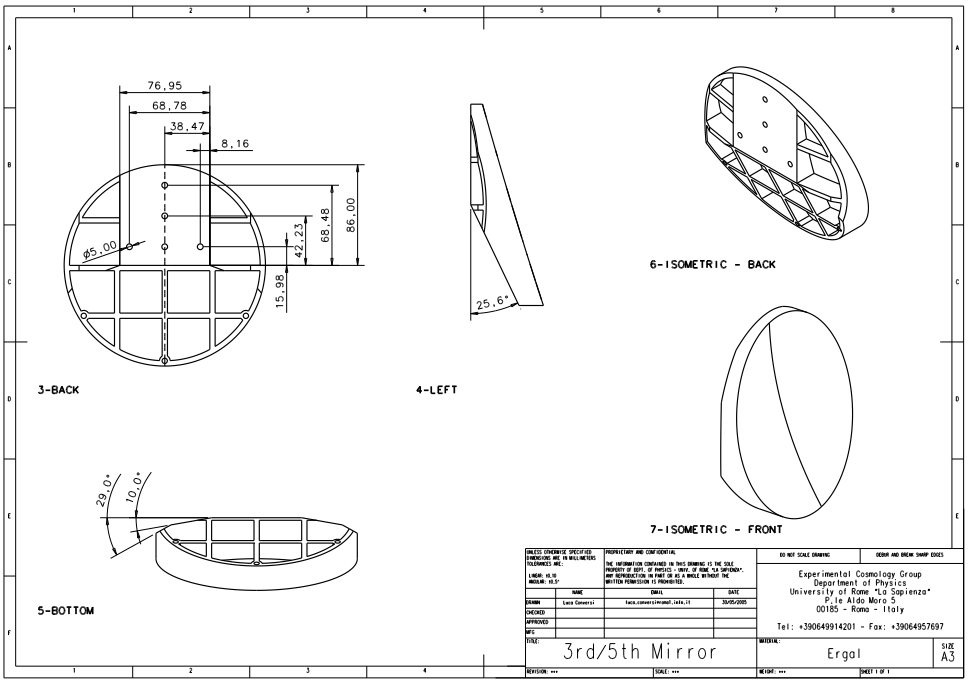

Figure 4.1: *Drawing of the tertiary and quinary mirrors. It shows the angles of the main cut and of the two side cuts.*

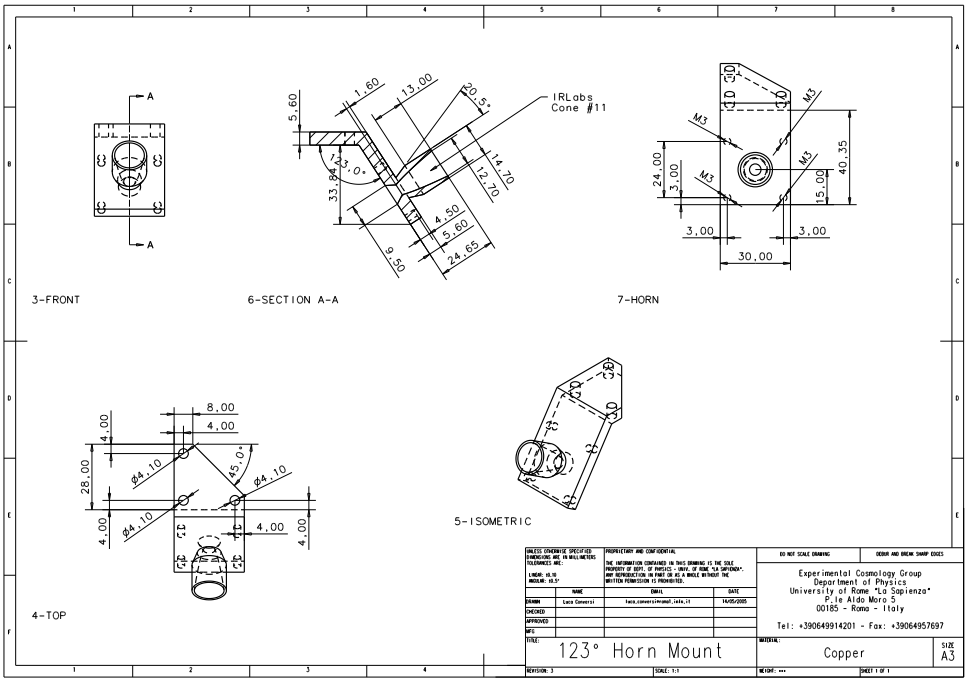

Figure 4.2: *Drawing of mount of the calibration lamp. The Winston cone will be placed inside the hole of the Lyot Stop.*

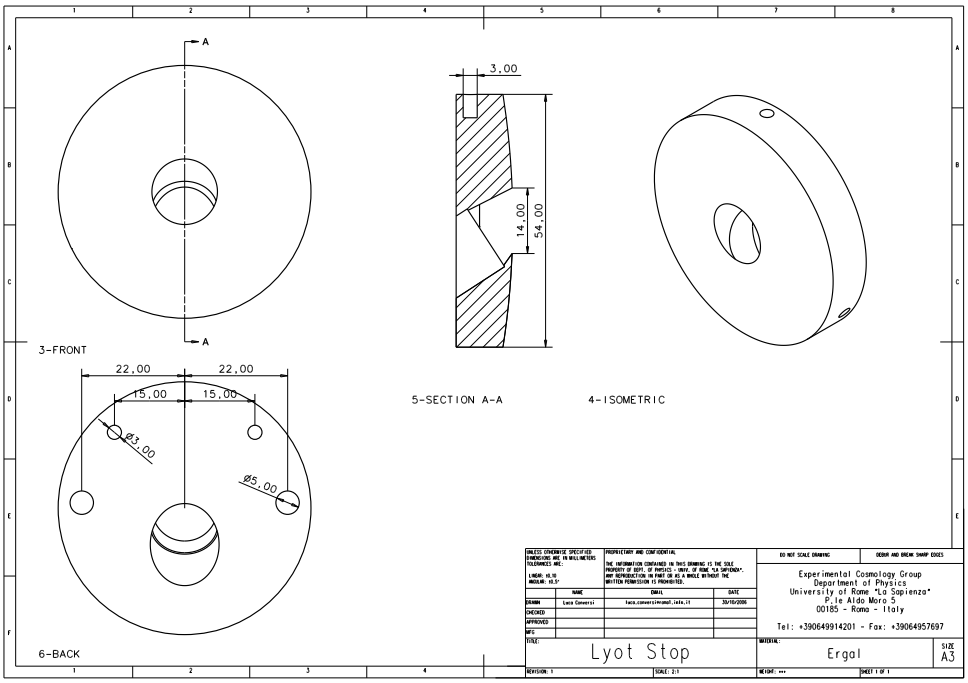

Figure 4.3: *Drawing of the Lyot Stop: the particular design of the hole permit to place the Winston cone of the calibration lamp.*

The front part of the mirror is fully occupied by the reflecting surface, which requires a finishing as precise as the used machine can do: thus, this part was the last to be manufactured. The machining of tertiary and quinary mirrors is realized with the controlled numerical milling cutter *C.B.Ferrari* managed using a CAD/CAM/CAE software (*Computer Aided Design, Manufacturing and Engineering*): the advantage is that machining is fully automated, the operator has to input only the type of material and the cutting tool to be used.

The manufacturing of the tertiary and quinary mirrors had many troubles. The particular form of the mirrors back, with two tilted surfaces forming an obtuse angle, produces an unstable base; moreover, a complication is given by the absence of a surface suited to clamp the material, excluding the planar back surfaces dedicated to this task. Thus, choosing as unique frame this planar surface, half of the mirror would be suspended favoring oscillations and vibrations. This problem was solved using a custom construction support to sustain and give reference, thus allowing a precise repositioning. This was made with two flat surfaces that perfectly fit the two planes of the back of the tertiary and quinary mirrors. Fastening and reference are given by appropriate holes and pins.

The first part of the manufacturing process starts from the rough piece of alloy, a $45mm$ thick plate: firstly it is rough machined, then rib structure, holes and external cylindrical contour are produced; finally, the two side cuts are made using a belt saw. This process can be subdivided in seven steps:

1. Removal of most of the material with a “step” process using a “candle” cutter of

diameter $\varnothing = 20mm$.

2. Rough machining of the nests of the rib structure with a spherical cutter with $\varnothing = 8mm$ and leaving a layer of $0.5mm$ of stock.

3. Removal of the enduring crests on the ribs using a "candle" cutter with $\varnothing = 8mm$; the persisting stock is $0.3mm$.

4. Finishing machining of the nests with a spherical cutter of $\varnothing = 8mm$.

5. Manufacturing of the pre-holes on the tilted surface, then camber, drilling, tapping and boring.

6. Smoothing of the back tilted planes in finishing machining with a leveling cutter of $\varnothing = 63mm$.

7. Finishing machining of the external profile: the two side cuts are made.

In second part of the manufacturing process, the third and fifth mirrors are fixed on the construction support and the reflecting spherical surfaces are machined using spherical cutting tools fitting the tridimensional shape of the surfaces; finishing machining foresees a gradual approach to the nominal quote with decreasing cutting width and lateral shift.

C.B.Ferrari cannot reach the rotation velocities required for a good finishing of the reflecting surface: this implies a proper choice of the cutting tool. Manufacturing a tridimensional surface imposes the use of a spherical or toroidal tool. Since it must be increased as much as possible the tool diameter, it is chosen the latter with a small radius ($0.4mm$) mounted on a flattening machine of $85mm$. This choice permit to reach quite high cutting velocities having a spindle of $5000r.p.m.$ while the small radius of the toroidal tool ensures a small thickness of the metal shaving, thus reducing the vibrations during machining.

The creation of the reflecting surface, which takes about 10 hours of machine continuum working time, can be subdivided into four steps:

1. Removal of most of the material with a "step" process using a "candle" cutter of diameter $\varnothing = 20mm$.

2. Rough machining with a spherical cutter of $\varnothing = 8mm$.

3. Semi-finishing machining with a toroidal diamond tool having diameter $\varnothing = 85mm$, radius of curvature $R = 0.4mm$ and making ~ 1000 passes.

4. Finishing machining with the same toroidal diamond tool as before, but making ~ 4000 passes; after this process, the thin layer of stock left is removed.

The manufacturing of the *Lyot Stop* is different: it is an axis-symmetric surface, i.e. its revolution axis is perpendicular and passes through the center of its back plane. Thus, its reflecting, spherical, front surface can be machined using a lathe instead of a milling machine.

First, the piece of alloy is placed on the *C.B.Ferrari*: here, the rough machining is made; furthermore, the sloped hole and the holes for fastening and positioning the mirror

are manufactured. The finishing machining of the reflecting surface is made mounting the *Lyot Stop* on the lathe *Shaublin*, where a very good surface roughness is achieved in a time much smaller than that required by the third and fifth mirrors.

4.2 Mirrors characterization

Once the mirrors are machined, the first test regards the comparison between nominal and real characteristics: parameters of the reflecting surface, thickness of the mirror and positions of the holes. This is achieved using the tridimensional measuring machine *Poli Galaxy Diamond*. This machine, placed in a room at a constant temperature of $21 \pm 0.5\,^{\circ}C$, has a movable granite plane which gives the movement along the z axis, while a movable arm provides the motion along the x and y axes. At the end of the arm is mounted an interchangeable touch probe free to rotate in any direction. The measuring machine is controlled by a CAD software, on which the 3D design of the mirror is uploaded: once a reference frame is provided manually touching the holes on the back, the touching process is fully automated.

For each of the five tertiary and quinary mirrors 184 points are taken, while 132 points are taken on the three *Lyot Stop* samples. A first fit is made directly by the measuring machine, comparing the theoretical and manufactured surface: hence, it can highlight only the differences between the two spherical surfaces, showing if there are any systematic deviations due to the machining process (see Fig. 4.4).

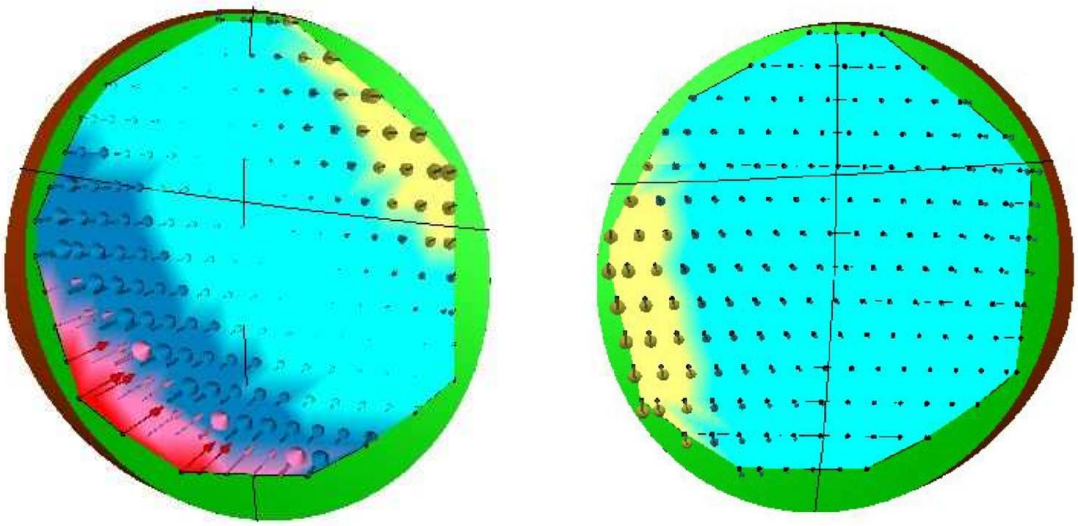

(a) *Surface comparison on mirror* #4 (b) *Surface comparison on mirror* #5

Figure 4.4: *Surface comparison computed directly by the measuring machine. It compares the theoretical and manufactured surfaces. Turquoise region is in the tolerance limit, i.e. each point deviates less than* $10\mu m$ *from the expected position; blue region indicates a negative deviation, yellow and red regions a positive deviation. However, the maximum deviation is* $20\mu m$.

The resolution of the measuring machine is very high, less than $1\mu m$. Nevertheless, each measured point has a higher uncertainty due to the errors in the definition of the reference frame and in the finite dimensions of the probe. Neglecting the inaccuracy due to the latter, a wrong definition of the reference frame could introduce three offsets x_0, y_0 and z_0 and three rotations around the x, y and z axes, i.e. the yaw ψ, pitch ϑ, and roll φ angles respectively.

Thus, a more accurate surface fitting must take into account such rotations and translations together with a variation in the radius of curvature of the surface R_C, and conic constant k. The three rotation matrices are:

$$\mathbf{M}_{Yaw} = \begin{pmatrix} 1 & 0 & 0 \\ 0 & \cos\psi & -\sin\psi \\ 0 & \sin\psi & \cos\psi \end{pmatrix} \tag{4.1a}$$

$$\mathbf{M}_{Pitch} = \begin{pmatrix} \cos\vartheta & 0 & \sin\vartheta \\ 0 & 1 & 0 \\ -\sin\vartheta & 0 & \cos\vartheta \end{pmatrix} \tag{4.1b}$$

$$\mathbf{M}_{Roll} = \begin{pmatrix} \cos\varphi & -\sin\varphi & 0 \\ \sin\varphi & \cos\varphi & 0 \\ 0 & 0 & 1 \end{pmatrix} \tag{4.1c}$$

Hence, the total rotation matrix is:

$$\mathbf{M}_{Tot} = \mathbf{M}_{Roll} \cdot \mathbf{M}_{Pitch} \cdot \mathbf{M}_{Yaw} =$$

$$\begin{pmatrix} \cos\varphi\cos\vartheta & \cos\varphi\sin\vartheta\sin\psi - \sin\varphi\cos\psi & \cos\varphi\sin\vartheta\cos\psi + \sin\varphi\sin\psi \\ \sin\varphi\cos\vartheta & \sin\varphi\sin\vartheta\sin\psi + \cos\varphi\cos\psi & \sin\varphi\sin\vartheta\sin\psi - \cos\varphi\sin\psi \\ -\sin\vartheta & \cos\vartheta\sin\psi & \cos\vartheta\sin\psi \end{pmatrix} \tag{4.2}$$

The corrected position in x and y coordinates is simply given by the subtraction of the offsets and the correction of the rotations:

$$\begin{aligned} x_{Err,i} &= (x_{Meas,i} - x_0)\cos\varphi\cos\vartheta + \\ &+ (y_{Meas,i} - y_0)\sin\varphi\cos\vartheta + \\ &- (z_{Meas,i} - z_0)\sin\vartheta \end{aligned} \tag{4.3}$$

$$\begin{aligned} y_{Err,i} &= (x_{Meas,i} - x_0)(\cos\varphi\sin\vartheta\sin\psi - \sin\varphi\cos\psi) + \\ &+ (y_{Meas,i} - y_0)(\sin\varphi\sin\vartheta\sin\psi + \cos\varphi\sin\psi) + \\ &+ (z_{Meas,i} - z_0)\cos\vartheta\sin\psi \end{aligned} \tag{4.4}$$

Instead, the correction on z depends on the errors on the reference frame and on the parameters of the reflecting surface:

$$\begin{aligned} z_{Err,i} &= (x_{Meas,i} - x_0)(\cos\varphi\sin\vartheta\cos\psi + \sin\varphi\sin\psi) + \\ &+ (y_{Meas,i} - y_0)(\sin\varphi\sin\vartheta\sin\psi - \cos\varphi\sin\psi) + \\ &+ \left(\frac{x_{Err,i}^2 + y_{Err,i}^2}{R_C + \sqrt{R_C^2 - (k+1)(x_{Err,i}^2 + y_{Err,i}^2)}} - z_0 \right) \cos\vartheta\sin\psi \end{aligned} \tag{4.5}$$

Thus, the χ^2 function to minimize is:

$$\chi^2(R_C, k, x_0, y_0, z_0, \psi, \vartheta, \varphi) = \sum_i \frac{(z_{Meas,i} - z_{Err,i})^2}{\sigma_i^2} \tag{4.6}$$

where σ_i is the error on each measurement, given by the resolution of the measuring machine. The χ^2 is computed for all the eight manufactured mirrors, both varying the conic constant k and taking it fixed: while the machining of the tertiary and quinary mirrors can diverge from a spherical surface because they are off-axis, this is improbable for the on-axis *Lyot Stop* machined on a lathe. Moreover, the *Lyot Stop* is a small portion ($d = 54mm$) of a sphere having a large radius ($R_C = 175mm$), thus the sampling is not accurate enough to measure a deviation from the spherical shape.

Tab. 4.1 reports the fit on the three samples of *Lyot Stop*: it is clear that mirror #2 is the best one. Tab. 4.2 shows the results of the computation on the five samples of tertiary and quinary mirrors. The ones that best fit the nominal surface are #3 and #4: both these mirrors have a positive conic constant which degrades a lot the optical performances. The only mirror with $k < 0$ is #5: it counterbalances the aberrations introduced by the deviation of the #4 by a perfect spherical surface. However, it is worth noting that the nominal parameters of the eight mirrors are always within 1σ of the experimental value. Fig. 4.5 shows the likelihood computed as a function of the conic curvature.

	R_C (mm)	k	$R_C\|_{k=0}$ (mm)
***Lyot Stop* #1**	178.7 ± 3.3	0.2 ± 2.2	174.5 ± 3.4
***Lyot Stop* #2**	178.5 ± 3.2	0.0 ± 2.2	174.2 ± 3.3
***Lyot Stop* #3**	178.6 ± 3.2	1.2 ± 2.0	174.3 ± 3.4

Table 4.1: *Parameters of the three Lyot Stop samples obtained by the χ^2 fit of* eq. (4.6). *The nominal values are $R_C = 175mm$ and $k = 0$.*

	R_C (mm)	k	$R_C\|_{k=0}$ (mm)
Mirror #1	-351.5 ± 1.1	$+0.04 \pm 0.15$	-349.5 ± 1.3
Mirror #2	-351.0 ± 1.2	$+0.04 \pm 0.08$	-350.0 ± 1.3
Mirror #3	-350.5 ± 1.2	$+0.04 \pm 0.18$	-349.6 ± 1.3
Mirror #4	-350.9 ± 1.1	$+0.01 \pm 0.12$	-350.0 ± 1.2
Mirror #5	-352.2 ± 1.1	-0.02 ± 0.07	-351.6 ± 1.2

Table 4.2: *Parameters of the five tertiary and quinary mirrors samples obtained by the χ^2 fit of* eq. (4.6). *The nominal values are $R_C = -350mm$ and $k = 0$.*

Given the experimental parameters obtained by fitting the surface of the mirrors, we compute again the spot diagram and the encircled energy with *ZEMAX*. Fig. 4.6 shows the spots diagram, while Figs. 4.7, 4.8, 4.9 and 4.10 show the encircled energy computed within the Airy disc at that wavelength.

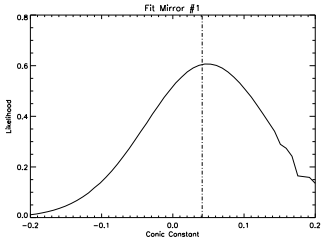

(a) *Fit on Mirror* #1

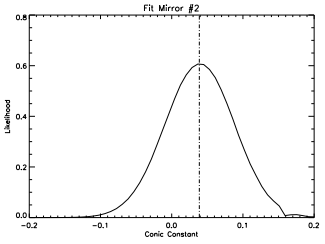

(b) *Fit on Mirror* #2

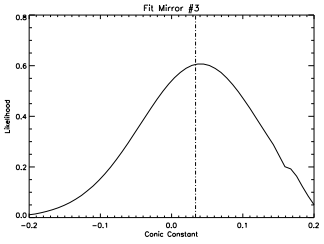

(c) *Fit on Mirror* #3

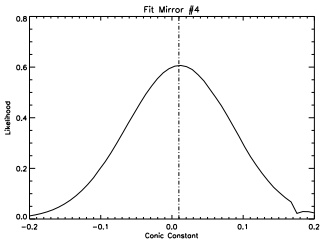

(d) *Fit on Mirror* #4

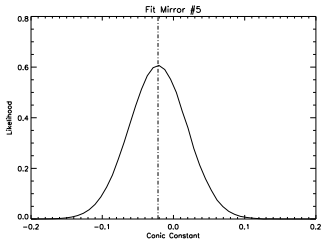

(e) *Fit on Mirror* #5

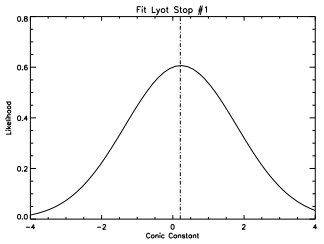

(f) *Fit on Lyot Stop* #1

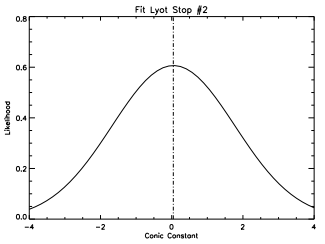

(g) *Fit on Lyot Stop* #2

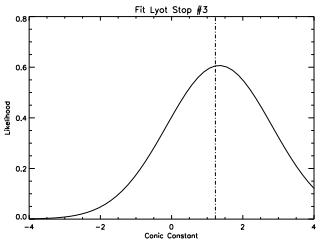

(h) *Fit on Lyot Stop* #3

Figure 4.5: *Fit on the surface of the three Lyot Stop and five tertiary/quinary mirrors samples. The fit is computed varying the conic constant of the surface.*

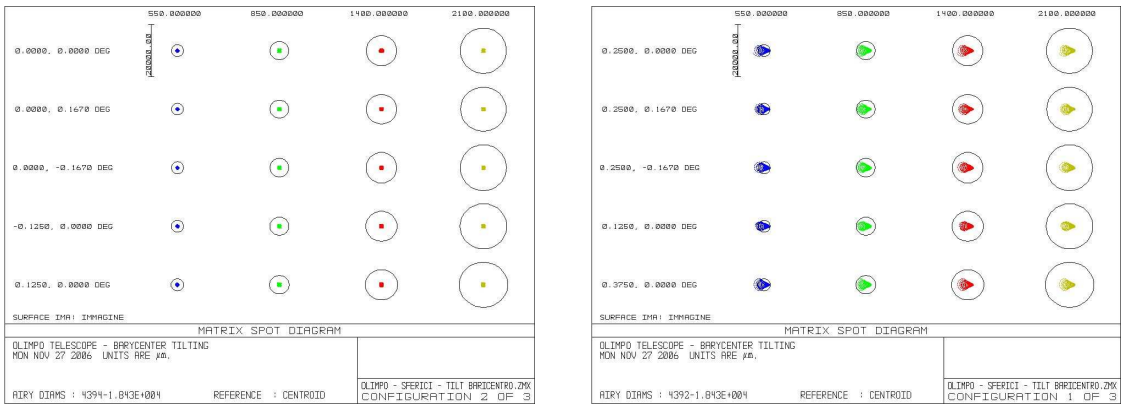

(a) *On-axis spot diagram* (b) *Off-axis spot diagram*

Figure 4.6: *Spots on the image surface using the parameters obtained by fits on mirrors surface. The chosen mirrors are Lyot Stop #2 and tertiary and quinary mirrors #4 and #5.*

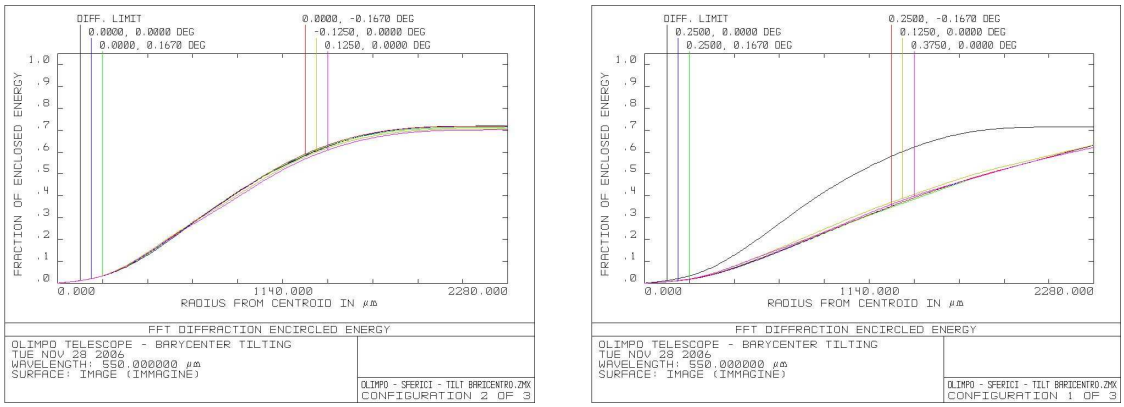

(a) *On-axis encircled energy* (b) *Off-axis encircled energy*

Figure 4.7: *Encircled energy at a wavelength* $\lambda = 550\mu m$ $(\nu = 545 GHz)$ *using the parameters obtained by fits on mirrors surface. Various curves describe the trend for each field of view; the black one represents the diffraction limit. The integration is computed up to the radius of Airy disc at* $\lambda = 550\mu m$.

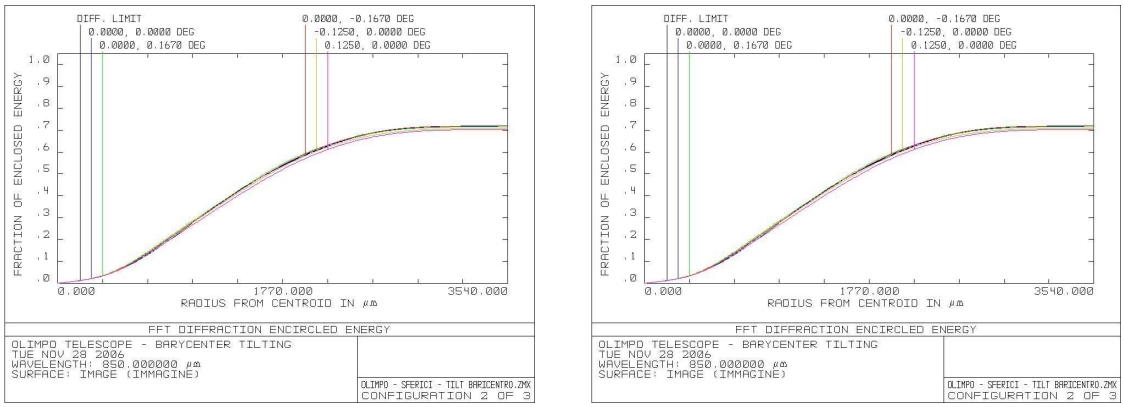

(a) *On-axis encircled energy* (b) *Off-axis encircled energy*

Figure 4.8: *Encircled energy at a wavelength* $\lambda = 850\mu m$ $(\nu = 353GHz)$ *using the parameters obtained by fits on mirrors surface. Various curves describe the trend for each field of view; the black one represents the diffraction limit. The integration is computed up to the radius of Airy disc at* $\lambda = 850\mu m$*.*

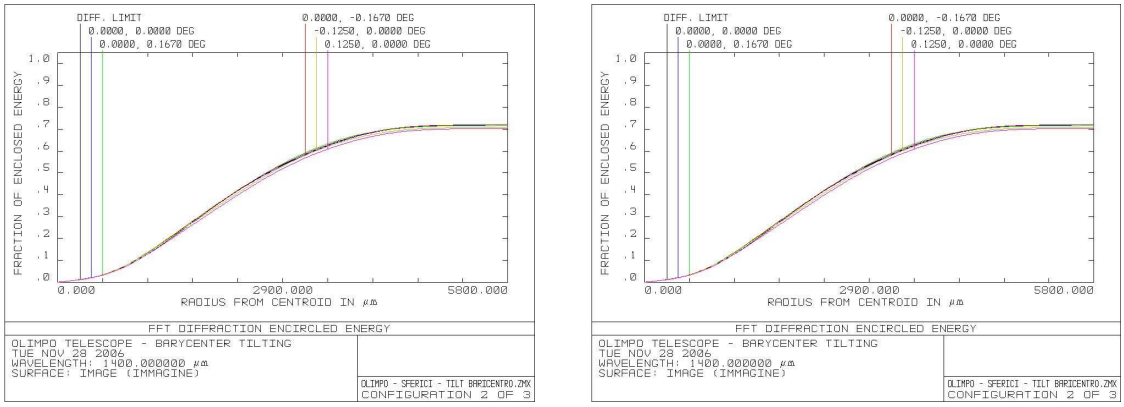

(a) *On-axis encircled energy* (b) *Off-axis encircled energy*

Figure 4.9: *Encircled energy at a wavelength* $\lambda = 1400\mu m$ $(\nu = 217GHz)$ *using the parameters obtained by fits on mirrors surface. Various curves describe the trend for each field of view; the black one represents the diffraction limit. The integration is computed up to the radius of Airy disc at* $\lambda = 1400\mu m$*.*

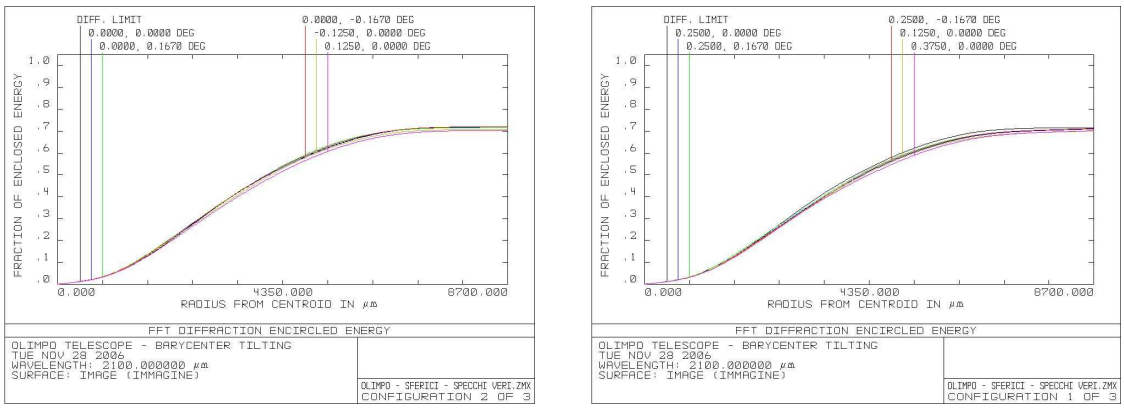

(a) *On-axis encircled energy* (b) *Off-axis encircled energy*

Figure 4.10: *Encircled energy at a wavelength* $\lambda = 2100\mu m$ $(\nu = 143\,GHz)$ *using the parameters obtained by fits on mirrors surface. Various curves describe the trend for each field of view; the black one represents the diffraction limit. The integration is computed up to the radius of Airy disc at* $\lambda = 2100\mu m$.

4.3 Mirrors polishing

The cutting width of the finishing machining process is $\sim 30\mu m$ for the tertiary and quinary mirrors and $\sim 10\mu m$ for the *Lyot Stop*. At millimeter and submillimeter wavelengths this is not an issue, but it prevents to do any sort of test at optical wavelengths. Optical methods are particularly suitable because they can be realized at room temperature, without the necessity of cooling down imposed by microwave measurements. Moreover, the provide a direct, "visual" test of the optical system performance.

Hence, we decided to manually polish the mirrors surfaces using suspensions of polycrystalline diamonds of decreasing diameter: 15, 9, 3 and $1\mu m$. Between each step, the mirror must be cleaned dipping it in an ultrasonic tank filled with isopropyl alcohol. A special polishing cloth is used in order to minimize the abrasion unrelated to diamond suspensions and it is attached to a piece of styrodur: this material is a good compromise between hardness and flexibility to follow the shape of the surface. The polishing procedure can be split into four cycles, each of which is subdivided into four steps:

1. The mirror is mounted on an appropriate stand; a small piece of *Buehler ULTRA-POL* polishing cloth is attached to the styrodur support.

2. *Buehler METADI SUPREME* polycrystalline diamond suspension of $15\mu m$ is sprayed on the mirror and the polishing procedure starts; if necessary, the suspension is sprayed more times: this step requires $\sim 60min$ for tertiary and quinary mirrors, $\sim 10min$ for a *Lyot Stop*.

3. The mirror is cleaned with water to remove most of the polishing residuals, then it is placed inside an ultrasonic tank filled with isopropyl alcohol: this solution removes all the small residuals of a polishing step.

4. After $\sim 5min$ in the ultrasonic tank, the mirror is dried with compressed air, avoiding the use of paper which can leave impurities.

Once finished the first cycle, the machining groves are not visible anymore and only casual grooves are present. The procedure starts again from the first point changing the suspension to $9\mu m$; the third and forth cycles (3 and $1\mu m$ suspensions respectively) use the *Buehler TRIDENT* polishing cloth, which has a lower roughness with respect to the *ULTRA-POL*.

The result we want to obtain is a random surface roughness, i.e. without the machining grooves, with a maximum width of $\sim 1\mu m$ and a *r.m.s.* value of $\sim 0.1\mu m$. Before presenting the results of the roughness measurements we carried out, we introduce a simple theory of the effect of surface roughness in optical measurements.

4.3.1 Theory of surface roughness

Surface roughness is the standard deviation of the real profile from the theoretical one, measured on scales much smaller than the dimensions of the surface. Furthermore, periodic grooves remain on materials machined with lathes or milling cutters: in the case of radiation of appropriate wavelength, they behave like a low efficiency diffraction grating. Together with this regular component, there is a casual one due to vibrations of the cutting tool and irregularities in the material. The roughness can be subdivided into three components:

1. Regular, periodic, unidimensional component.

2. Casual, unidimensional component.

3. Casual, bidimensional component.

The simplest method of measuring the surface roughness consists in using a probe similar to the gramophone needle: it moves on the surface measuring its profile. The drawback is that it scratches the surface; moreover, the measure is unreliable on curved surfaces.

Another method consists in studying the Kirchhoff diffraction, i.e. the pattern of the incident radiation scattered by the mirror at a far distance. The quantity that describes the scattered radiation is the *Bidirectional Reflectance Distribution Function* $BRDF = f(\vartheta_i, \varphi_i; \vartheta_s, \varphi_s)$, which is a function of the radiation wavelength and of the incidence and scattering angles (subscripts i and s respectively). If we suppose to illuminate with a plane wave a small portion of the mirror, so that it can be considered flat, the intensity of the light scattered into the solid angle element $d\Omega_s$ is [19, 117]:

$$\left(\frac{dI}{d\Omega}\right)_s d\Omega_s = I_i \, f \cos\vartheta_s \, d\Omega_s \tag{4.7}$$

where I_i is the total incident intensity and $d\Omega_s = \sin\vartheta_s \, d\vartheta_s \, d\varphi_s$. The $BRDF$ is generally a complicated function: in the case of a strong specular reflection characterized by a narrow diffraction cone, the reflected intensity I_r is equal to the incident intensity I_i multiplied

by the Fresnel intensity coefficient $R(\vartheta)$ of the surface: $I_r = I_i \cdot R(\vartheta)$. The leading term in the expansion of the *BRDF* outside the specular cone is:

$$f = 4\,k^2 \cos\vartheta_i \cos\vartheta_s\, Q\, W(p,q) \tag{4.8}$$

where $k = 2\pi/\lambda$, Q depends on the surface material and W is the bidimensional power spectral density of the surface roughness, which contains the entire dependence of the scattering on the topography of the source. W is a function of the deviation $\mathcal{Z}(x,y)$ of the surface contour from its average. For a square scatterer of side $2L$ it is:

$$W(q,p) = \frac{1}{(2L^2)} \left| \frac{1}{2\pi} \int_{-L}^{+L} \int_{-L}^{+L} e^{i(px+qy)}\, \mathcal{Z}(x,y)\, dx\, dy \right|^2 \tag{4.9}$$

W is seen to be the square magnitude of the bidimensional Fourier transform of the surface contour at wavenumbers p and q: these can be viewed as the x and y components of the momentum given by the scattered photons by the surface roughness, and $W(p,q)$ is the "strength" of those components. The connection between p and q and the scattering angles are given by:

$$p = k\,(\sin\vartheta_s \cos\varphi_s - \sin\vartheta_i) \tag{4.10a}$$

$$q = k\,(\sin\vartheta_s \sin\varphi_s) \tag{4.10b}$$

The factor Q contains the dependences of the scattering on the permittivity of the surface material and the incident and final states of polarization of the radiation. In the limit of small scattering angles, Q equals the Fresnel intensity reflection coefficient of the surface. Hence, the scattering theory result permits to determine the power spectral density, which is purely a function of the surface topography.

It is important for practical purposes to characterize the properties of the surface topography deduced from scattering measurements in terms of quantitative roughness parameters. The most important of them is the surface height variance, i.e. the zeroth moment of the power spectral density:

$$\sigma^2 = \int_{-\infty}^{+\infty} \int_{-\infty}^{+\infty} W(p,q)\, dp\, dq = \frac{1}{(2L)^2} \int_{-L}^{+L} \int_{-L}^{+L} \mathcal{Z}^2(x,y)\, dx\, dy \tag{4.11}$$

Periodic roughness

As already pointed out, machined surfaces show a highly structured surface topography, the most conspicuous feature of which is the presence of periodic tool marks. If the machined grooves are taken to be parallel to the y axis, their contribution to the total surface roughness may be expanded in Fourier series:

$$\mathcal{Z}(x,y) = \sum_{n=1}^{\infty} a_n \cos\left(2\pi\,\frac{nx}{d} + \psi_n\right) \tag{4.12}$$

where d is the fundamental period of the tool marks. If the size of illuminated area is much larger than the period ($2L \gg d$), thus ensuring adequate sampling, the spectral density becomes:

$$W(p,q) = \frac{1}{4} \sum_{n=1}^{\infty} a_n^2\, \delta\left(p \pm 2\pi\,\frac{n}{d}\right) \delta(q) \tag{4.13}$$

where $\delta(z) = L\sin^2(Lz)/(\pi Lz)^2$ is the characteristic diffraction line shape of the square scatterer. The detector aperture must be large enough to average over unwanted detail in the scattering spectrum, but small enough to preserve information about the structure of the surface power spectral density.

The form of W given by eq. (4.13) shows that the scattering from periodic surface roughness is bunched into discrete regions of the scattering spectrum at positions given by the familiar grating equation $\sin\vartheta_s = \sin\vartheta_i + N\lambda/d$. The integrated intensities of these diffraction lines are seen to be proportional to the square of the amplitudes a_n of the harmonics of the surface contour. In the perturbation limit of small grating amplitudes, each harmonic diffracts only to first order and there is a one to one correspondence between the intensity of the n^{th} diffraction line and the amplitude of the n^{th} harmonic of the surface contour. However, all informations about the phase angles is lost, so it is impossible to reconstruct the original contour from scattering data alone.

Random roughness

It can be viewed as a superposition of a large number of surface periods which have no simple relationship between each other. These lead to scattering in the form of diffraction spots or lines which are more or less continuously distributed in the scattering spectrum (*speckle*), rather than being bunched into well separated and intense peaks as for the periodic component.

The distribution of the intensity contains detailed information about the roughness of the surface examined. We do not need any particular detail, but want to extract only general features of the scattering spectrum. This is done by smoothing the scattering spectrum with a detector aperture which is large compared to the speckle size but small compared to the important structural features of the smoothed spectra.

The contribution of the random unidimensional roughness to the total power spectrum of the surface may be separated in the form $W(p,q) = W(q)\cdot\delta(q)$. For a finite turning radius the factor δ is factorized out; instead, the form of $W(p)$ must be determined empirically for the surface of interest. Usually, it can be expressed as:

$$W(p) = \frac{1}{\pi}\,\frac{\sigma_1^2\, l_1}{1+(l_1\,p)^2} \tag{4.14}$$

where σ_1 is the vertical *r.m.s.* roughness and l_1 is the transverse length of the surface. When $(l_1 p) \gg 1$ the small scattering angle approximation implies:

$$W(p) \simeq \frac{1}{\pi}\,\frac{\sigma_1^2}{k^2\, l_1}\,\frac{1}{(\vartheta_s-\vartheta_i)^2} \tag{4.15}$$

Machined surfaces also show a bidimensional random roughness, which is the only component expected for conventional polished surfaces. Its contribution to the total power spectral density can be written as $W(p,q) = W(r)$ with $r = \sqrt{p^2+q^2}$. The bidimensional analogue of eq. (4.14) is:

$$W(r) = \frac{1}{2\pi}\,\frac{\sigma_2^2\, l_2^2}{[1+(l_2\,r)^2]^{3/2}} \tag{4.16}$$

When $(l_2^2 r)^2 \gg 1$, eq. (4.16) approximates as:

$$W(r) \simeq \frac{1}{2\pi} \frac{\sigma_2^2}{k^3\, l_2} \frac{1}{|\vartheta_s - \vartheta_i|^3} \tag{4.17}$$

It is worth noting that the contribution of unidimensional roughness to the total scattering falls off as the second power of the scattering angle away from the specular direction, while the contribution of bidimensional roughness falls off as the third power.

4.3.2 Measuring setup and results

As already described in § 4.3.1, a first measuring method consist in using a probe similar to the gramophone needle. We used the *Federal Pocket Surf* surface roughness tester, which has a resolution of $0.01\mu m$; it can measure the peak to peak amplitude or the *r.m.s.* value of along the path. If the probe covers a length l_m along the x direction, the computed *r.m.s.* roughness is:

$$\sigma_{rms} = \sqrt{\frac{1}{l_m} \int_0^{l_m} \mathcal{Z}^2(x)\, dx} \tag{4.18}$$

The results range from $\sigma_{rms} \simeq 7\mu m$ ($\sigma_{pp} \simeq 30\mu m$) for the finishing machined surface to $\sigma_{rms} \simeq 0.1\mu m$ ($\sigma_{pp} \simeq 1\mu m$) for the $1\mu m$ polishing.

Studying Kirchhoff diffraction involves scatterometers, which are made of three basic elements: a light source, the scatterer and a detector. We used a monochromatic $\lambda = 633nm$ He−Ne laser as source, thus minimizing chromatic aberrations and reducing the illuminated area. Mirrors are positioned near the laser so the illuminated area can be considered flat and the incident and reflected angles are equal to 45°. Light is then recollected by a photodiode and produces an electric signal that can be easily analyzed. The detector is mounted on a motorized controlled sledge in order to evaluate the whole scattering pattern (see Fig. 4.11).

The scattered intensity I_s is the integral over the detector aperture of the differential scattered intensity $(dI/d\Omega)_s$ defined in eq. (4.7); in the limit of small aperture of area A this gives:

$$I_s(\vartheta_i; \vartheta_s, \varphi_s) = I_i \cdot 4\, k^2 \cos\vartheta_i \cos\vartheta_s\, Q \iint_A W(p,q)\, dp\, dq \tag{4.19}$$

where the angles on the left are those of the center of the aperture and the integral on the right is taken over the aperture itself. The evaluation of the aperture integral depends on the class of surface roughness being examined. Given the geometry used in our setup, it is useful to express the scattered angle as $\vartheta_s = 45° \pm \xi$, while $\vartheta_i = 45°$. Hence, eq. (4.19) becomes:

$$\frac{I_s(\xi)}{I_r} = 2\, k^2 \cos(2\xi)\, \frac{Q(\xi)}{R(45°)} \iint_A W(p,q)\, dp\, dq \tag{4.20}$$

where we used the relation $I_r = I_i \cdot R(\vartheta)$ introduced in § 4.3.1; the aperture integral is centered around the wavenumbers $p = -\sqrt{2}\, k \sin\xi$ and $q = 0$. It is worth noting that in the limit of small scattering angles ($\xi \ll 1$), $R(45°) \simeq Q$.

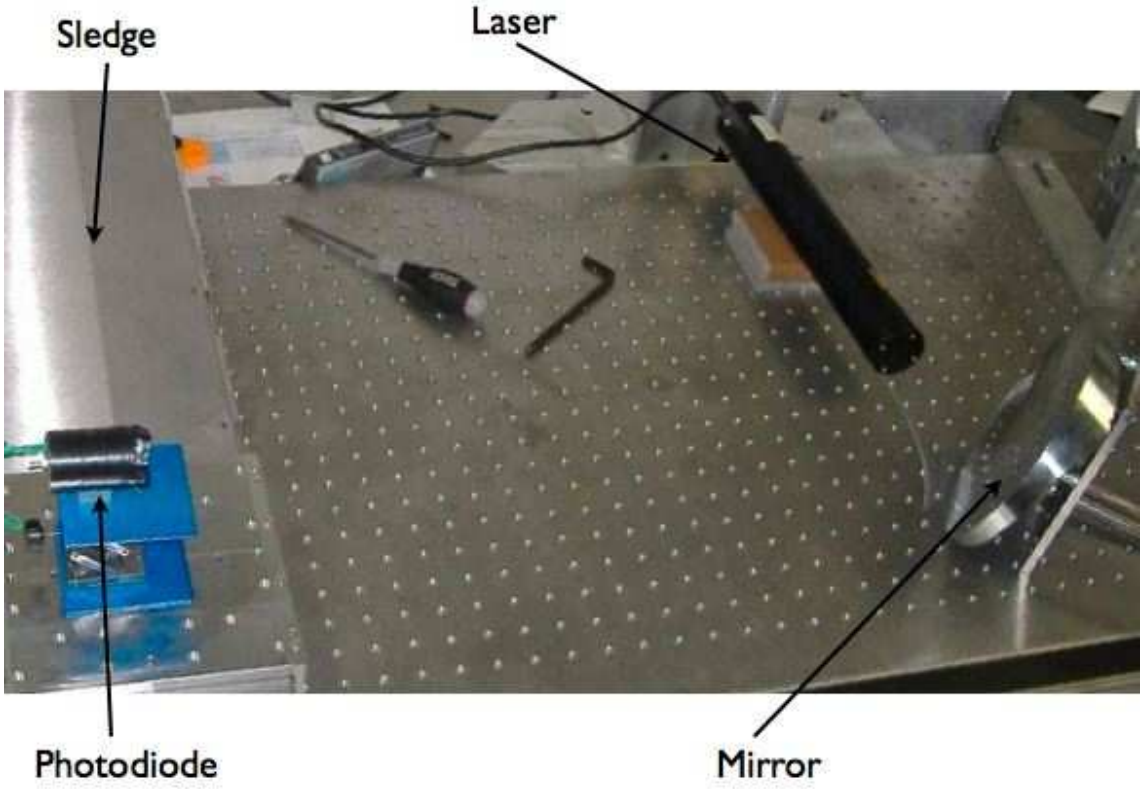

(a) *Measurements setup*

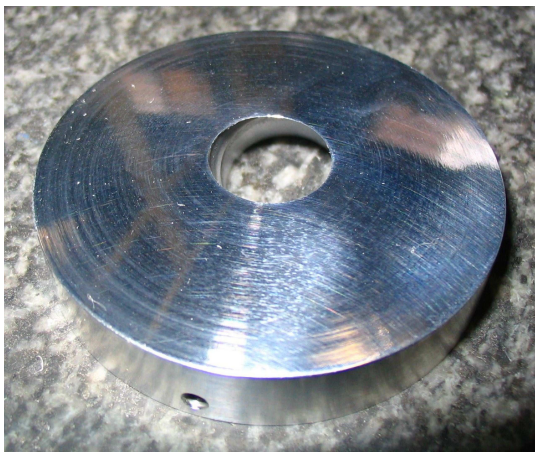

(b) *Lyot Stop before polishing*

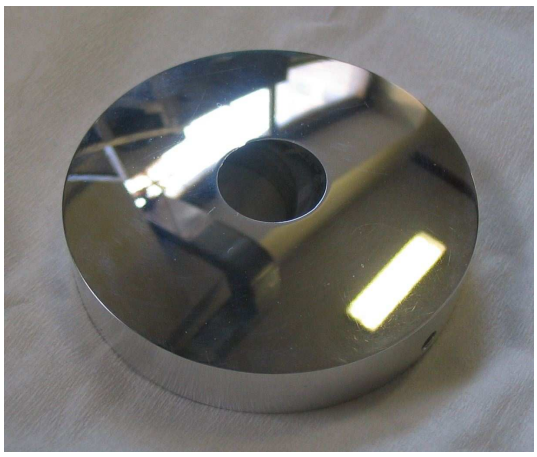

(c) *Lyot Stop after polishing*

Figure 4.11: *Roughness measurements: the setup, the Lyot Stop surface before and after polishing are shown.*

In the case of periodic roughness, substituting eq. (4.13) into eq. (4.20) the integrals over the δ functions may be carried out immediately. The results show that the diffraction peaks are located at discrete angles ξ_N given by:

$$\sin \xi_N = -\frac{N}{\sqrt{2}} \frac{\lambda}{d} \tag{4.21}$$

where d is the fundamental period of the tool marks. Hence, the positive and negative orders of a given order number $n = |N|$ appear at equal and opposite values of ξ and the successive orders are approximately linearly spaced in ξ.

Unidimensional roughness can be analyzed using eq. (4.20) and remembering that $W(p, q) = W(q) \cdot \delta(q)$, which lead to:

$$W(\xi) = \frac{I_s(\xi)}{I_r} \cdot \frac{1}{k^3 \sqrt{2}} \cdot \frac{1}{\Delta} \cdot \frac{R(45°)}{Q(\xi)} \cdot \frac{(1 + \tan \xi)^{-1}}{\cos \xi \cos(2\xi)} \tag{4.22}$$

where Δ is the transverse angular width of the detector aperture in radians. Finally, from eq. (4.11) we get the expression for the height and slope variances:

$$\sigma^2 = \sqrt{2}\, k \int W(\xi) \cos \xi \, d\xi \tag{4.23}$$

We used two setups for the measurements: the first is based on modulating the radiation by means of a chopper, so that the electric signal can be measured using a lock-in, thus significantly decreasing the noise (see § 2.2); the second setup makes a continuos data acquisition. All the mirrors in each of the five "states" (finishing machining, polishing till 15, 9, 3 and $1\mu m$) are measured with these two setups and the results are consistent.

Figs. 4.12 and 4.13 show the scattered radiation as a function of the angle $\xi = \arctan(x/l)$, where $l = 795 \pm 1mm$ is the distance between the mirror and the photodiode and x the position of the receiver on the sledge, referred to the maximum. Peaks are normalized to unity so that it is easier to see how the tails drop down as the roughness decreases.

Five measurements are taken on each mirror, one on the center and four near the edge: the average values are reported in Tabs. 4.3.

4.4 Optics box

A great part of this thesis work consisted in projecting, designing and manufacturing the optics box that will contain all the elements thermally linked to the ^{4}He bath: reimaging mirrors, beam splitters, filters, horns and receivers, together with the ^{3}He fridge. All the executive drawings are reported in App. A; all parts were machined by Cecom S.n.c. The optics box is designed to satisfy the following requirements:

- It must fit inside the ^{4}He *Shield*, a cylinder having inner diameter $D = 478mm$ and thickness $1mm$ (see Fig. A.13); on this shield, it is welded the mounting ring of the $2K$ filter (see Fig. A.12).

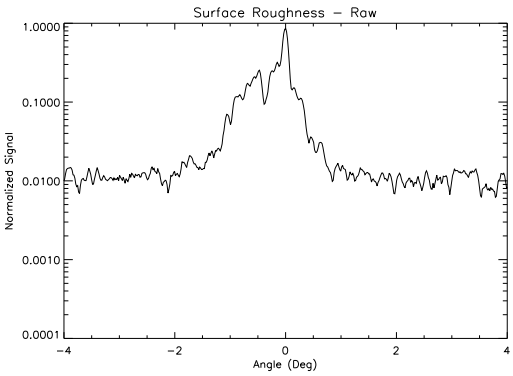

(a) *Machined surface scattering pattern*

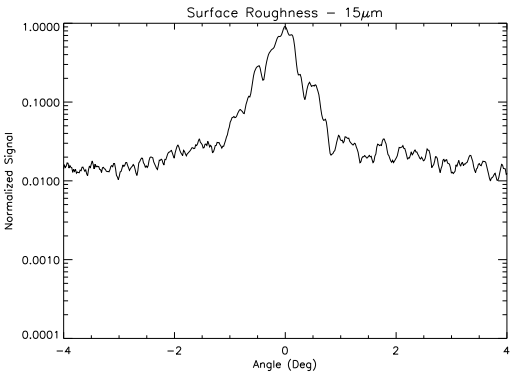

(b) 15μm *surface polishing scattering pattern*

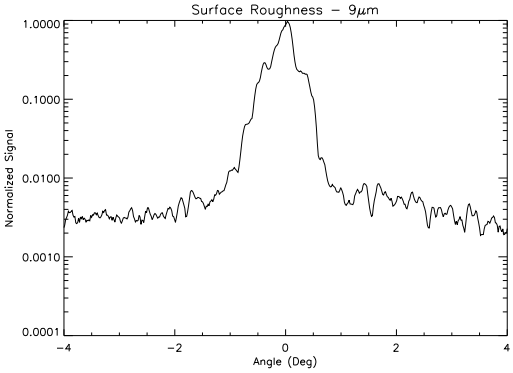

(c) 9μm *surface polishing scattering pattern*

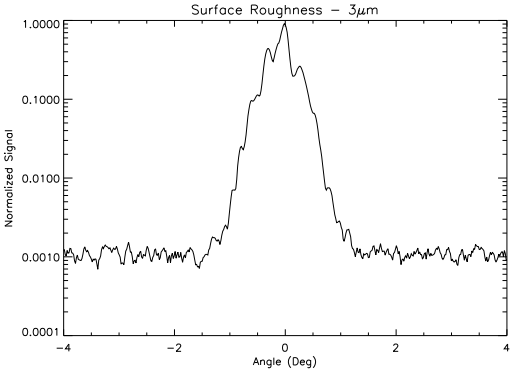

(d) 3μm *surface polishing scattering pattern*

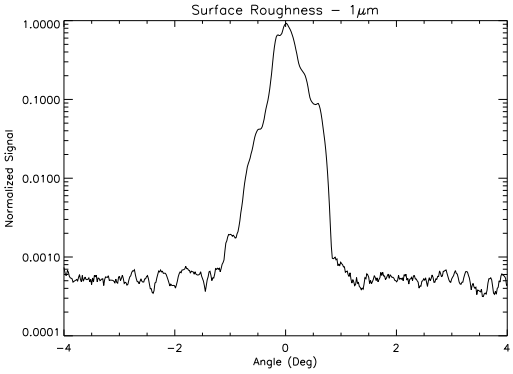

(e) 1μm *surface polishing scattering pattern*

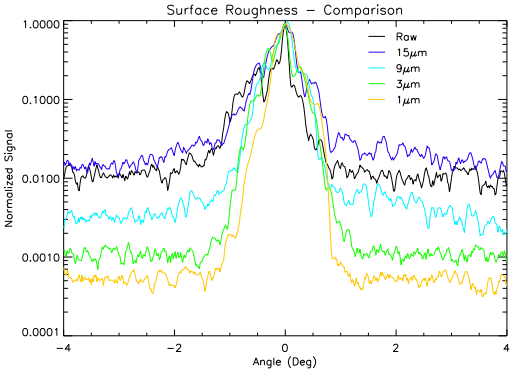

(f) *Comparison between scattering patterns*

Figure 4.12: *Patterns of scattered radiation due to surface roughness of the Lyot Stop, after the different polishing steps. It is worth noting that the peak is broad, because the Lyot Stop diverges the beam, and that the* 15μm *pattern is worse than the one related to machined surface: this demonstrates that the initial roughness was less than* 15μm.

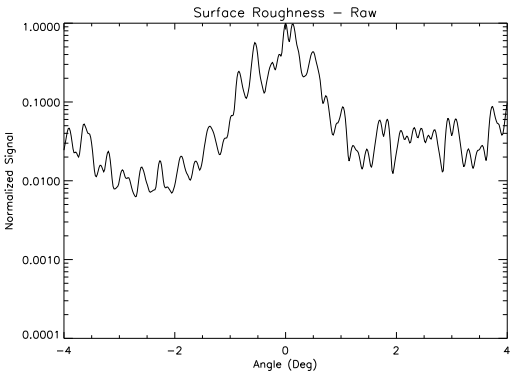

(a) *Machined surface scattering pattern*

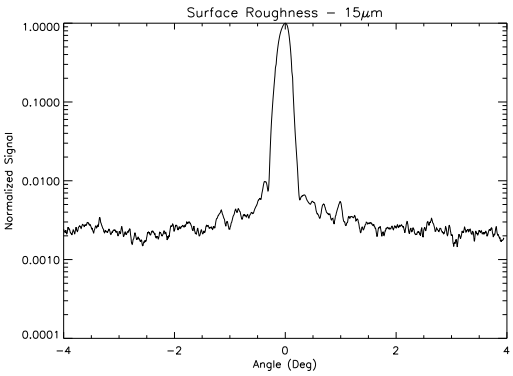

(b) $15\mu m$ *surface polishing scattering pattern*

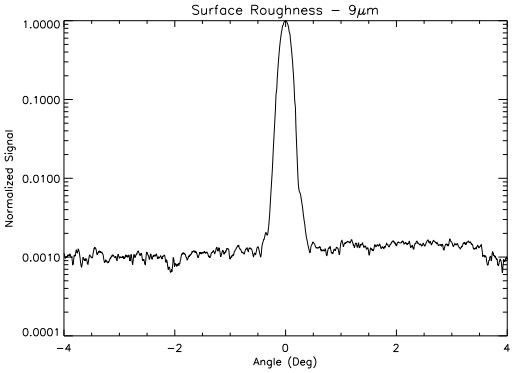

(c) $9\mu m$ *surface polishing scattering pattern*

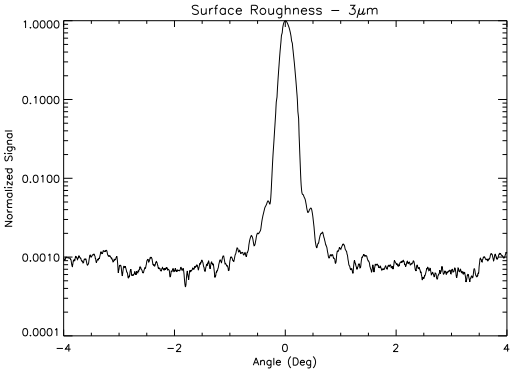

(d) $3\mu m$ *surface polishing scattering pattern*

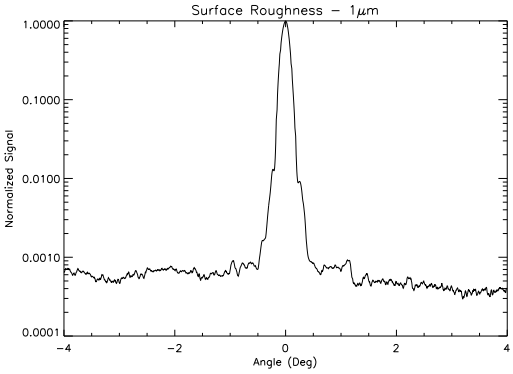

(e) $1\mu m$ *surface polishing scattering pattern*

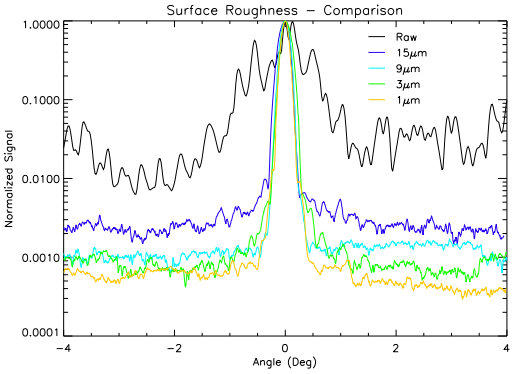

(f) *Comparison between scattering patterns*

Figure 4.13: *Patterns of scattered radiation due to surface roughness of the tertiary and quinary mirrors, after the different polishing steps. It is worth noting that the peak is narrow, because the mirror concentrates the beam.*

	Raw	$15\mu m$	$9\mu m$	$3\mu m$	$1\mu m$
Mirror #1	7.82 ± 0.73	5.32 ± 0.54	3.95 ± 0.18	0.485 ± 0.062	0.115 ± 0.015
Mirror #2	7.55 ± 0.77	5.43 ± 0.59	3.24 ± 0.13	0.454 ± 0.066	0.121 ± 0.017
Mirror #3	7.12 ± 0.71	5.39 ± 0.51	3.12 ± 0.15	0.419 ± 0.063	0.118 ± 0.013
Mirror #4	6.94 ± 0.75	5.32 ± 0.49	2.81 ± 0.13	0.393 ± 0.060	0.108 ± 0.011
Mirror #5	7.03 ± 0.70	5.35 ± 0.47	3.01 ± 0.11	0.401 ± 0.059	0.102 ± 0.010
***Lyot Stop* #1**	5.35 ± 0.57	5.25 ± 0.51	3.44 ± 0.15	0.454 ± 0.066	0.123 ± 0.016
***Lyot Stop* #2**	5.48 ± 0.53	5.32 ± 0.53	3.11 ± 0.11	0.485 ± 0.062	0.105 ± 0.011
***Lyot Stop* #3**	5.42 ± 0.51	5.40 ± 0.49	3.52 ± 0.19	0.419 ± 0.063	0.119 ± 0.018

Table 4.3: *R.m.s. roughness in μm for the eight mirror samples: first column reports the average values obtained from machined mirrors, the other refer to mirrors polished with diamond suspensions of different grain size. It is worth noting that the machined Lyot Stop had a better surface roughness than the other machined mirrors.*

- Distances between *Lyot Stop*, tertiary and quinary mirrors must be the ones decided with the optical optimization: this is achieved reducing as much as possible the number of mirror holders. The elements *Reggetta Plane* (see Fig. A.17) set the horizontal distance between *Lyot Stop* and the other two mirrors; moreover, all the other elements (calibration lamp, dichroics and horns holders) are attached to it, so that this element is a sort of "optical bench". Tertiary and quinary mirrors are mounted on the same strap (*Reggetta Mirrors*, see Fig. A.16), which ensures the correct vertical distance.

- The element ^{4}He *Cover* is attached to the ^{4}He tank: apart from the fridge, it gives the thermal link and sustains the whole system. ^{4}He *Cover*, *Reggetta Plane*, *Reggetta Mirrors* and *Splitter Plane* #1 are connected to form a rectangular box: hence, this design establishes the correct positioning between mirrors.

- All the holder elements are made of the same aluminum alloy the mirrors are made of: Ergal 7075. This guarantees that all the parts behave in the same way when cooling. The thinner parts, mainly shields, are made of Peraluman 5754.

- The fridge is mounted to the ^{4}He by means of its own strap, *Fridge Cover* (see Figs. A.8 and A.9), made of *Oxigen Free High Conductivity* (OFHC) copper. This solution has two advantages: OFHC copper has a thermal conductivity much higher than aluminum, which is of fundamental importance for the ^{3}He cooling cycle; furthermore, it permits to dismount the whole optics box without uninstalling the fridge.

- The optical axes of the four channels of *OLIMPO* are at 90° from each other, thus dichroics must be tilted at 45°: this is achieved using the *Splitter Plane* #1, #2, and

#3 (see Figs. A.22, A.23 and A.24). The main complication resides in the dimensions of the ring that holds the beam splitters, which is 20% larger than the dichroics diameter ($120mm$ for an effective diameter of $100mm$) and has a total thickness of $25mm$ ($20mm$ for the ring itself, plus $5mm$ for the holders of the splitter planes). Using an on-axis configuration, the three rings would touch: the solution is to move the two second dichroics orthogonally to incident radiation, which is allowed because they are underilluminated. Finally, the dichroics must be mounted on the splitter planes using only three fastening points, hence the use of single clamps.

- The four horn arrays and pass band filters will be mounted on the *Box* $10mm$ #1 ($143GHz$ channel), #2 ($353GHz$ channel) and on the *Reggetta Plane* ($217GHz$ and $545GHz$ channels). The horn arrays, shown in Figs. 5.10 and fig:horns:1400, will be made of OFHC copper and cooled down to $300mK$: consequently, they must be thermally insulated by means of kevlar strings or vespel bars.

- *Reggetta In* (see Fig. A.15) will hold a motorized neutral density filter. This is necessary for ground tests since, as described in § 2.4, bolometers are optimized for balloon measurements. During ground tests the background would be too high.

- All the elements have a rib structure which minimizes the total weight keeping the stiffness. The whole system has a mass of $\sim 20kg$: since it must resist $10g$ vertical accelerations, a detailed stress analysis has been done for the ^{4}He *Cover*, which will support all the optics box. The results, shown in Fig. 4.14, reveal that ^{4}He *Cover* would suffer a maximum deformation of $0.198mm$.

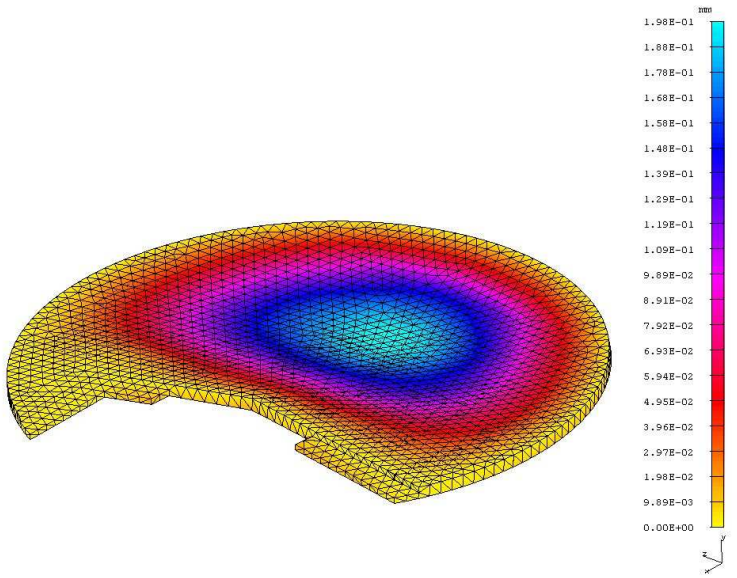

Figure 4.14: *Stress analysis on the* ^{4}He *Cover. Considering that the whole optics box, mirrors and horns weight* $\sim 20Kg$*, applying a vertical acceleration of 10g and imposing that the edge of* ^{4}He *Cover is screwed on the* ^{4}He *tank bottom, the maximum deformation is* $0.198mm$ *in the center.*

- The whole optics box is closed and painted using absorbing microwave material, such as lampblack loaded stycast epoxy. Only the radiation reflected by the mirrors and passing through the dichroics can reach the detectors. In particular, *Shield Dx Sup*, *Shield Dx Inf*, *Shield Sx*, *Box* 1*mm* #1 and *Reggetta Bottom* shield from fridge and unwanted incoming radiation; *Shield Lyot Stop* and the thin layer on the *Reggetta Plane* select only rays coming from the portion of sky observed; finally, *Box* 1*mm* #2 and *Splitter Plane* #1, #2 and #3 themselves shield the receivers from stray light and contamination from the other channels.

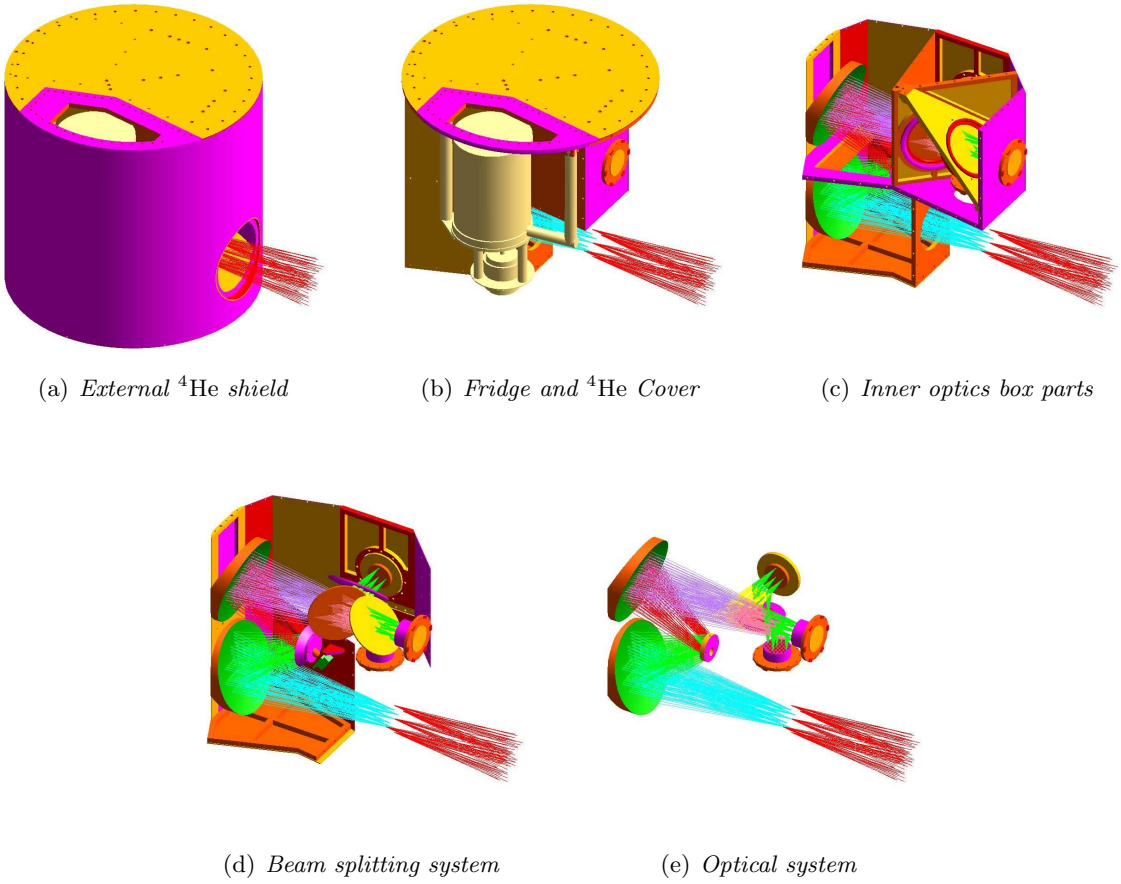

(a) *External* ^{4}He *shield* (b) *Fridge and* ^{4}He *Cover* (c) *Inner optics box parts*

(d) *Beam splitting system* (e) *Optical system*

Figure 4.15: 3*D design of the optics box: it is shown the whole system and its inner elements, together with the* ^{3}He *fridge.*

4.5 Alignment tests

The last test made at room temperature is the alignment of the optics box and of the mirrors. The optics box is designed so that every part, including mirrors, must fit in the proper way: there are no adjustable parts. The advantage is that the is no danger of losing the alignment during transportation or launching of the experiment; the drawback is that it would be very difficult to fix any misalignment.

(a) *External* ^{4}He *shield*

(b) *Optics box: right view*

(c) *Optics box: left view*

(d) *Optics box: back view*

Figure 4.16: *Pictures of the optics box: external shields. It is also shown the two copper bars that will sustain the* ^{3}He *fridge. The whole optics box will be mounted upside down.*

(a) *Splitting system*

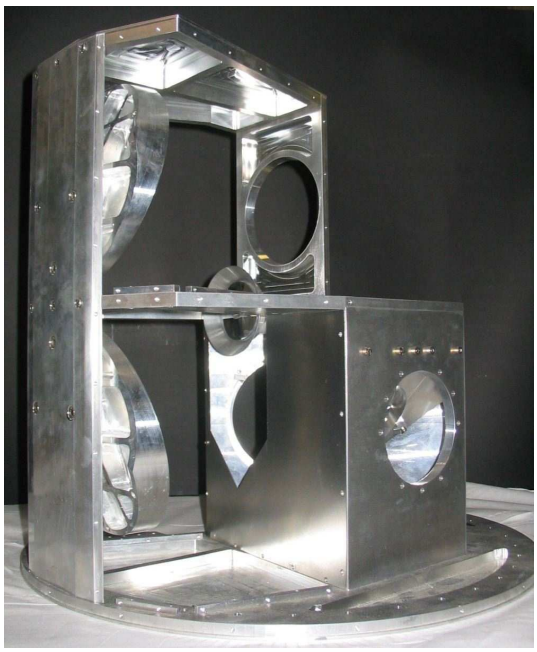

(b) *Internal shielding*

(c) *Optical system: front view*

(d) *Optical system: back view*

Figure 4.17: *Pictures of the optics box: internal shields. Around the Lyot Stop and between the quinary and the first dichroic are mounted shields which prevent stray light to reach the focal plane.*

The use of high accuracy, controlled numerical milling cutters strongly reduces possible misalignments. Despite of this, it is fundamental to verify the correct positioning of every element: this is achieved making two tests, one mechanical and one optical.

The first test uses the same tridimensional measuring machine *Poli Galaxy Diamond* used to verify the machined mirrors (see § 4.2). In particular, we measured the angles between *Reggetta Plane* and *Reggetta Mirrors*, which is fundamental since it defines the distance between the *Lyot Stop* and the tertiary and quinary mirrors. The other angles checked are those between the *Reggetta Plane* and the three *Splitter Plane*: they define the position and the angle of beam splitting, hence have to be as accurate as possible. The nominal and measured values are reported in Tab. 4.4.

	Reggetta Plane	
	Nominal	**Measured**
Reggetta Mirrors	$90°$	$89° 55' \pm 10'$
Splitter Plane #1	$90°$	$90° 03' \pm 10'$
Splitter Plane #2	$45°$	$45° 05' \pm 30'$
Splitter Plane #3	$45°$	$45° 14' \pm 30'$

Table 4.4: *Measured angles referred to the Reggetta Plane. They are computed using the same tridimensional measuring machine Poli Galaxy Diamond used to verify the machined mirrors* (*see* § 4.2). *The errors, calculated directly by the machine software, depend on the number of samples points: Splitter Planes* #2 *and* #3 *are more difficult to touch with the probe, thus only three points* (*the minimum required to define a plane*) *have been measured.*

The second test consists in simulating the beam coming from the telescope and verifying that it is refocused on the four focal planes. The radiation is generated by the same monochromatic laser He−Ne at $\lambda = 633nm$ used to measure the mirrors surface roughness; then a suitable optical setup, made of a beam expander and a lens (see Fig. 4.18), is used to simulate the $f/\# = 3.45$ of the telescope.

The lens has a diameter $d_{Lens} = 25.4mm$ and a focal distance $f_{Lens} = -75mm$, which is negative because we used a diverging bi-concave spherical lens. Assuming that the incident beam is parallel, i.e. it comes from infinity, the $f/\#$ produced by the lens is $f/\# = f_{Lens}/d$, where d is the portion of lens diameter used: hence, $f/\# \geqslant 2.95$.

The beam expander enlarges the wavefront of the radiation generated by the laser, so that it illuminates the whole lens. Moreover, beam expander should produce parallel rays, but we found that this is not the case in practice. We must conclude that the effective focal distance f_{Eff} of the lens differs from the nominal one; they are related by the equation:

$$\frac{1}{f_{Eff}} = \frac{1}{f_{Beam}} + \frac{1}{f_{Lens}} \tag{4.24}$$

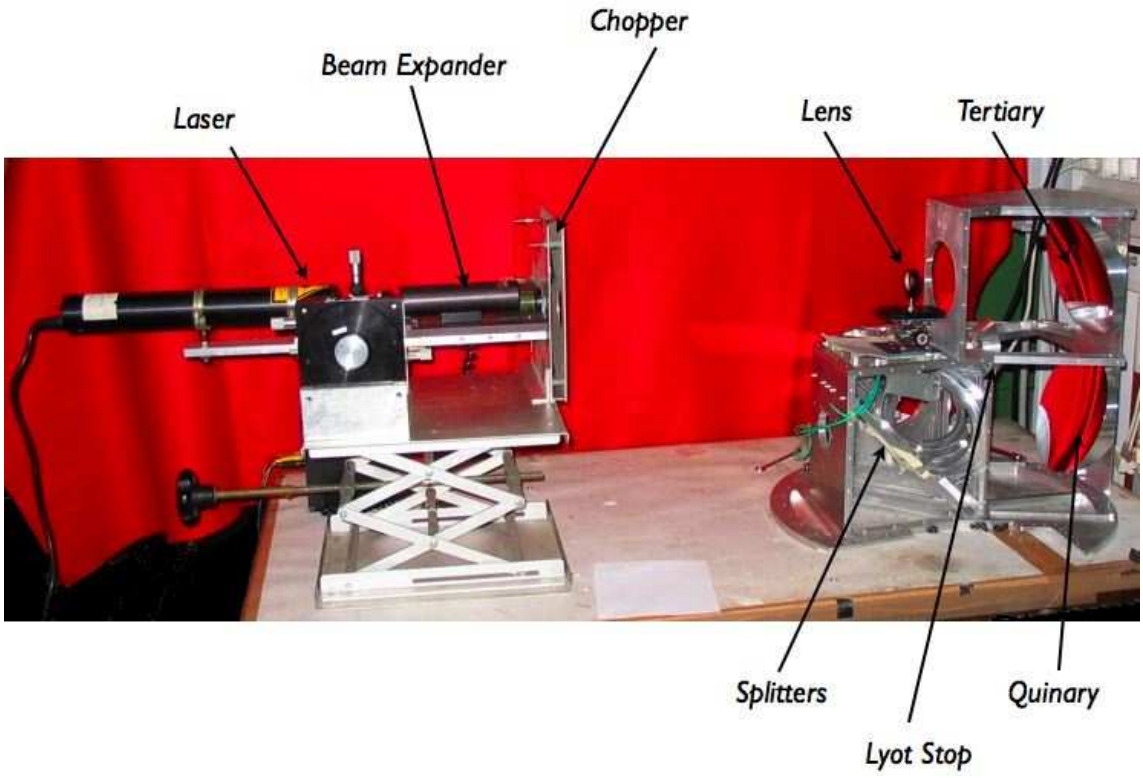

Figure 4.18: *Alignment measuring setup: the lens diverges the radiation coming from the beam expander, which is refocused by the optical system on the four focal plane of the experiment, where the receiver is positioned.*

where f_{Beam} is the focal distance of the beam generated by the beam expander. We measured $f_{Beam} = 1200mm$, which gives $f_{Eff} = -80mm$. However, the imperfection of the beam expander has an advantage: dimension of the beam at its exit is too small to fill the lens diameter; hence, moving the lens far away the expander permits to illuminate its whole surface, obtaining the desired $f/\#$.

Since the telescope focal plane is placed between the ^{4}He window and the *Reggetta In*, all the distances are taken from the latter. A first measurement showed that placing the lens in the nominal position, i.e. $80mm$ from the focal plane, is not the best choice: the dimensions of the spots on the image surface are larger than expected. Consequently, we decided to move the lens back and forward to find the optimal position, that is $2mm$ in the direction of the *Reggetta In*, hence an offset that can be adjusted when integrating the cryostat and the telescope.

The following measurements consist in verifying the refocusing properties at the edge of the telescope focal plane and on the four image surfaces; moreover, we want to characterize the total field of view, which is limited by the dimensions of the beam splitters. These results are reported in Tab. 4.5

	Signal (mV)			
	$143\,GHz$	$217\,GHz$	$353\,GHz$	$545\,GHz$
Field #1	59.92 ± 0.11	56.19 ± 0.19	54.14 ± 0.13	55.45 ± 0.18
Field #2	60.91 ± 0.15	56.77 ± 0.16	50.69 ± 0.19	56.49 ± 0.14
Field #3	67.24 ± 0.13	51.19 ± 0.13	49.54 ± 0.12	55.78 ± 0.19
Field #4	60.58 ± 0.12	50.22 ± 0.11	56.54 ± 0.10	51.22 ± 0.13
Field #5	56.28 ± 0.10	51.16 ± 0.14	50.11 ± 0.15	53.31 ± 0.11

Table 4.5: *Alignment and refocusing tests results. For reference, the signal obtained observing directly the laser is* $109.22 \pm 0.14 mV$*: note that this is obtained without the beam expander and the lens, which scatter a lot of radiation. Hence, the efficiency of the optical system is very high even at optical wavelength. The coordinates of the five fields are described in* Tab. 3.1.

Chapter 5

Focal plane design

An expert is one who knows
more and more about less and less,
until he knows everything about nothing.

Max Weber

Geometrical Optics deals with radiation in the limit $\lambda/D \to 0$, i.e. small wavelength if compared to the typical dimensions D of the optical elements. Starting with the basic rules of propagation of rays, this theory includes rigorous and complete methods for analyzing an optical system having elements (such as lenses, mirrors or apertures) large enough with respect to the wavelength.

At the opposite corner is *Diffractive Optics*: diffraction is the tendency of source radiation to change its distribution as the distance from the source varies. When the dimensions of the optical components are much smaller than the wavelengths ($\lambda/D \to \infty$), diffraction effects dominate the propagation of radiation: this is the case of the near field of an aperture or antenna. In this situation, a complex formalism to analyze characteristics of the beam is required, and performing accurate computations is time-consuming and sometimes impossible.

When the dimensions of the optical components and radiation wavelengths are comparable ($\lambda \sim D$), beam propagation can be studied using *Gaussian Optics* or *Quasioptical Physics*. This theory uses the formalism of *Gaussian Beam*, taking in consideration diffractive effects and wavelengths dependance, while it is still a fast computing method. Quasioptics converges to geometrical optics in the limit $\lambda \to 0$.

As seen in § 2.4, from far infrared to millimeter bands, experiments use receivers that integrate the incident signal, instead of measuring the energy and direction of each photon: these experiments do *non-imaging photometry*. Given the very small energy of photons, it is more important to concentrate incoming radiation on the receiver as much as possible, even at the cost of loosing information on the photons origin: this is achieved using feed horns.

The design of horns that will be used in *OLIMPO* experiment has been done using Gaussian beam analysis, because the dimensions of antennas and waveguides are com-

parable to radiation wavelengths in each band. As it will be shown in this chapter, the characteristics of the feed horn define how the beam propagates. The analysis consists in propagating the beam from the horn to the *Lyot Stop* and studying its energy distribution and angular resolution as a function of horn characteristics.

5.1 Gaussian beam propagation

Let us consider a beam that propagates from a starting point S along the z direction. In the geometrical optics approximation, the beam is characterized in each point P by a radius of curvature R and a beam half width ω. The former is equal to the distance between S and P, while $\omega = R \cdot \sin\alpha$ where α is the angle of divergence of the beam (see Fig. 5.1).

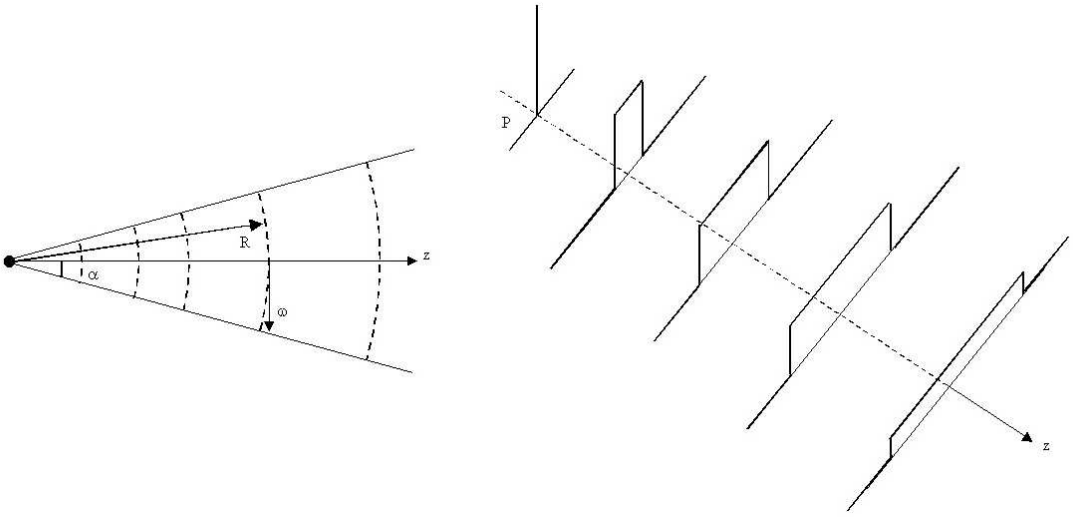

Figure 5.1: *Geometric beam propagation: the radiation starts from a point and the wavefront has a "step" shape.*

In Gaussian optics, the electrical field of a beam propagating along the z direction has a Gaussian distribution along the axes perpendicular to z. In each propagation point, a Gaussian beam is characterized by a beam width (*beam radius*), equal to the distance from the axis of propagation where the electric field is $1/e$ of its maximum (see Fig. 5.2). It is also possible to define a beam radius of curvature R, which defines the equiphase surfaces of radiation: in the limit of far field, $R \to \infty$, the radius of curvature characterizes the distance between the origin and the point of interest. Moreover, a Gaussian beam cannot be neither focused nor have origin in a single point: it propagates from a region of minimum dispersion called *beam waist*, whose dimensions depend on wavelengths. A Gaussian beam is assumed to have an infinite radius of curvature in the beam waist (see Fig. 5.2).

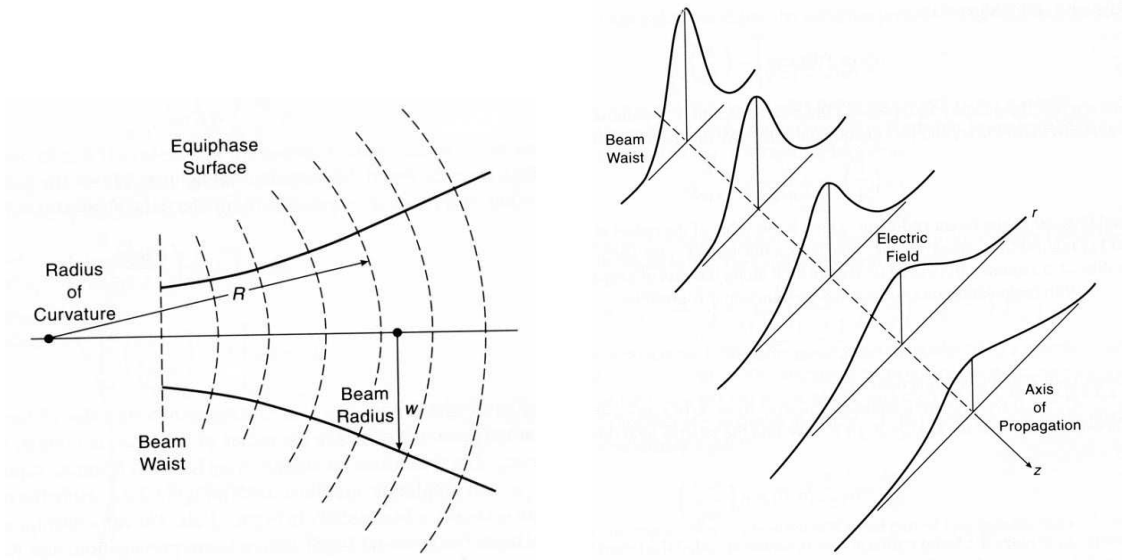

(a) *Gaussian beam propagation in 2D* (b) *Gaussian beam propagation in 3D*

Figure 5.2: *Schematic of Gaussian beam propagation. On the left, cut through beam showing equiphase surfaces (broken lines), beam radius ω and radius of curvature R. On the right, propagating beam indicating increase in beam radius and diminution of peak amplitude as distance from the beam waist increase.*

5.1.1 Gaussian optics from paraxial equation

A single component ψ of the electric field $\vec{E}$ or of the magnetic field $\vec{B}$ of an electromagnetic wave propagating in a uniform medium satisfies the Helmholtz equation:

$$(\nabla^2 + k^2)\,\psi = 0 \tag{5.1}$$

where $k = 2\pi/\lambda$ is the wavenumber. For a plane wave, the amplitudes of electric and magnetic fields are constant, their direction are mutually perpendicular and perpendicular to the propagation vector. For a beam of radiation similar to a plane wave but has some variation perpendicular to the axis of propagation, we can still assume that electric and magnetic fields are mutually perpendicular and perpendicular to the direction of propagation. Assuming that the direction of propagation is in the positive z direction, we can write the distribution for any component of the electric field in exponential form:

$$E(x, y, z) = u(x, y, z)\, e^{-jkz} \tag{5.2}$$

where u is the complex scalar function that defines the non-plane wave part of the beam. In rectangular coordinates, eq. (5.1) is:

$$\frac{\partial^2 E}{\partial x^2} + \frac{\partial^2 E}{\partial y^2} + \frac{\partial^2 E}{\partial z^2} + k^2 E = 0 \tag{5.3}$$

and substituting eq. (5.2) into eq. (5.3), we obtain the *reduced wave equation*:

$$\frac{\partial^2 u}{\partial x^2} + \frac{\partial^2 u}{\partial y^2} + \frac{\partial^2 u}{\partial z^2} - 2jk\,\frac{\partial u}{\partial z} = 0 \tag{5.4}$$

The paraxial approximation consists in assuming a small variation of u along the direction of propagation, so that it can be neglected when compared to the variations perpendicular to it: this allows to neglect the third term of eq. (5.4). In cylindrical coordinates, considering the symmetry properties of complex scalar function $u(r, \varphi, z) = u(r, z)$, the simplified eq. (5.4) becomes:

$$\frac{\partial^2 u}{\partial r^2} + \frac{1}{r}\frac{\partial u}{\partial r} - 2jk\frac{\partial u}{\partial z} = 0 \tag{5.5}$$

The simplest solution of eq. (5.5) is:

$$u(r, z) = A(z)\,\exp\left[-\frac{jkr^2}{2q(z)}\right] \tag{5.6}$$

where A and q are two complex functions of z, still to be determined. It is worth noting that the dependence of $u(r, z)$ with r is obtained in closed form and has a Gaussian shape. Substituting eq. (5.6) in eq. (5.5), we obtain:

$$-2jk\left(\frac{A}{q} + \frac{\partial A}{\partial z}\right) + \frac{k^2 r^2 A}{q^2}\left(\frac{\partial q}{\partial z} - 1\right) = 0 \tag{5.7}$$

Since the two functions A and q are completely independent, this implies:

$$\frac{\partial q}{\partial z} = 1 \tag{5.8a}$$

$$\frac{\partial A}{\partial z} = -\frac{A}{q} \tag{5.8b}$$

Solution of eq. (5.8a) is $q(z) = q(0) + z$ and it is called the *complex beam parameter*. Since q is a complex function, it can be decomposed in a real and an imaginary part:

$$\frac{1}{q} = \left(\frac{1}{q}\right)_{\Re} - j\left(\frac{1}{q}\right)_{\Im} \tag{5.9}$$

Substituting in eq. (5.6), the result is:

$$\exp\left[-\frac{jkr^2}{2q}\right] = \exp\left[-\left(\frac{jkr^2}{2}\right)\left(\frac{1}{q}\right)_{\Re} - \left(\frac{kr^2}{2}\right)\left(\frac{1}{q}\right)_{\Im}\right] \tag{5.10}$$

In eq. (5.10), the imaginary part of the exponent has the form of a phase variation produced by a spherical wavefront. In fact, if the equiphase surface has radius of curvature R and $\phi(r)$ is defined as the phase variation relative to a plane for a fixed value of z as a function of r (see Fig. 5.3), in the limit $r \ll R$, phase delay is approximately equal to $\phi(r) \simeq \pi r^2/\lambda R$. Hence, the real part of $1/q$ is related to the radius of curvature by:

$$\left(\frac{1}{q}\right)_{\Re} = \frac{1}{R} \tag{5.11}$$

The second part of eq. (5.10) is real and has a Gaussian variation as a function of the distance from the axis of propagation. Taking the standard form for a Gaussian

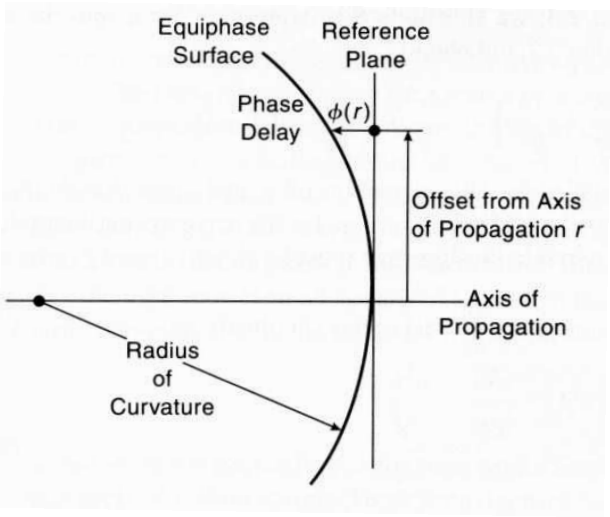

Figure 5.3: *Phase shift of spherical wave relative to the plane wave. The phase delay of the spherical wave, at a distance r from the axis defined by the propagation direction of the plane wave, is* $\phi(r)$.

distribution to be $\mathcal{N}(r) = \mathcal{N}(0)\exp(-r^2/r_0^2)$, we see that the quantity r_0 represents the distance to the $1/e$ point relative to the on-axis value, i.e. the beam radius ω. To make the second part of eq. (5.10) have this form it must be:

$$\left(\frac{1}{q}\right)_{\Im} = \frac{2}{k\omega^2(z)} = \frac{\lambda}{\pi\omega^2} \tag{5.12}$$

Since q is a function of z, both beam and curvature's radii will depend on the position along the axis of propagation. With these definitions, eq. (5.9) becomes:

$$\frac{1}{q} = \frac{1}{R(z)} - \frac{j\lambda}{\pi\omega^2(z)} \tag{5.13}$$

The *beam waist radius* ω_0 will be obtained imposing $z = 0$ so that $\omega_0 = \sqrt{\lambda q_0/j\pi}$ and considering the relation $q(z) = z + q(0)$ we get:

$$q = z + \frac{j\pi\omega_0^2}{\lambda} = z + j\, z_c \tag{5.14}$$

where $z_c = \pi\omega_0^2/\lambda$ is defined as the *confocal distance* or *confocal parameter*. Moreover, using eqs. (5.13) and (5.14) we find the relations:

$$R = z + \frac{1}{z}\left(\frac{\pi\omega_0^2}{\lambda}\right)^2 = z + \frac{z_c^2}{z} \tag{5.15}$$

$$\omega = \omega_0\sqrt{1 + \left(\frac{\lambda z}{\pi\omega_0^2}\right)^2} = \omega_0\sqrt{1 + \left(\frac{z}{z_c}\right)^2} \tag{5.16}$$

As already said, ω_0 is the minimum value that beam radius can assume and it occurs at the beam waist, where the radius of curvature is infinite (plane wavefront). Considering eqs. (5.8a), (5.8b) and (5.14), the solution of eq. (5.8b) is:

$$\frac{A(z)}{A(0)} = \frac{1 + j\lambda z/\pi\omega_0^2}{1 + (\lambda z/\pi\omega_0^2)^2} = \frac{1 + jz/z_c}{1 + (z/z_c)^2} \tag{5.17}$$

Defining the *Gaussian beam phase shift* ϕ_0 so that $\tan(\phi_0) = \lambda z/\pi\omega_0^2$, previous equation becomes:

$$\frac{A(z)}{A(0)} = \frac{\omega_0}{\omega} \cdot e^{j\phi_0} \tag{5.18}$$

and substituting in eqs. (5.2) and (5.6), we find the expression of the electric field of the beam as a function of r and z:

$$E(r,z) = \frac{\omega_0}{\omega} \cdot \exp\left(-\frac{r^2}{\omega^2} - jkz - \frac{j\pi r^2}{\lambda R} + j\phi_0\right) \tag{5.19}$$

Finally, it is possible to normalize the equation of electric field, $2\pi \int |E|^2 \, r \, dr = 1$, so that eq. (5.19) becomes:

$$E(r,z) = \sqrt{\frac{2}{\pi\omega^2}} \cdot \exp\left(\frac{-r^2}{\omega^2} - jkz - \frac{j\pi r^2}{\lambda R} + j\phi_0\right) \tag{5.20}$$

5.1.2 Edge Taper

Eq. (5.20) shows the characteristics of the distribution of a Gaussian beam, the transported energy during its propagation (increasing z) and its removal from the axis of propagation (increasing r).

The field distribution is maximum in the beam waist ($z = 0$) and on the axis of propagation ($r = 0$). For each value of z, the energy transported by the beam monotonically decreases as r increases with a Gaussian shape. When $r \leqslant \omega_0/\sqrt{2}$, energy transported by beam monotonically decreases as z increase; instead, when $r > \omega_0/\sqrt{2}$ the shape is no more monotonic: a relative maximum as a function of z is observed. This is due to the distribution effect: the Gaussian distribution that describes the beam is less concentrate in the center as z increase.

For each z, the Gaussian shape of the electric field can be described as:

$$\left|\frac{E(r,z)}{E(0,z)}\right| = \exp\left[-\left(\frac{r}{\omega}\right)^2\right] \tag{5.21}$$

while the distribution of power density is proportional to the square of the previous quantity:

$$\frac{P(r)}{P(0)} = \exp\left[-2\left(\frac{r}{\omega}\right)^2\right] \tag{5.22}$$

It is possible to characterize the Gaussian beam in terms of the relative power level at a specified radius. The *edge taper* T_e is the relative power density at a radius r_e and it is given by:

$$T_e(r_e) = \frac{P(r_e)}{P(0)} = \exp\left[-2\,\frac{r_e^2}{\omega^2}\right] \tag{5.23}$$

Usually, the edge taper is expressed in decibels:

$$T_e(dB) = -10\log(T_e) = 20\,\frac{r_e^2}{\omega^2}\,\log(e) \tag{5.24}$$

Radius corresponding to a given level of relative power is:

$$\frac{r_e}{\omega} = 0.3393 \cdot \sqrt{T_e(dB)} \tag{5.25}$$

Finally, from the above equations the fraction of power $F_e(r_e)$ enclosed in a radius r_e is:

$$F_e(r_e) = 2\pi \int_0^{r_e} |E(r)|^2\, r\, dr = 1 - T_e(r_e) \tag{5.26}$$

Thus, the fractional power that falls outside radius r_e is equal to the edge taper at that radius: so, T_e describes the portion of energy loss. A summary of the main Gaussian beam parameters and formulas to compute them is reported in Tabs. 5.1 and 5.2.

Transverse field distribution	$E(r,z) = \sqrt{\dfrac{2}{\pi\omega^2(z)}}\left(-\dfrac{r^2}{\omega^2} - jkz - \dfrac{j\pi r^2}{\lambda R} + j\phi_0\right)$
Beam radius	$\omega = \omega_0\sqrt{1 + \left(\dfrac{\lambda z}{\pi\omega_0^2}\right)^2}$
Radius of curvature	$R = z + \dfrac{1}{z}\left(\dfrac{\pi\omega_0^2}{\lambda}\right)^2$
Edge taper	$T_e(r_e) = \exp\left(-2\dfrac{r_e^2}{\omega^2}\right)$

Table 5.1: *Summary of main Guassian beam formulas. It is assumed a symmetric Gaussian beam with waist radius ω_0 located at $z = 0$ and propagating along the z axis. The transverse coordinate is r, which is limited by the edge radius r_e for a truncated beam.*

5.2 Gaussian beam transformation

A quasioptical system is a tool used to modify, direct and restrict a beam of electromagnetic radiation according to the requirements of the experiment. This process is carried out in a manner similar to that employed in "traditional" optical systems, i.e. using lenses or mirrors that modify the beam radius of curvature in order to converge or diverge it. The process of altering the properties of a Gaussian beam is called *beam transformation.*

The analogy between the real part of the complex q parameter and the radius of curvature, characteristic of a beam in the geometrical optics approximation, suggests to

ω_0	z	$\omega = \omega_0\sqrt{1+\left(\frac{\lambda z}{\pi\omega_0^2}\right)^2}$	$R = z\left[1+\left(\frac{\pi\omega_0^2}{\lambda z}\right)^2\right]$
R	z	$\omega_0^2 = \frac{\lambda}{\pi}\sqrt{z(R-z)}$	ω from ω_0 and z
ω	z	$\omega_0^2 = \frac{\omega^2}{2}\left[1 \pm \sqrt{1-\left(\frac{2\lambda z}{\pi\omega^2}\right)^2}\right]$	R from ω_0 and z
ω	ω_0	$z = \frac{\pi\omega_0}{\lambda}\sqrt{\omega^2-\omega_0^2}$	R from ω_0 and z
ω_0	R	$z = \frac{R}{2}\left[1 \pm \sqrt{1-\left(\frac{2\pi\omega_0^2}{\lambda R}\right)^2}\right]$	ω from ω_0 and z
ω	R	$\omega_0 = \frac{\omega}{\sqrt{1+\left(\frac{\pi\omega^2}{\lambda R}\right)^2}}$	$z = \frac{R}{1+\left(\frac{\lambda R}{\pi\omega^2}\right)^2}$

Table 5.2: *Relationship between main Gaussian beam parameters: these formulas permit to determine every parameter given only a known pair of them.*

extend the formalism used in geometrical optics to systems that require Gaussian beam propagation. In this approach, the location and the slope of a ray at the output plane of a paraxial system are defined to be linear functions of the parameters of the input ray. Denoting the position as r and the slope as α, the linear relationship between input and output position and slope of a ray is:

$$r_{Out} = A \cdot r_{In} + B \cdot \alpha_{In} \tag{5.27a}$$
$$\alpha_{Out} = C \cdot r_{In} + D \cdot \alpha_{In} \tag{5.27b}$$

Using the matrix formalism, eq. (5.27) can be written as:

$$\begin{pmatrix} r_{Out} \\ \alpha_{Out} \end{pmatrix} = \begin{pmatrix} A & B \\ C & D \end{pmatrix} \cdot \begin{pmatrix} r_{In} \\ \alpha_{In} \end{pmatrix} \tag{5.28}$$

A succession of elements is handled by multiplication of the appropriate 2×2 matrices to find the overall system matrix. Since the radius of curvature is defined as the ratio between the position and the slope, $R = r/\alpha$, the relationship between the input and output radii of curvature is:

$$R_{Out} = \frac{A \cdot R_{In} + B}{C \cdot R_{In} + D} \tag{5.29}$$

The extension of eq. (5.29) to Gaussian optics leads to the *ABCD* law in which the four parameters operate on the complex parameter q:

$$q_{Out} = \frac{A \cdot q_{In} + B}{C \cdot q_{In} + D} \tag{5.30}$$

The four parameters A, B, C and D are the same for the geometrical optical system element, so that all of the geometrical optics theory can be applied to Gaussian beams.

In multielements systems, we place the matrices in the matrix equation from right to left in the order that the beam encounters the constituent parts of the system, i.e. the right-most matrix represent the first distance or interface encountered, the next to its left describes the following distance or interface, and so on. Hence, from eqs. (5.11) and (5.12), we get:

$$R = \left[\mathrm{Re}\left(\frac{1}{q}\right)\right]^{-1} \tag{5.31}$$

$$\omega = \sqrt{\frac{\lambda}{\pi\,\mathrm{Im}\left(-\frac{1}{q}\right)}} \tag{5.32}$$

5.2.1 Transformation matrices

The most basic ray transfer matrix is the translation one, which describes the beam propagation in a uniform material of a uniform refraction index for a distance L. As shown in Fig. 5.4, it changes the offset of the ray from the axis by an amount proportional to α_{In} but does not change its slope. It is described by the matrix:

$$\mathbf{M}_{Dist} = \begin{pmatrix} 1 & L \\ 0 & 1 \end{pmatrix} \tag{5.33}$$

A second fundamental ray transfer matrix is the interface between media of different indices of refraction n_a and n_b: passing trough this interface changes the slope of a ray but does not affect its position (see Fig. 5.4). The matrix is found by applying the Snell law to a ray incident on the surface. If the surface has a radius of curvature R (so that flat interface is given by $R \to \infty$), the corresponding matrix is:

$$\mathbf{M}_{Ref} = \begin{pmatrix} 1 & 0 \\ \frac{n_b - n_a}{n_b R} & \frac{n_b}{n_a} \end{pmatrix} \tag{5.34}$$

Given these two transformation matrices, it is possible to construct matrices for more complex quasioptical systems.

Lossless dielectric This is a flat plate of material having refraction index n_b and thickness L embedded in a medium having refraction index n_a so that it satisfies the equation:

$$\mathbf{M}_{Diel} = \mathbf{M}_{Ref}(b \to a, R \to \infty) \cdot \mathbf{M}_{Dist}(L) \cdot \mathbf{M}_{Ref}(a \to b, R \to \infty) \tag{5.35}$$

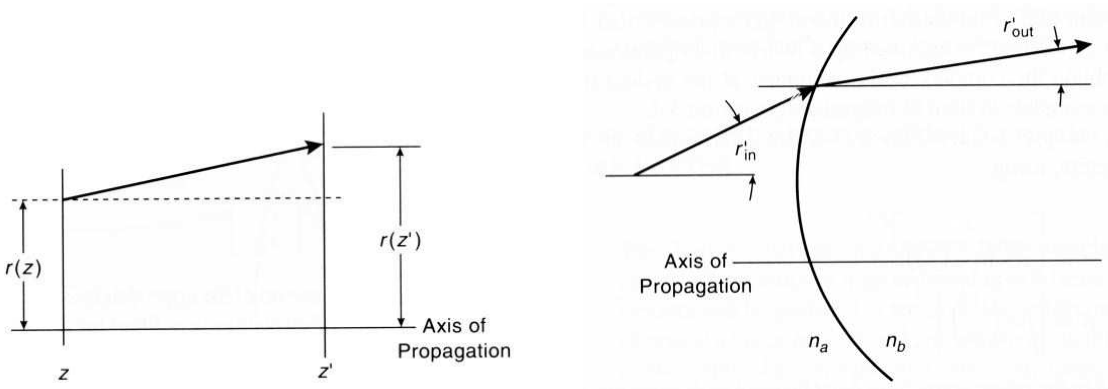

(a) *Transformation in free space* (b) *Transformation between different media*

Figure 5.4: *Gaussian beam transformation in the two simplest cases. On the left, ray propagation in free space as described by* eq. (5.33)*: the distance of the ray from the axis of propagation is r, and its slope is α. On the right, ray propagation at interface between two media having different indices of refraction n_a and n_b: the corresponding matrix is given in* eq. (5.34)*.*

and the result is:

$$\mathbf{M}_{Diel} = \begin{pmatrix} 1 & \dfrac{L\, n_a}{n_b} \\ 0 & 1 \end{pmatrix} \tag{5.36}$$

Thin lens It is a focusing element that consist of one or two curved interfaces. Beam crosses from outside to inside the lens ($a \to b$) passing through a surface of radius R_a, then it travels inside the lens and crosses it again ($b \to a$ with exit surface radius R_b). The thin lens approximation consist in neglecting physical separation and thickness, i.e. the translation of the beam inside the lens. Transformation matrix will be:

$$\mathbf{M}_{Thin} = \mathbf{M}_{Ref}(b \to a, R = R_b) \cdot \mathbf{M}_{Ref}(a \to b, R = R_a) \tag{5.37}$$

thus obtaining:

$$\mathbf{M}_{Thin} = \begin{pmatrix} 1 & 0 \\ \dfrac{n_b - n_a}{n_a}\left(\dfrac{1}{R_a} - \dfrac{1}{R_b}\right) & 1 \end{pmatrix} \tag{5.38}$$

Note that a biconvex lens has $R_a < 0$ and $R_b > 0$ and thus for $n_b > n_a$ the matrix element C is always negative. Usually, the thin lens is described by its focal length f, thus the slope of the beam is proportional to $-1/f$. In fact, if the beam propagates parallel the z axis, it will crosses the z axis at a distance f after passing through the lens. Thus, the matrix describing thin lens can be written as:

$$\mathbf{M}_{Thin} = \begin{pmatrix} 1 & 0 \\ -\dfrac{1}{f} & 1 \end{pmatrix} \tag{5.39}$$

which gives the relationship between focal length of thin lens and its properties:

$$\frac{1}{f_{Thin}} = \frac{n_b - n_a}{n_a}\left(\frac{1}{R_b} - \frac{1}{R_a}\right) \tag{5.40}$$

Spherical mirror In the paraxial limit, this mirror is equivalent to a thin lens of focal length $f = R/2$, where R is the mirror radius of curvature. So, the matrix describing a spherical mirror is:

$$\mathbf{M}_{Sphe} = \begin{pmatrix} 1 & 0 \\ -\dfrac{2}{R} & 1 \end{pmatrix} \tag{5.41}$$

5.2.2 Transformation by a thin lens

Let us suppose to have a thin lens with focal length f at a distance d_{In} from the origin of the beam ($z = 0$): we want to study how the beam is transformed at a distance d_{Out} from the lens (see Fig. 5.5). The resulting matrix is:

$$\begin{aligned} \mathbf{M}_{Tot} &= \mathbf{M}_{Dist}(L = d_{Out}) \cdot \mathbf{M}_{Thin} \cdot \mathbf{M}_{Dist}(L = d_{In}) = \\ &= \begin{pmatrix} 1 & d_{Out} \\ 0 & 1 \end{pmatrix} \cdot \begin{pmatrix} 1 & 0 \\ -\dfrac{1}{f} & 1 \end{pmatrix} \cdot \begin{pmatrix} 1 & d_{In} \\ 0 & 1 \end{pmatrix} = \\ &= \begin{pmatrix} 1 - \dfrac{d_{Out}}{f} & d_{In} + d_{Out}\left(1 - \dfrac{d_{In}}{f}\right) \\ -\dfrac{1}{f} & 1 - \dfrac{d_{In}}{f} \end{pmatrix} \end{aligned} \tag{5.42}$$

Since the input is a beam waist, eq. (5.14) implies $q_{In} = j\, z_c$; from eq. (5.30) we get that the output complex parameter q_{Out} is:

$$q_{Out} = \frac{\left(1 - \dfrac{d_{Out}}{f}\right) j\, z_c + d_{In} + d_{Out}\left(1 - \dfrac{d_{In}}{f}\right)}{\left(1 - \dfrac{d_{In}}{f}\right) - j\, \dfrac{z_c}{f}} \tag{5.43}$$

This equation gives the following information:

- At the entrance of the lens ($f = \infty$ and $d_{Out} = 0$), the beam radius of curvature $R_{L_{In}}$ is:

$$\frac{1}{R_{L_{In}}} = \frac{d_{In}}{d_{In}^2 + z_c^2} \tag{5.44}$$

- At the exit of the lens ($d_{Out} = 0$) the beam radius of curvature is:

$$\frac{1}{R_{L_{Out}}} = \frac{d_{In}}{d_{In}^2 + z_c^2} - \frac{1}{f} = \frac{1}{R_{L_{In}}} - \frac{1}{f} \tag{5.45}$$

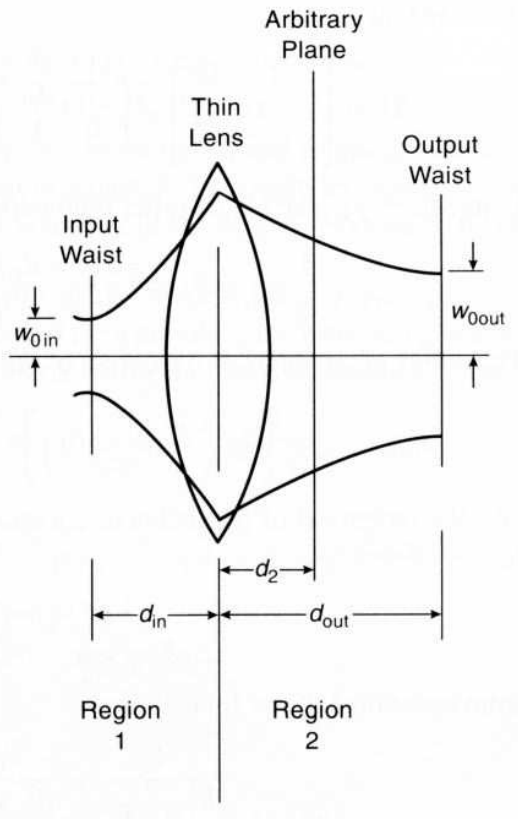

Figure 5.5: *Schematic of Gaussian beam transformation by a thin lens.*

- Eq. (5.43) gives the beam properties at every distance d_{Out} from the lens. For example, position and value of the beam waist exiting the lens are:

$$d_{\omega_{0,\,Out}} = f + \frac{d_{In} - f}{\left(\frac{d_{In}}{f} - 1\right)^2 + \frac{z_c^2}{f^2}} \tag{5.46}$$

$$\omega_{0,\,Out} = \frac{\omega_{0,\,In}}{\sqrt{\left(\frac{d_{In}}{f} - 1\right)^2 + \frac{z_c^2}{f^2}}} \tag{5.47}$$

5.3 Gaussian beam analysis

As explained in the previous paragraphs, in Gaussian optics, a beam does not have a unique point of origin, but rather a beam waist ω_0 where the beam is minimized and its wavefront is flat. As the beam propagates, it expands and its wavefront has a Gaussian distribution (see Fig. 5.2).

Since microwave experiments use receivers that integrate the incident signal, the incoming radiation is concentrated using feed horns. Reversing the optical system, the

beam originates in the horn and starts propagating along the mirrors chain. Gaussian beam analysis permits to choose the best characteristics of the horns.

5.3.1 Feed Horn

A feed horn is a radiation collector of conic or pyramidal shape that allows to efficiently couple the receivers to the Gaussian beam of radiation coming from optical system. Usually, feed horns are corrugated: the teeth inside the horns typically have a depth of $\lambda/4$, where λ is the wavelength of the radiation of interest. Corrugated horns of the kind shown in Fig. 5.6 have many advantages: the beam that originates from these horns is an almost perfect Gaussian, conic, symmetric beam without sidelobes; moreover, they preserve the polarization of the incoming radiation. The coupling efficiency between the optical system and a corrugated feed horn can reach 95%. The main drawbacks are the cost and difficulties of machining such horns.

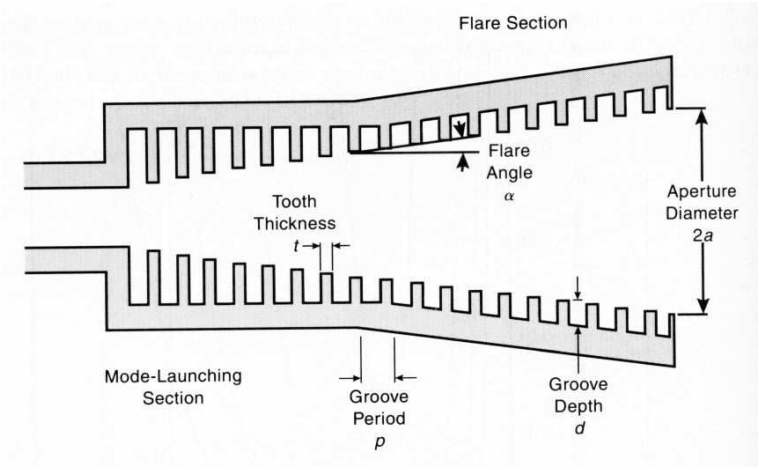

Figure 5.6: *Cross section of corrugated feed horn. The input from the left is assumed to be a smooth-walled circular waveguide.*

A feed horn having an aperture radius a and a slant length R_h produces a Gaussian beam with a radius of curvature at the horn aperture R_h. The position of the beam waist is obtained maximizing the energy emitted by the horn: given the aperture a and Gaussian beam radius at horn aperture ω_a (see Fig. 5.7), their ratio is constant and depends only on the characteristics of the horn [46].

From eqs. (5.11) and (5.12), obtaining the position of the beam waist referred to the aperture of the horn (waist offset $z = d_0$) and its value ω_0 is straightforward:

$$d_0 = \frac{R_h}{1 + \left(\frac{\lambda R_h}{\pi \omega_a^2}\right)^2} \tag{5.48}$$

$$\omega_0 = \frac{\omega_a}{1 + \left(\frac{\pi \omega_a^2}{\lambda R_h}\right)^2} \tag{5.49}$$

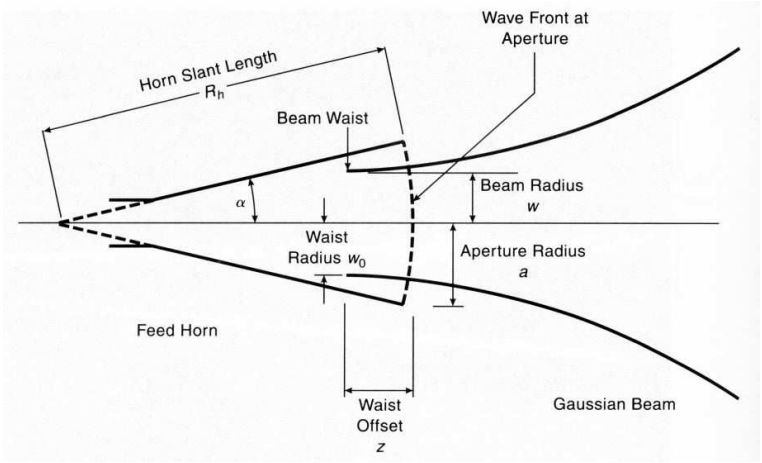

Figure 5.7: *Gaussian beam originated by a feed horn. The figure also shows the main parameters of the horn. It is worth noting that the slant length R_h is the whole length of the horn, i.e. that obtained propagating the horn wall inside the waveguide.*

5.3.2 Horn design

As shown in Fig. 5.7, the beam waist is *inside* the horn, at a distance d_0 from the entrance. Eqs. (5.48) and (5.49) show that ω_0 and d_0 depend on four parameters:

1. Wavelength λ of the radiation of interest, i.e. the radiation exiting the horn.

2. Entrance aperture radius a of the horn.

3. Coupling between horn and outgoing beam, described by the ratio between the horn aperture a and the Gaussian beam radius at the horn aperture ω_a.

4. Horn slant length R_h.

ω_a/a is a constant that depends only on the type of the chosen horn: in our case, we have a *smooth-walled conical feed horn*, which has $\omega_a/a = 0.768$ [46]. This horn has not the advantages of a corrugated one, but it is much cheaper and it is good enough for our purposes, since beam selection is made using a cold *Lyot Stop* and we are not interested in preserving information on polarized radiation.

As the beam starts propagating from the beam waist inside the horn, it expands until it reaches the fifth mirror, which refocuses the beam on the *Lyot Stop* (see Fig. 3.1). As shown in § 5.2.1, a spherical mirror acts on a Gaussian beam in the same way as a thin lens acts and the relation $f_{Thin\ Lens} = f_{5^{th}} = R_{5^{th}}/2$ subsists. The propagation of the beam from the horn to the *Lyot Stop* follows the calculations done in § 5.2.2 for a thin lens. In the case of the *OLIMPO* optical system, d_{In} is the distance between the quinary mirror and the image surface, i.e. beam waist ($d_{5^{th}-\omega_0}$), while d_{Out} is the one between the

Lyot Stop and the fifth mirror ($d_{LS-5^{th}}$). Thus, eq. (5.42) becomes:

$$\begin{aligned}
\mathbf{M}_{LS-\omega_0} &= \mathbf{M}_{Dist}(L = d_{LS-5^{th}}) \cdot \mathbf{M}_{Thin}(f = f_{5^{th}}) \cdot \mathbf{M}_{Dist}(L = d_{5^{th}-\omega_0}) = \\
&= \begin{pmatrix} 1 & d_{LS-5^{th}} \\ 0 & 1 \end{pmatrix} \cdot \begin{pmatrix} 1 & 0 \\ -\dfrac{1}{f_{5^{th}}} & 1 \end{pmatrix} \cdot \begin{pmatrix} 1 & d_{5^{th}-\omega_0} \\ 0 & 1 \end{pmatrix} = \\
&= \begin{pmatrix} 1 - \dfrac{d_{LS-5^{th}}}{f_{5^{th}}} & d_{5^{th}-\omega_0} + d_{LS-5^{th}} \left(1 - \dfrac{d_{5^{th}-\omega_0}}{f_{5^{th}}}\right) \\ -\dfrac{1}{f_{5^{th}}} & 1 - \dfrac{d_{5^{th}-\omega_0}}{f_{5^{th}}} \end{pmatrix}
\end{aligned} \tag{5.50}$$

Considering eq. (5.30) and starting the beam starts from the beam waist, where $q_{In} = j\, z_c$, the q_{LS} parameter on the *Lyot Stop* is:

$$q_{LS} = \frac{\left(1 - \dfrac{d_{LS-5^{th}}}{f_{5^{th}}}\right) j\, z_c + d_{5^{th}-\omega_0} + d_{LS-5^{th}} \left(1 - \dfrac{d_{5^{th}-\omega_0}}{f_{5^{th}}}\right)}{\left(1 - \dfrac{d_{5^{th}-\omega_0}}{f_{5^{th}}}\right) - j\, \dfrac{z_c}{f_{5^{th}}}} \tag{5.51}$$

and from eq. (5.32) we get the beam radius on the *Lyot Stop*:

$$\omega_{LS} = \frac{\omega_0}{z_c} \sqrt{f_{5^{th}}^2 \left[1 - \left(1 - \frac{d_{5^{th}-\omega_0}}{f_{5^{th}}}\right)\left(1 - \frac{d_{LS-5^{th}}}{f_{5^{th}}}\right)\right]^2 + z_c^2 \left(1 - \frac{d_{LS-5^{th}}}{f_{5^{th}}}\right)^2} \tag{5.52}$$

We can also calculate the edge taper on the *Lyot Stop*, i.e. the power at the edge of the mirror relative to its central value:

$$T_e(R_{LS}) = \exp\left[-\frac{2R_{LS}^2}{\omega_{LS}^2}\right] \tag{5.53}$$

Finally, we want to compute the angular resolution given by the chosen horn. As already described in § 3.2.1, the *Lyot Stop* is the mirror onto which the image of the primary is focused: thus, properties of the beam are almost equal on the *Lyot Stop* and the primary mirror. The relation between the shape of the beam on the sky and the one on the primary mirror is obtained using *Fraunhofer diffraction*.

5.3.3 Far field diffraction

Fraunhofer diffraction is also known as the far field diffraction. Essentially it represents the electromagnetic field produced by an aperture at a very large distance from the aperture. Given the field in the aperture plane $E(x_0, y_0)$, i.e. the primary mirror, the field in the observation plane $E(x_1, y_1)$, i.e. the sky, at a distance z from the aperture plane is given by the convolution:

$$E(x_1, y_1) = \iint_{A(x_0,y_0)} h(x_1 - x_0, y_1 - y_0)\, E(x_0, y_0)\, dx_0\, dy_0 \tag{5.54}$$

where

$$h(x_1 - x_0, y_1 - y_0) = \exp(jkr_{01}) \cdot \frac{1}{j\lambda r_{01}} \tag{5.55a}$$

$$r_{01} = \sqrt{(x_0 - x_1)^2 + (y_0 - y_1)^2 + z^2} \tag{5.55b}$$

The term r_{01} in the exponential cannot be approximated by z because it is multiplied by k, which is big, so small changes in r_{01} can produce large differences. This can be done in the denominator, while the term in the exponential can be expanded to first order, thus obtaining:

$$E(x_1, y_1) = \iint_{A(x_0,y_0)} \frac{1}{j\lambda z}\, e^{jk\left[z + \frac{(x_0-x_1)^2}{2z} + \frac{(y_0-y_1)^2}{2z}\right]} E(x_0, y_0)\, dx_0\, dy_0 \tag{5.56}$$

which can be rewrite multiplying out the squares and factoring out the quantities independent of x_0 and y_0:

$$\begin{aligned} E(x_1, y_1) &= \frac{1}{j\lambda z}\, e^{jk\left(z + \frac{x_1^2+y_1^2}{2z}\right)} \cdot \\ &\iint_{A(x_0,y_0)} e^{jk\left[\frac{-2x_0x_1-2y_0y_1}{2z} + \frac{(x_0+y_0)^2}{2z}\right]} E(x_0, y_0)\, dx_0\, dy_0 \end{aligned} \tag{5.57}$$

Let $D = x_0^2 + y_0^2$ be the size of the aperture: the far field approximation implies $kD^2/2 \ll 1$, so that the quadratic term in the integral of eq. (5.57) can be neglected:

$$\begin{aligned} E(x_1, y_1) &= \frac{1}{j\lambda z}\, e^{jk\left(z + \frac{x_1^2+y_1^2}{2z}\right)} \cdot \\ &\iint_{A(x_0,y_0)} e^{-\frac{jk}{z}(x_0x_1+y_0y_1)} E(x_0, y_0)\, dx_0\, dy_0 \end{aligned} \tag{5.58}$$

It is worth noting that the far field approximation is valid when $z \gg kD^2/2 = \pi D^2/\lambda$: in the case of the OLIMPO experiment, $D = 2000mm$ and $\lambda = 2.1 \div 0.5mm$, which implies $z \gg 6 \div 25km$. Since the incident radiation is a plane wave, $E(x_0, y_0)$ is constant with respect to x_0 and y_0 and can be factorized out of the integral. Expliciting the aperture function $A(x_0, y_0)$ and ignoring the phase factors in front of the integral, we get:

$$E(x_1, y_1) \propto \int_{-\infty}^{+\infty} \int_{-\infty}^{+\infty} \exp\left[-\frac{jk}{z}(x_0x_1 + y_0y_1)\right] A(x_0, y_0)\, dx_0\, dy_0 \tag{5.59}$$

which is clearly a Fourier transform from the position x_0 on the aperture to another position variable x_1 in another plane: thus, the far field radiation is the Fourier transform of the aperture field. The conjugate variables here are x_0 and $k_x = k\, x_1/z$, which have reciprocal units.

Using the properties of Fraunhofer diffraction, it is possible to estimate the resolution as a function of the horn characteristics. The beam on the *Lyot Stop* is:

$$A_{LS}(x_0, y_0) = \exp\left[-2\,\frac{r^2(x_0, y_0)}{\omega_{LS}^2}\right] \tag{5.60}$$

and we assume it is the same (apart from a scale factor) on the primary mirror. Thus, the beam on the sky in the Fourier transform of the beam on the primary. The position of the first minimum is $\vartheta = R_{LS}/R_{1^{th}} \cdot \lambda/x_0$: this set the scale of the far field coordinates. Then, computing the corresponding full width half maximum of the beam is straightforward.

5.3.4 Results

The Gaussian beam analysis was computed for $\lambda = 2.1mm$ $(143GHz)$. In principle, the best solution minimizes the power loss (and so the edge taper) and gives the best resolution.

The latter is almost independent of the horn parameters while it depends strongly on the wavelengths (see Fig. 5.8): it is $\vartheta_{FWHM} = 5.6'$ at $\lambda = 2100\mu m$, $\vartheta_{FWHM} = 3.7'$ at $\lambda = 1400\mu m$, $\vartheta_{FWHM} = 2.3'$ at $\lambda = 850\mu m$ and $\vartheta_{FWHM} = 1.5'$ at $\lambda = 550\mu m$.

Instead the edge taper decreases as the aperture a and the length R_h of the antenna

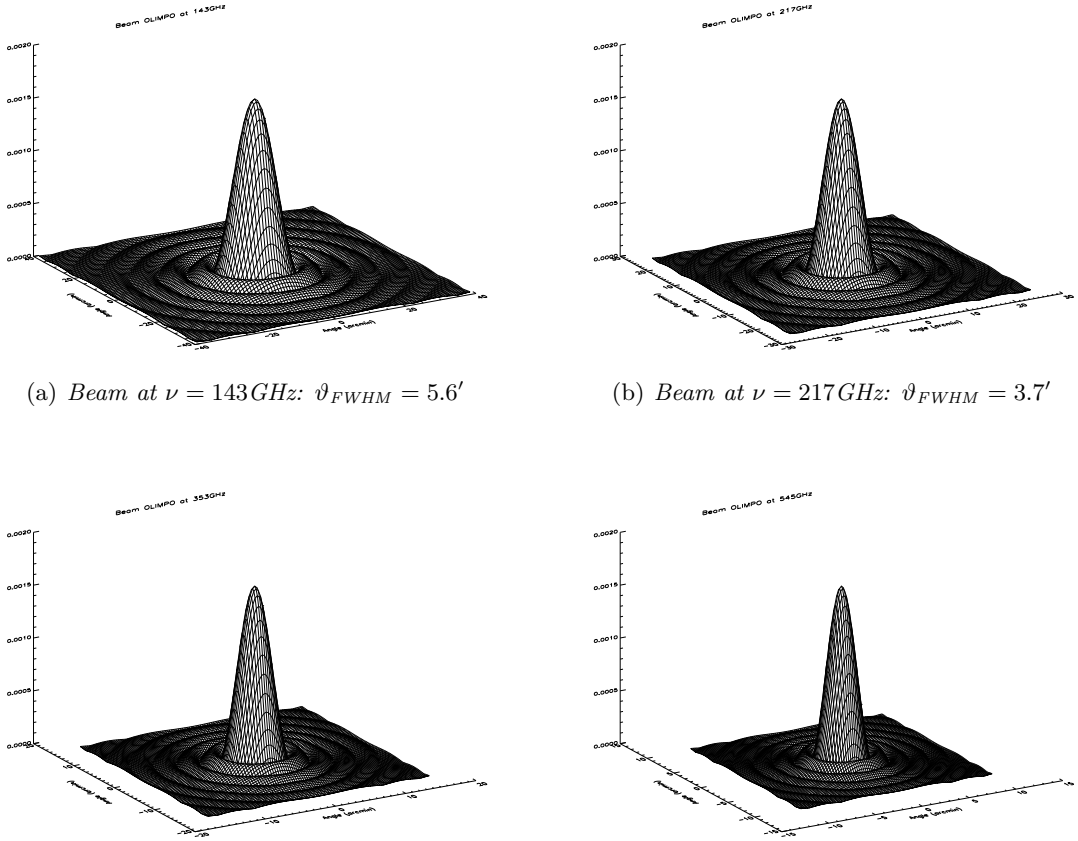

(a) *Beam at* $\nu = 143GHz$*:* $\vartheta_{FWHM} = 5.6'$

(b) *Beam at* $\nu = 217GHz$*:* $\vartheta_{FWHM} = 3.7'$

(c) *Beam at* $\nu = 353GHz$*:* $\vartheta_{FWHM} = 2.3'$

(d) *Beam at* $\nu = 545GHz$*:* $\vartheta_{FWHM} = 1.5'$

Figure 5.8: *Beam of OLIMPO in the four bands. It is clear its dependence on the frequency: as the wavelength decreases, the beam full width half maximum decreases as well, thus the angular resolution of OLIMPO increases. Note that x and y axes change scale between the four figures.*

increase: its variation as a function of the horn aperture and length is shown in Fig. 5.9. In order to minimize the power loss one should decrease the beam radius on the *Lyot Stop*: it reduces the portion of the mirror illuminated, thus diminishing the collected power. This effect is emphasized by the presence of the hole on the *Lyot Stop*. The best compromise is a horn that produces a beam having $T_e(R_{LS}) \sim 10dB$ [46].

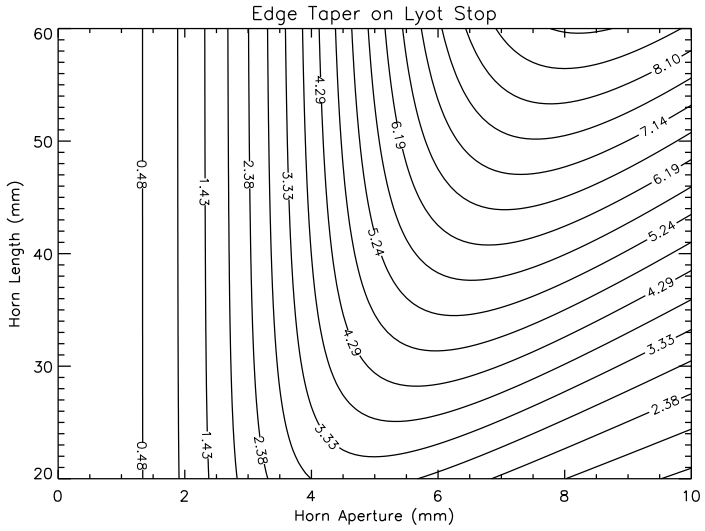

Figure 5.9: *Edge taper on the Lyot Stop as a function of the aperture length of the feed horn for* $\nu = 143GHz$ ($\lambda = 2100\mu m$)*: units are decibels. As explained in* § 5.3.4*, horns cannot have an aperture larger than* $5mm$ *and cannot be longer than* $40mm$*. It is clear that ideal value* $T_e \simeq 10dB$ [46] *is inaccessible with these constrains.*

In choosing the parameters of the *OLIMPO* feed horns, it must be noted that:

- The horn aperture must be larger than the Airy disc at that wavelength: D_{Airy} ($\lambda = 2.1mm$) $\simeq 7mm \Rightarrow D_{Horn} = 2a > 7mm$.
- At $\lambda = 2.1mm$ there will be 19 bolometers, 5 in the central row (see Fig. 5.10); the diameter of the focal plane is $52mm$, so $D_{Horn} = 2a < 10mm$.
- Because of space issues in the cryostat, the feed length must be $R_h < 45mm$. Note that R_h is the *total* length of the horn, where the horn would "finish" if there was no waveguide (see Fig. 5.7).
- The horn finishes in a circular waveguide, whose length and diameter define the cut-off wavelength and select the modes that can propagate. The higher cut-off wavelength for a particular transverse-electrical (TE) or transverse-magnetic (TM) mode in circular waveguide is given by:

$$\lambda_{Cut-Off,\,mn} = \frac{\pi\, d_{Out}}{f_{mn}} \tag{5.61}$$

The fundamental mode, i.e. the one having the highest cut-off wavelength, is TE_{11} ($f_{11} = 1.841$). If the waveguide is long at least 2λ and has a diameter of $d_{Out} \simeq \lambda/1.7$,

only the TE_{11} mode can propagate. We choosed to use single mode horns: the advantage is an almost perfect Gaussian beam shape, the drawback is the loss of energy related to the higher modes.

These constraints define the parameters of the horns at $143\,GHz$, as reported in Tab. 5.3: the edge taper is $T_e(R_{LS}) = 4.52\,dB$. It is worth noting that the contribution due to sidelobes is negligible, because the *Lyot Stop* is enclosed in a cold absorbing cavity with very low and constant emission (see § 3.2.1). Assuming the reflectivity is 10^{-3}, the edge taper outside the *Lyot Stop* is $T_e \sim 35\,dB$.

Regarding the $217\,GHz$ channel, the dimensions of the horns roughly scale proportionally to the wavelength. Thus, the receivers are 37 (instead of 19), 7 in the central row (see Fig. 5.11), and the horns dimensions must decrease of $\sim 33\%$ in order to fill the focal plane. The exact properties are chosen imposing the conservation of the edge taper.

	143 *GHz*	**217 *GHz***
Number of receivers (*mm*)	19	37
Horn Aperture (*mm*)	9.00	6.42
Horn Slant Length (*mm*)	40.00	28.00
Waveguide Diameter (*mm*)	1.50	1.00
Waveguide Length (*mm*)	6.67	3.91

Table 5.3: *Chosen dimensions of the OLIMPO horns for* 143 *and* 217 *GHz channels.*

Regarding the two higher frequency channels, the layout is still under discussion. The number of receivers will be the same of the $217\,GHz$ channel, so there are three possible solutions:

1. We scale the dimensions of the horns proportionally to the wavelength and increase their number in order to fill the focal plane: the drawback is that each receiver sees many horns, thus we cannot estimate the shape of the beam and the angular resolution.

2. We scale the dimensions proportionally to the wavelength but we keep the same number as for the $217\,GHz$ channel (i.e. 37 horns): we control the shape of the beam and the angular resolution but we do not fill the focal plane, hence we reduce the collected power.

3. The aperture of the horns remains the same as the $217\,GHz$ channel and we change only their length so that the edge taper is the same at all the wavelengths: we can predict the shape of the beam and the angular resolution, but the latter will be different in the four bands.

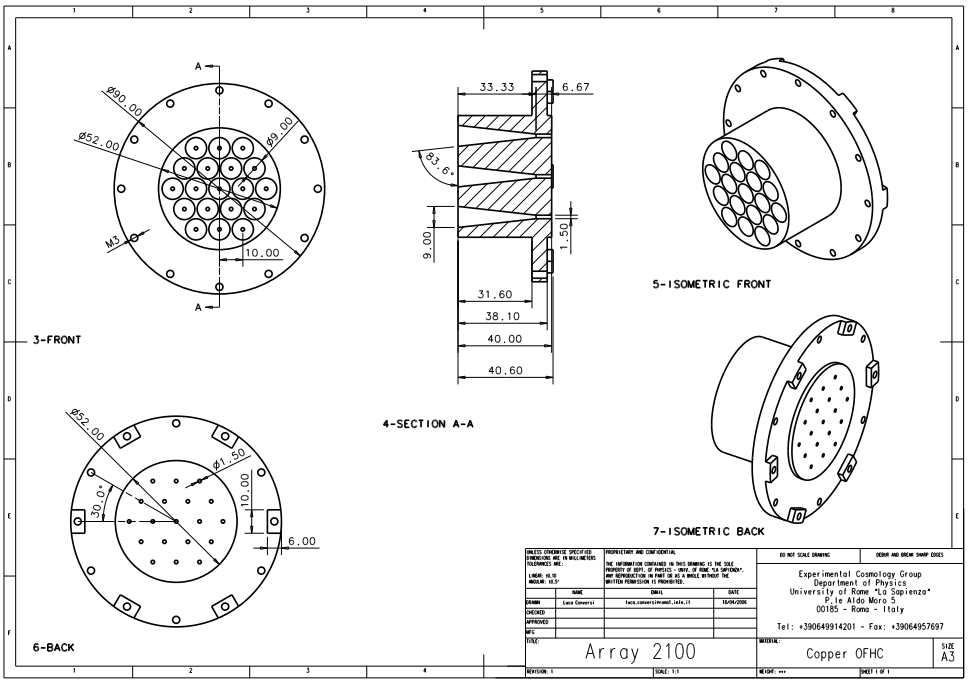

Figure 5.10: *Executive project of the horns for first OLIMPO channel* ($\nu = 143 GHz$, $\lambda = 2100 \mu m$). *Their characteristics are reported in* Tab. 5.3.

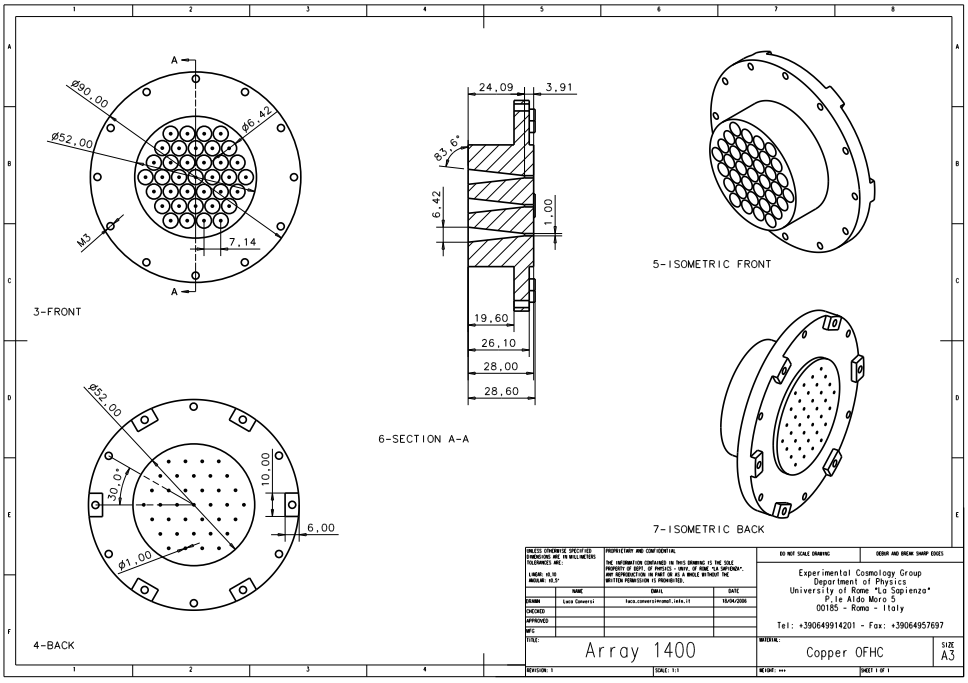

Figure 5.11: *Executive project of the horns for second OLIMPO channel* ($\nu = 217 GHz$, $\lambda = 1400 \mu m$). *Their characteristics are reported in* Tab. 5.3.

Chapter 6

Simulations

Theory is when someone knows everything,
but nothing works.
Practice is when everything works,
but no one knows why.

Hermann Hesse

As described in Chap. 1, the main components that contribute in the four *OLIMPO* bands are cosmic microwave background, Sunyaev-Zel'dovich effect, galactic dust emission and far infrared background. In this chapter, we want to predict the maps in the four bands and see if *OLIMPO* is able to separate the signals, reconstruct the input maps and disentangle between different models.

Contributions due to cosmic microwave background and Sunyaev-Zel'dovich effect are well known, hence producing maps due to these signals at different frequencies is quite simple.

The former is an almost gaussian distribution of anisotropies having the angular power spectrum shown in Fig. 1.5; the full sky map, as obtained by WMAP, is displayed in Fig. 1.3.

The latter, in the Kompaneets approximation, is described by eq. (1.44), hence it is the product between the analytic expression of the spectrum and the comptonization parameter y. The former is a function of the temperature of the intracluster gas only, and it is shown in Fig. 1.9. Comptonization parameter is obtained from hydrodynamical simulations [11, 106]: they follow the process of formation and evolution of galaxy clusters in a cosmological framework. These simulations include a advanced treatment of several processes, such as radiative cooling, star formation, thermal conduction, release of metals and energy feedback from supernovae type Ia and II. The result of these simulations is a box containing a very high number of particles ($\sim 10^{10}$ in the largest one, the *Millennium Simulation* [107]): integrating along the line of sight, it is possible to obtain an accurate simulation of a map of the comptonization parameter.

Galactic dust emission and far infrared background are not well known yet, in particular at millimeter and submillimeter wavelengths. Thus, models of these contributions are still uncertain: we will explain and use two of the most appreciated. Upcoming ground,

balloon and satellite experiments such as *OLIMPO* will put stronger constraints.

6.1 Galactic dust model

The model #8 by Schlegel, Finkbeiner and Davis [38] is thought to be the most accurate model that describes the far infrared and microwave emission from the diffuse interstellar dust in the Galaxy. It starts from the high resolution, far infrared *IRAS* data and calibrates it with the *DIRBE* data ($\nu = 3000 GHz$). This model is then extended to *FIRAS* and *DMR* frequencies, $100 \div 2100 GHz$ and $31.5 \div 90 GHz$ respectively. The outputs of the model are full sky maps at submillimeter and microwave bands.

This is a multicomponent model, because it takes into account the presence in the interstellar medium of many types of molecules and dust grains, and it fits all the available data in the range $200 \leqslant \nu \leqslant 3000 GHz$. The previous model has a single component and estimates a ν^2 dust emissivity power law: this is inconsistent with the *FIRAS* data below $800 GHz$.

The model analyzes only the sky regions where the far infrared emission is expected to be dominated by diffuse interstellar medium. Hence, a spatial mask that excludes the Galactic plane below $|b| = 7°$ is created, the Magellanic Clouds and the HII regions in Orion and Ophiuchus. Another 1.3% of the sky is masked where the *FIRAS* coverage is missing or incomplete, and a further 15% where the *FIRAS* pixel weight is less than 0.4. Overall, 4378 pixels are included: they cover $\sim 71\%$ of the sky observed by *FIRAS*, at 123 frequencies, thus a total of ~ 540000 data. Moreover, a fit on each frequency is made considering an unbound starting point: this avoids that the solution is influenced by uncertainties in the infrared background radiation.

This model has been developed in the limit of quite big grains, $0.01 < a < 0.25 \mu m$, where a is the grain radius: they are not heated up for a small amount of time, but remain in thermal equilibrium with the surrounding radiation field (see § 1.4). Furthermore, since the grain's emission wavelength scales proportionally to its volume a^3, bigger grains dominate the submillimeter emission. Smaller grains, $a < 0.01 \mu m$, can be heated up temporarily at very high temperatures and dominate the emission at $\lambda \lesssim 100 \mu m$ ($\nu \gtrsim 3000 GHz$), but they do not contribute significantly to submillimeter emission, nor are important in the *FIRAS* frequencies interval.

6.1.1 Multicomponent models

Assuming for each component an emissivity following a power law in the *FIRAS* bands, it is possible to sum all the elements in order to construct a multicomponent model:

$$I_{p,\nu} = \frac{\sum_k f_k \, Q_k(\nu) \, B_\nu(T_{pk})}{\sum_k f_k \, Q_k(\nu_0) \, B_{\nu_0}(T_{pk}) \, K_{100}(\alpha_k, T_{pk})} \cdot I_{p,100} \tag{6.1}$$

where f_k is the normalization factor for the k^{th} component; T_{pk} is the temperature in the pixel p of the component k; $I_{p,100}$ is the flux in the pixel p of a *DIRBE* calibrated map at $\lambda = 100 \mu m$.

$Q_k(\nu)$ is the emission efficiency, i.e. the ratio between the grain cross section and the geometric one. Since the grains taken in consideration are very small in respect to the emission wavelength, $Q(\nu) \propto a$: this is due to the fact that the grains are so small that all the parts of the grains are close enough to the grain surface to take part in the emission.

$K_{100}(\alpha, T)$ is the color correction factor of the *DIRBE* filter at $100\mu m$, when observing a spectrum $\nu^\alpha B_\nu(T)$. The emissivity ε_ν of the dust and the *DIRBE* frequency response $W(\nu)$ are combined to form the color correction factor K_b in the band b. Using an emissivity model $\varepsilon = \nu^\alpha$, we get:

$$K_b(\alpha, T) = \int B_\nu(T)\, \nu^\alpha\, W(\nu)\, d\nu \tag{6.2}$$

These correction factors are well approximated by the function:

$$K(\alpha, T) = \frac{\sum_n a_n(\alpha)\, \tau^n}{\sum_m b_m(\alpha)\, \tau^m} = \log T \tag{6.3}$$

where the a and b coefficients depend only on α. Moreover, we can define the emission opacity as the emission cross section per unit mass:

$$\kappa(\nu) = \frac{\pi\, a^2}{\varrho\, V}\, Q(\nu) = \frac{3}{4\varrho\, a}\, Q(\nu) \tag{6.4}$$

Since in the limit $a \ll \lambda$, Q/a does not depend on a, the opacity $\kappa^{em}(\nu)$ does not depend on the dimensions of the grains too. The frequency dependance is a power law:

$$\kappa^{em}(\nu) = \kappa^{em}(\nu_0)\, \left(\frac{\nu}{\nu_0}\right)^{\alpha_k} \tag{6.5}$$

where α_k is the emissivity index of the k^{th} component and $\kappa^{em}(\nu_0)$ is the opacity of the k species at the reference frequency $\nu_0 = 3000\, GHz$.

f_k can be interpreted as the fraction of power absorbed by the interstellar medium and re-emitted in the far infrared band by the k^{th} component, so that $\sum_k f_k = 1$.

In order to decrease the degrees of freedom of the model, the components are assumed to be in thermal equilibrium with the *InterStellar Radiation Field* (ISRF) that is assumed to have everywhere a constant spectrum varying only in intensity. Thus, the total power per unit mass absorbed by the species k is:

$$U_k^{in} = \kappa_k^* \int_0^\infty I_{ISRF}(\nu)\, d\nu \tag{6.6}$$

where κ_k^* represents the effective absorption opacity (cross-section per mass) to the ISRF in the limit of low optical depth, i.e. the one integrated over the whole band. The absorbed power is then re-emitted at infrared wavelengths:

$$U_k^{out} = \int_0^\infty \kappa_k^{em}\, B_\nu(T_k)\, d\nu \tag{6.7}$$

If every species is in thermal equilibrium with the external field, the equality $U_k^{in} = U_k^{out}$ holds and it is possible to obtain the temperature of a component as a function of that of the other components temperature:

$$T_i^{4+\alpha_i} = \frac{q_j\, Z(\alpha_j)}{q_i\, Z(\alpha_i)} \left(\frac{h\nu_0}{k_B}\right)^{\alpha_i-\alpha_j} T_i^{4+\alpha_j} \tag{6.8}$$

where $q = \kappa^{em}(\nu_0)/\kappa^*$ is the ratio of far-IR emission cross section to the UV/optical absorption cross section. The integrals are included in the function $Z(\alpha)$.

In conclusion, every component is described by three global parameters (f_k, q_k and α_k) and a parameter that varies with the position on the sky, $T_k(x, y, z)$. From eq. (6.8), it follows that there is only one independent temperature per line of sight, related to the $100\mu m/200\mu m$ *DIRBE* flux ratio. Temperatures of the various species are coupled, so that they all correspond to the same interstellar radiation field.

6.1.2 Results

Thermal emission of galactic dust is well estimated in the millimeter and submillimeter bands by a model with only two components with temperatures varying on the sky. The best estimation of the model is obtained for $\alpha_1 = 1.67$, $\alpha_2 = 2.70$, $f_1 = 0.0363$, $f_2 = 1 - f_1$ and $q_1/q_2 = 13.0$ and gives $\chi^2 = 1.85 \cdot DOF$. For such a model, the relation between the temperatures of the two components is:

$$T_1 = 0.352\, T_2^{1.18} \tag{6.9}$$

The mean temperatures are $\langle T_1 \rangle = 9.4K$ and $\langle T_2 \rangle = 16.2K$ for the 71% of the sky used for the model. The colder component is related to amorphous silicates with emissivity $\nu^{1.7}$ and the hotter one to carbon having emissivity $\nu^{2.7}$.

Even if there is good agreement between the best fit model and *FIRAS* data, there are some differences on some sky regions: in order to find them, the sky is divided in many areas according to the observables. If the subdivision is made according to the temperature or dust column density, no discrepancy is found. Sectioning according to the dust-to-gas ratio, regions where the dust-to-gas ratio exceeds the high-latitude average by more than a factor of 2 are designated "molecular" (14% of the sky), while remaining pixels are designated "atomic". Since the full sky fits are dominated by the molecular sky, the model fits that zone with a correlation slope near unity at all frequencies. However, atomic regions show deviations relative to the model that approach $\sim 15\%$ at low frequencies. Presumably, the difference between molecular and atomic areas depends on the intrinsic characteristic of the grains. Since there is a degeneration of parameters, it is possible to vary their values in the fit in order to fit data better (see Fig. 6.1).

As the model agrees with *FIRAS* data at $500\,GHz$, we can assume this model to be a good representation of the sky emission. Hence, it will be used to simulate the dust emission in the *OLIMPO* bands.

Nevertheless, this model underestimates the dust emission at *DMR* frequencies: at $90\,GHz$, the excess is only a factor 1.2, while it increases to 2.5 and 20 for 53 and $31.5\,GHz$ respectively. This excess microwave emission is clearly correlated with the dust, but not

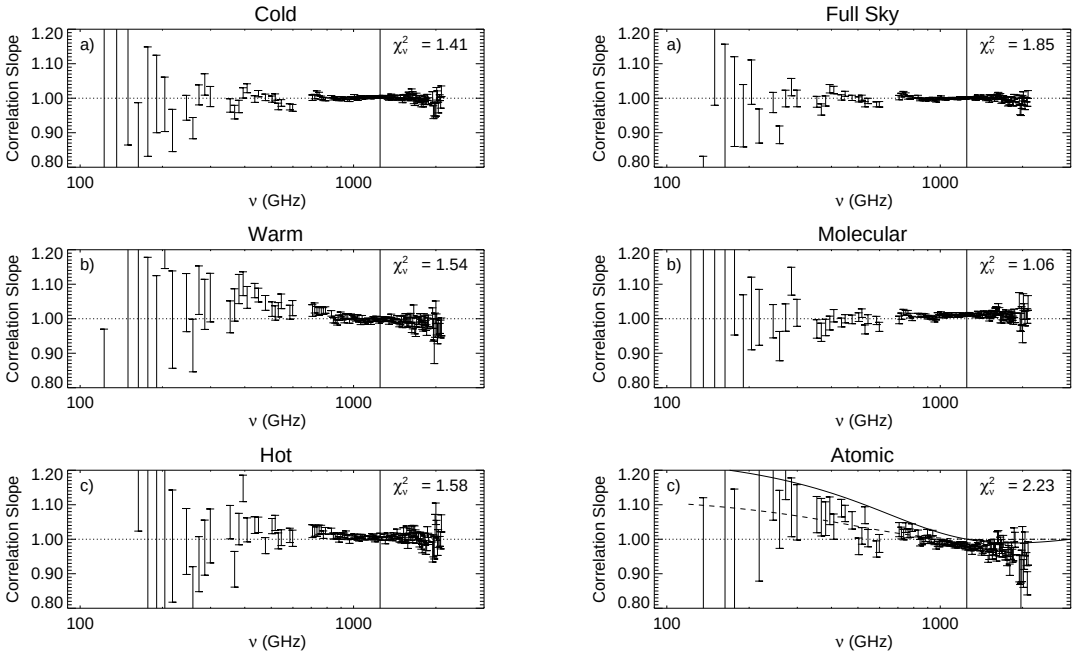

(a) *Sky division based upon dust temperature* (b) *Sky division based upon dust to gas ratio*

Figure 6.1: *FIRAS versus best fit model correlation slopes. On the left, the sky is divided into three zones based upon temperature: cold regions* ($\mathcal{R} = I_{100\mu m}/I_{240\mu m} < 0.62$)*, warm regions* ($0.62 < \mathcal{R} < 0.69$)*, and hot regions* ($\mathcal{R} > 0.69$)*. On the right, sky is divided into two zones based upon dust to gas ratio: full sky, areas dominated by molecular clouds, and areas dominated by atomic gas. In this latter case, modified best fit models are overplotted. Solid line:* $f_1 = 0.0465$*; dashed line:* $q_1/q_2 = 15.0$*. The vertical line is drawn at* $240\mu m$ ($\nu = 1250 GHz$)*, where the models are constrained to fit the DIRBE measurements.*

due to its thermal (vibrational) emission. There are three possible causes, not well understood yet: magnetic dipole emission from paramagnetic grains, electric dipole emission from rapidly spinning dust grains or correlation between dust and *bremsstrahlung* emission; galactic synchrotron emission is not a favored explanation because it is unlikely to be highly correlated with the dust.

6.2 Far infrared background model

As described in § 1.5, the origin of the cosmic infrared background is due to unresolved point sources: this signal is expected to dominate the two higher channels of *OLIMPO*, together with the galactic dust emission. There is not a universally accepted model, since the far infrared background is still not well understood.

Among others, the model made by Lagache, Dole and Puget [65] has the advantage of being simple, with a low number of parameters and components and to fit the available observations. It constrains in a simple way the galaxy luminosity function evolution with redshift, fits the existing source counts and redshift distributions, CIB intensity and ob-

servations of fluctuations, from the mid infrared to the submillimeter bands. The model is based on local template spectra of *starburst* and *normal* galaxies, and on the local infrared luminosity function.

6.2.1 Ingredients of the model

The originality of this model consists in distinguishing the sources of CIB in two categories, *starburst* and *normal* galaxies, and in empirically separating their evolution.

At long wavelengths, resolving the sources is quite difficult; thus, the characterization of the galaxies is a time-consuming process. The *FIRBACK* survey at $170\mu m$ detected about 200 galaxies [29], which constitute about 10% of the CIB. Sources detected by *FIRBACK* can be subdivided into two population:

- One cold and faint ($L \sim 10^9 \div 10^{11} L_\odot$).
- One cold or hot, but bright ($L \sim 10^{12} L_\odot$), with redshift $z \lesssim 1.2$.

Optical spectroscopy reveals that the brightest *FIRBACK* sources have a starburst nature with a moderate star formation rate ($10 M_\odot/yr$).

In the submillimeter band, most of the indications come from the *SCUBA* deep surveys: they suggest that faint $850\mu m$ sources are ultraluminous galaxies at redshift between 1 and 4 [36] and are related to merging processes [70]. The results show that the integrated power of the luminosity function, at $z \gtrsim 0.5$, must be dominated by sources having a luminosity $L \sim 10^{11} L_\odot$, while the local luminosity function is dominated by sources with $L \sim 5 \cdot 10^{10} L_\odot$.

At low redshifts, most of the infrared sources are starburst; the AGNs contribution dominates only at very high luminosities: $L > 2 \cdot 10^{12} L_\odot$. The AGNs background energy is $\sim 10\%$ of that of stars: this is obtained considering the whole CIB energy budget, and based on the assumptions that 10% of the mass accreting into black hole is turned into energy and that the black hole masses measured in the *Hubble Deep Field* are typical for all galaxies. Nevertheless, starburst galaxies evolve more rapidly than AGNs, which give a negligible contribution to the CIB.

It is clear that AGNs do not dominate the output energy of the infrared band; thus, we can conclude that infrared galaxies are dominated by processes of star formation and that it is correct to use a spectral energy density typical of these star forming galaxies. The differences in SEDs for the small fraction of AGNs neglected does not affect significantly the results of the model, which is built with only two galaxy populations, normal and starburst, defined by their SEDs [65].

Starburst galaxies These galaxies emit more than 95% of their energy in the far infrared. Their spectra are predicted using the emission model of the dust [27] and the observational correlation for the *Bright Galaxy Sample* of *IRAS* between the flux ratios 12/60, 25/60 and 60/100 and the infrared luminosity. The model used here starts from the latter, which is modified on the basis of newer constraints coming from recent observations. The significant improvements are:

1. The substitution of the PAH templates, keeping the same amount of the energy in the mid infrared: the original model uses a template by [27], now replaced by that of [23].
2. The shape of the spectrum is modified in the near and mid infrared: the proportions between PAH and small grains are increased by a factor ~ 2, adding extinction terms slowly increasing with luminosity.
3. At longer wavelengths, spectrum has been flattened and the infrared peak broadened.

The representation of the adopted galactic SED assigns only one spectrum per luminosity, neglecting the color dispersion observed for a given luminosity. This is due to the fact that there are not enough measured colors to do an accurate statistical analysis of their variation with luminosity. The resulting template is shown in Fig. 6.2.

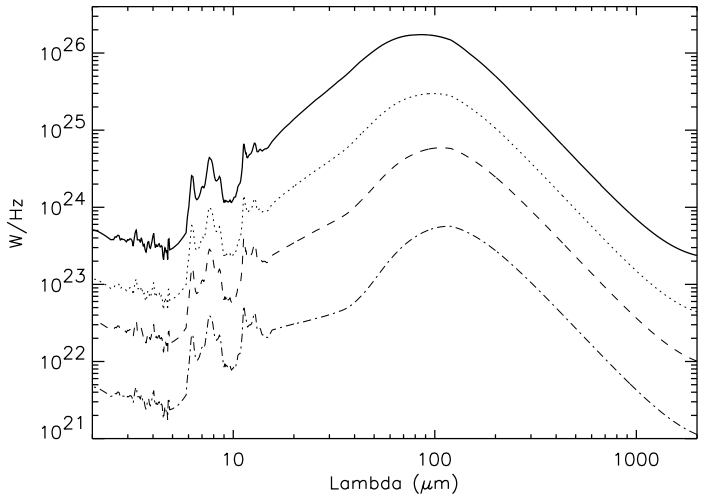

Figure 6.2: *Starburst model spectra for different luminosities. Solid line:* $L = 3 \cdot 10^{12} L_{\odot}$*; dotted line:* $L = 5 \cdot 10^{11} L_{\odot}$*; dashed line:* $L = 1 \cdot 10^{11} L_{\odot}$*; dot-dashed line:* $L = 1 \cdot 10^{10} L_{\odot}$.

Normal galaxies Normal galaxies are defined as the standard infrared counterpart of spiral galaxies, which emit more than half of their energy in the optical band. They are described by a unique spectrum, mainly derived from the *ISOPHOT* survey [109]. Data of the normal galaxies are well fit by the "cold" template presented in Fig. 6.3. In the mid infrared part of the template, the spectral signature that applies to the majority of star forming galaxy is used. More observations around the maximum intensity ($\sim 100 \div 200 \mu m$) and in the submillimeter band are needed in order to improve the template and describe its variations with luminosity.

Luminosity function A detailed comparison between the luminosity function of bright infrared galaxies and that of other extragalactic objects is described by Sanders &

Mirabel [101]: it shows an excess in the expected values with respect to the Press-Schechter function. Moreover, below $\sim 10^{11} L_{\odot}$, most of the objects selected in the optical band are faint far infrared sources. The infrared luminosity function can be subdivided in two parts: one at "low luminosity", dominated by normal galaxies, which follow the form of the optical luminosity function; the other at "high luminosity", dominated by starburst galaxies. The luminosity function used in the model is shown in Fig. 6.4.

It is worth noting that the evolution with redshift of sampled spectra is neglected, both for normal and starburst galaxies. Available data of the high redshift galaxies in the far infrared band do not reveal any evidence for a strong evolution in the characteristic temperature of the color distribution over $0 < z < 3$.

Cosmic infrared background intensity

Given a source at redshift z, its flux S_ν at a certain wavelength $\lambda = \lambda_0$ can be written as a function of the rest frame luminosity L_ν (expressed in *W/Hz*):

$$S_\nu(L, z, \lambda = \lambda_0) = \frac{(1+z)\, K(L,z)\, L_\nu(L, \lambda = \lambda_0)}{4\pi\, D_L^2} \tag{6.10}$$

where D_L is the luminosity distance, which is related to the angular distance defined in eq. (1.50) by $D_L = D_A \cdot (1+z)^2$. $K(L,z)$ is the *K-correction* factor (see § 1.5.2), defined as:

$$K(L,z) = \frac{L_{\nu(1+z)}}{L_{\nu(z=0)}} \tag{6.11}$$

This correction is specific for the spectrum of the considered population given the values of L and z. Hence, the rest frame luminosity L_ν is convolved with the pass band filter centered on $\lambda = \lambda_0$.

The number of sources per solid angle and redshift interval is:

$$\frac{dN}{dz\, d\log L}\,(L,z) = N_0(L,z)\,(1+z)^3\,\frac{dV}{dz} \tag{6.12}$$

where dV/dz is the differential element of volume, once the cosmological parameters are fixed; N is the number of sources per unit volume and luminosity interval as a function of redshift; N_0 is given by the luminosity function.

Differential and integrated counts for a given flux S and at wavelength $\lambda = \lambda_0$ can be written as:

$$\frac{dN}{dS} = \int_L \int_z \frac{dN}{dz\, d\log L}\,(L,z)\,\frac{dz}{dS}\,(L,z)\, d\log L \tag{6.13}$$

$$N(>S) = \int \frac{dN}{dS}\, dS \tag{6.14}$$

Hence, the intensity of the cosmic infrared background I_{CIB} produced by sources with flux $S < S_{Max}$, expressed in *Jy/sr*, is:

$$I_{CIB} = \int_0^{S_{Max}} S\,\frac{dN}{dS}\, dS \tag{6.15}$$

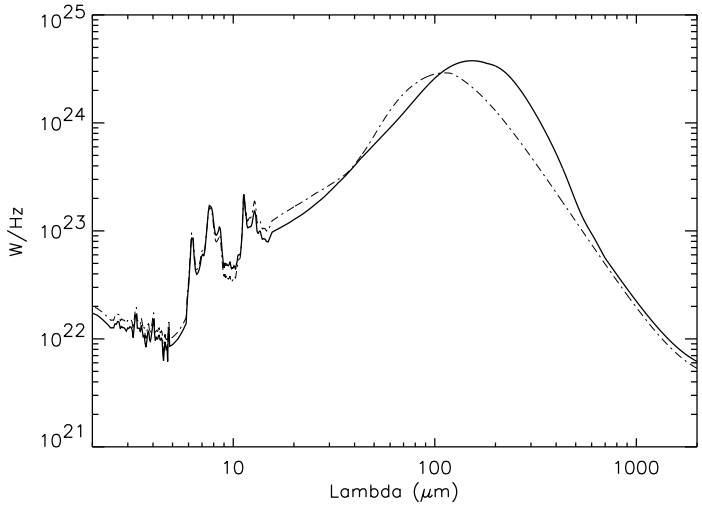

Figure 6.3: *Comparison between the template spectrum for the normal galaxies, represented by the solid line, and the template spectrum for the starburst galaxies, dot-dashed line, for the same luminosity* $L = 5 \cdot 10^{10} L_{\odot}$.

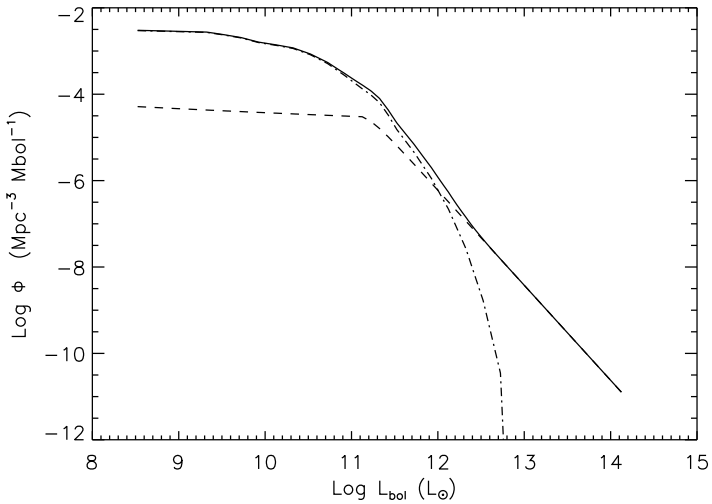

Figure 6.4: *Bolometric luminosity function at* $z = 0$. *Dot-dashed line: normal galaxies; dashed line: starburst galaxies; solid line: total.*

while the fluctuation densities (*shot noise*) due to the sources below the observational flux limit S_0, which corresponds both to the confusion noise (see § 1.5.7) and to the sensibility limit of the experiment, are given by:

$$P_{fluc} = \int_0^{S_0} S^2 \frac{dN}{dS}\, dS \tag{6.16}$$

thus P_{fluc} is expressed in Jy^2/sr.

Cosmological parameters are set joining measurements of distance−luminosity relation from type Ia supernovae [90, 99], galaxy distances using Cepheids [43] and CMB anisotropies (see Tab. 1.1). Then, the sampled spectrum of the normal and starburst galaxies must be computed: a spectrum is associated for each population and luminosity. Finally, the best evolution of the luminosity function, described by eq. (6.12), is determined, in order to reproduce the number counts, the CIB and its fluctuations (eqs. (6.13), (6.14), (6.15) and (6.16) respectively). The luminosity function is assumed to have an independent evolution for the two populations.

The intensity of the cosmic infrared background at various wavelengths is shown in Tab. 6.1 and Fig. 6.5, compared to recent observations. It is worth noting the good agreement between the estimates at $170\mu m$ and the measurements of *FIRAS*.

λ (μm)	**Predicted CIB** (MJy/sr)	**Predicted CIB** (Wm^{-2}/sr)	**Measured CIB** (Wm^{-2}/sr)
15	$1.25 \cdot 10^{-2}$	$2.5 \cdot 10^{-9}$	$> 2.4 \pm 0.5 \cdot 10^{-9}$
60	0.12	$2.5 \cdot 10^{-9}$	–
100	0.35	$6.1 \cdot 10^{-8}$	$\sim 1.5 \cdot 10^{-8}$
170	0.76	$1.3 \cdot 10^{-8}$	$1.4 \pm 0.3 \cdot 10^{-8}$
350	0.76	$6.5 \cdot 10^{-9}$	$5.63^{+4.30}_{-2.80} \cdot 10^{-9}$
850	0.20	$6.9 \cdot 10^{-10}$	$5.04^{+4.31}_{-2.61} \cdot 10^{-10}$

Table 6.1: *Predicted intensity of the cosmic infrared background at* $15\mu m$ (*ISOCAM*), $60\mu m$ *and* $100\mu m$ (*IRAS*), $170\mu m$ (*ISOPHOT*), $350\mu m$ *and* $850\mu m$ (*SCUBA*) *compared to measurements: see* [65] *and references therein.*

6.2.2 Confusion noise

As already described in § 1.5.7, the confusion noise is defined as the fluctuation of the sky brightness due to the sources that cannot be individually resolved. These fluctuations are caused by the intrinsically discrete nature of the source: in the far infrared, submillimeter and millimeter bands, due to the limited dimensions of the telescope if compared to the wavelength, confusion noise plays a fundamental role in the total noise budget. In fact, it is usually larger than instrument noise, thus it limits the survey depth. The total variance σ^2 of the signal, due to the extragalactic sources having a flux lower than S_{min}, is given by:

$$\sigma^2 = \int f^2(\vartheta, \varphi)\, d\vartheta\, d\varphi \int_0^{S_{lim}} S^2 \frac{dN}{dS}\, dS \tag{6.17}$$

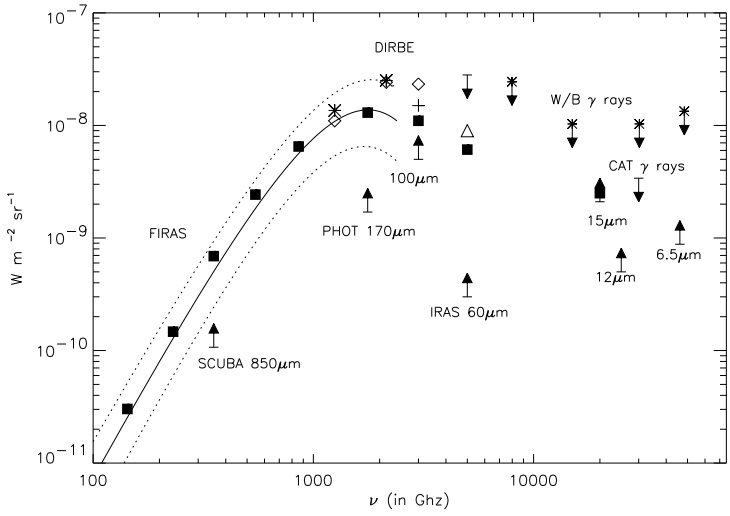

Figure 6.5: *Cosmic infrared background intensity in the mid infrared and millimeter bands. The CIB derived by model at selected wavelengths is represented by colored squares.*

where $f(\vartheta, \varphi)$ is the bidimensional beam profile in sr, S in the flux measured in Jy and dN/dS are the differential counts in $Jy^{-1} sr^{-1}$ given by eq. (6.13); S_{lim} is called the *confusion limit.*

Confusion noise is determined using a photometric criterion: it is related to the quality of photometry of the sources having a measured flux near S_{lim}. It is defined by the equation:

$$S_{lim} = q_{phot}\, \sigma(S_{lim}) \tag{6.18}$$

where q_{phot} measures the photometric accuracy and it is usually taken between 3 and 5.

Confusion limits are computed using Ω rather than the integral of the bidimensional beam profile of eq. (6.17). This leads to an overestimate of σ by a factor 1.33.

6.3 Map making

OLIMPO will produce four maps, one for each band: in order to increase the signal-to-noise ratio, each small patch of sky will be scanned many times, resulting in an integration time of $\sim 30s$ per beam. Producing maps from real, noisy data is a difficult and time-consuming task [81]: in the following, we assume the maps have been already produced, calibrated and smoothed to have the same beam size at each frequency.

Once the models are chosen, the next step consist in simulating the maps of the four components (CMB, SZ, galactic dust and FIRB) in the four bands of *OLIMPO* and summing them together with a noise map for each frequency. Each map is subdivided into many pixels, each of which corresponds to an angular dimension usually taken to be $\vartheta_{pixel} = \vartheta_{FWHM}/3$, where ϑ_{FWHM} is the value of the full width half maximum of the beam in *arcmin.*

Maps are generated by inserting in the models described in the previous paragraphs the *OLIMPO* characteristics: beam size, integration time, observed region in the sky, number and noise of the receivers. Here we describes the results for a simulation of an observation of $10^\circ \times 10^\circ$ using the following specifications:

Beam size We assume it is the same at each frequency; with real data, this can be achieved by smoothing the higher resolution maps to the largest beam size. In our case, it is $\vartheta_{FWHM}(\nu = 143\,GHz) = 5'$.

Integration time We take it to be $T_{int} = 1h = 3600s$ per deg^2, hence for a map of $10^\circ \times 10^\circ = 100 deg^2$ it is $T_{int} = 100h$.

Observed region This input defines the central position of the map. It is required by the program that simulates the galactic dust component. Choosing a clean region, i.e. one at high galactic latitudes, is important. The choice is made together with the cluster selection (see § 2.2), and leads to a galactic latitude of 65° and longitude 155°.

Receivers They are 19 at $143\,GHz$ and 37 in the other channels. The noise of each receiver is obtained by interpolating to our frequencies the ones measured with *BOOMERanG* 2003 flight [72]. The computed *Noise Equivalent Temperature* (NET) for each bolometer of the four bands is reported in Tab. 6.2.

	BOOMERanG			***OLIMPO***			
ν (GHz)	145	245	345	143	217	353	545
NEP $(10^{-17}\,W/\sqrt{Hz})$	2.49	3.89	8.95	2.46	3.50	9.35	19.07
NET $(\mu K/\sqrt{Hz})$	137.0	281.0	309.0	137.2	240.7	316.4	828.3

Table 6.2: *Estimated Noise Equivalent Power* (*NEP*) *and Temperature* (*NET*) *values for the OLIMPO experiment. They are obtained interpolating to our frequencies the values measured in the BOOMERanG* 2003 *flight* [72].

Once the parameters are set, maps of each component at the four frequencies are computed. These are expressed in μK, so that the CMB anisotropy signal is the same in each channel: hence, the other maps must be divided by the derivative of the black body function computed at $T_{CMB} = 2.735K$. Then, the signal of each pixel is convolved with the pass band filter function. Finally, the map is convolved with the beam experiment function.

Cosmic microwave background anisotropies map

Since we decided to express the maps in μK, i.e. in terms of thermodynamic temperature fluctuations of a $2.725K$ blackbody, the signal due to CMB anisotropies is frequency independent. The map is Gaussian random realization having a null average value and the angular power spectrum measured by WMAP, shown in Fig. 1.5 and defined by the cosmological parameters reported in Tab. 1.1. Then, the map is spatially convolved with the beam function:

$$f(\vartheta, \varphi) = \frac{1}{\sqrt{2\pi}\,\sigma} \exp\left(\frac{1}{2}\frac{\vartheta^2 + \varphi^2}{\sigma^2}\right) \tag{6.19}$$

Hence, it is a Gaussian function with a symmetric shape; the standard deviation is related to the full width half maximum as $\sigma = \vartheta_{FWHM}/\sqrt{8\ln 2}$. Finally, the convolution is computed:

$$\mathcal{S}_{CMB}(\vartheta, \varphi) = \int_0^{\vartheta}\int_0^{\varphi} \Delta_{CMB}(\vartheta', \varphi')\, f(\vartheta', \varphi')\, d\vartheta'\, d\varphi' \tag{6.20}$$

Sunyaev-Zel'dovich effect map

In order to realize this map, we calculate the SZ spectrum in the Kompaneets approximation, as given by eq. (1.41). This is due to the fact that hydrodynamical simulations are computed in the non relativistic limit, hence the map of the comptonization parameter has the same approximation.

As a consequence, the spectrum of all the clusters present in the map is independent of the gas temperature. With these approximations, spatial information are given by the map of the comptonization parameter $y(\vartheta, \varphi)$, which multiplies a constant signal that, in μK, is given by:

$$\begin{aligned} \Delta_{SZ,B} &= \frac{2(k_B T_0)^4}{h^3 c^2} \int_0^{\infty} 10^6\, T_0\, E_B(\nu)\, \frac{g(\nu)}{\left.\dfrac{\partial B\,(\nu, T)}{\partial T}\right|_{T=T_0}}\, d\nu \\ &= 10^6\, T_0 \int_0^{\infty} E_B(\nu) \left[\frac{h\nu}{kT_0} \cdot \coth\left(\frac{h\nu}{2kT_0}\right) - 4\right] d\nu \end{aligned} \tag{6.21}$$

where $E_B(\nu)$ represents the pass band filter spectrum of the four channels. Δ_{SZ} is multiplied by the map of the comptonization parameter $y(\vartheta, \varphi)$ and then normalized in respect to $E_B(\nu)$, i.e. it is divided by the integral of its spectrum. Finally, the map is convolved with the beam as done for the anisotropies' map in eq. (6.20):

$$\mathcal{S}_{SZ,B}(\vartheta, \varphi) = \int_0^{\vartheta}\int_0^{\varphi} \Delta_{SZ,B} \cdot y(\vartheta', \varphi')\, f(\vartheta', \varphi')\, d\vartheta'\, d\varphi' \tag{6.22}$$

Galactic dust map

The model described in § 6.1 comes with a complete IDL program, which rescales the IRAS $100\mu m$ map to the desired frequency. It requires as inputs the galactic latitudes and longitudes of the pixels and the frequency of each band.

The region of sky to observe is chosen so that the dust contribution is as small as possible and it is rich of known clusters (see § 2.2). Since the program requires a lot of time to run ($\sim 3min$ for a map of $10^\circ \times 10^\circ$ and one frequency), we cannot compute the signal on the whole pass band filter spectrum. Hence, in order to compute the mean frequency of each band, we convolve *a priori* the filter transmission function with a simplified dust model having a ν^2 emissivity:

$$\langle \nu_B \rangle = \frac{\displaystyle\int_0^\infty E_B(\nu)\, B(\nu, T_{Dust}) \left(\frac{\nu}{\nu_{Dust}}\right)^2 \nu\, d\nu}{\displaystyle\int_0^\infty E_B(\nu)\, B(\nu, T_{Dust}) \left(\frac{\nu}{\nu_{Dust}}\right)^2 d\nu} \tag{6.23}$$

where $T_{Dust} = 20K$ and $\nu_{Dust} = 300\,GHz$. Finally, the resulting map is convolved with the beam as done before, obtaining $\mathcal{S}_{Dust,B}(\vartheta, \varphi)$.

Far infrared background map

The far infrared background map is computed assuming a Gaussian random distribution $\mathcal{N}(\Delta_{FIRB,B}, \sigma_{FIRB,B}, \vartheta, \varphi)$ which is then convolved with the experiment beam function. The model described in § 6.2 requires the flux limit, the redshift and luminosity intervals of integration, together with the *OLIMPO* characteristics.

The *flux limit* F_{lim}, or confusion limit, can be expressed as:

$$F_{lim} = \frac{\Delta W_B}{A_{tel}} \cdot N_\sigma \tag{6.24}$$

where ΔW_B is the power variance of the receivers in each band, $A_{tel} = \pi\, 2^2\, m^2$ is the area of the telescope and N_σ defines the threshold limit. Thus, from eq. (6.28), considering that ΔW_B is expressed in W so that we must use the *Noise Equivalent Power* (NEP) instead of the NET, we get:

$$F_{lim} = \frac{3}{5} \frac{NEP_B}{A_{tel}} \cdot N_\sigma \tag{6.25}$$

Together with the flux limit and band, the model requires appropriate redshift and luminosity intervals: $0.008 \leqslant z \leqslant 8$ and $10^9 \leqslant L/L_\odot \leqslant 10^{14}$. We used the values of the fluxes and differential counts $dN/d\ln L/dz$ (source number per unit luminosity and redshift) obtained by the simulations on the *Planck* surveys. The values obtained for the source counts as a function of flux ($\log N - \log S$) of the two populations are shown in Fig. 6.6.

Choosing a threshold flux small enough, $S_{lim} = 10^{-8} mJy$ (where $1Jy = 10^{-26}\ W\, m^{-2}\ Hz^{-1}$), it is possible to obtain the total signal of the far infrared background, at a given frequency, due to the contribution of all the sources (starburst and normal galaxies) and their fluctuations.

The program returns the average FIRB signal $\Delta_{FIRB,B}$ in Jy/sr and its standard deviation $\sigma_{FIRB,B}$ in $Jy/\sqrt{sr}$ for each galaxy population. The total signal is just the sum of the two populations, while the total fluctuation is computed summing in quadrature the two contribution.

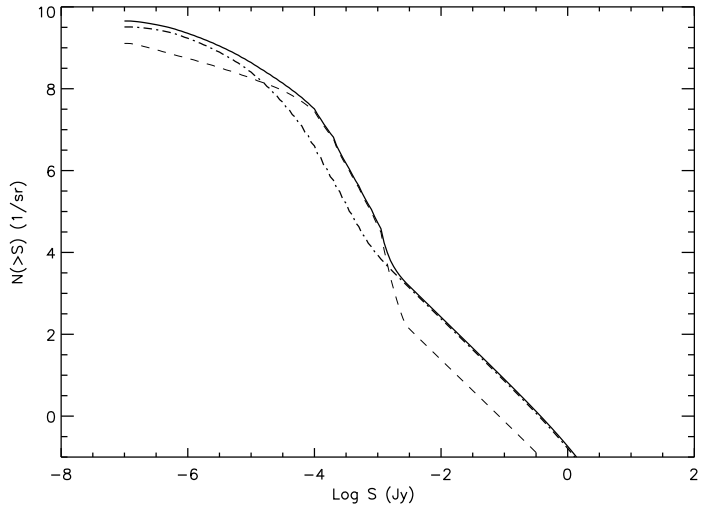

Figure 6.6: *Distribution of the source counts as a function of the flux* ($\log N - \log S$). *Dashed line: source counts distribution due to starburst galaxies; dot-dashed line:* ($\log N - \log S$) *due to normal galaxies; solid line: it represents the sum of the two populations.*

The total signal is then converted in μK using the same integral of eq. (6.21). Since the fluctuations are given in Jy^2/sr, in order to express them in μK, they must be divided by the beam computed in sr: $\Omega_{Beam} = \lambda^2/A_{tel}$. Hence, eq. (6.21) becomes:

$$\sigma_{FIRB,B}[\mu K] = \int_0^\infty 10^6\, T_0\, E_B(\nu)\, \frac{\sqrt{\sigma_{FIRB,B}[Jy^2/sr]}}{\sqrt{\Omega_{Beam}}\, \left.\dfrac{\partial B\,(\nu,T)}{\partial T}\right|_{T=T_0}}\, d\nu \tag{6.26}$$

Then, the final signal is the convolution between the beam experiment and the Gaussian distribution of the FIRB sources:

$$\mathcal{S}_{FIRB,B}(\vartheta,\varphi) = \int_0^\vartheta \int_0^\varphi \mathcal{N}(\Delta_{FIRB,B}, \sigma_{FIRB,B}, \vartheta', \varphi')\, f(\vartheta',\varphi')\, d\vartheta'\, d\varphi' \tag{6.27}$$

Noise map

The final map to generate is the noise one. We assume that the noise has a Gaussian random distribution, which is a strong constrain since real data are usually affected by correlated noise between pixels. Obviously, the noise has a null average value, while the standard deviation is:

$$\Delta_{Noise,B} = \frac{NET_B\, N_{pixel}}{\sqrt{T_{int}\, N_{bolo,B}}} = \frac{3}{5}\, \frac{NEP_B}{\sqrt{N_{bolo,B}}} \tag{6.28}$$

where NET_B is the noise in $\mu K/\sqrt{Hz}$ of each bolometer, $N_{bolo,B}$ is the number of receivers in each channel, T_{int} is the integration time and N_{pixel} is the number of pixel in a row (or

column) of the map, hence:

$$\frac{N_{pixel}}{\sqrt{T_{int}}} = \frac{3 \cdot 60' \cdot deg}{5' \cdot \sqrt{3600s \cdot deg^2}} = \frac{3}{5}\frac{1}{\sqrt{s}} \tag{6.29}$$

Results

Tab. 6.3 shows the total signal, in Jy/sr, coming from the two populations, while the fluctuations, in Jy^2/sr, are summed in quadrature. The analysis is done using the flux limit per unit frequency, i.e. $F_{lim,\nu} = F_{lim}/\nu$, with $N_\sigma = 5$ and $A_{tel} = 2^2\pi\, m^2$.

Figs. 6.7 and 6.8 show the spectra of the four components, representing brightness and temperature respectively. Tab. 6.4 reports the minimum and maximum values of the different components at each frequency band. The produced maps are shown in Fig. 6.9.

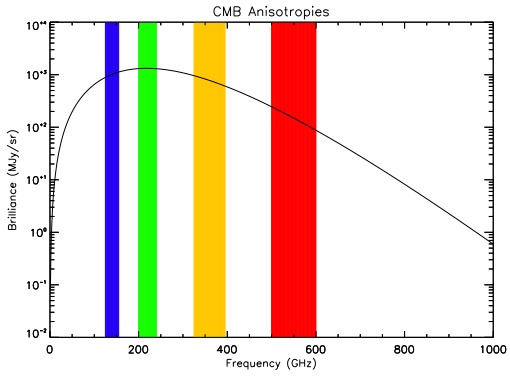

(a) *CMB anisotropies spectrum in MJy/sr*

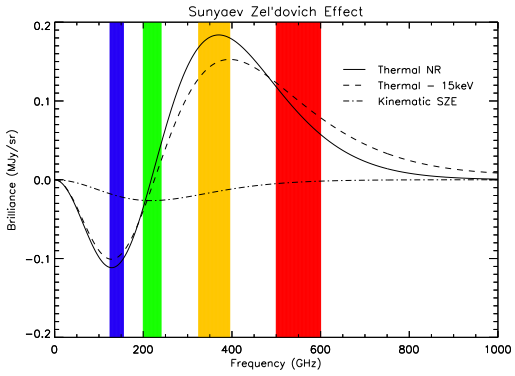

(b) *SZ effect spectrum in MJy/sr*

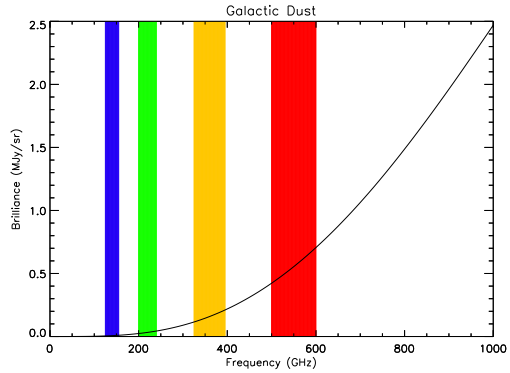

(c) *Galactic dust spectrum in MJy/sr*

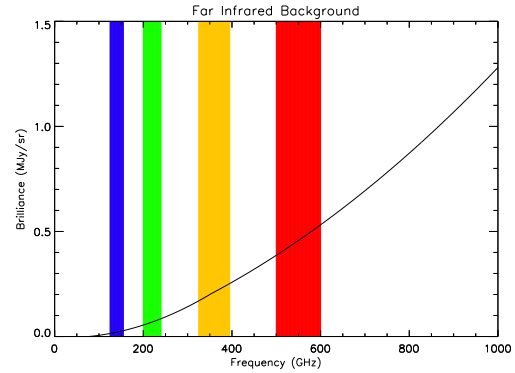

(d) *FIRB background spectrum in MJy/sr*

Figure 6.7: *Brightness spectra of the four components simulated. The four frequency bands of OLIMPO are also shown. The Sunyaev-Zel'dovich effect is computed for a cluster having* $y = 10^{-4}$*, both with and without relativistic corrections.*

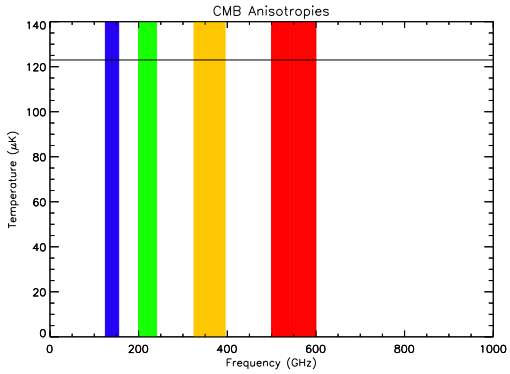

(a) *CMB anisotropies spectrum in μK*

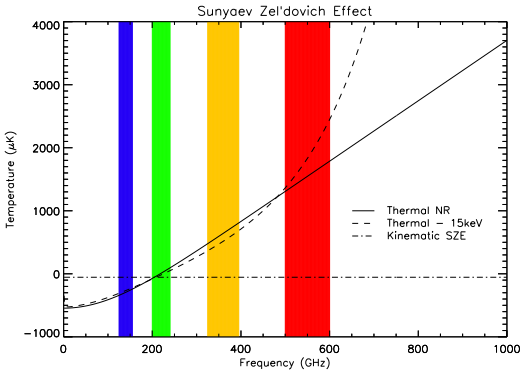

(b) *SZ effect spectrum in μK*

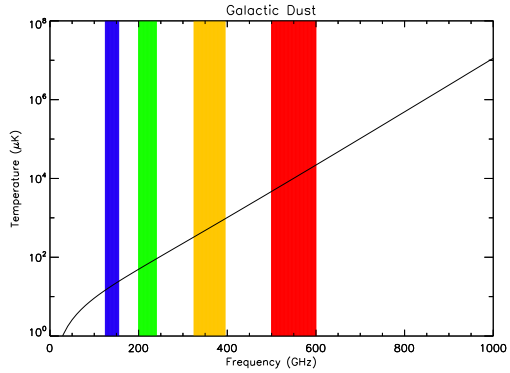

(c) *Galactic dust spectrum in μK*

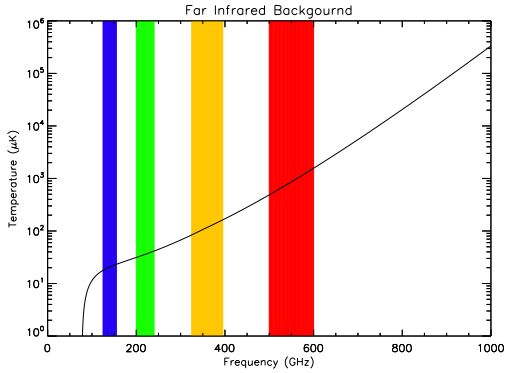

(d) *FIRB spectrum in μK*

Figure 6.8: *Temperature spectra of the four components simulated. The four frequency bands of OLIMPO are also shown. The CMB anisotropies spectrum is flat, while dust and far infrared background models do not work below* $100\,GHz$*. It is worth noting that the relativistic corrections to Sunyaev-Zel'dovich effect diverges from classic thermal component at high frequencies, but they are much smaller than galactic dust contribution at the same frequency.*

$\nu\ (GHz)$	143	217	353	545
Number of sources	$4.24 \cdot 10^9$	$4.58 \cdot 10^9$	$4.47 \cdot 10^9$	$4.33 \cdot 10^9$
$F_{lim,\nu}\ (mJy)$	0.50	0.63	1.04	1.37
$\Delta_{FIRB}\ (Jy/sr)$	$2.20 \cdot 10^4$	$6.67 \cdot 10^4$	$2.04 \cdot 10^5$	$4.50 \cdot 10^5$
$\sigma_{FIRB}\ (Jy^2/sr)$	2.02	11.46	145.78	1043.59
$\Delta_{FIRB}\ (\mu K)$	58.20	132.12	675.32	9286.52
$\sigma_{FIRB}\ (\mu K)$	2.92	5.37	31.26	532.82

Table 6.3: *Expected values of far infrared background component for the OLIMPO experiment, assuming an integration time of* $100h$ *on a region of* $10^\circ \times 10^\circ$. *Signal and fluctuations of the FIRB data is computed in the case of the OLIMPO flux limit. These quantities are then convolved with the pass band filter function to express them in* μK.

$\nu\ (GHz)$	143	217	353	545
$\mathcal{S}_{CMB}\ (\mu K)$	$-130 \div 125$	$-130 \div 125$	$-130 \div 125$	$-130 \div 125$
$\mathcal{S}_{SZ}\ (\mu K)$	$-305 \div -3$	$-12 \div 0$	$6 \div 623$	$15 \div 1578$
$\mathcal{S}_{Dust}\ (\mu K)$	$13 \div 46$	$43 \div 150$	$339 \div 1193$	$6560 \div 23076$
$\mathcal{S}_{FIRB}\ (\mu K)$	$55 \div 61$	$127 \div 137$	$646 \div 705$	$8787 \div 9787$
$\mathcal{S}_{Noise}\ (\mu K)$	$-164 \div 166$	$-262 \div 257$	$-347 \div 386$	$-711 \div 792$

Table 6.4: *Expected values of the different components for the OLIMPO experiment, assuming an integration time of* $100h$ *on a region of* $10^\circ \times 10^\circ$. *Table reports the maximum and minimum values for each component at every frequency.*

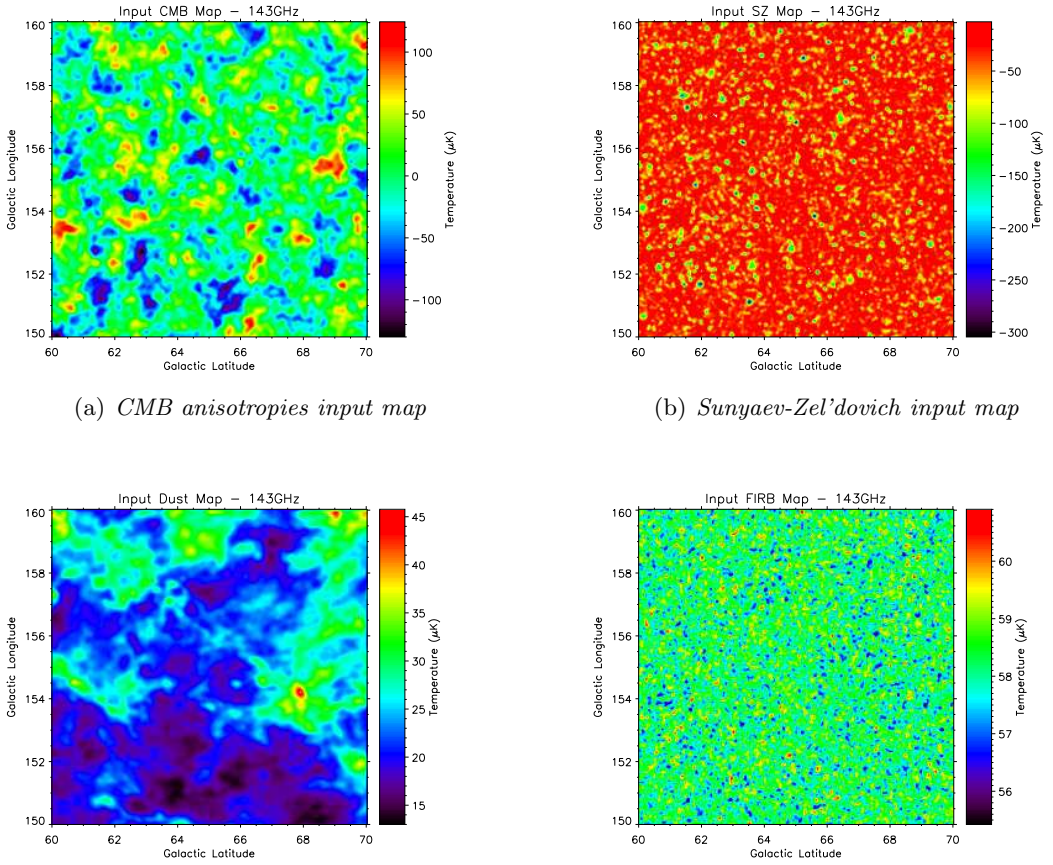

(a) *CMB anisotropies input map*

(b) *Sunyaev-Zel'dovich input map*

(c) *Galactic dust input map*

(d) *Far infrared background input map*

Figure 6.9: *Input maps of the four components at* $143\,GHz$*. Signals are expressed in* μK*. At this frequency, apart from the biggest clusters that produce intense Sunyaev-Zel'dovic effect, the main contribution is due to CMB anisotropies.*

6.4 Map extraction

Once the maps of each component, for each frequency band, are made, they are summed, obtaining the four maps shown in Fig. 6.9. Thus, we finally get four maps, one per each channel, having a signal given by:

$$\begin{aligned} \mathcal{S}_{Tot,B}(\vartheta,\varphi) &= \mathcal{S}_{CMB}(\vartheta,\varphi) + \mathcal{S}_{SZ,B}(\vartheta,\varphi) + \\ &+ \mathcal{S}_{Dust,B}(\vartheta,\varphi) + \mathcal{S}_{FIRB,B}(\vartheta,\varphi) + \mathcal{S}_{Noise,B}(\vartheta,\varphi) \end{aligned} \tag{6.30}$$

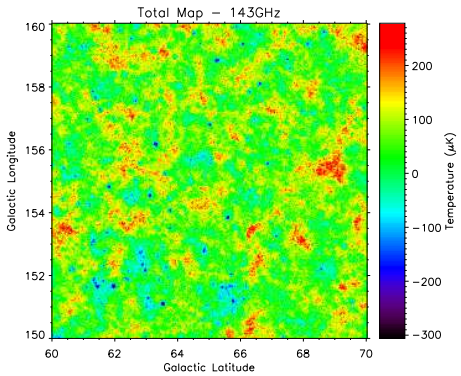

(a) *Total map at* $143GHz$

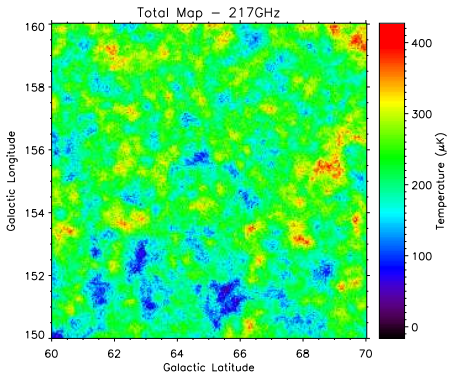

(b) *Total map at* $217GHz$

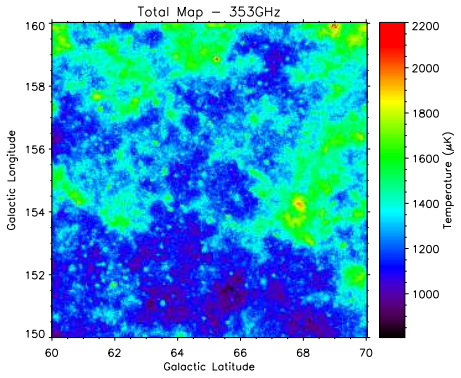

(c) *Total map at* $353GHz$

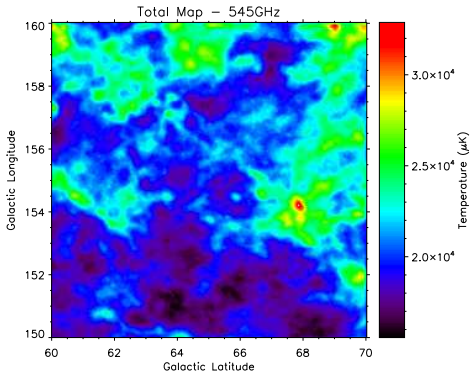

(d) *Total map at* $545GHz$

Figure 6.10: *Total maps predicted at the four frequency bands of OLIMPO: these are the sum of the CMB anisotropies, SZ effect, dust and FIRB components plus the expected noise in the four bands. Signals are expressed in* μK*. It is worth noting how the CMB anisotropy component dominates the* 143 *and* $217GHz$ *channels, while the* 353 *and* $545GHz$ *channels are dominated by galactic dust.*

It is clear how the signal due to Sunyaev-Zel'dovich effect is subdominant in each band; the cosmic microwave background anisotropies dominate the two lower channels, while galactic dust is the main component at 353 and $545GHz$. The far infrared background contribution is comparable to the galactic dust one, but seeing it is more difficult since it lacks of structures at scales larger than beam size.

In order to separate the various components, we compute a χ^2 and minimize it: this method requires the assumption that all the components, including noise, are uncorrelated; moreover, having an *a priori* knowledge of the models that describe the four components is required. The χ^2 is then computed varying the parameters on each pixel of the four maps, obtaining:

$$\chi^2(\mathcal{P}_{CMB}, \mathcal{P}_{SZ}, \mathcal{P}_{Dust}, \mathcal{P}_{FIRB}, \vartheta, \varphi) = \sum_{B=1}^{4} \frac{1}{\Delta^2_{Noise,B}} \cdot \Big[\mathcal{S}_{Tot,B}(\vartheta, \varphi) - \Big(\mathcal{P}_{CMB} + \mathcal{P}_{SZ} \cdot \mathcal{R}_{SZ,B} + \mathcal{P}_{Dust} \cdot \mathcal{R}_{Dust,B} + \mathcal{P}_{FIRB} \cdot \mathcal{R}_{FIRB,B}\Big)\Big]^2 \tag{6.31}$$

where $\mathcal{P}$ are the parameters varied to evaluate the χ^2, while $\mathcal{R}$ represents the scale factor of the various component: obviously, the CMB component does not change with frequency.

The range of variation of the parameters is defined by the expected range of values that a component will have at a given frequency (see Tab. 6.4): it is evident that the signal due to SZ effect cannot be positive at $143\,GHz$, as well as the dust and FIRB components must be always positive; as a consequence, it would be useless to calculate the χ^2 outside these ranges. Hence, we are assuming a flat prior on the interval of definition of the parameter.

The probability distribution associated to the χ^2 is called *likelihood*, defined as $\mathcal{L} = \exp(-\chi^2/2)$. Thus, the best estimation of a component at $143\,GHz$ in a given pixel is:

$$\mathcal{S}_{CMB,Ext}(\vartheta, \varphi) = \frac{\displaystyle\int_{\mathcal{P}^{min}_{CMB}}^{\mathcal{P}^{Max}_{CMB}} \int_{\mathcal{P}^{min}_{SZ}}^{\mathcal{P}^{Max}_{SZ}} \int_{\mathcal{P}^{min}_{Dust}}^{\mathcal{P}^{Max}_{Dust}} \int_{\mathcal{P}^{min}_{FIRB}}^{\mathcal{P}^{Max}_{FIRB}} \mathcal{P}_{CMB} \exp\left(-\frac{\chi^2}{2}\right) d^4\mathcal{P}}{\displaystyle\int_{\mathcal{P}^{min}_{CMB}}^{\mathcal{P}^{Max}_{CMB}} \int_{\mathcal{P}^{min}_{SZ}}^{\mathcal{P}^{Max}_{SZ}} \int_{\mathcal{P}^{min}_{Dust}}^{\mathcal{P}^{Max}_{Dust}} \int_{\mathcal{P}^{min}_{FIRB}}^{\mathcal{P}^{Max}_{FIRB}} \exp\left(-\frac{\chi^2}{2}\right) d^4\mathcal{P}} \tag{6.32}$$

and the same for the other three components. This integral is computed using an optimized routine based on the direction set method described in [93]. The results of this extraction are shown in Fig. 6.11: it is clear that cosmic background anisotropies are well extracted, as well as the Sunyaev-Zel'dovich map. Instead, galactic dust and far infrared background are not separated, since their spectra are too similar: a possible solution is to remove the scales larger than $\sim 1^\circ$, which are related to the dominant dust component.

The main advantage of using a model dependent separation criterion is the control you have on the calculations. The drawback is that you must be confident with your models. Moreover, you do not consider the angular power spectra of the components, i.e. their spatial distribution.

CMB anisotropies and Sunyaev-Zel'dovich effect spectra are well known and experimentally confirmed; even the galactic dust model of Schlegel, Finkbeiner and Davis [38] is widely accepted and fits data for $\nu \gtrsim 300\,GHz$, while the dust contribution to lower frequencies is not precisely known yet. The FIRB emission is the less known component of the four considered, hence we decided to slightly change the parameters of the simulation to verify if *OLIMPO* can distinguish between different models.

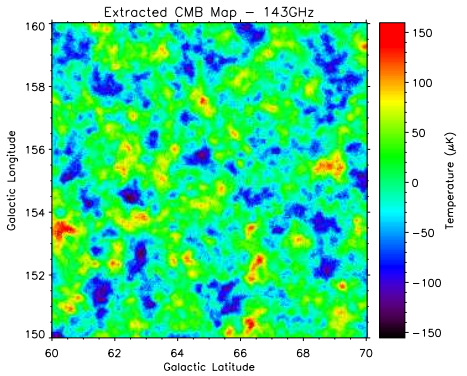

(a) *CMB anisotropies extracted map*

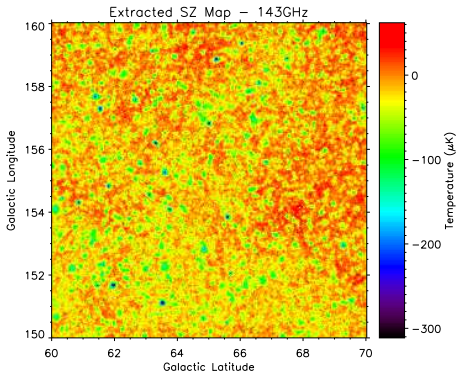

(b) *Sunyaev-Zel'dovich extracted map*

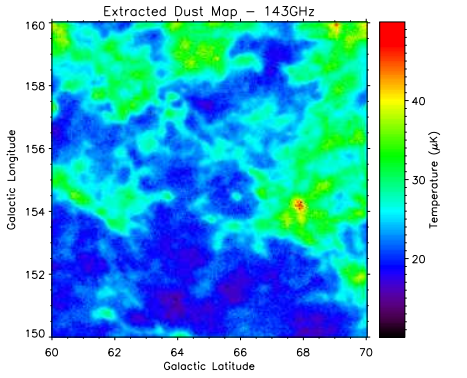

(c) *Galactic dust extracted map*

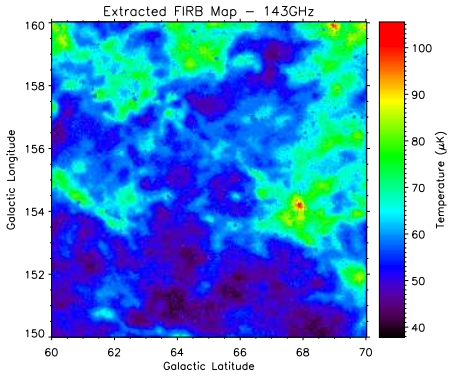

(d) *Far infrared background extracted map*

Figure 6.11: *Extracted maps of the four components at* $143GHz$*. Signals are expressed in* μK*. The anisotropies map is the best extracted; the SZ map clearly shows the brighter clusters; the dust and FIRB component are not separated each other, because their spectra are too similar.*

6.4.1 Variation of the FIRB model

In order to verify if *OLIMPO* is able to distinguish between different models of the FIRB, we modified some of the assumptions of model used, in order to get difference source counts and luminosities. This is achieved with two different hypothesis:

1. We consider one redshift interval $\Delta z = 1$ in the range $z = 0 \div 6$ and we double the number of sources with respect to the original model; this simulates a higher value of the star formation rate in that redshift interval.

2. We consider one redshift interval $\Delta z = 1$ in the range $z = 0 \div 6$ and we double the luminosity of sources with respect to the original analysis, while the number of sources remains the same.

In the first case, we modify the number of sources, their luminosities and their fluxes: in fact, doubling the number of sources requires to double the considered luminosity and the flux as well. The modified signals of the FIRB is computed again in each frequency band and reported in Fig. 6.12: it is clear the strong dependency on the star formation rate of the ratios between the signals due to modified and original models.

Variations are always larger than the confusion limit and *OLIMPO* intrinsic noise: hence, in principle it is possible to disentangle between different models and obtain a good estimation of the star formation rate and luminosity function at different redshifts. The main issue remains the separation of the FIRB and galactic dust components.

6.4.2 Analysis of the SZ map

The last analysis done regards the counts of clusters which produce Sunyaev-Zel'dovich effect. As shown in Fig. 6.11, the extraction of the SZ signal from the total maps is quite good, thanks to the *OLIMPO* characteristics.

We use the *SExtractor* program to select the clusters present in the original map and in the extracted one. The complete analysis of an image is done in two passes through the data. During the first pass, a model of the sky background is built and two statistical estimators are computed. During the second pass, the estimated background of the image is subtracted, then the map is filtered and thresholded. Detections are then deblended, pruned, photometered, classified and finally written to the output catalog. The main inputs required by this program are:

- The full width half maximum of the experiment that produced the map to analyze, in *arcsec*; hence, for *OLIMPO* we have: $\vartheta_{FWHM} = 5' = 300''$.

- The size associated to the pixel in *arcsec*: $\vartheta_{pixel} = \vartheta_{FWHM}/3 = 100''$.

- The definition of a threshold, computed in units of standard deviation of the map background.

- a minimum area of detection, i.e. the area above the threshold, given in $pixel^2$.

As a consequence, a source is identified only if its signal is above the threshold over a region larger than the minimum area of detection.

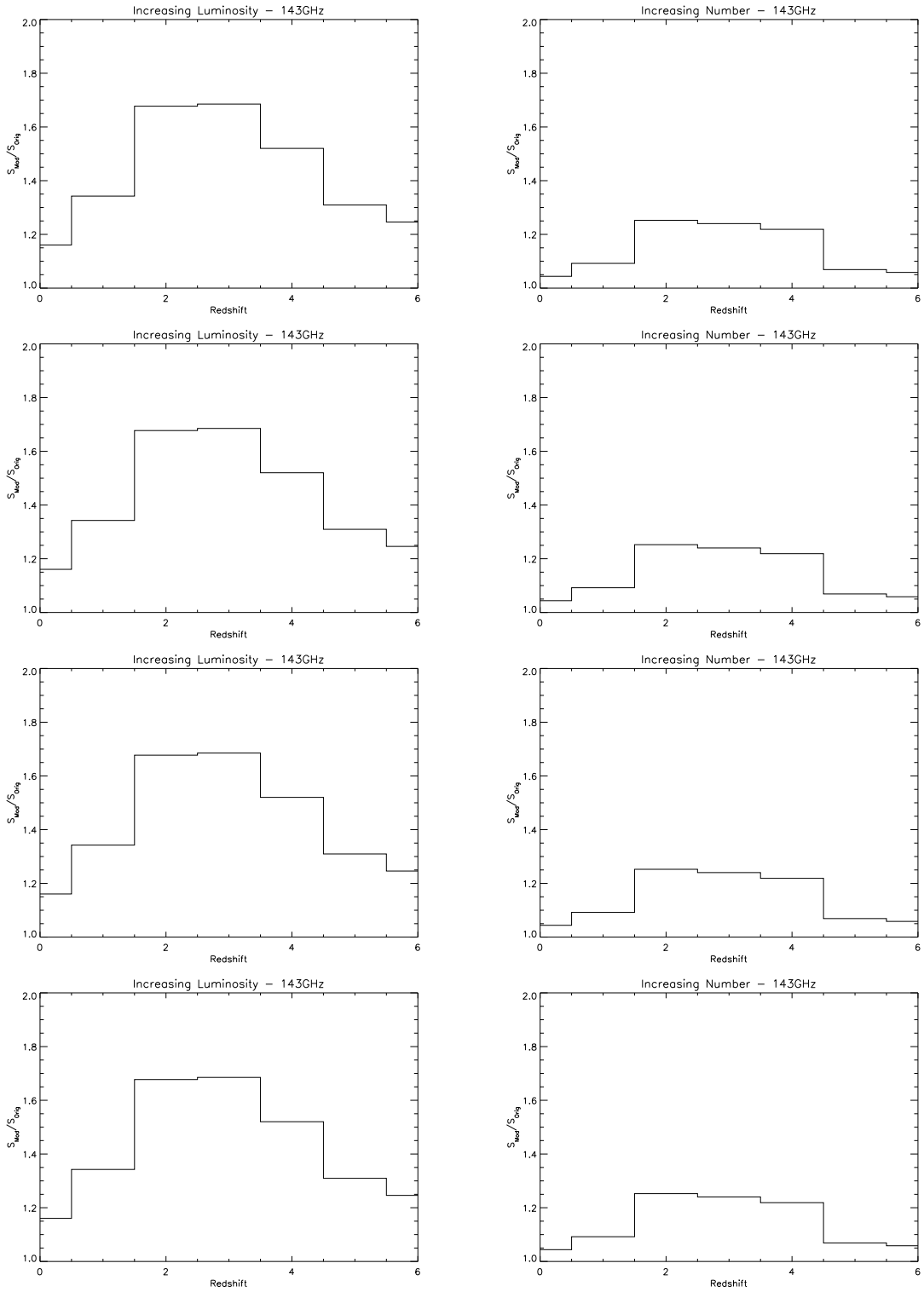

Figure 6.12: *Modifications to FIRB model, doubling the luminosity or number of the sources in each redshift interval. Ratios between the original signal and that obtained by the modified model in the four bands are reported.*

The dimensions of this area are related to the physical dimensions of the pixel and of the source we want to extract. A cluster of galaxies has a typical core radius of $\sim 4'$, which implies a minimum area of detection equal to $16 pixel^2$. Setting the threshold to be $3\sigma_{Sky}$, where σ_{Sky} is the variance of the local background, 268 sources are extracted: if we use the same parameters for the SZ map extracted by the total maps, we find 89 clusters. Decreasing the threshold to 2.5σ, the number of detected sources increases up to 423 in the original map and 152 in the extracted one (see Fig. 6.13).

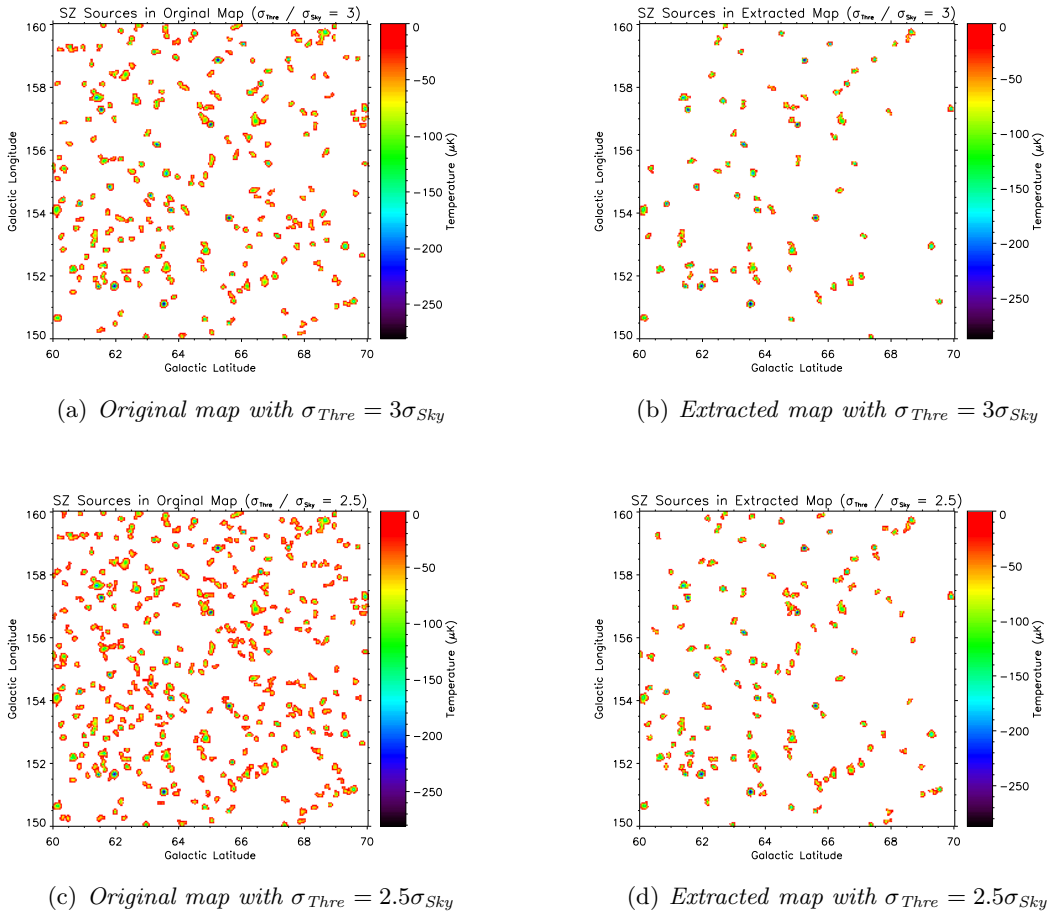

(a) *Original map with* $\sigma_{Thre} = 3\sigma_{Sky}$

(b) *Extracted map with* $\sigma_{Thre} = 3\sigma_{Sky}$

(c) *Original map with* $\sigma_{Thre} = 2.5\sigma_{Sky}$

(d) *Extracted map with* $\sigma_{Thre} = 2.5\sigma_{Sky}$

Figure 6.13: *Source detected in the SZ map using the SExtractor algorithm: with a threshold of* $3\sigma_{Sky}$ *and detectable minimum area of* $16 pixel^2$*, the identified clusters are* 268 *in the original map,* 89 *in the extracted one. Lowering the threshold to* $2.5\sigma_{Sky}$*, the detected sources become* 423 *and* 152 *respectively.*

Finally, we computed the temperature differences for the clusters detected in both the original and extracted maps (see Fig. 6.14). With $\sigma_{Thre} = 3\sigma_{Sky}$, the error is $\sim 15\mu K$. Lowering the threshold to $2.5\sigma_{Sky}$, we detect many clusters that has a temperature lower than the original one (see Fig. 6.14c, second peak centered on $\sim 80\mu K$): this is due to the higher background present in the extracted map. Since *SExtractor* removes it from the whole map, part of the clusters signal is also removed.

The temperature difference is then converted into the difference of the comptonization parameter, obtaining an error on its estimation that is $\sim 5 \cdot 10^{-6}$: note that it is still convolved with the beam, hence the error on the real comptonization parameter is about five times higher.

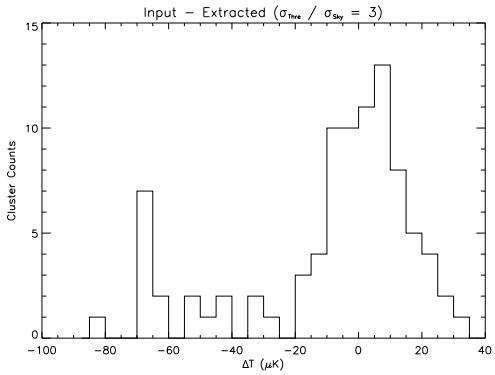

(a) ΔT *with* $\sigma_{Thre} = 3\sigma_{Sky}$

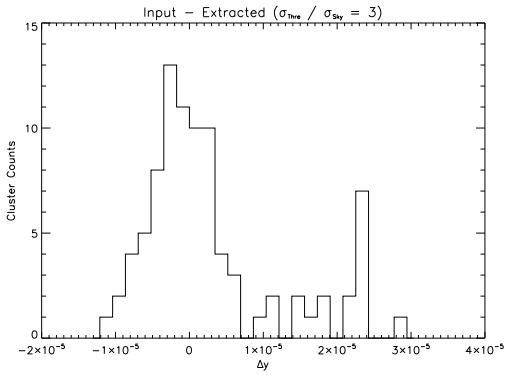

(b) Δy *with* $\sigma_{Thre} = 3\sigma_{Sky}$

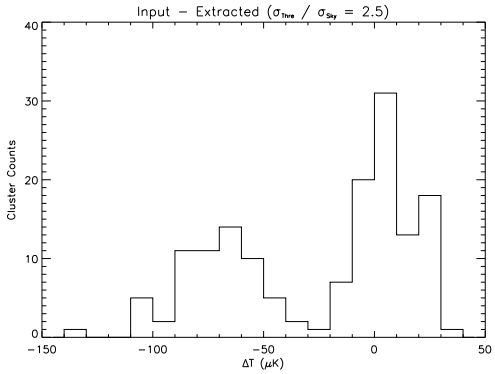

(c) ΔT *with* $\sigma_{Thre} = 2.5\sigma_{Sky}$

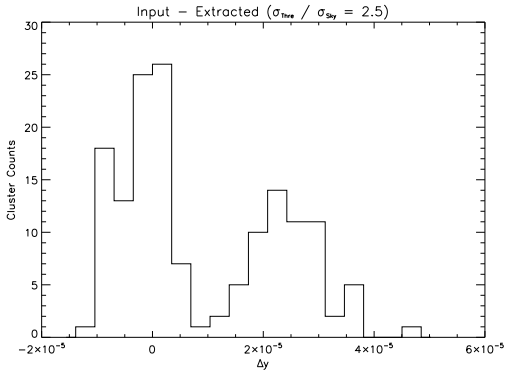

(d) Δy *with* $\sigma_{Thre} = 2.5\sigma_{Sky}$

Figure 6.14: *Difference between original and extracted signal for the clusters detected in both maps. It is clear the lowering the threshold to* $2.5\sigma_{Sky}$*, the errors on temperature and comptonization parameter estimation increase.*

Conclusioni

La prima parte del lavoro si è focalizzata sulla progettazione del sistema ottico criogenico, il quale è in contatto termico con lo stadio a $2K$. Si sono studiate diverse possibili configurazioni, che differiscono per il sistema di modulazione adottato: oscillazione del *Lyot Stop*, oscillazione dello specchio primario attorno al proprio fuoco e al proprio baricentro. Quest'ultima si è infine rivelata l'unica soluzione effettivamente realizzabile meccanicamente, benché comporti l'insorgere di aberrazioni nella posizione di massima oscillazione dello specchio. Esse sono state però minimizzate introducendo un opportuno schema ottico in grado di contenerle all'interno del limite diffrattivo per i due canali a 143 e $217 GHz$. Alla fine del processo di ottimizzazione, le prestazioni del sistema ottico sono eccellenti sia nella configurazione in asse, sia in quella fuori asse. L'efficienza del progetto è stata valutata attraverso l'analisi delle funzioni caratterizzanti il sistema ottico: *Spot Diagram*, *Encircled Energy*, *Point Spread Function*, *Modulation Transfer Function*.

La seconda parte del lavoro ha riguardato il realizzazione degli specchi e della scatola delle ottiche: per la progettazione di quest'ultima non è stato facile ottenere il giusto compromesso tra i diversi requisiti spesso in conflitto. Nel momento in cui tutti gli elementi erano pronti, sono stati assemblati ed eseguiti i test per verificare l'allineamento delle ottiche: la radiazione viene rifuocheggiata in *spot* aventi una dimensione inferiore al millimetro. Possiamo perciò affermare che le ottiche criogeniche sono pronte.

Ci si è poi occupati del progetto del profilo delle antenne: la scelta delle loro caratteristiche è fondamentale per ottimizzare l'accoppiamento tra bolometri e radiazione incidente. Poiché le dimensioni di queste antenne sono confrontabili con la lunghezza d'onda della radiazione in esame, tale studio è stato effettuato in ottica Gaussiana.

Infine, si sono effettuate delle simulazioni dettagliate sulle componenti presenti nelle quattro bande di *OLIMPO* (ν = 143, 217, 353 e $545 GHz$): radiazione di fondo cosmico e sue anisotropie, effetto Sunyaev-Zel'dovich prodotto da ammassi di galassie, polvere interstellare e fondo infrarosso dovuto a sorgenti non risolte ad alto redshift. Le simulazioni dimostrano come *OLIMPO* sia in grado di separare le diverse componenti, requisito fondamentale per effettuare misure di precisione: tra le possibili analisi, si è studiata la capacità dell'esperimento di distinguere diversi modelli per l'emissione del fondo infrarosso, oltre ovviamente alla precisione nella misura dell'effetto Sunyaev-Zel'dovich dovuta agli ammassi presenti nella regione di cielo osservata. Con una soglia limite pari a 3σ vengono rilevati 268 cluster nella mappa iniziale, 89 in quella estratta, senza "falsi positivi".

Sebbene tali analisi devono essere ulteriormente ottimizzate, queste prime simulazioni dimostrano la bontà dell'esperimento *OLIMPO*.

Conclusions

The first part of this work is focused on the design of the optical cryogenic system, which is thermally linked to the $2K$ stage. I analyzed three possible configurations, which differ by the modulation system adopted: wobbling of the *Lyot Stop*, wobbling of the primary mirror around its focus and its barycenter. The latter is the chosen one, since it is the simplest to mechanically realize, even if it implies the presence of aberrations when the telescope is tilted. These have been minimized introducing a suitable optical system that keeps them in the diffraction limit for the two channels at 143 and $217 GHz$. At the end of the optimization process, optical system performances are excellent both in the on-axis and off-axis configurations. The efficiency of the design was evaluated analyzing the functions that characterize the optical system: *Spot Diagram*, *Encircled Energy*, *Point Spread Function*, *Modulation Transfer Function*.

The second part of this work regards the machining of mirrors and optics box: regarding the design of the latter, it was not easy to get the best compromise between different requirements often conflicting. When all the elements were ready, they were assembled together and tested to verify the correct alignment of the optics: radiation is refocused in spots having dimensions below one millimeter. Hence, we can say that the cryogenics optics are ready.

Later on, I designed the profile of the feed horns: the choice of their characteristics is fundamental to optimize the coupling between bolometers and incident radiation. Since the dimensions of these antennas are comparable to the wavelength of the radiation of interest, this study was computed in Gaussian optics.

Finally, I realized detailed simulations on the components that dominate the four bands of *OLIMPO* ($\nu = 143$, 217, 353 e $545 GHz$): cosmic microwave background radiation and its anisotropies, Sunyaev-Zel'dovich effect produced by cluster of galaxies, galactic dust and far infrared background due to unresolved sources at high redshift. Simulations show how *OLIMPO* is able to separate the different components, a fundamental requirement in order to achieve accurate measurements: among the possible analysis, I studied the ability of the instrument to distinguish between various models of the far infrared background emission, as well as the accuracy in the measure of the Sunyaev-Zel'dovich effect due to the clusters present in the observed region of sky. With a threshold of 3σ, 268 clusters are detected in the input map, 89 in the extracted one, without "false positives".

Even if these analyses must be improved, these preliminary simulations demonstrate the quality of the *OLIMPO* experiment.

Appendix A

Optics box executive drawings

Fig. A.1:	External Assembly
Fig. A.2:	Internal Assembly
Fig. A.3:	Splitters Assembly
Fig. A.4:	Box $10mm$ #1
Fig. A.5:	Box $10mm$ #2
Fig. A.6:	Box $1mm$ #1
Fig. A.7:	Box $1mm$ #2
Fig. A.8:	Fridge Cover − Part A
Fig. A.9:	Fridge Cover − Part B
Fig. A.10:	^{4}He Bottom Shield
Fig. A.11:	^{4}He Cover
Fig. A.12:	^{4}He Filter
Fig. A.13:	^{4}He External Shield
Fig. A.14:	Reggetta Bottom
Fig. A.15:	Reggetta In
Fig. A.16:	Reggetta Mirrors
Fig. A.17:	Reggetta Plane
Fig. A.18:	Shield Dx Inf
Fig. A.19:	Shield Dx Sup
Fig. A.20:	Shield Lyot Stop
Fig. A.21:	Shield Sx
Fig. A.22:	Splitter Plane #1
Fig. A.23:	Splitter Plane #2
Fig. A.24:	Splitter Plane #3

Table A.1: *List of the optics box executive drawings reported.*

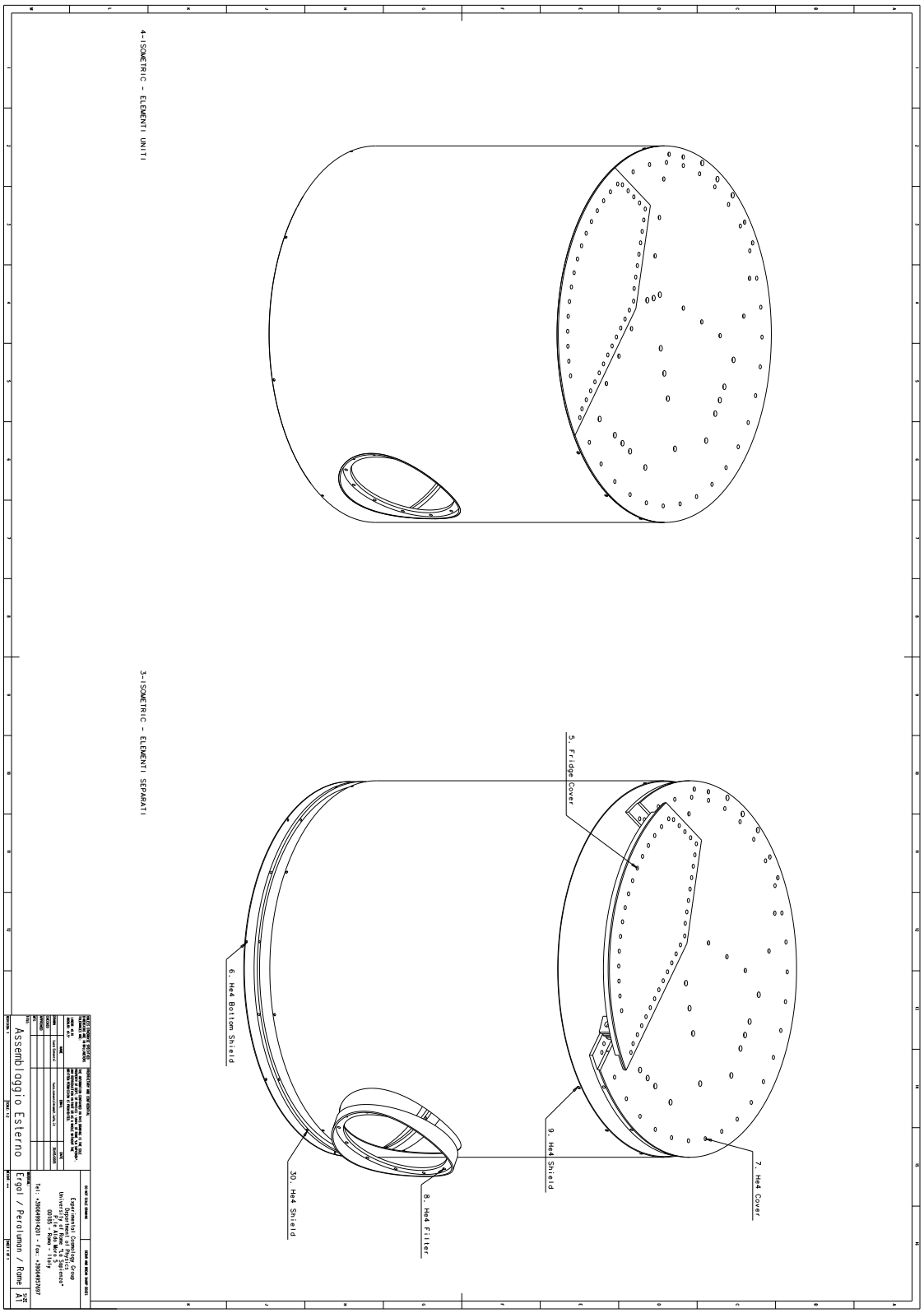

Figure A.1: *Optics box: external assembly.*

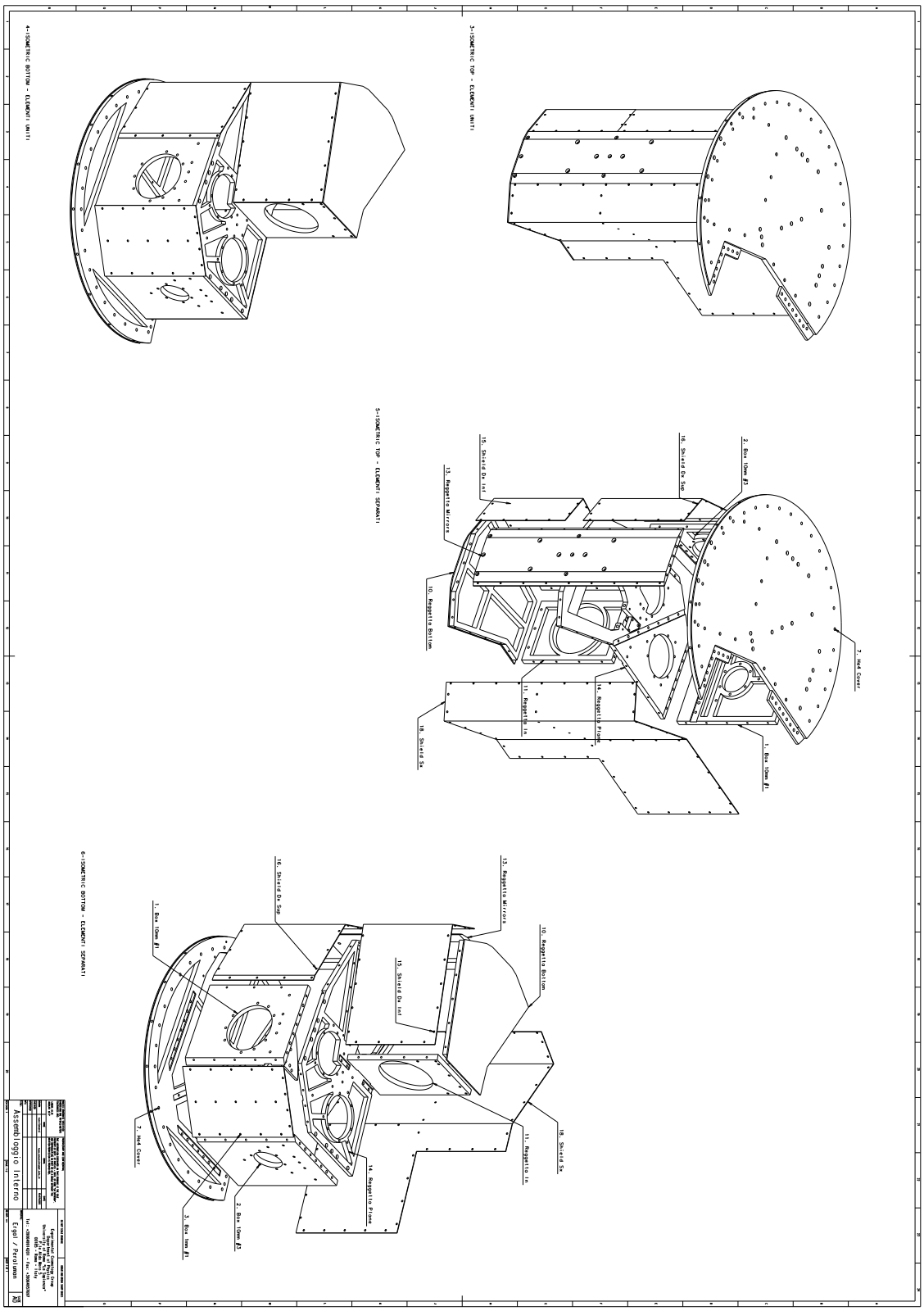

Figure A.2: *Optics box: internal assembly.*

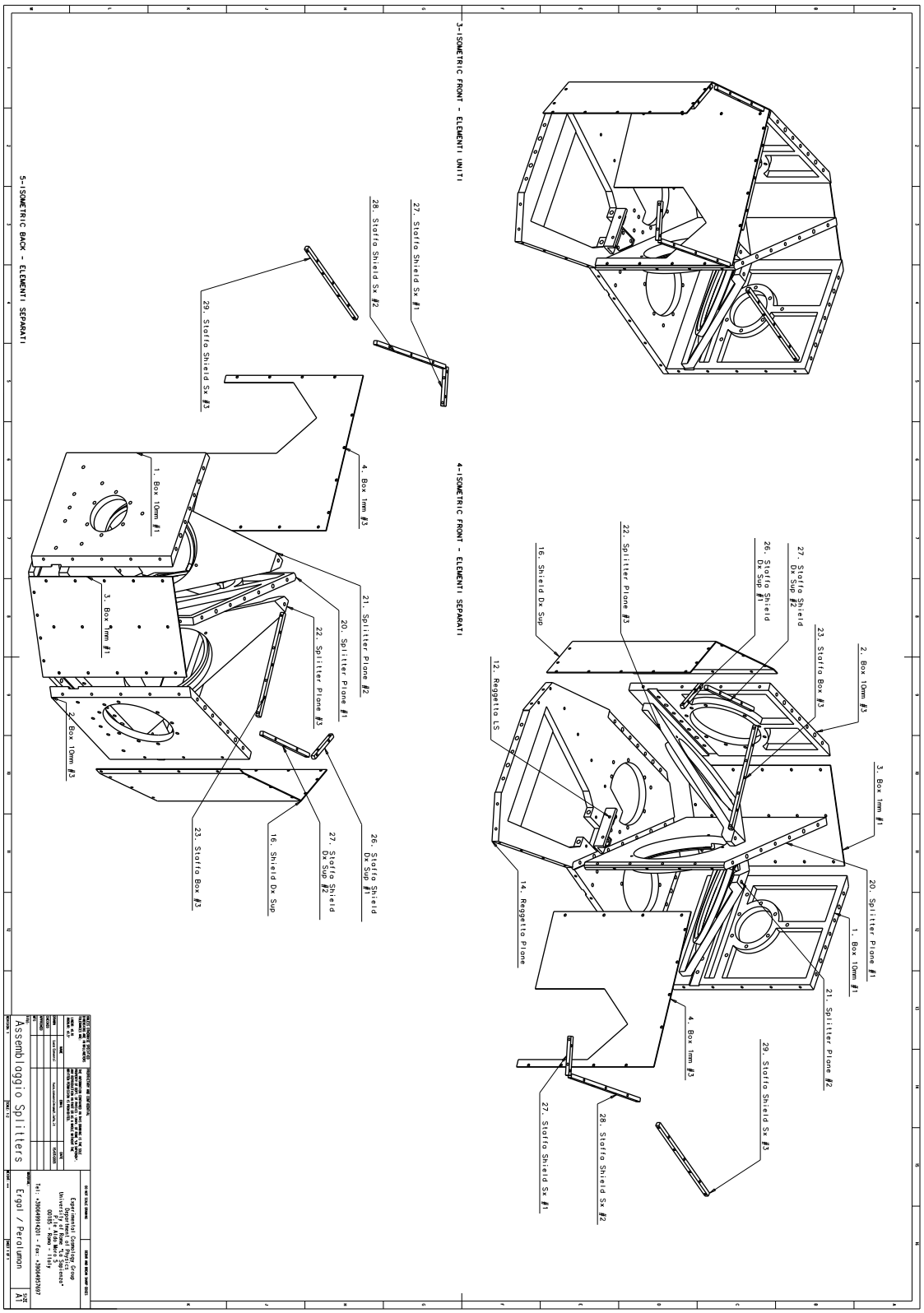

Figure A.3: *Optics box: splitters assembly.*

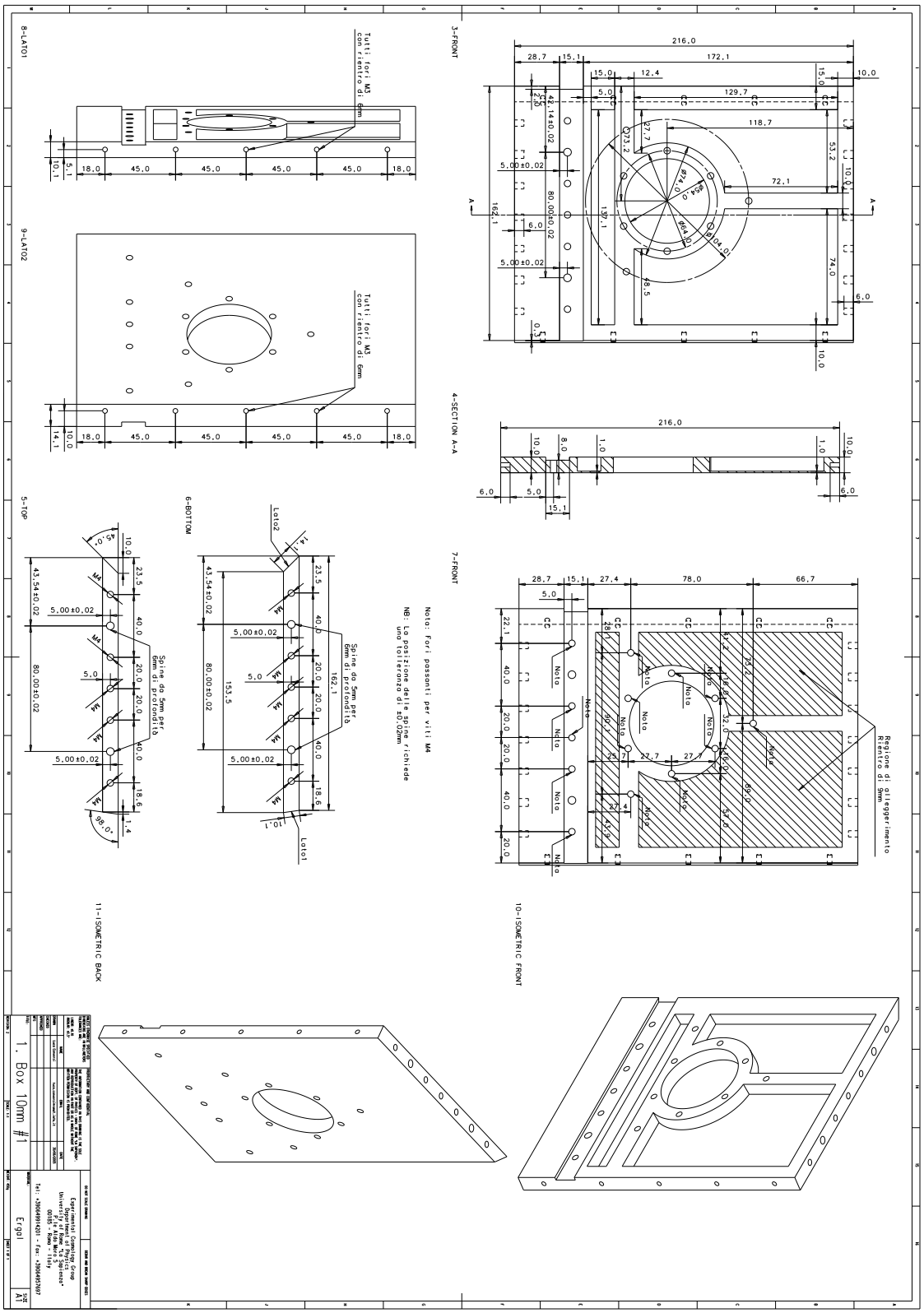

Figure A.4: *Box* 10*mm* #1.

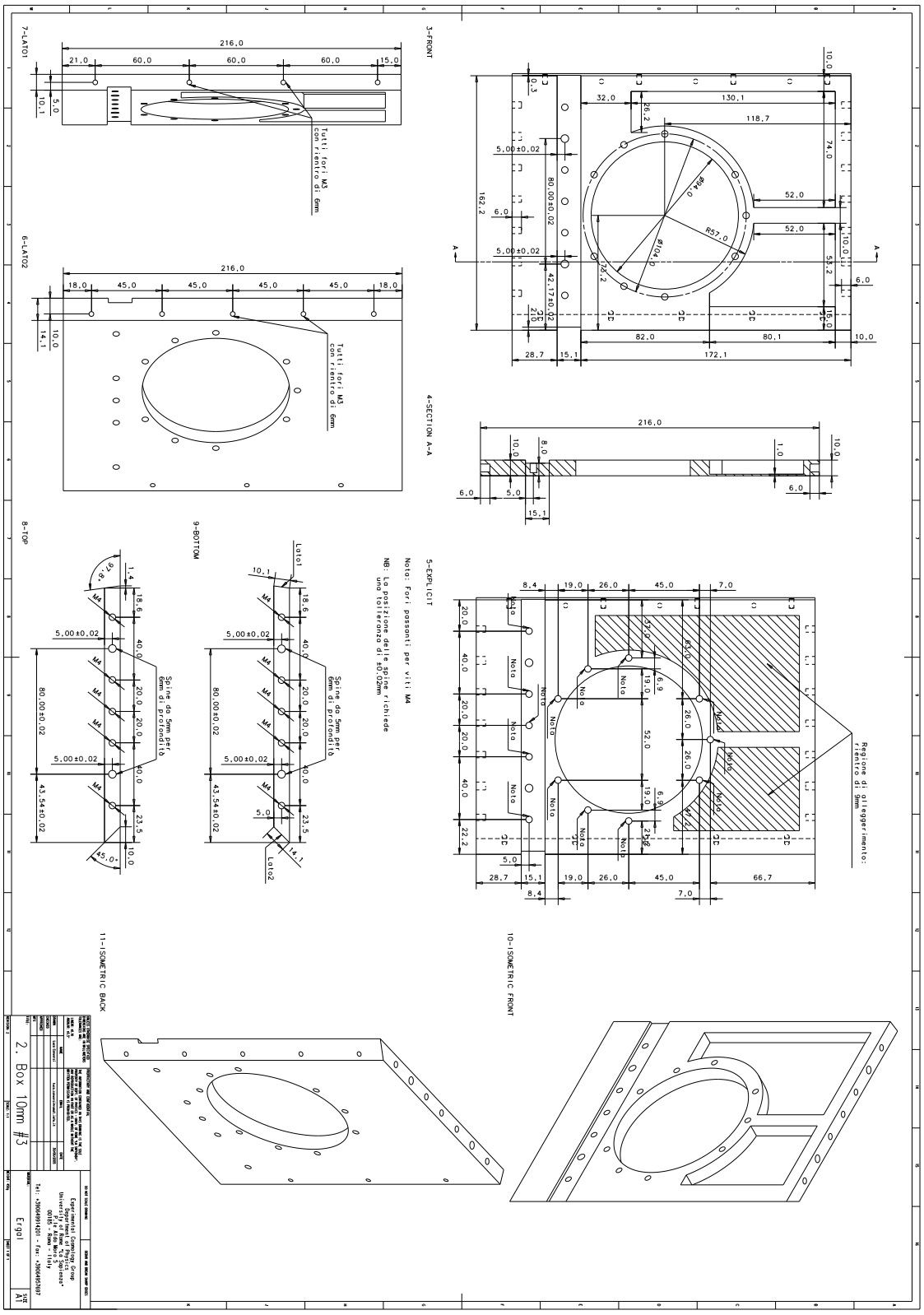

Figure A.5: *Box* 10*mm* #2.

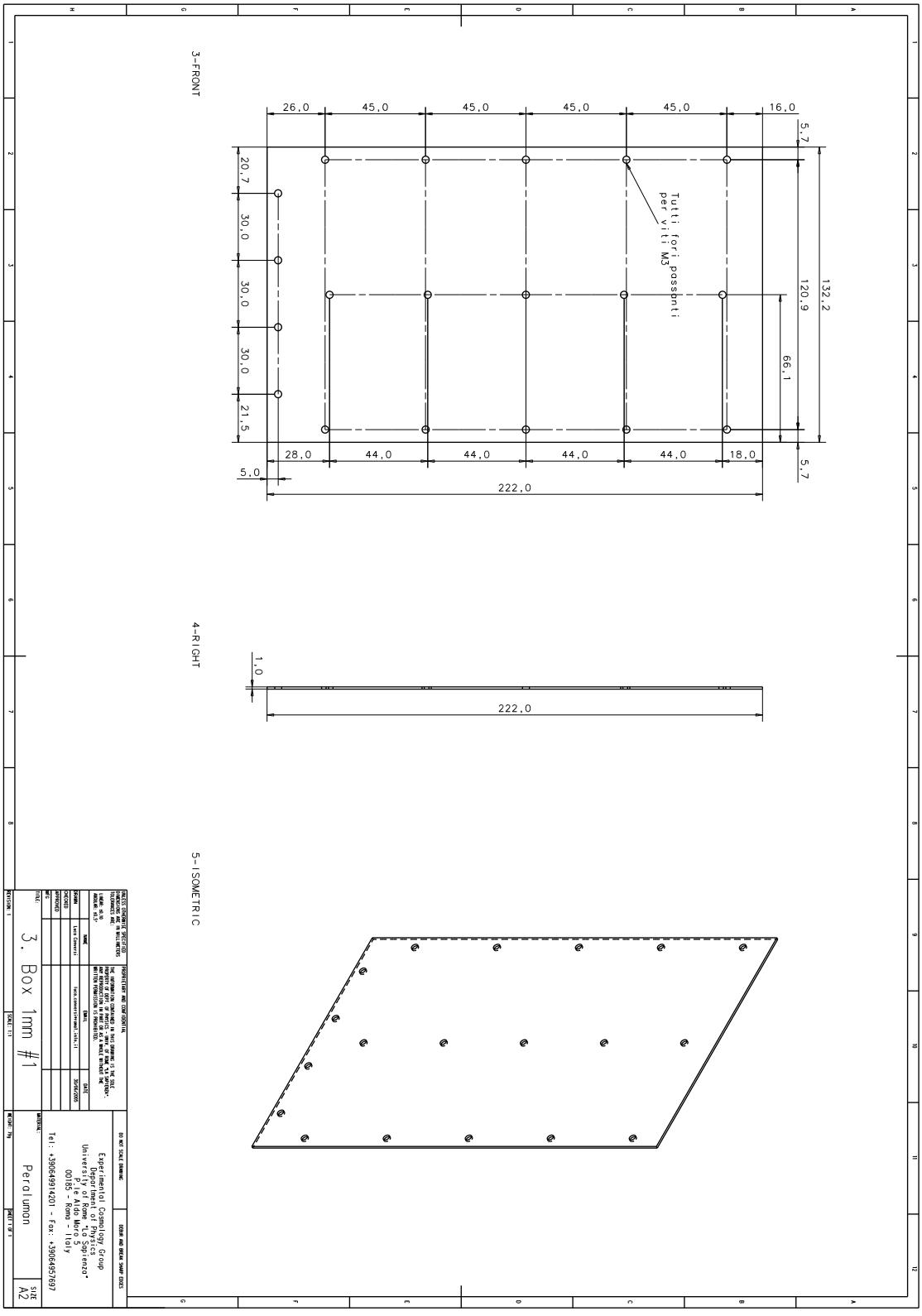

Figure A.6: *Box* 1*mm* #1.

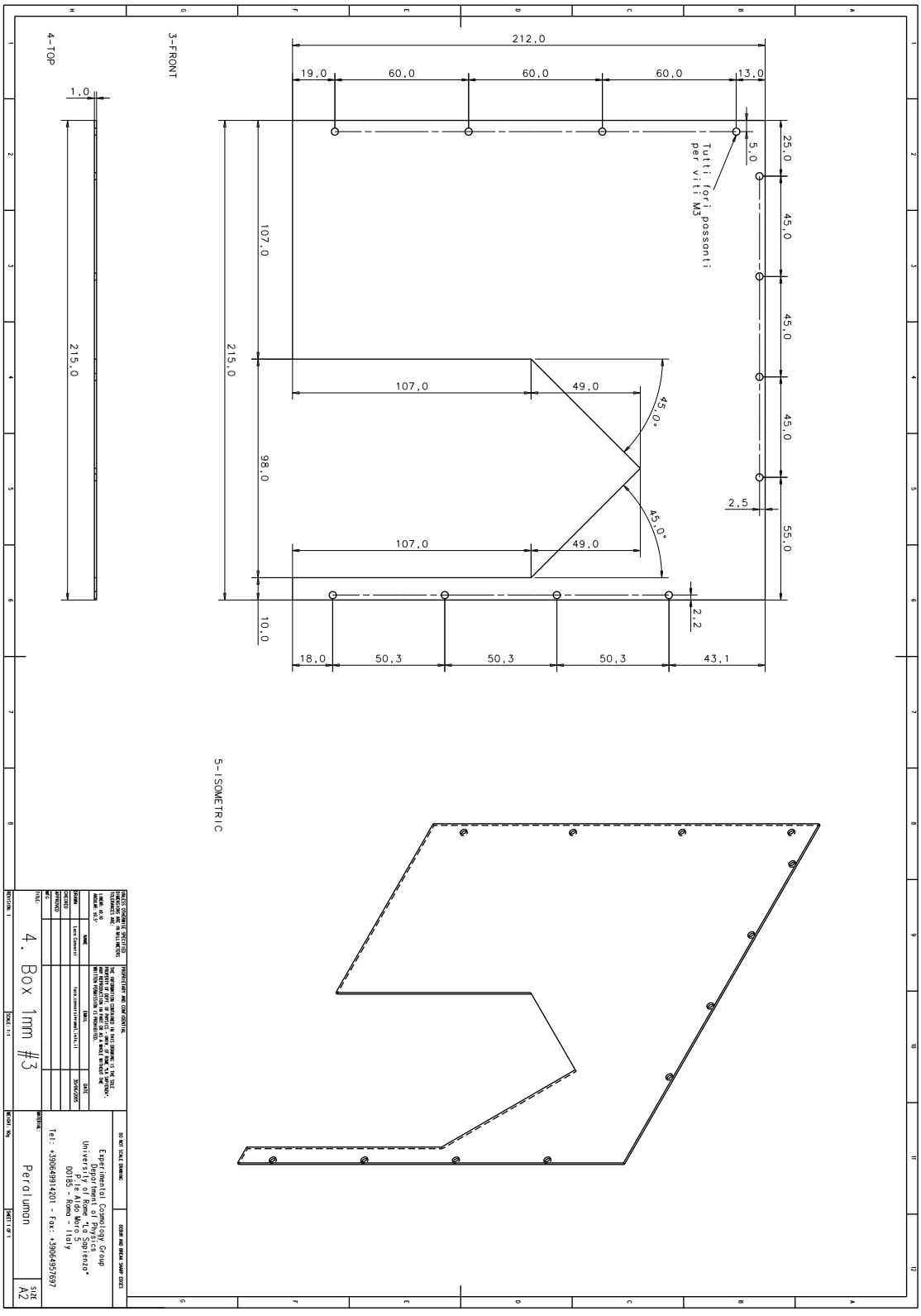

Figure A.7: *Box* 1*mm* #2.

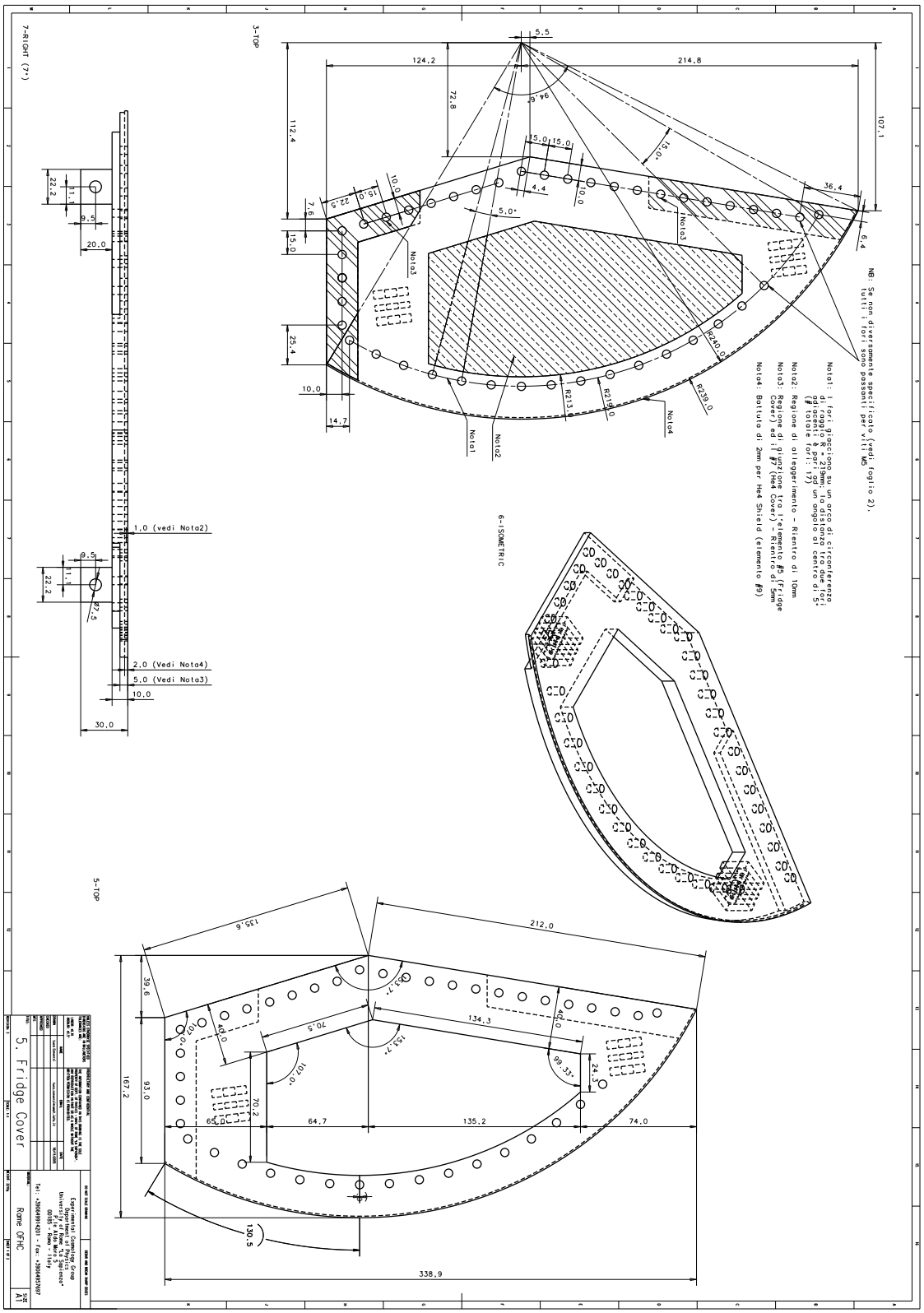

Figure A.8: *Fridge Cover – Part A.*

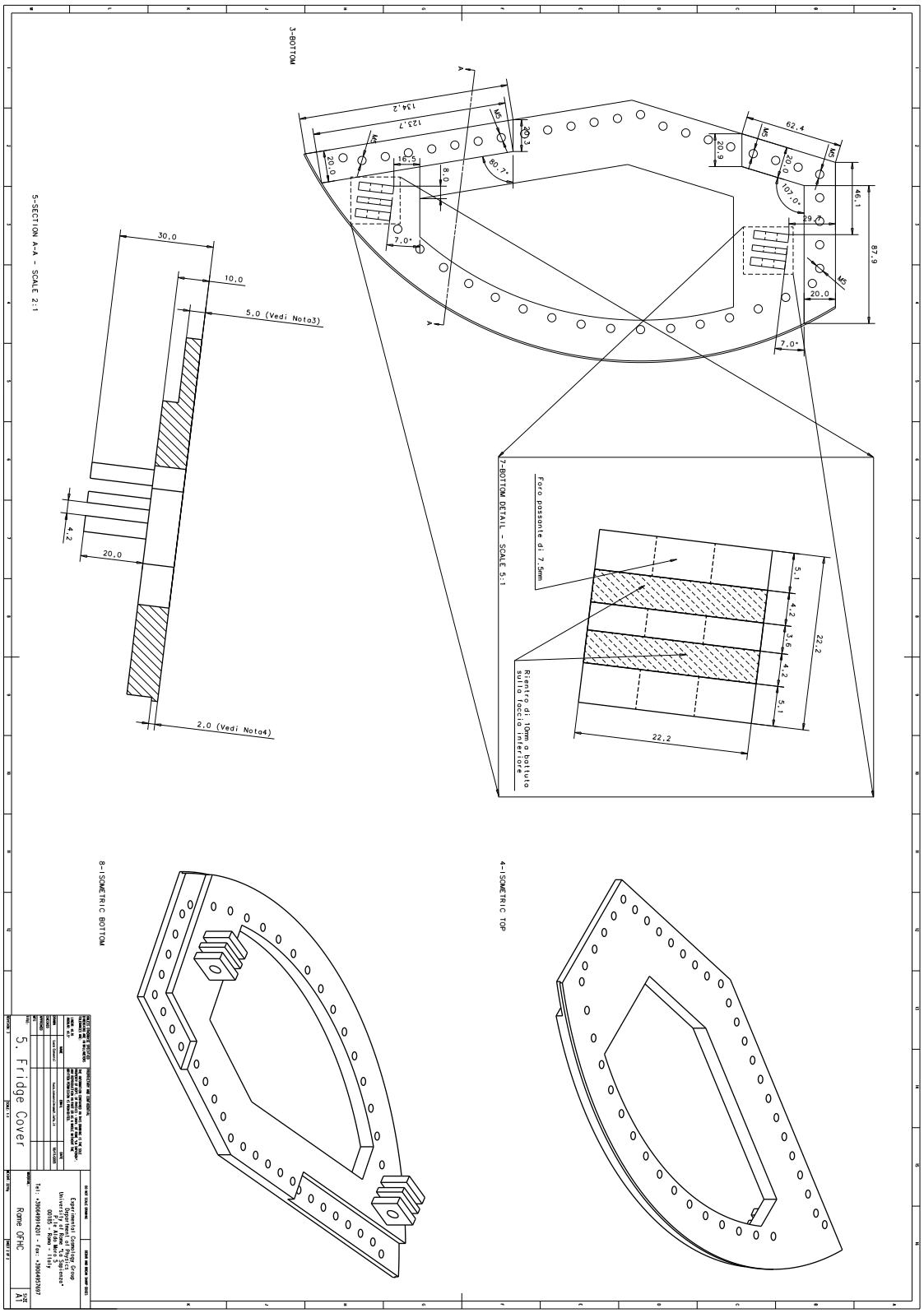

Figure A.9: *Fridge Cover – Part B.*

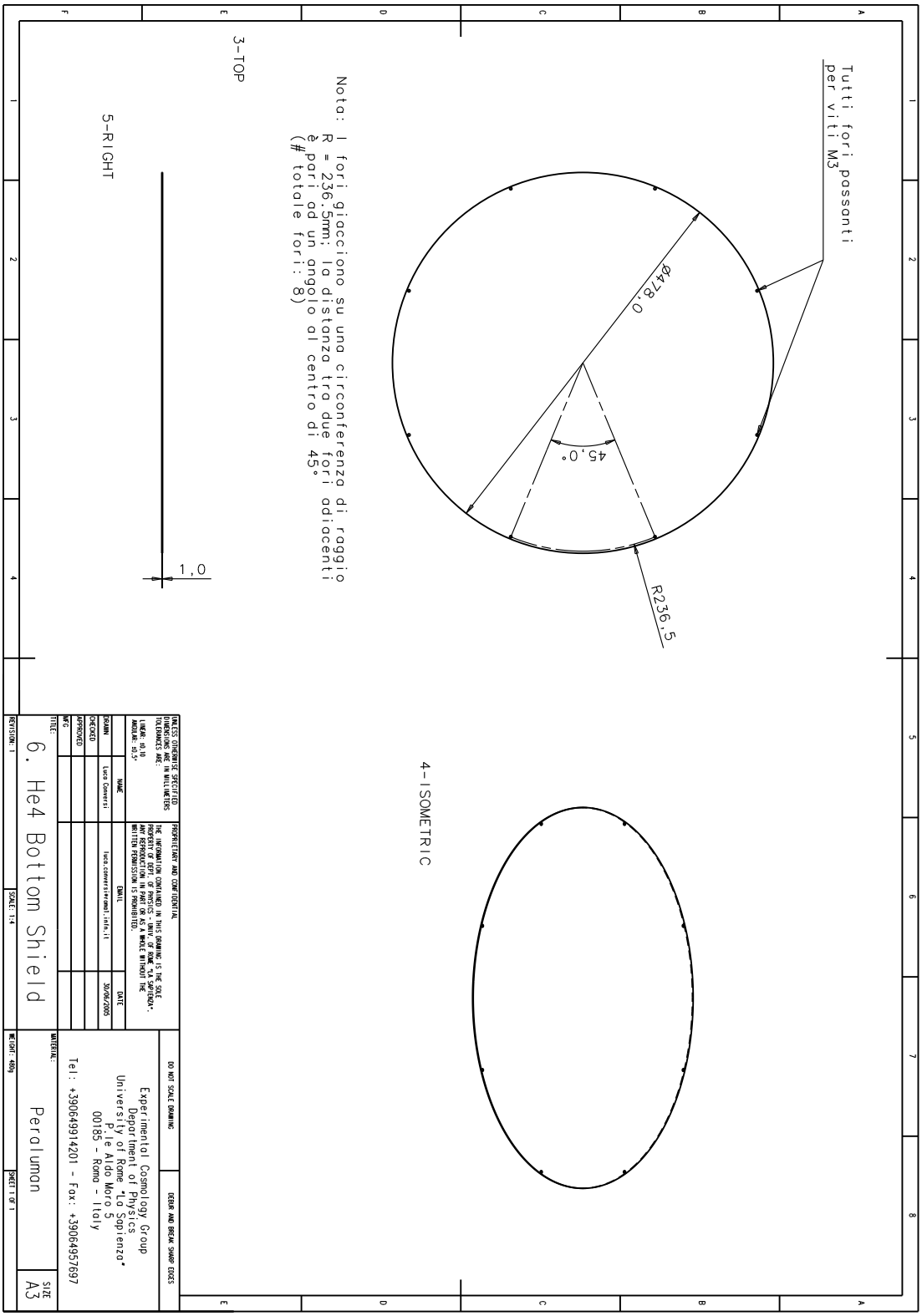

Figure A.10: ^{4}He *bottom shield.*

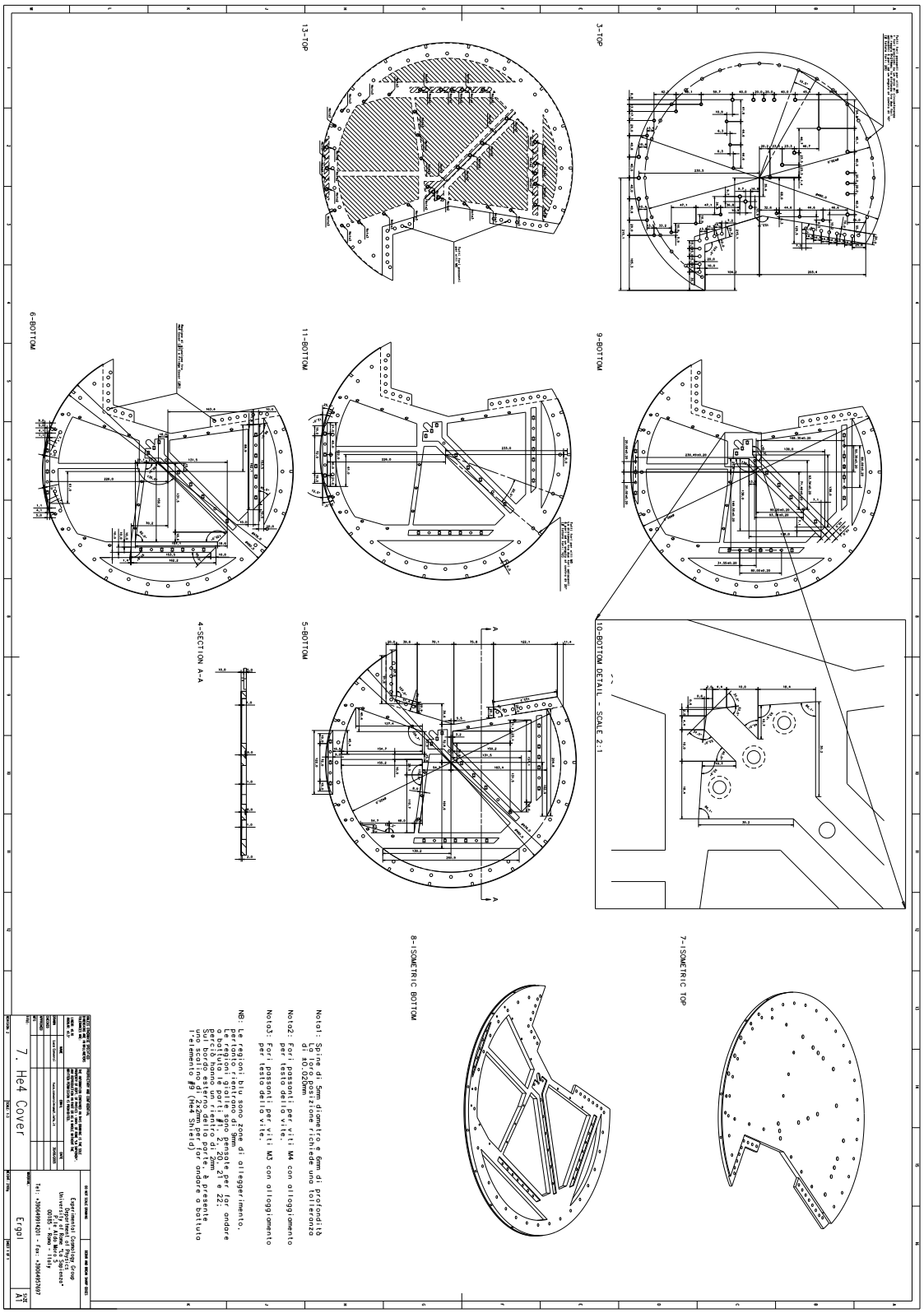

Figure A.11: ^{4}He *cover*.

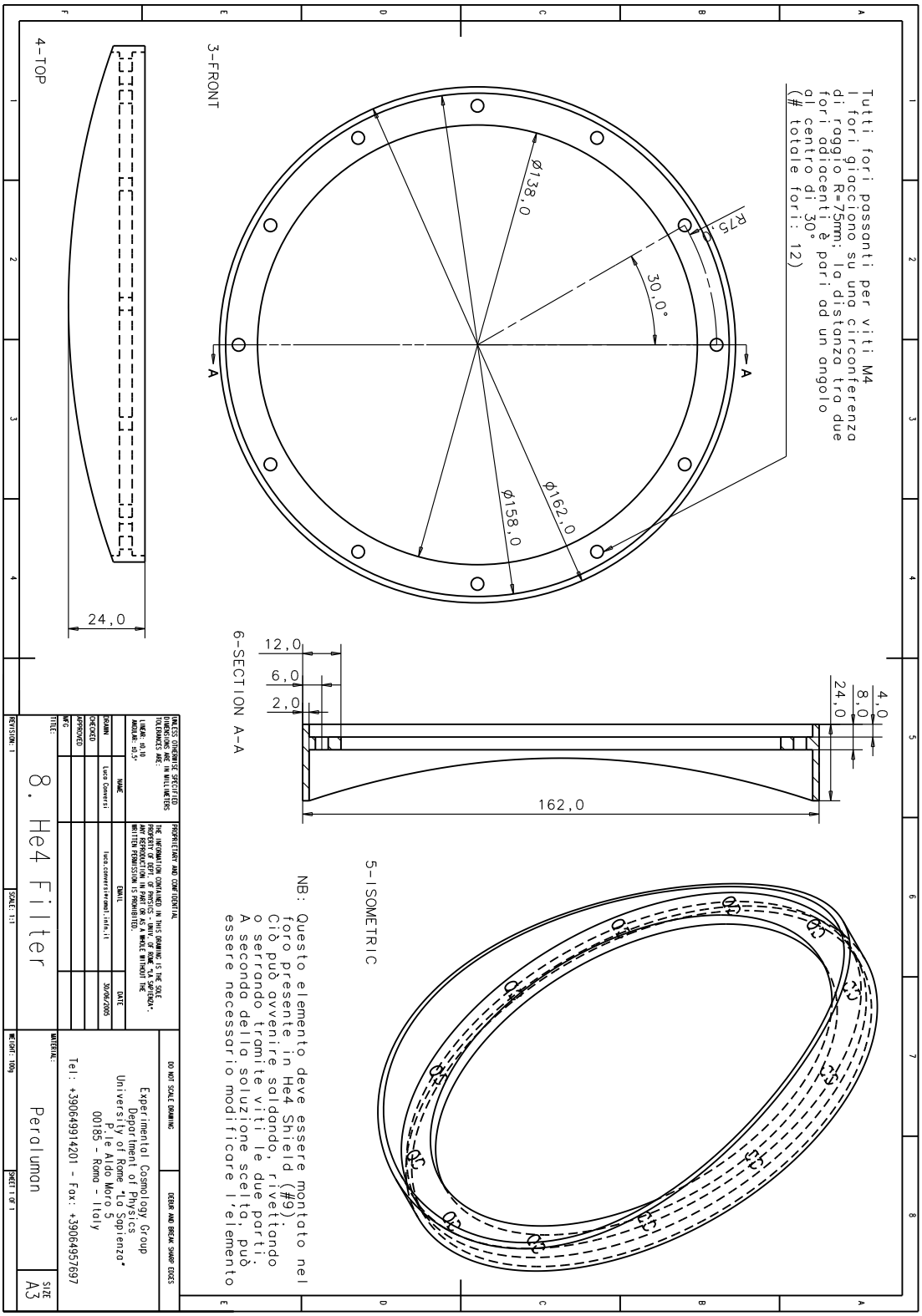

Figure A.12: ^{4}He *filter*.

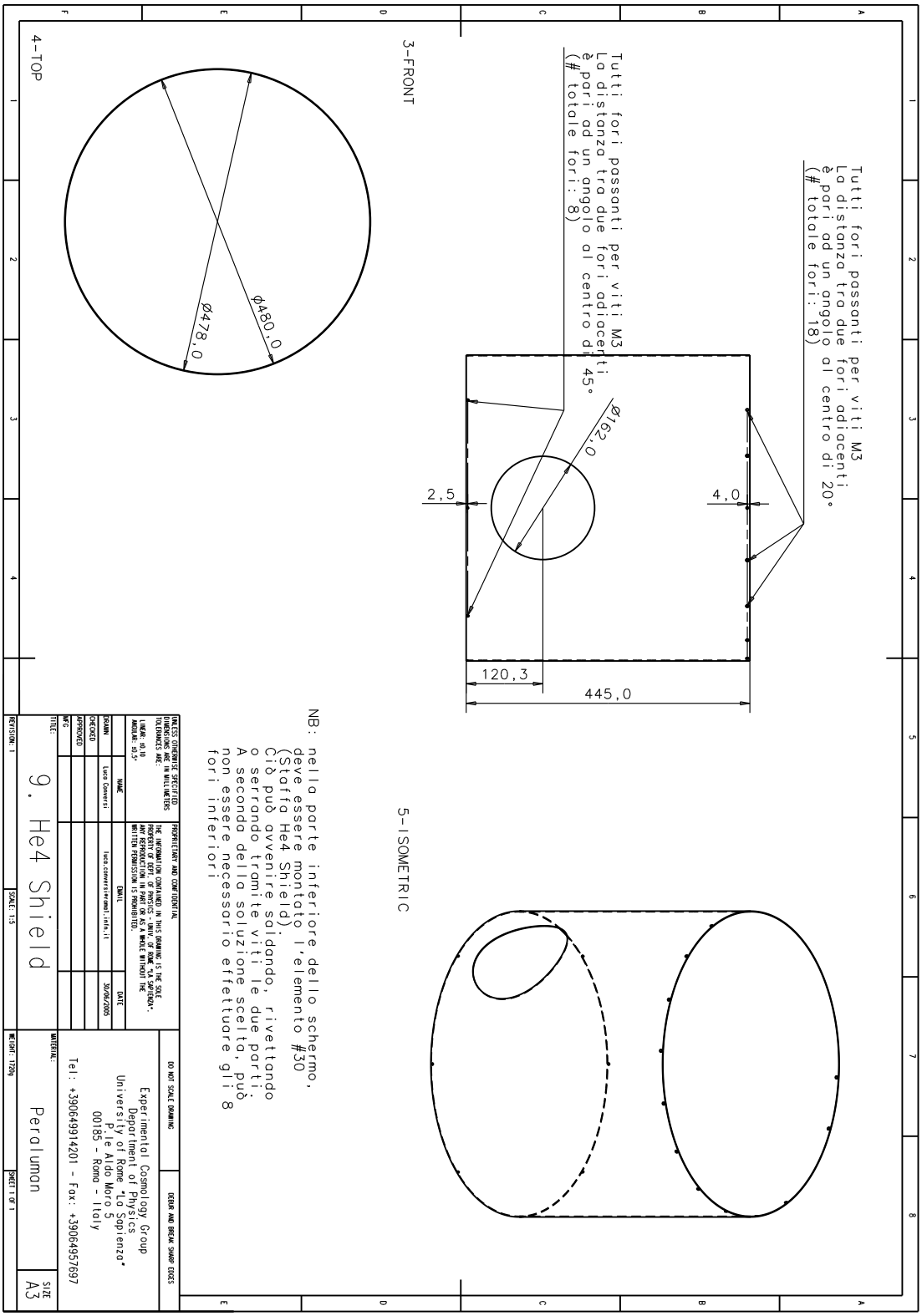

Figure A.13: ^{4}He *external shiels.*

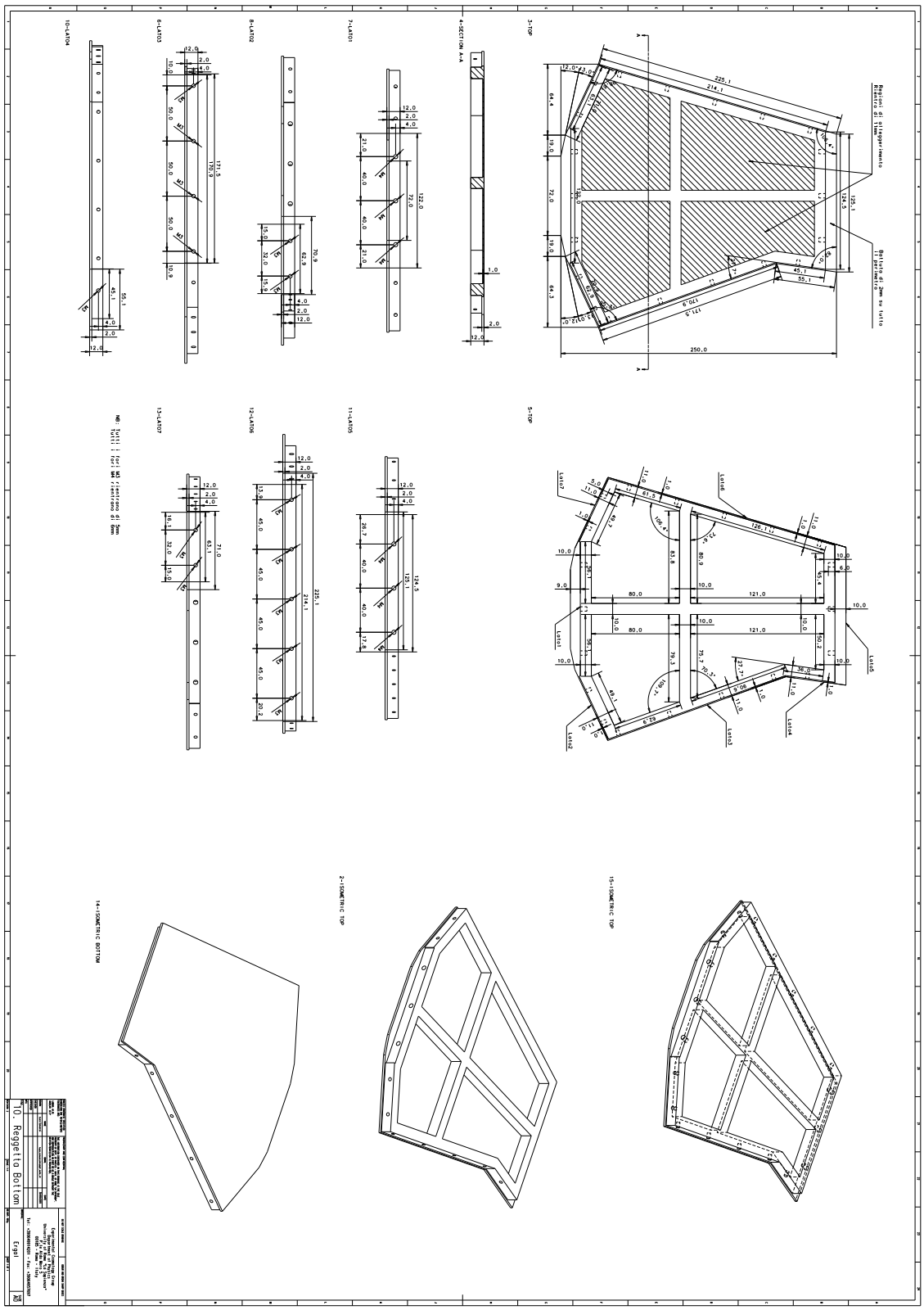

Figure A.14: *Reggetta Bottom.*

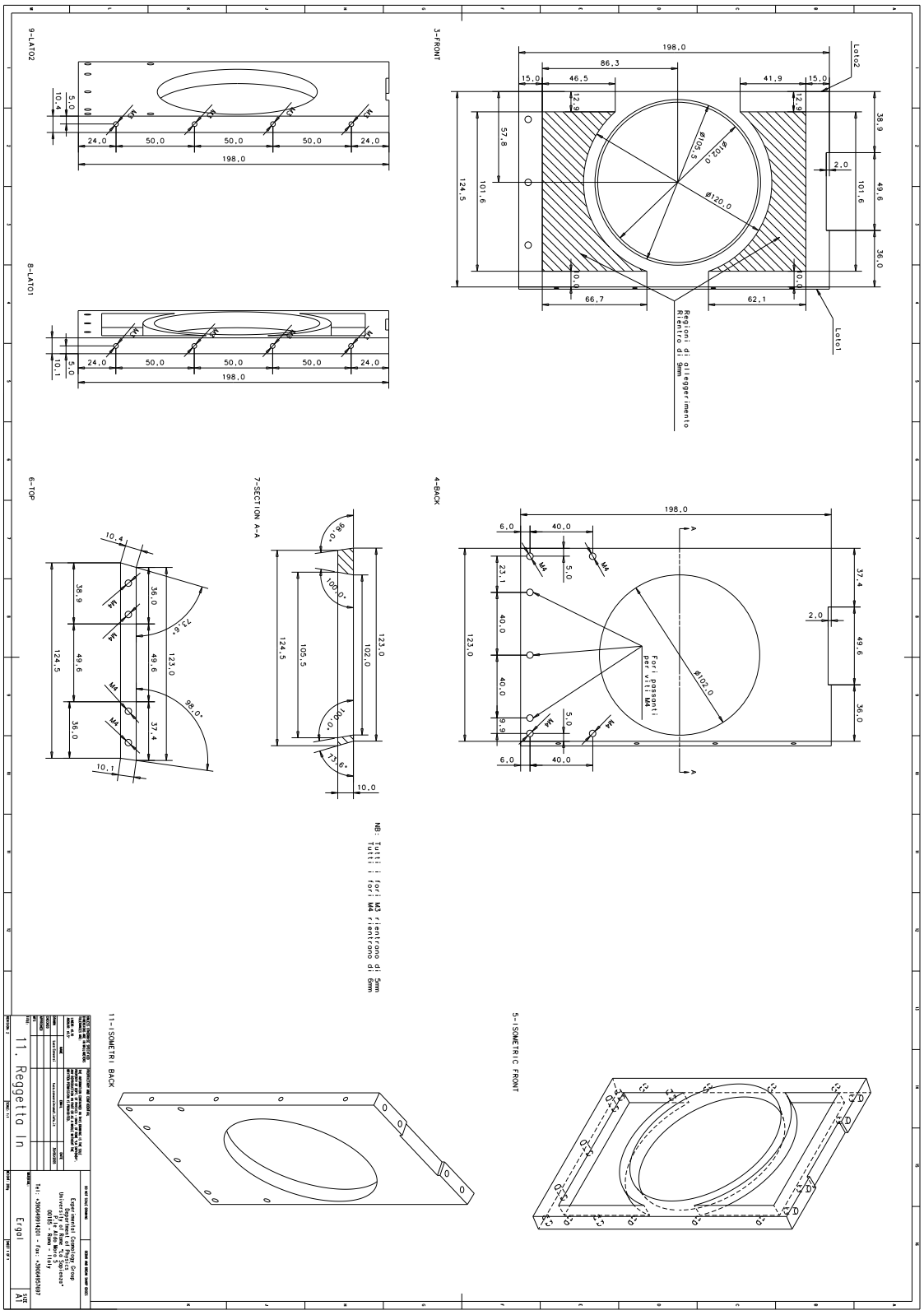

Figure A.15: *Reggetta In.*

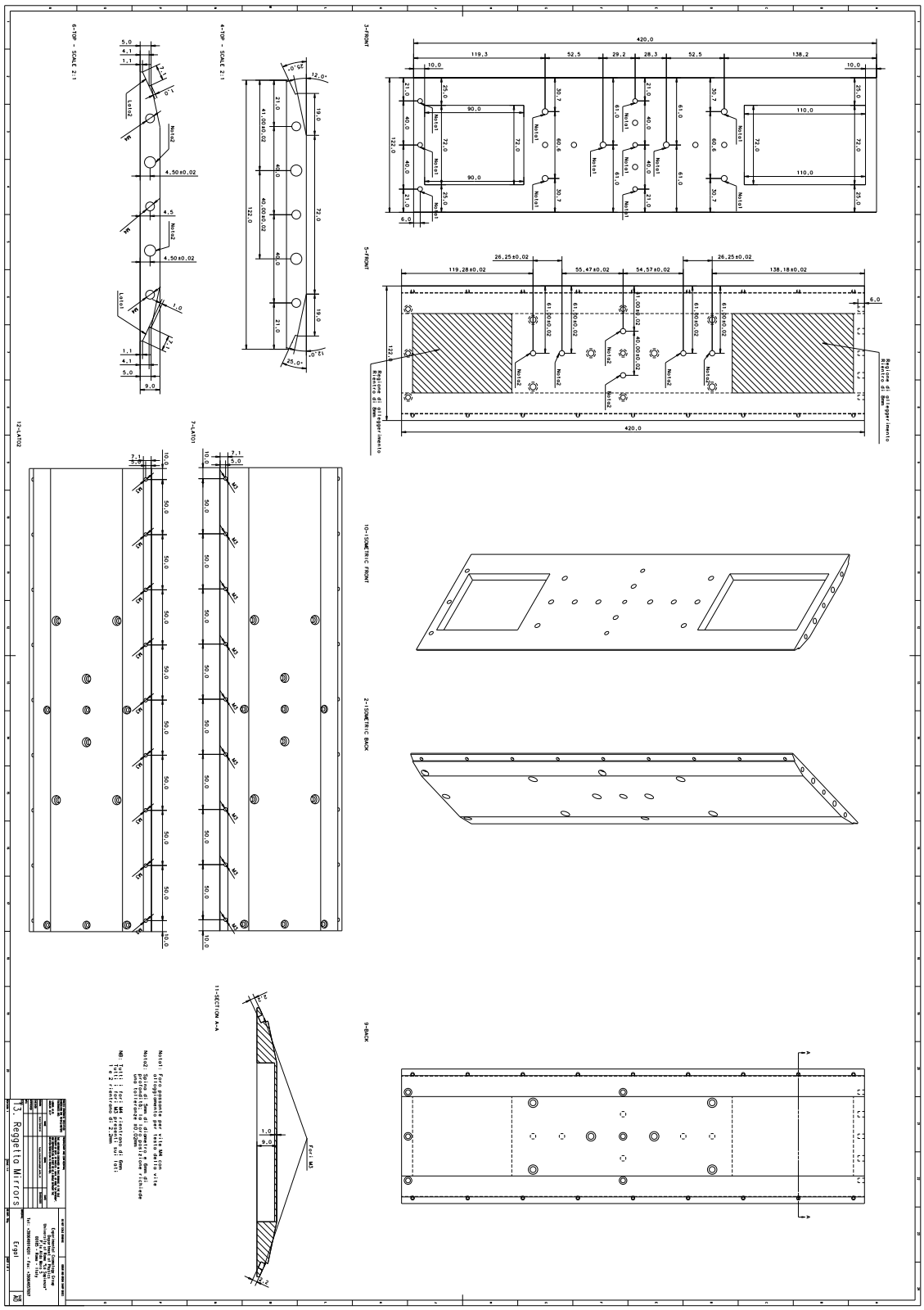

Figure A.16: *Reggetta Mirrors.*

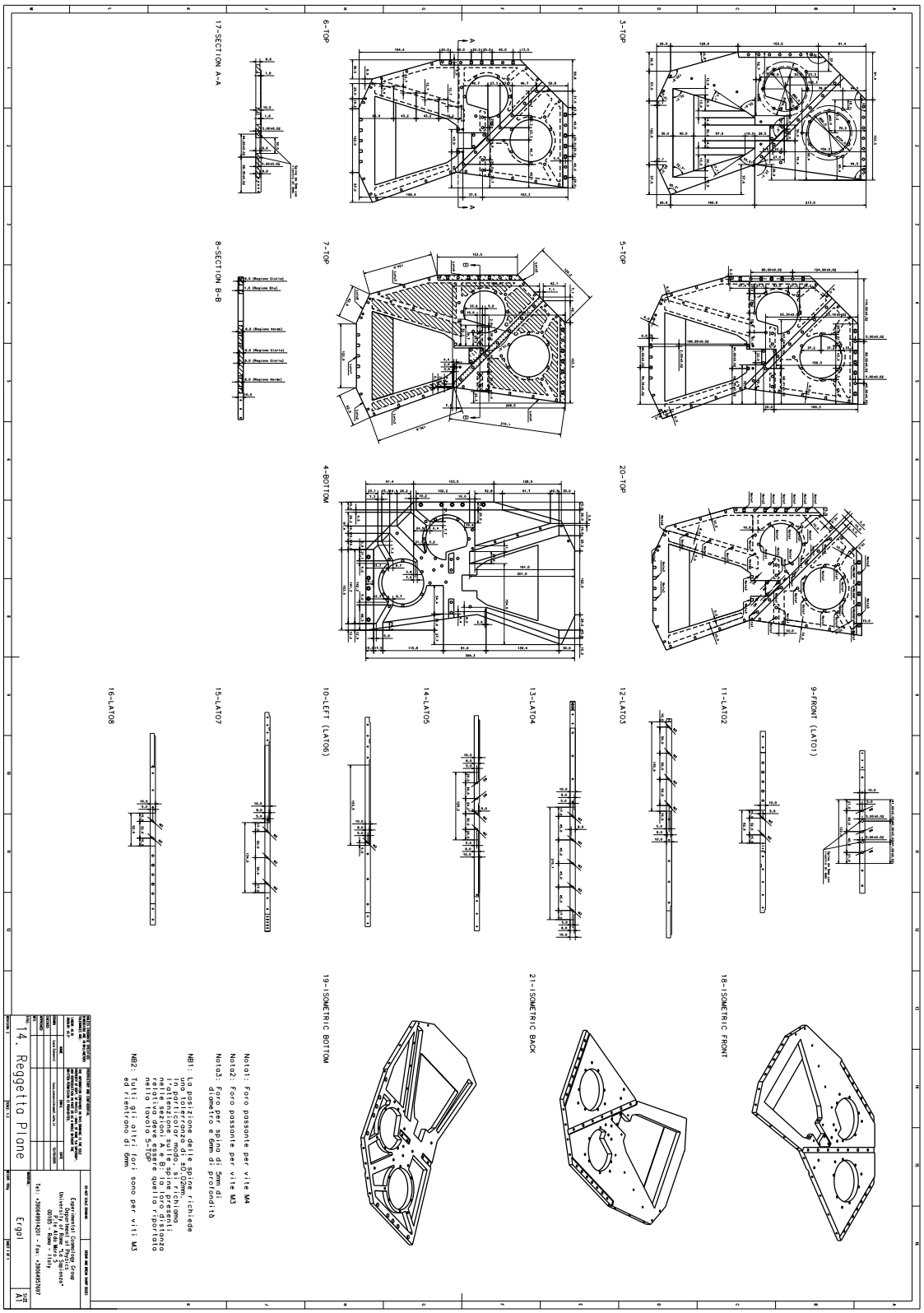

Figure A.17: *Reggetta Plane.*

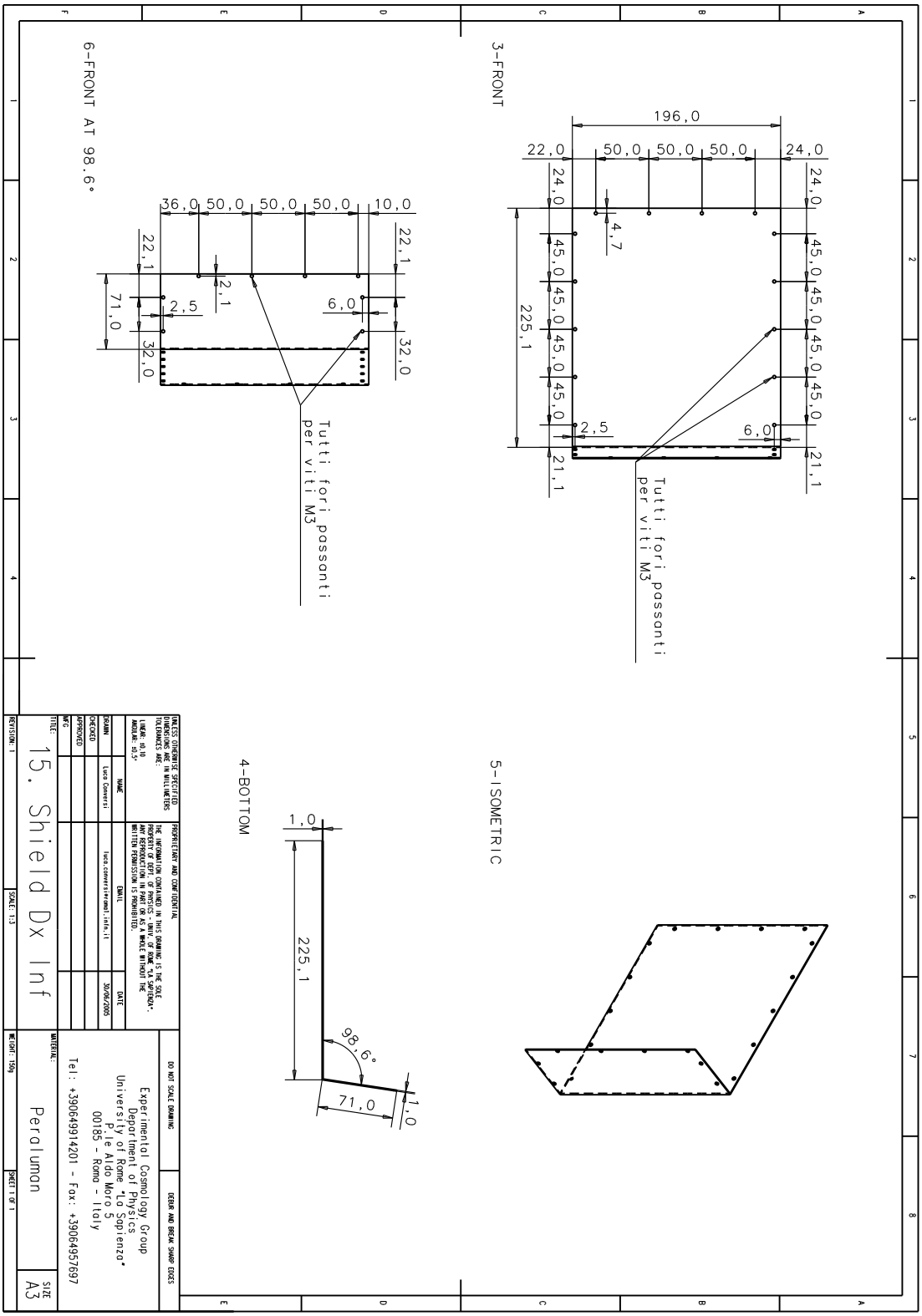

Figure A.18: *Shield Dx Inf.*

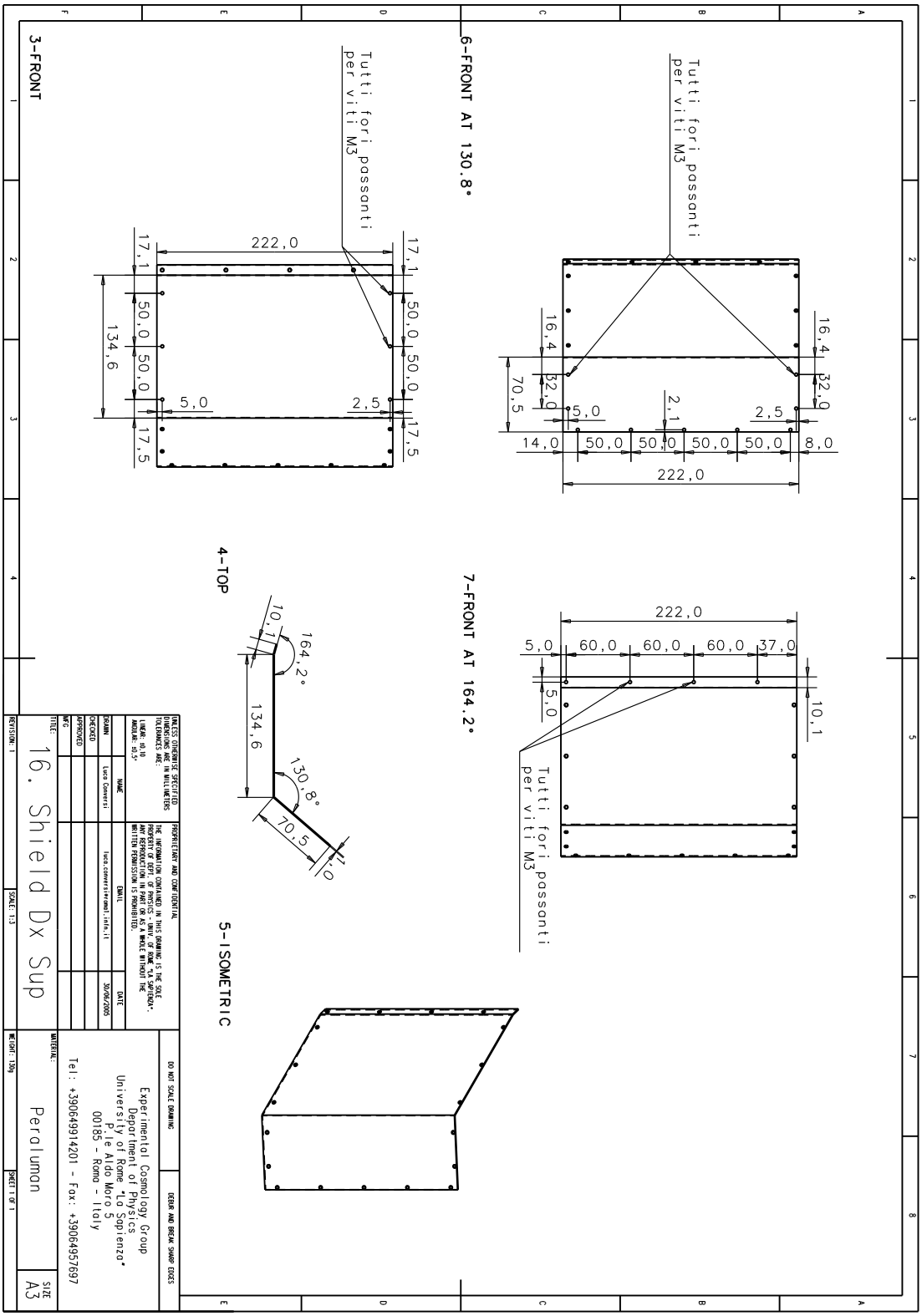

Figure A.19: *Shield Dx Sup.*

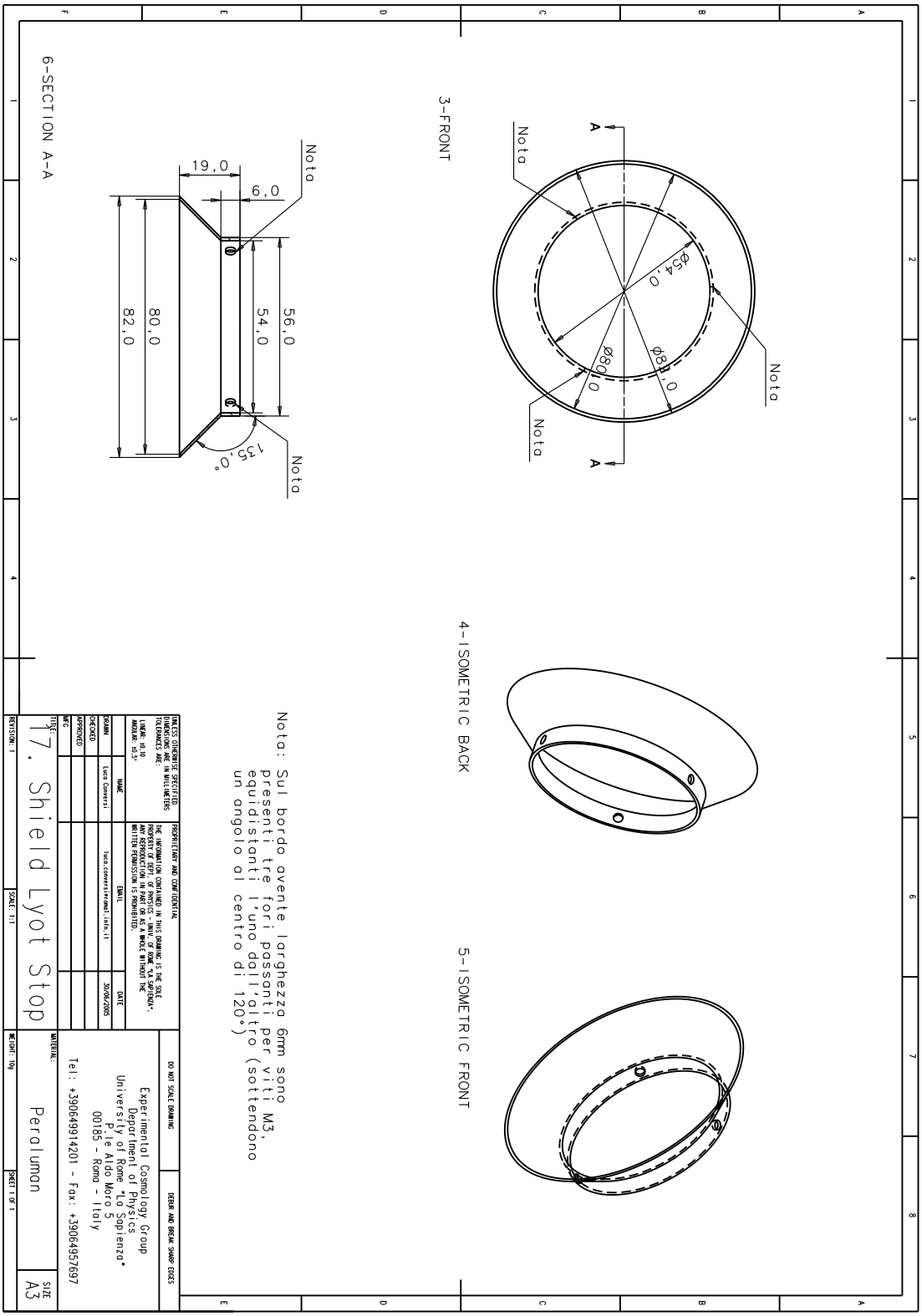

Figure A.20: *Shield Lyot Stop.*

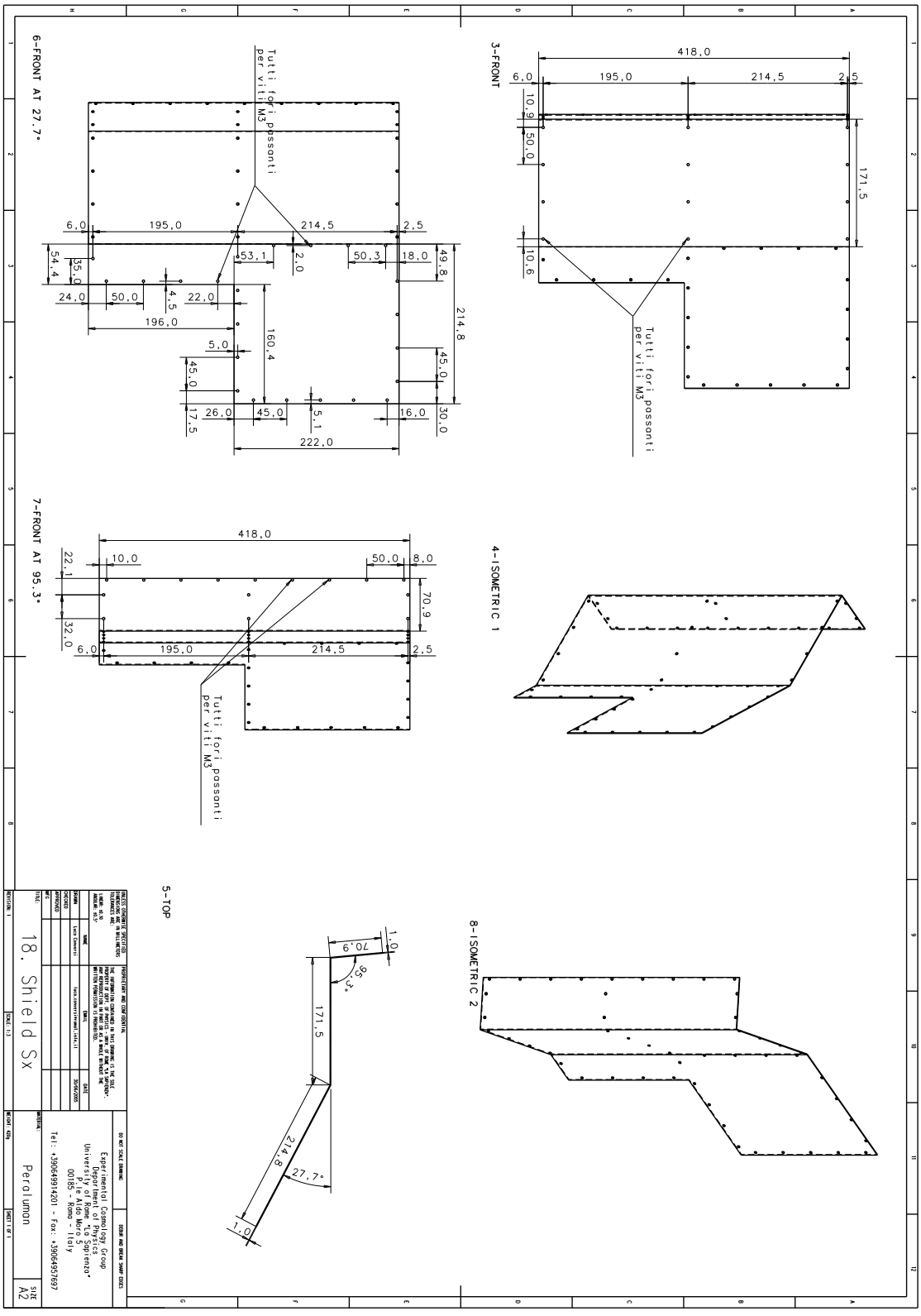

Figure A.21: *Shield Sx.*

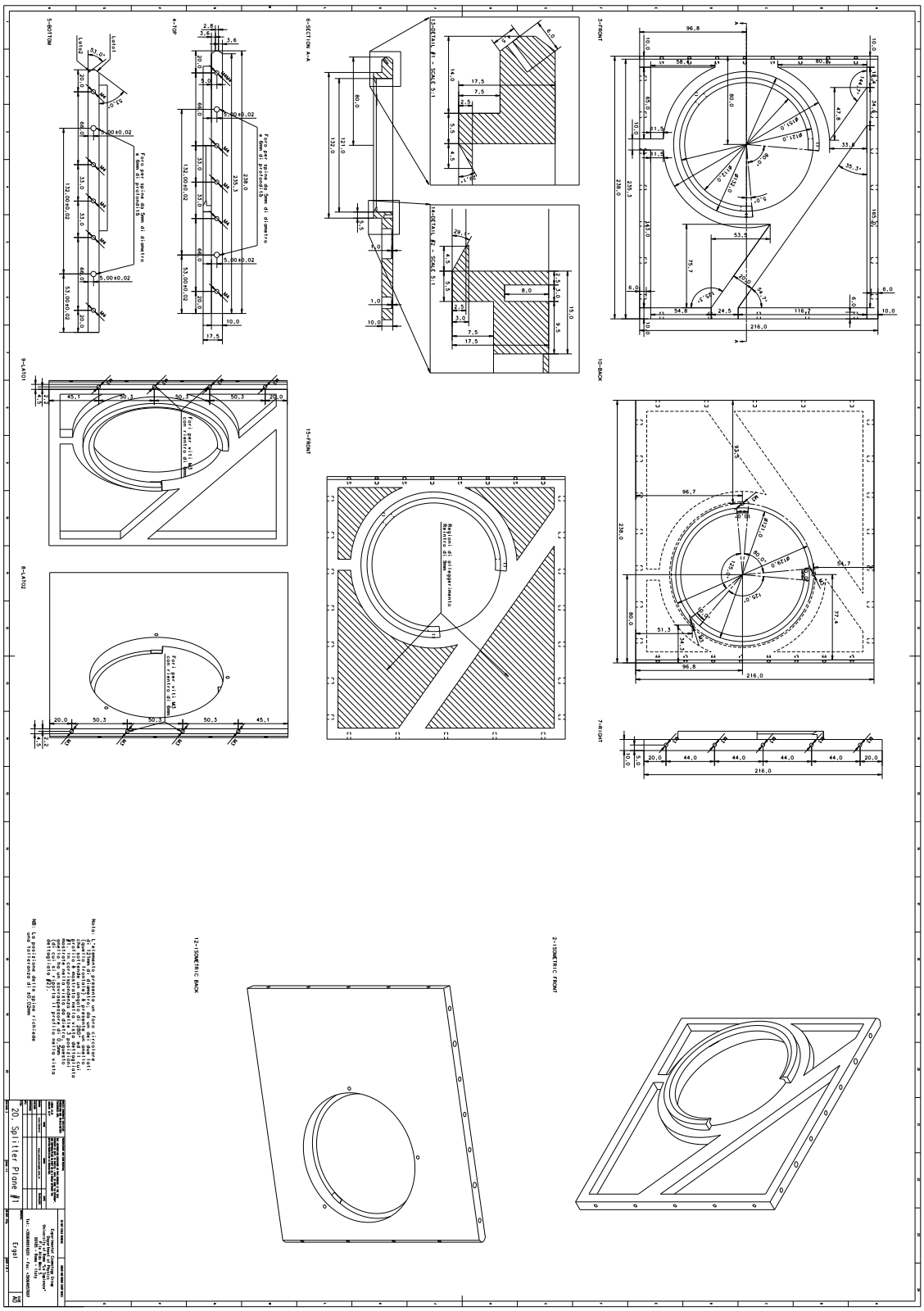

Figure A.22: *Splitter Plane* #1.

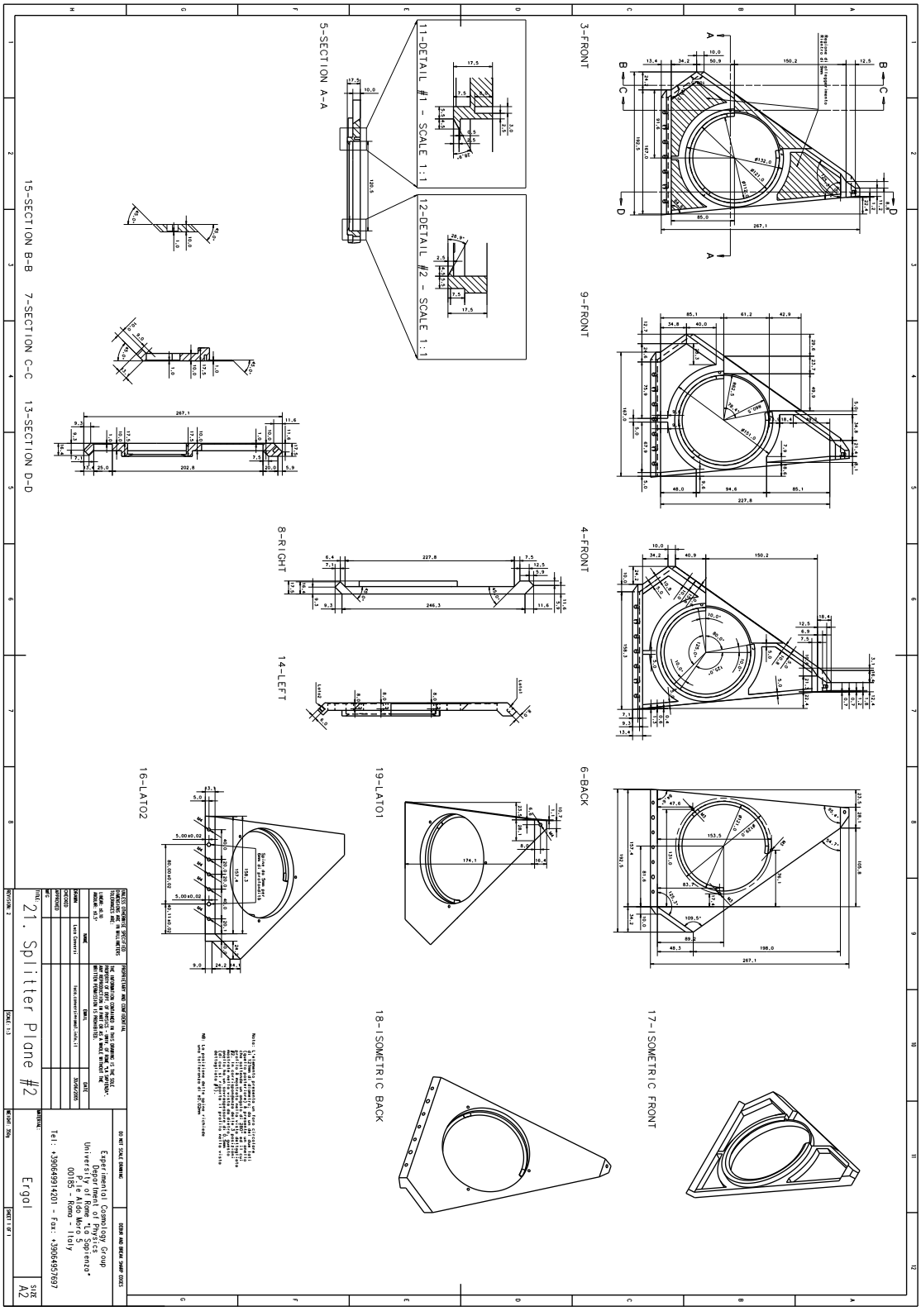

Figure A.23: *Splitter Plane #2*.

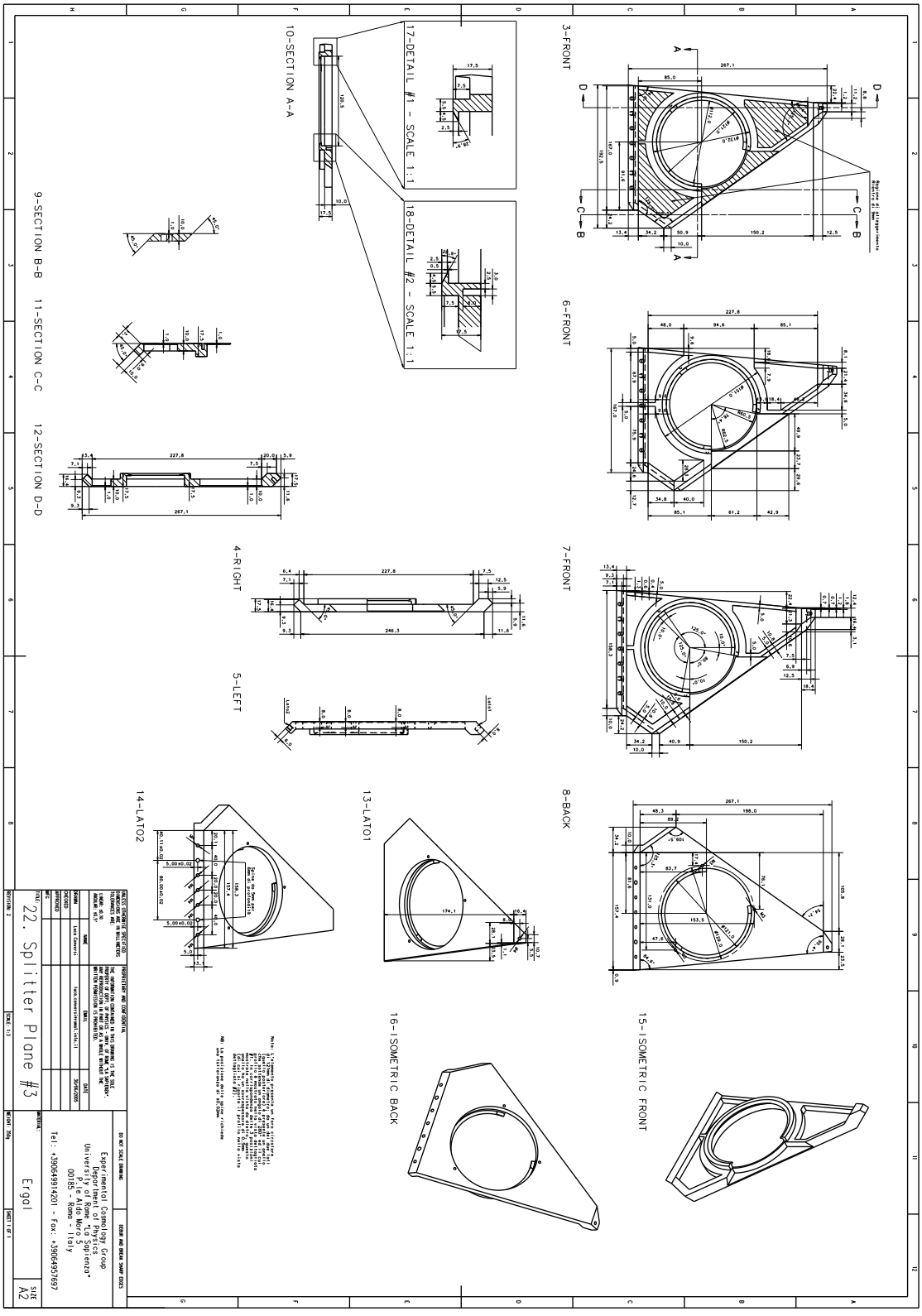

Figure A.24: *Splitter Plane* #3.

Bibliography

[1] R. G. Arendt, N. Odegard, J. L. Weiland, T. J. Sodroski, M. G. Hauser, E. Dwek, T. Kelsall, S. H. Moseley, R. F. Silverberg, D. Leisawitz, K. Mitchell, W. T. Reach, and E. L. Wright. *The COBE Diffuse Infrared Background Experiment Search for the Cosmic Infrared Background. III. Separation of Galactic Emission from the Infrared Sky Brightness. ApJ*, **508**:74–105, 1998.

[2] R. B. Barreiro. *The cosmic microwave background State of the art. New A Rev.*, **44**:179–204, 2000.

[3] C. L. Bennett, M. Halpern, G. Hinshaw, N. Jarosik, A. Kogut, M. Limon, S. S. Meyer, L. Page, D. N. Spergel, G. S. Tucker, E. Wollack, E. L. Wright, C. Barnes, M. R. Greason, R. S. Hill, E. Komatsu, M. R. Nolta, N. Odegard, H. V. Peiris, L. Verde, and J. L. Weiland. *First-Year Wilkinson Microwave Anisotropy Probe (WMAP) Observations: Preliminary Maps and Basic Results. ApJ*, **148**:1–27, 2003.

[4] A. Benoît, P. Ade, A. Amblard, R. Ansari, É. Aubourg, S. Bargot, J. G. Bartlett, J.-P. Bernard, R. S. Bhatia, A. Blanchard, J. J. Bock, A. Boscaleri, F. R. Bouchet, A. Bourrachot, P. Camus, F. Couchot, P. de Bernardis, J. Delabrouille, F.-X. Désert, O. Doré, M. Douspis, L. Dumoulin, X. Dupac, P. Filliatre, P. Fosalba, K. Ganga, F. Gannaway, B. Gautier, M. Giard, Y. Giraud-Héraud, R. Gispert, L. Guglielmi, J.-C. Hamilton, S. Hanany, S. Henrot-Versillé, J. Kaplan, G. Lagache, J.-M. Lamarre, A. E. Lange, J. F. Macías-Pérez, K. Madet, B. Maffei, C. Magneville, D. P. Marrone, S. Masi, F. Mayet, A. Murphy, F. Naraghi, F. Nati, G. Patanchon, G. Perrin, M. Piat, N. Ponthieu, S. Prunet, J.-L. Puget, C. Renault, C. Rosset, D. Santos, A. Starobinsky, I. Strukov, R. V. Sudiwala, R. Teyssier, M. Tristram, C. Tucker, J.-C. Vanel, D. Vibert, E. Wakui, and D. Yvon. *Cosmological constraints from Archeops. A&A*, **339**:L25–L30, 2003.

[5] M. Birkinshaw. *The Sunyaev-Zel'dovich effect. Phys. Rep.*, **310**:97–195, 1999.

[6] A. W. Blain, D. T. Frayer, J. J. Bock, and N. Z. Scoville. *Millimetre/submillimetre-wave emission-line searches for high-redshift galaxies. MNRAS*, **313**:559–570, April 2000.

[7] A. W. Blain, A. Jameson, I. Smail, M. S. Longair, J.-P. Kneib, and R. J. Ivison. *Dust-obscured star formation and AGN fuelling in hierarchical models of galaxy evolution. MNRAS*, **309**:715–730, November 1999.

[8] A. W. Blain and M. S. Longair. *Millimetre background radiation and galaxy formation. MNRAS*, **265**:L21–L24, November 1993.

[9] A. W. Blain and M. S. Longair. *Submillimetre Cosmology. MNRAS*, **264**:509–+, September 1993.

[10] A. W. Blain, I. Smail, R. J. Ivison, J.-P. Kneib, and D. T. Frayer. *Submillimeter galaxies. Phys. Rep.*, **369**:111–176, October 2002.

[11] S. Borgani, A. Finoguenov, S. T. Kay, T. J. Ponman, V. Springel, P. Tozzi, and G. M. Voit. *Entropy amplification from energy feedback in simulated galaxy groups and clusters. MNRAS*, **361**:233–243, July 2005.

[12] F. Boulanger and M. Perault. *Diffuse infrared emission from the galaxy. I - Solar neighborhood. ApJ*, **330**:964–985, 1988.

[13] A. H. Bridle. *The spectrum of the radio background between 13 and 404 MHz. MNRAS*, **136**:219–+, 1967.

[14] W. B. Burton and D. Hartmann. *The Leiden/Dwingeloo survey of emission from galactic HI. Ap&SS*, **217**:189–193, July 1994.

[15] A. Cavaliere and R. Fusco-Femiano. *X-rays from hot plasma in clusters of galaxies. A&A*, **49**:137–144, 1976.

[16] A. Cavaliere and R. Fusco-Femiano. *The Distribution of Hot Gas in Clusters of Galaxies. A&A*, **70**:677–+, 1978.

[17] A. Challinor and A. Lasenby. *Relativistic Corrections to the Sunyaev-Zeldovich Effect. ApJ*, **499**:1–+, 1998.

[18] S. Chandrasekhar. *Radiative transfer.* Oxford, Clarendon Press, 1950., 1950.

[19] E. L. Church, H. A. Jenkinson, and J. M. Zavada. *Measurement of the Finish of Diamond-Turned Metal Surfaces by Differential Light Scattering. Optical Engineering*, **16**(4):360–374, 1977.

[20] S. Cole, C. G. Lacey, C. M. Baugh, and C. S. Frenk. *Hierarchical galaxy formation. MNRAS*, **319**:168–204, November 2000.

[21] S. Cole, W. J. Percival, J. A. Peacock, P. Norberg, C. M. Baugh, C. S. Frenk, I. Baldry, J. Bland-Hawthorn, T. Bridges, R. Cannon, M. Colless, C. Collins, W. Couch, N. J. G. Cross, G. Dalton, V. R. Eke, R. De Propris, S. P. Driver, G. Efstathiou, R. S. Ellis, K. Glazebrook, C. Jackson, A. Jenkins, O. Lahav, I. Lewis, S. Lumsden, S. Maddox, D. Madgwick, B. A. Peterson, W. Sutherland, and K. Taylor. *The 2dF Galaxy Redshift Survey: power-spectrum analysis of the final data set and cosmological implications. MNRAS*, **362**:505–534, September 2005.

[22] R. G. Crittenden, D. Coulson, and N. G. Turok. *Polarization-Temperature correlation from Tensor Fluctuations. Phys. Rev. D*, **52**:5402, 1995.

[23] D. A. Dale, G. Helou, A. Contursi, N. A. Silbermann, and S. Kolhatkar. *The Infrared Spectral Energy Distribution of Normal Star-forming Galaxies. ApJ*, **549**:215–227, March 2001.

[24] P. de Bernardis, P. A. R. Ade, J. J. Bock, J. R. Bond, J. Borrill, A. Boscaleri, K. Coble, B. P. Crill, G. De Gasperis, P. C. Farese, P. G. Ferreira, K. Ganga, M. Giacometti, E. Hivon, V. V. Hristov, A. Iacoangeli, A. H. Jaffe, A. E. Lange, L. Martinis, S. Masi, P. V. Mason, P. D. Mauskopf, A. Melchiorri, L. Miglio, T. Montroy, C. B. Netterfield, E. Pascale, F. Piacentini, D. Pogosyan, S. Prunet, S. Rao, G. Romeo, J. E. Ruhl, F. Scaramuzzi, D. Sforna, and N. Vittorio. *A flat Universe from high-resolution maps of the cosmic microwave background radiation. Nature*, **404**:955–959, 2000.

[25] A. de Oliveira-Costa, A. Kogut, M. J. Devlin, C. B. Netterfield, L. A. Page, and E. J. Wollack. *Galactic Microwave Emission at Degree Angular Scales. ApJL*, **482**:L17+, 1997.

[26] M. de Petris, M. Gervasi, and F. Liberati. *New far infrared and millimetric telescopes for differential measurements with a large chopping angle in the sky. Appl. Opt.*, **28**:1785–1792, May 1989.

[27] F.-X. Desert, F. Boulanger, and J. L. Puget. *Interstellar dust models for extinction and emission. A&A*, **237**:215–236, October 1990.

[28] C. Dickinson, R. A. Battye, P. Carreira, K. Cleary, R. D. Davies, R. J. Davis, R. Genova-Santos, K. Grainge, C. M. Gutiérrez, Y. A. Hafez, M. P. Hobson, M. E. Jones, R. Kneissl, K. Lancaster, A. Lasenby, J. P. Leahy, K. Maisinger, C. Ödman, G. Pooley, N. Rajguru, R. Rebolo, J. A. Rubiño-Martin, R. D. E. Saunders, R. S. Savage, A. Scaife, P. F. Scott, A. Slosar, P. Sosa Molina, A. C. Taylor, D. Titterington, E. Waldram, R. A. Watson, and A. Wilkinson. *High-sensitivity measurements of the cosmic microwave background power spectrum with the extended Very Small Array. MNRAS*, **353**:732–746, September 2004.

[29] H. Dole, R. Gispert, G. Lagache, J.-L. Puget, F. R. Bouchet, C. Cesarsky, P. Ciliegi, D. L. Clements, M. Dennefeld, F.-X. Désert, D. Elbaz, A. Franceschini, B. Guiderdoni, M. Harwit, D. Lemke, A. F. M. Moorwood, S. Oliver, W. T. Reach, M. Rowan-Robinson, and M. Stickel. *FIRBACK: III. Catalog, source counts, and cosmological implications of the 170 mu m ISO. A&A*, **372**:364–376, June 2001.

[30] B. T. Draine and A. Lazarian. *Electric Dipole Radiation from Spinning Dust Grains. ApJ*, **508**:157–179, 1998.

[31] B. T. Draine and A. Lazarian. *Magnetic Dipole Microwave Emission from Dust Grains. ApJ*, **512**:740–754, 1999.

[32] L. Dunne, D. L. Clements, and S. A. Eales. *Constraining the radio-submillimetre redshift indicator using data from the SCUBA Local Universe Galaxy Survey. MNRAS*, **319**:813–820, December 2000.

[33] L. Dunne and S. A. Eales. *The SCUBA Local Universe Galaxy Survey - II. 450-μm data: evidence for cold dust in bright IRAS galaxies. MNRAS*, **327**:697–714, November 2001.

[34] E. Dwek. *The Evolution of the Elemental Abundances in the Gas and Dust Phases of the Galaxy. ApJ*, **501**:643–+, July 1998.

[35] E. Dwek, R. G. Arendt, M. G. Hauser, D. Fixsen, T. Kelsall, D. Leisawitz, Y. C. Pei, E. L. Wright, J. C. Mather, S. H. Moseley, N. Odegard, R. Shafer, R. F. Silverberg, and J. L. Weiland. *The COBE Diffuse Infrared Background Experiment Search for the Cosmic Infrared Background. IV. Cosmological Implications. ApJ*, **508**:106–122, November 1998.

[36] S. Eales, S. Lilly, T. Webb, L. Dunne, W. Gear, D. Clements, and M. Yun. *The Canada-UK Deep Submillimeter Survey. IV. The Survey of the 14 Hour Field. AJ*, **120**:2244–2268, November 2000.

[37] A. C. Fabian and X. Barcons. *The origin of the X-ray background. ARA&A*, **30**:429–456, 1992.

[38] D. P. Finkbeiner, M. Davis, and D. J. Schlegel. *Extrapolation of Galactic Dust Emission at 100 Microns to Cosmic Microwave Background Radiation Frequencies Using FIRAS. ApJ*, **524**:867–886, 1999.

[39] D. J. Fixsen, E. S. Cheng, J. M. Gales, J. C. Mather, R. A. Shafer, and E. L. Wright. *The Cosmic Microwave Background Spectrum from the Full COBE FIRAS Data Set. ApJ*, **473**:576, 1996.

[40] D. J. Fixsen, E. Dwek, J. C. Mather, C. L. Bennett, and R. A. Shafer. *The Spectrum of the Extragalactic Far-Infrared Background from the COBE FIRAS Observations. ApJ*, **508**:123–128, November 1998.

[41] A. Franceschini, P. Mazzei, G. de Zotti, and L. Danese. *Luminosity evolution and dust effects in distant galaxies: Implications for the observability of the early evolutionary phases. ApJ*, **427**:140–154, May 1994.

[42] D. T. Frayer, S. C. Chapman, L. Yan, L. Armus, G. Helou, D. Fadda, R. Morganti, M. A. Garrett, P. Appleton, P. Choi, F. Fang, I. Heinrichsen, M. Im, M. Lacy, F. Marleau, F. J. Masci, D. L. Shupe, B. T. Soifer, G. K. Squires, L. J. Storrie-Lombardi, J. A. Surace, H. I. Teplitz, and G. Wilson. *Infrared Properties of Radio-selected Submillimeter Galaxies in the Spitzer First Look Survey Verification Field. ApJS*, **154**:137–141, September 2004.

[43] W. L. Freedman, B. F. Madore, B. K. Gibson, L. Ferrarese, D. D. Kelson, S. Sakai, J. R. Mould, R. C. Kennicutt, Jr., H. C. Ford, J. A. Graham, J. P. Huchra, S. M. G. Hughes, G. D. Illingworth, L. M. Macri, and P. B. Stetson. *Final Results from the Hubble Space Telescope Key Project to Measure the Hubble Constant. ApJ*, **553**:47–72, May 2001.

[44] J. M. Gildemeister, A. T. Lee, and P. L. Richards. *A fully lithographed voltage-biased superconducting spiderweb bolometer*. *Appl. Phys. Lett.*, **74**:868–870, 1999.

[45] R. Gispert, G. Lagache, and J. L. Puget. *Implications of the cosmic infrared background for light production and the star formation history in the Universe*. *A&A*, **360**:1–9, August 2000.

[46] P. F. Goldsmith. *Quasioptical Systems*. IEEE Press, 1998.

[47] B. Guiderdoni, E. Hivon, F. R. Bouchet, and B. Maffei. *Semi-analytic modelling of galaxy evolution in the IR/submm range*. *MNRAS*, **295**:877–898, April 1998.

[48] A. H. Guth. *Inflationary Universe: a possible solution to the horizon and flatness problems*. *Phys. Rev. D*, **23**:347, 1980.

[49] M. Harwit. *The Cosmic Infrared Background Radiation, Star Formation Rate, and Metallicity*. *ApJL*, **510**:L83–L86, January 1999.

[50] M. G. Hauser and E. Dwek. *The Cosmic Infrared Background: Measurements and Implications*. *ARA&A*, **39**:249–307, 2001.

[51] G. Hinshaw, D. N. Spergel, L. Verde, R. S. Hill, S. S. Meyer, C. Barnes, C. L. Bennett, M. Halpern, N. Jarosik, A. Kogut, E. Komatsu, M. Limon, L. Page, G. S. Tucker, J. L. Weiland, E. Wollack, and E. L. Wright. *First-Year Wilkinson Microwave Anisotropy Probe (WMAP) Observations: The Angular Power Spectrum*. *ApJS*, **148**:135–159, 2003.

[52] W. Hu and M. White. *A CMB Polarization Primer*. *New A*, **2**:323, 1997.

[53] E. Hubble. *A Relation between distance and radial velocity among extra-galactic nebulae*. *Astron. Notes*, **222**:21, 1924.

[54] N. Itoh, Y. Kohyama, and S. Nozawa. *Relativistic Corrections to the Sunyaev-Zeldovich Effect for Clusters of Galaxies*. *ApJ*, **502**:7–+, 1998.

[55] W. C. Jones, P. A. R. Ade, J. J. Bock, J. R. Bond, J. Borrill, A. Boscaleri, P. Cabella, C. R. Contaldi, B. P. Crill, P. de Bernardis, G. De Gasperis, A. de Oliveira-Costa, G. De Troia, G. di Stefano, E. Hivon, A. H. Jaffe, T. S. Kisner, A. E. Lange, C. J. MacTavish, S. Masi, P. D. Mauskopf, A. Melchiorri, T. E. Montroy, P. Natoli, C. B. Netterfield, E. Pascale, F. Piacentini, D. Pogosyan, G. Polenta, S. Prunet, S. Ricciardi, G. Romeo, J. E. Ruhl, P. Santini, M. Tegmark, M. Veneziani, and N. Vittorio. *A Measurement of the Angular Power Spectrum of the CMB Temperature Anisotropy from the 2003 Flight of BOOMERanG*. *ApJ*, **647**:823–832, 2006.

[56] B. Keating et al. *Large angular scale Polarization of the CMBR and the feasibility of its detection*. *ApJ*, **495**:580, 1997.

[57] A. Kogut, D. N. Spergel, C. Barnes, C. L. Bennett, M. Halpern, G. Hinshaw, N. Jarosik, M. Limon, S. S. Meyer, L. Page, G. S. Tucker, E. Wollack, and E. L. Wright. *First-Year Wilkinson Microwave Anisotropy Probe (WMAP) Observations: Temperature-Polarization Correlation*. *ApJS*, **148**:161–173, 2003.

[58] E. W. Kolb and M. S. Turner. *The Early Universe*. Addison Wesley Publishing Company, 1990.

[59] E. Komatsu, A. Kogut, M. R. Nolta, C. L. Bennett, M. Halpern, G. Hinshaw, N. Jarosik, M. Limon, S. S. Meyer, L. Page, D. N. Spergel, G. S. Tucker, L. Verde, E. Wollack, and E. L. Wright. *First-Year Wilkinson Microwave Anisotropy Probe (WMAP) Observations: Tests of Gaussianity*. *ApJS*, **148**:119–134, 2003.

[60] A. Kompaneets. *The Establishment of Thermal Equilibrium between Quanta and Electrons. J. Exp. Theor. Phys.*, **4**:730–737, 1957.

[61] A. Kosowsky. *Cosmic Microwave Background Polarization. Annals Phys.*, **246**:49, 1996.

[62] A. Kosowsky. *Introduction to Microwave Background Polarization. New A Rev.*, **43**:157, 1999.

[63] J. M. Kovac, E. M. Leitch, C. Pryke, J. E. Carlstrom, N. W. Halverson, and W. L. Holzapfel. *Detection of polarization in the cosmic microwave background using DASI*. *Nature*, **420**:772–787, 2002.

[64] C. L. Kuo, P. A. R. Ade, J. J. Bock, C. Cantalupo, M. D. Daub, J. Goldstein, W. L. Holzapfel, A. E. Lange, M. Lueker, M. Newcomb, J. B. Peterson, J. Ruhl, M. C. Runyan, and E. Torbet. *High-Resolution Observations of the Cosmic Microwave Background Power Spectrum with ACBAR. ApJ*, **600**:32–51, January 2004.

[65] G. Lagache, H. Dole, and J.-L. Puget. *Modelling infrared galaxy evolution using a phenomenological approach. MNRAS*, **338**:555–571, January 2003.

[66] G. Lagache and J. L. Puget. *Detection of the extra-Galactic background fluctuations at 170 mu m. A&A*, **355**:17–22, March 2000.

[67] A. T. Lee, P. Ade, A. Balbi, J. Bock, J. Borrill, A. Boscaleri, P. de Bernardis, P. G. Ferreira, S. Hanany, V. V. Hristov, A. H. Jaffe, P. D. Mauskopf, C. B. Netterfield, E. Pascale, B. Rabii, P. L. Richards, G. F. Smoot, R. Stompor, C. D. Winant, and J. H. P. Wu. *A High Spatial Resolution Analysis of the MAXIMA-1 Cosmic Microwave Background Anisotropy Data. ApJL*, **561**:L1–L5, 2001.

[68] S. F. Lee, J. M. Gildemeister, W. Holmes, A. T. Lee, and P. L. Richards. *Voltage-biased superconducting transition-edge bolometer with strong electrothermal feedback operated at* $370mK$. *Appl. Opt.*, **37**:3391–3397, 1998.

[69] E. M. Leitch, J. M. Kovac, C. Pryke, J. E. Carlstrom, N. W. Halverson, W. L. Holzapfel, M. Dragovan, B. Reddall, and E. S. Sandberg. *Measurement of polarization with the Degree Angular Scale Interferometer. Nature*, **420**:763–771, 2002.

[70] S. J. Lilly, S. A. Eales, W. K. P. Gear, F. Hammer, O. Le Fèvre, D. Crampton, J. R. Bond, and L. Dunne. *The Canada-United Kingdom Deep Submillimeter Survey. II. First Identifications, Redshifts, and Implications for Galaxy Evolution. ApJ*, **518**:641–655, June 1999.

[71] C. J. MacTavish, P. A. R. Ade, J. J. Bock, J. R. Bond, J. Borrill, A. Boscaleri, P. Cabella, C. R. Contaldi, B. P. Crill, P. de Bernardis, G. De Gasperis, A. de Oliveira-Costa, G. De Troia, G. di Stefano, E. Hivon, A. H. Jaffe, W. C. Jones, T. S. Kisner, A. E. Lange, A. M. Lewis, S. Masi, P. D. Mauskopf, A. Melchiorri, T. E. Montroy, P. Natoli, C. B. Netterfield, E. Pascale, F. Piacentini, D. Pogosyan, G. Polenta, S. Prunet, S. Ricciardi, G. Romeo, J. E. Ruhl, P. Santini, M. Tegmark, M. Veneziani, and N. Vittorio. *Cosmological Parameters from the 2003 Flight of BOOMERanG*. *ApJ*, **647**:799–812, 2006.

[72] S. Masi, P. A. R. Ade, J. J. Bock, J. R. Bond, J. Borrill, A. Boscaleri, P. Cabella, C. R. Contaldi, B. P. Crill, P. de Bernardis, G. de Gasperis, A. de Oliveira-Costa, G. de Troia, G. di Stefano, P. Ehlers, E. Hivon, V. Hristov, A. Iacoangeli, A. H. Jaffe, W. C. Jones, T. S. Kisner, A. E. Lange, C. J. MacTavish, C. Marini Bettolo, P. Mason, P. D. Mauskopf, T. E. Montroy, F. Nati, L. Nati, P. Natoli, C. B. Netterfield, E. Pascale, F. Piacentini, D. Pogosyan, G. Polenta, S. Prunet, S. Ricciardi, G. Romeo, J. E. Ruhl, P. Santini, M. Tegmark, E. Torbet, M. Veneziani, and N. Vittorio. *Instrument, method, brightness, and polarization maps from the 2003 flight of BOOMERanG*. *A&A*, **458**:687–716, November 2006.

[73] S. Masi, M. Calvo, L. Conversi, P. de Bernardis, M. de Petris, G. de Troia, A. Iacoangeli, L. Lamagna, C. Marini Bettolo, A. Melchiorri, F. Melchiorri, L. Nati, F. Nati, F. Piacentini, G. Polenta, E. Valiante, P. Ade, P. Hargrave, P. Mauskopf, A. Orlando, G. Pisano, G. Savini, C. Tucker, A. Boscaleri, S. Peterzen, S. Colafrancesco, Y. Rephaeli, G. Romeo, L. Salvaterra, A. Delbart, J. B. Juin, C. Magneville, J. P. Pansart, and D. Yvon. *A balloon-borne survey of the mm/sub-mm sky: OLIMPO*. In B. Warmbein, editor, *ESA SP-590: 17th ESA Symposium on European Rocket and Balloon Programmes and Related Research*, pages 581–586, August 2005.

[74] S. Masi, M. Calvo, L. Conversi, P. de Bernardis, M. de Petris, G. de Troia, A. Iacoangeli, L. Lamagna, C. Marini Bettolo, A. Melchiorri, F. Melchiorri, L. Nati, F. Nati, F. Piacentini, G. Polenta, E. Valiante, P. Ade, P. Hargrave, P. Mauskopf, A. Orlando, G. Pisano, G. Savini, C. Tucker, A. Boscalieri, S. Peterzen, S. Colafrancesco, Y. Rephaeli, G. Romeo, L. Salvaterra, A. Delbart, J. B. Juin, C. Magneville, J. P. Pansart, and D. Yvon. *OLIMPO: A multi-frequency survey of galaxy clusters and of the cosmic millimetric background*. In F. Melchiorri and Y. Rephaeli, editors, *Background Microwave Radiation and Intracluster Cosmology*, pages 359–+, 2005.

[75] J. C. Mather, E. S. Cheng, D. A. Cottingham, R. E. Eplee, Jr., D. J. Fixsen, T. Hewagama, R. B. Isaacman, K. A. Jensen, S. S. Meyer, P. D. Noerdlinger, S. M. Read, L. P. Rosen, R. A. Shafer, E. L. Wright, C. L. Bennett, N. W. Boggess, M. G. Hauser, T. Kelsall, S. H. Moseley, Jr., R. F. Silverberg, G. F. Smoot, R. Weiss, and D. T. Wilkinson. *Measurement of the cosmic microwave background spectrum by the COBE FIRAS instrument*. *ApJ*, **420**:439–444, 1994.

[76] J. C. Mather, E. S. Cheng, R. E. Eplee, Jr., R. B. Isaacman, S. S. Meyer, R. A. Shafer, R. Weiss, E. L. Wright, C. L. Bennett, N. W. Boggess, E. Dwek, S. Gulkis, M. G. Hauser, M. Janssen, T. Kelsall, P. M. Lubin, S. H. Moseley, Jr., T. L. Murdock,

R. F. Silverberg, G. F. Smoot, and D. T. Wilkinson. *A preliminary measurement of the cosmic microwave background spectrum by the Cosmic Background Explorer (COBE) satellite*. *ApJL*, **354**:L37–L40, 1990.

[77] J. S. Mathis. *Interstellar dust and extinction*. *ARA&A*, **28**:37–70, 1990.

[78] H. Matsuhara, K. Kawara, Y. Sato, Y. Taniguchi, H. Okuda, T. Matsumoto, Y. Sofue, K. Wakamatsu, L. L. Cowie, R. D. Joseph, and D. B. Sanders. *ISO deep far-infrared survey in the "Lockman Hole". II. Power spectrum analysis: evidence of a strong evolution in number counts*. *A&A*, **361**:407–414, September 2000.

[79] T. E. Montroy, P. A. R. Ade, J. J. Bock, J. R. Bond, J. Borrill, A. Boscaleri, P. Cabella, C. R. Contaldi, B. P. Crill, P. de Bernardis, G. De Gasperis, A. de Oliveira-Costa, G. De Troia, G. di Stefano, E. Hivon, A. H. Jaffe, T. S. Kisner, W. C. Jones, A. E. Lange, S. Masi, P. D. Mauskopf, C. J. MacTavish, A. Melchiorri, P. Natoli, C. B. Netterfield, E. Pascale, F. Piacentini, D. Pogosyan, G. Polenta, S. Prunet, S. Ricciardi, G. Romeo, J. E. Ruhl, P. Santini, M. Tegmark, M. Veneziani, and N. Vittorio. *A Measurement of the CMB EE Spectrum from the 2003 Flight of BOOMERanG*. *ApJ*, **647**:813–822, 2006.

[80] F. Nati, L. Nati, L. Conversi, S. Masi, M. Calvo, P. de Bernardis, M. De Petris, G. De Troia, A. Iacoangeli, L. Lamagna, C. Marini Bettolo, A. Melchiorri, F. Melchiorri, F. Piacentini, G. Polenta, E. Valiante, P. Ade, P. Hargrave, P. Mauskopf, A. Orlando, G. Pisano, G. Savini, C. Tucker, A. Boscaleri, S. Peterzen, S. Colafrancesco, Y. Rephaeli, G. Romeo, L. Salvaterra, A. Delbart, J.B. Juin, C. Magneville, J.P. Pansart, and D. Yvon. *A long duration balloon-borne mm/sum-mm telescope for multi-frequency survey of galaxy cluters and CMB*. In M. Magneville, J. Dumarchez, and J. Trân Thanh Vân, editors, *Contents and Structures of the Universe*, pages 269–275, 2006.

[81] P. Natoli, G. de Gasperis, C. Gheller, and N. Vittorio. *A Map-Making algorithm for the Planck Surveyor*. *A&A*, **372**:346–356, June 2001.

[82] T. Onaka, I. Yamamura, T. Tanabe, T. L. Roellig, and L. Yuen. *Detection of the Mid-Infrared Unidentified Bands in the Diffuse Galactic Emission by IRTS*. *PASJ*, **48**:L59–L63, 1996.

[83] T. Padmanabhan. *Structure formation in the Universe*. Cambridge University Press, 1993.

[84] L. Page, M. R. Nolta, C. Barnes, C. L. Bennett, M. Halpern, G. Hinshaw, N. Jarosik, A. Kogut, M. Limon, S. S. Meyer, H. V. Peiris, D. N. Spergel, G. S. Tucker, E. Wollack, and E. L. Wright. *First-Year Wilkinson Microwave Anisotropy Probe (WMAP) Observations: Interpretation of the TT and TE Angular Power Spectrum Peaks*. *ApJS*, **148**:233–241, 2003.

[85] R. B. Partridge and P. J. E. Peebles. *Are Young Galaxies Visible? II. The Integrated Background*. *ApJ*, **148**:377–+, May 1967.

[86] J. A. Peacock, M. Rowan-Robinson, A. W. Blain, J. S. Dunlop, A. Efstathiou, D. H. Hughes, T. Jenness, R. J. Ivison, A. Lawrence, M. S. Longair, R. G. Mann, S. J. Oliver, and S. Serjeant. *Starburst galaxies and structure in the submillimetre background towards the Hubble Deep Field. MNRAS*, **318**:535–546, October 2000.

[87] C. Pearson and M. Rowan-Robinson. *Starburst galaxy contributions to extragalactic source counts. MNRAS*, **283**:174–192, November 1996.

[88] P. J. E. Peebles. *Principles of Physical Cosmology.* Princeton University Press, 1993.

[89] A. A. Penzias and R. W. Wilson. *A measurement of excess antenna temperature at 4080 Mc/s. ApJ*, **142**:419, 1965.

[90] S. Perlmutter, G. Aldering, G. Goldhaber, R. A. Knop, P. Nugent, P. G. Castro, S. Deustua, S. Fabbro, A. Goobar, D. E. Groom, I. M. Hook, A. G. Kim, M. Y. Kim, J. C. Lee, N. J. Nunes, R. Pain, C. R. Pennypacker, R. Quimby, C. Lidman, R. S. Ellis, M. Irwin, R. G. McMahon, P. Ruiz-Lapuente, N. Walton, B. Schaefer, B. J. Boyle, A. V. Filippenko, T. Matheson, A. S. Fruchter, N. Panagia, H. J. M. Newberg, W. J. Couch, and The Supernova Cosmology Project. *Measurements of Omega and Lambda from 42 High-Redshift Supernovae. ApJ*, **517**:565–586, June 1999.

[91] F. Piacentini, P. A. R. Ade, J. J. Bock, J. R. Bond, J. Borrill, A. Boscaleri, P. Cabella, C. R. Contaldi, B. P. Crill, P. de Bernardis, G. De Gasperis, A. de Oliveira-Costa, G. De Troia, G. di Stefano, E. Hivon, A. H. Jaffe, T. S. Kisner, W. C. Jones, A. E. Lange, S. Masi, P. D. Mauskopf, C. J. MacTavish, A. Melchiorri, T. E. Montroy, P. Natoli, C. B. Netterfield, E. Pascale, D. Pogosyan, G. Polenta, S. Prunet, S. Ricciardi, G. Romeo, J. E. Ruhl, P. Santini, M. Tegmark, M. Veneziani, and N. Vittorio. *A Measurement of the Polarization-Temperature Angular Cross-Power Spectrum of the Cosmic Microwave Background from the 2003 Flight of BOOMERanG. ApJ*, **647**:833–839, 2006.

[92] W. H. Press and P. Schechter. *Formation of Galaxies and Clusters of Galaxies by Self-Similar Gravitational Condensation. ApJ*, **187**:425–438, February 1974.

[93] W. H. Press, S. A. Teukolsky, W. T. Vetterling, and B. P. Flannery. *Numerical recipes in C. The art of scientific computing.* Cambridge: University Press, —c1992, 2nd ed., 1992.

[94] J.-L. Puget, A. Abergel, J.-P. Bernard, F. Boulanger, W. B. Burton, F.-X. Desert, and D. Hartmann. *Tentative detection of a cosmic far-infrared background with COBE. A&A*, **308**:L5+, April 1996.

[95] A. C. S. Readhead, B. S. Mason, C. R. Contaldi, T. J. Pearson, J. R. Bond, S. T. Myers, S. Padin, J. L. Sievers, J. K. Cartwright, M. C. Shepherd, D. Pogosyan, S. Prunet, P. Altamirano, R. Bustos, L. Bronfman, S. Casassus, W. L. Holzapfel, J. May, U.-L. Pen, S. Torres, and P. S. Udomprasert. *Extended Mosaic Observations with the Cosmic Background Imager. ApJ*, **609**:498–512, July 2004.

[96] Y. Rephaeli. *Comptonization Of The Cosmic Microwave Background: The Sunyaev-Zeldovich Effect. ARA&A*, **33**:541–580, 1995.

[97] Y. Rephaeli. *Cosmic microwave background comptonization by hot intracluster gas. ApJ*, **445**:33–36, 1995.

[98] Y. Rephaeli and O. Lahav. *Peculiar cluster velocities from measurements of the kinematic Sunyaev-Zeldovich effect. ApJ*, **372**:21–24, 1991.

[99] A. G. Riess, L.-G. Strolger, J. Tonry, S. Casertano, H. C. Ferguson, B. Mobasher, P. Challis, A. V. Filippenko, S. Jha, W. Li, R. Chornock, R. P. Kirshner, B. Leibundgut, M. Dickinson, M. Livio, M. Giavalisco, C. C. Steidel, T. Benítez, and Z. Tsvetanov. *Type Ia Supernova Discoveries at $z > 1$ from the Hubble Space Telescope: Evidence for Past Deceleration and Constraints on Dark Energy Evolution. ApJ*, **607**:665–687, June 2004.

[100] M. Rowan-Robinson, T. Broadhurst, S. J. Oliver, A. N. Taylor, A. Lawrence, R. G. McMahon, C. J. Lonsdale, P. B. Hacking, T. Conrow, W. Saunders, R. S. Ellis, G. P Efstathiou, and J. J. Condon. *A high-redshift IRAS galaxy with huge luminosity - Hidden quasar or protogalaxy? Nature*, **351**:719–721, June 1991.

[101] D. B. Sanders and I. F. Mirabel. *Luminous Infrared Galaxies. ARA&A*, **34**:749–+, 1996.

[102] C. L. Sarazin. *X-Ray Emissions from Clusters of Galaxies. S&T*, **76**:639–+, 1988.

[103] D. J. Schroeder. Astronomical Optics. San Diego: Academic Press, 1987, 1987.

[104] G. F. Smoot, C. L. Bennett, A. Kogut, E. L. Wright, J. Aymon, N. W. Boggess, E. S. Cheng, G. de Amici, S. Gulkis, M. G. Hauser, G. Hinshaw, P. D. Jackson, M. Janssen, E. Kaita, T. Kelsall, P. Keegstra, C. Lineweaver, K. Loewenstein, P. Lubin, J. Mather, S. S. Meyer, S. H. Moseley, T. Murdock, L. Rokke, R. F. Silverberg, L. Tenorio, R. Weiss, and D. T. Wilkinson. *Structure in the COBE differential microwave radiometer first-year maps. ApJL*, **396**:L1–L5, 1992.

[105] D. N. Spergel, L. Verde, H. V. Peiris, E. Komatsu, M. R. Nolta, C. L. Bennett, M. Halpern, G. Hinshaw, N. Jarosik, A. Kogut, M. Limon, S. S. Meyer, L. Page, G. S. Tucker, J. L. Weiland, E. Wollack, and E. L. Wright. *First-Year Wilkinson Microwave Anisotropy Probe (WMAP) Observations: Determination of Cosmological Parameters. ApJS*, **148**:175–194, 2003.

[106] V. Springel. *The cosmological simulation code GADGET-2. MNRAS*, **364**:1105–1134, December 2005.

[107] V. Springel, S. D. M. White, A. Jenkins, C. S. Frenk, N. Yoshida, L. Gao, J. Navarro, R. Thacker, D. Croton, J. Helly, J. A. Peacock, S. Cole, P. Thomas, H. Couchman, A. Evrard, J. Colberg, and F. Pearce. *Simulations of the formation, evolution and clustering of galaxies and quasars. Nature*, **435**:629–636, June 2005.

[108] P. Sreekumar, D. L. Bertsch, B. L. Dingus, J. A. Esposito, C. E. Fichtel, R. C. Hartman, S. D. Hunter, G. Kanbach, D. A. Kniffen, Y. C. Lin, H. A. Mayer-Hasselwander, P. F. Michelson, C. von Montigny, A. Muecke, R. Mukherjee, P. L. Nolan, M. Pohl, O. Reimer, E. Schneid, J. G. Stacy, F. W. Stecker, D. J. Thompson, and T. D. Willis. *EGRET Observations of the Extragalactic Gamma-Ray Emission. ApJ*, **494**:523–+, February 1998.

[109] M. Stickel, D. Lemke, U. Klaas, C. A. Beichman, M. Rowan-Robinson, A. Efstathiou, S. Bogun, M. F. Kessler, and G. Richter. *The ISOPHOT 170 μ m serendipity survey. I. Compact sources with galaxy associations. A&A*, **359**:865–875, July 2000.

[110] R. Stompor, M. Abroe, P. Ade, A. Balbi, D. Barbosa, J. Bock, J. Borrill, A. Boscaleri, P. de Bernardis, P. G. Ferreira, S. Hanany, V. Hristov, A. H. Jaffe, A. T. Lee, E. Pascale, B. Rabii, P. L. Richards, G. F. Smoot, C. D. Winant, and J. H. P. Wu. *Cosmological Implications of the MAXIMA-1 High-Resolution Cosmic Microwave Background Anisotropy Measurement. ApJL*, **561**:L7–L10, 2001.

[111] R. A. Sunyaev and I. B. Zeldovich. *Microwave background radiation as a probe of the contemporary structure and history of the universe. ARA&A*, **18**:537–560, 1980.

[112] R. A. Sunyaev and I. B. Zeldovich. *The velocity of clusters of galaxies relative to the microwave background - The possibility of its measurement. MNRAS*, **190**:413–420, 1980.

[113] R. A. Sunyaev and Y. B. Zeldovich. *Distortions of the Background Radiation Spectrum. Nature*, **223**:721–+, 1969.

[114] R. A. Sunyaev and Y. B. Zeldovich. *The Observations of Relic Radiation as a Test of the Nature of X-Ray Radiation from the Clusters of Galaxies. Comments on Astrophysics and Space Physics*, **4**:173–+, 1972.

[115] T. T. Takeuchi and T. T. Ishii. *A dust emission model of Lyman-break galaxies. A&A*, **426**:425–435, November 2004.

[116] M. Tanaka, T. Matsumoto, H. Murakami, M. Kawada, M. Noda, and S. Matsuura. *IRTS Observation of the Unidentified 3.3-Micron Band in the Diffuse Galactic Emission. PASJ*, **48**:L53–L57, 1996.

[117] W. T. Welford. *Optical estimation of statistics of surface roughness from light scattering measurements. Optical and Quantum Electronics*, **9**:269–287, 1977.

[118] C. Wirtz. *De Sitters cosmologie und die radialbewegungen der spiralnebel. Proc. Nat. Acad. Sci.*, **15**:168, 1929.

[119] E. L. Wright. *Distortion of the microwave background by a hot intergalactic medium. ApJ*, **232**:348–351, 1979.

[120] X. Wu, T. Hamilton, D. J. Helfand, and Q. Wang. *The intensity and spectrum of the diffuse X-ray background. ApJ*, **379**:564–575, October 1991.

[121] M. Zaldarriaga. *The nature of the E-B decomposition of the CMB Polarization. Phys. Rev. D*, **64**:103001, 2001.

[122] Y. B. Zeldovich and R. A. Sunyaev. *The Interaction of Matter and Radiation in a Hot-Model Universe. Ap&SS*, **4**:301–+, 1969.

List of Figures

List of Tables